Title
Modular Syntheses and Applications of Functionalized Graphene Nanoribbons

Author
Joshi, Dharati P

Publication Date
2019

Peer reviewed|Thesis/dissertation

Modular Syntheses and Applications of Functionalized Graphene Nanoribbons

By

Dharati P Joshi

A dissertation submitted in partial satisfaction of the

requirements for the degree of

Doctor of Philosophy

in

Chemistry

in the

Graduate Division

of the

University of California, Berkeley

Committee in charge

Professor Felix Fischer, Chair
Professor Thomas Maimone
Professor Thomas Devine

Spring 2019

Modular Syntheses and Applications of Functionalized Graphene Nanoribbons

Abstract

Modular Syntheses and Applications of Functionalized Graphene Nanoribbons

By

Dharati P Joshi

Doctor of Philosophy in Chemistry

University of California, Berkeley

Professor Felix Fischer, Chair

Laterally confining graphene into 1D strips known as graphene nanoribbons (GNRs) opens up a tunable bandgap dependent on width, edge structure, and dopant atoms, while still preserving the exceptional physical and electronic properties associated with graphene. As a result, GNRs have been heralded as materials for post-silicon electronics development and recently have become promising candidates as catalytic support materials. Deterministic bottom up synthesis is key to accessing atomically precise GNRs and has the powerful capability of "writing-in" selective properties by controlling the structure. The solution synthesis of these materials enables large scale production of GNRs; however, their integration into organic electronic devices is hampered by their visualization and localization on the surface by scanning probe microscopies and the functionalities that can be installed must survive the harsh parameters of synthesis. To this end, we have developed an azide functionalized GNR to enable late stage modification via copper-catalyzed click-chemistry (Chapter 2). "Clicking" on Cy5 fluorescent dyes gives rise to GNRs decorated along the edges with fluorescent tags detectable by optical microscopy and thus can be more efficiently visualized and localized by super resolution imaging. Bandgap engineering by tuning the width and edge structure of GNRs, as well as global alignment of GNRs is also required for their integration into next generation electronic devices (Chapter 4). Furthermore, bulk GNRs are proven to have practical applications beyond functioning as channel materials for electronic devices as tunable catalytic support materials (Chapter 3).

In loving memory of

Thakorlal Vyas

My grandfather, who always wanted me to be a doctor…

Contents

List of Figures

Acknowledgements

I would like to thank my amazing family, especially my Mom, Dad, and Niki, for their support, unconditional love and unwavering confidence in me. Despite being so far away, you have all always been close to my heart and I appreciate everything you have done for me. I would also like to thank my wonderful husband David, without whom I would be lost. I am also grateful to my fur babies, Beanie and Winston, who never stop making me laugh and smile with their silly bunny antics. The nature of my work is very interdisciplinary and thus a lot of this work could not be possible without the help of my collaborators: Meghan Hauser, Professor Ke Xu, Lennie Klebanoff, Don Cowgill, Dan Rizzo, and Professor Michael Crommie. I would also like to thank my friends and fellow group members for their support, advice, scientific discussions and fun over the past five years. This work was also done with the help of my amazing undergraduate student, Alexandra Berl, who always had a pun for every lab scenario. I am very grateful to Felix Fischer for his mentorship and scientific guidance. I am also thankful to Felix for the scientific freedom he gave me to pursue the work I found interesting and fulfilling and without whom this work would not be possible.

Chapter 1

Introduction

The first chapter of this thesis provides the literature foundation on synthetic methods, characterization and applications of GNRs required for chapters 2–4. An introduction to graphene is presented followed by the motivation for laterally confining graphene into 1D strips known as graphene nanoribbons. Two different synthetic methods have been employed to access GNRs: top down approaches and bottom up synthesis, which will be compared in this chapter. The existing characterization tools and applications of GNRs is also provided.

1.1 Graphene

Graphene is a two-dimensional one-atom thick hexagonal lattice of sp^2-hybridized carbon atoms. It was first isolated in 2004 using the "Scotch–tape method" to isolate a single sheet of graphene from graphite by Novoselov and Geim, who were awarded the Nobel Prize in physics in 2010 for this work. Graphene has many notable physical and, more interestingly, electronic properties. [1–5] Specifically, graphene has a high thermal conductivity of 3,000–5,000 W m^{-1} K^{-1}, an intrinsic tensile strength of ~130 GPa, and a Young's modulus of ~1 TPa. Additionally, graphene has been heralded for its high charge carrier mobility of μ = 200 000 cm^2 V^{-1} s^{-1}, at room temperature, a value that surpasses μ for any other semiconductor measured.[6] Unlike traditional semiconductors, the conduction and valence bands of graphene meet at the Dirac point causing graphene to be a zero band gap semiconductor.[7] Despite graphene's many remarkable properties, the lack of a band gap limits the use of this material in electronic devices. However, narrow strips of graphene known as graphene nanoribbons (GNRs) do exhibit a band gap due to lateral quantum confinement, making them promising candidates for devices such as field effect transistors (FETs) and chemical senors.[8–11]

1.2 Graphene Nanoribbons

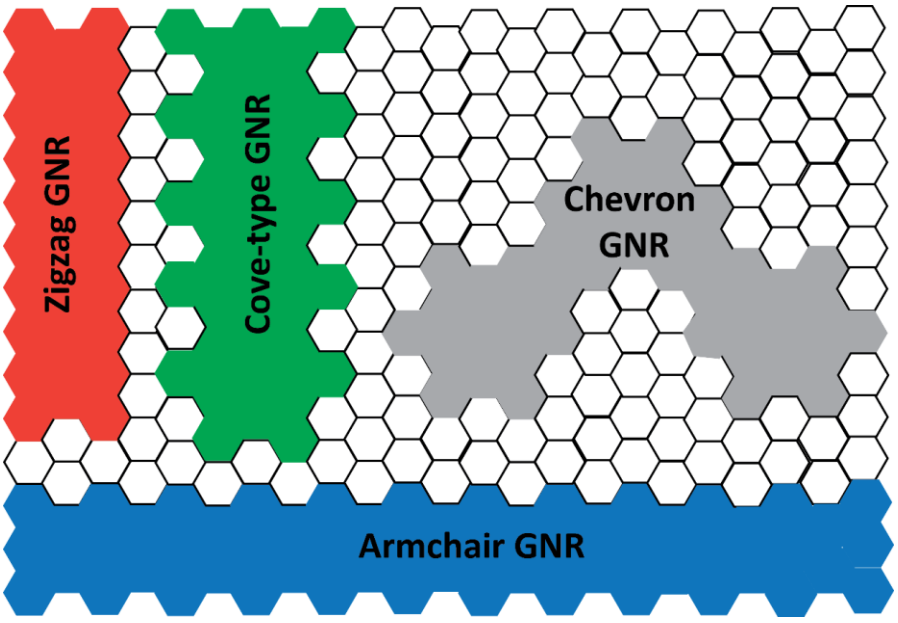

Figure 1.1 The four most common GNR edge structures: armchair GNRs (AGNR), zigzag GNRs (zGNRs), cove-type GNRs (cGNR), and chevron GNRs (CGNRs).

The quantum mechanical confinement of two dimensional infinite sheets of graphene into one dimension narrow graphene nanoribbons (GNRs) leads to an opening of a band gap between the conduction and valence band. This band gap is heavily dependent upon the edge, width and

dopant structure of the resulting GNRs. Thus, having atomic control of these properties allows one to tune the electronic properties of GNRs. This, together with graphene's high mobility and high current carrying capabilities, has raised GNRs to be a widely sought after material in the next generation semiconductor industry.

GNRs have a variety of different edge structures, and the four main commonly studied edge structures, depicted in Figure 1.1, are armchair (AGNRs), zigzag (ZGNRs) cove-type (cGNRs) and chevron type (CGNRs). This dissertation will focus on different types of AGNRs, cGNRs, and CGNRs. Density functional theory (DFT) calculations and experimental evidence have shown that most GNRs have an inverse relationship with the width and the size of the band gap and thus narrower ribbons have larger energy differences.[12–15] AGNRs can be divided into three families of ribbons, N = 3*p*, 3*p*+1, and 3*p*+2, where N is the number of atoms across the width of the ribbon and *p* is an integer. The GNRs are divided according to their electronic structures, and the energy gaps for the three families are quite different even with the same *p*. The bandgap of AGNRs is inversely proportional to its width and according to the hierarchy of gap size given by N = 3*p*+1 > 3*p* > 3*p*+2 (Figure 1.2).[16,17] Two different synthetic methods have been employed to access GNRs: top down patterning of large graphitic structures and controlled bottom up synthesis from small molecule precursors.

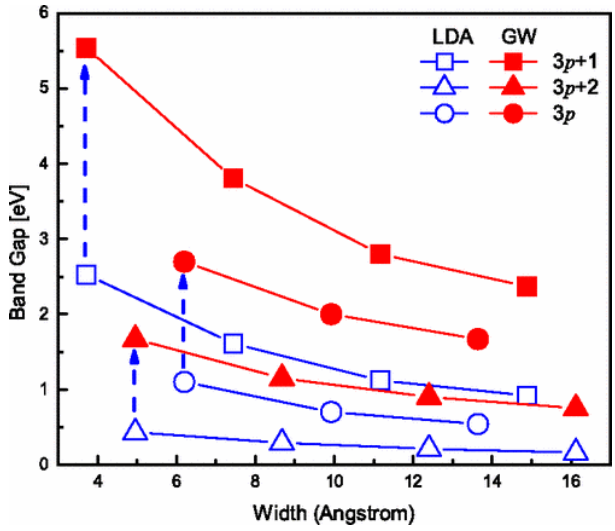

Figure 1.2 LDA and GW predictions of AGNR bandgap dependence on width of ribbon. Image reproduced from *Phys. Rev. Lett.* **99**, (2007).[15]

1.2.1 Top Down Approach

GNRs were first isolated via top down synthesis. These methods start with large graphitic structures such as graphene, graphite and carbon nanotubes (CNTs), and laterally confine them into narrow ribbons and will be discussed in more detail below. While top down synthesis has the advantage of synthesizing large amounts of material, they suffer from two main drawbacks. First, top down syntheses are not atomically precise and thus control of edge structure and defect sites

are major challenges. Second, these methods are unable to reproducibly synthesize GNRs with widths less than 10 nm.

Lithographic Patterning and Etching of Graphene

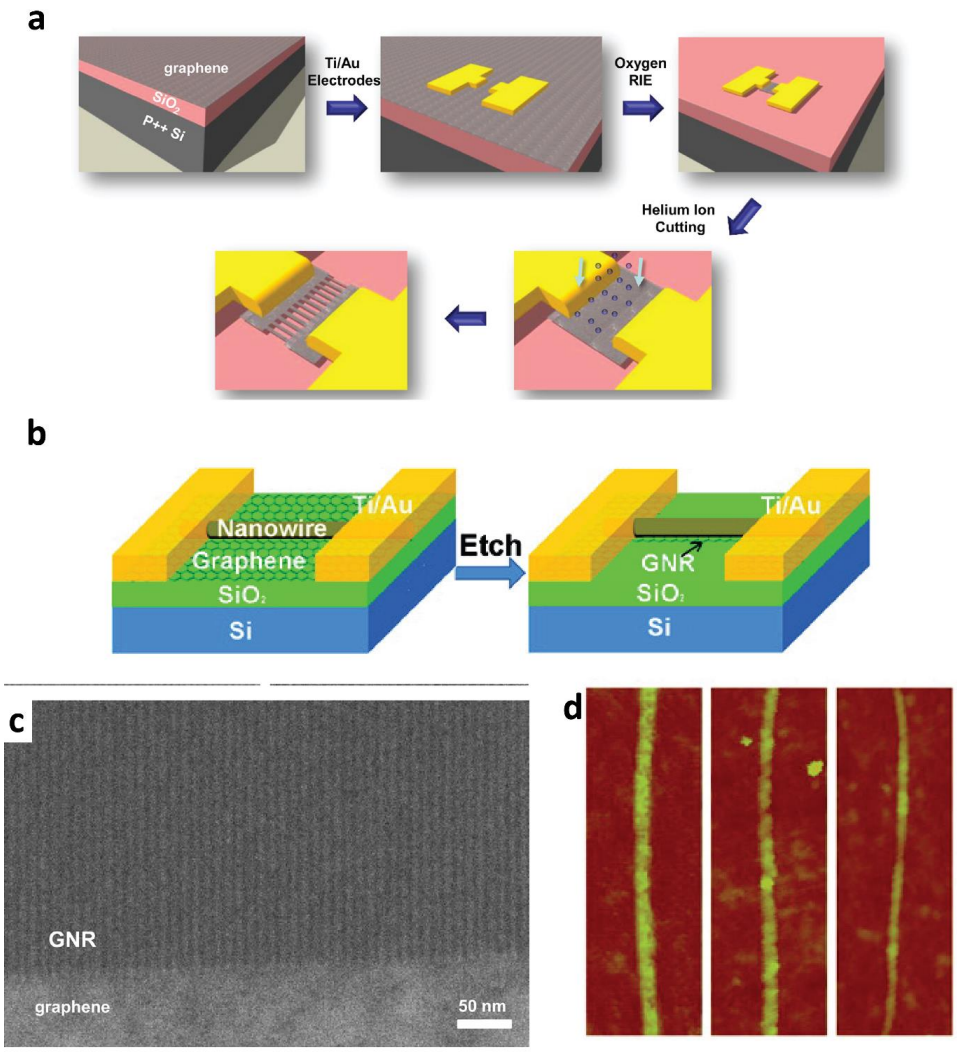

Figure 1.3 Lithographic patterning and etching graphene (a) Scheme of GNRs fabricated by helium ion beam lithography. Image reproduced from *ACS Nano* **8,** 1538–1546 (2014).[18] (b) Schematic representation of a device based on GNRs etched from graphene using nanowire etch masks. Image reproduced from *Nano Lett.* **9,** 2083–2087 (2009).[22] (c) Helium ion microscope image shows smooth interface between graphene and patterned GNR arrays. Image reproduced from *ACS Nano* **8,** 1538–1546 (2014).[18] (d) AFM images of selected GNRs with various width after etching with nanowire mask. Image reproduced from *Nano Lett.* **9,** 2083–2087 (2009).[22]

Etching or cutting graphene sheets to form GNRs has the advantage of producing aligned arrays of GNRs and fabricating GNRs on pre-patterned contacts facilitating device fabrication (Figure 1.3a).[18,19] In 2007, Han et al. contacted individual graphene with metal electrodes and then patterned etch masks using electron beam (e-beam) lithography. Subsequent oxygen plasma

etching produced GNRs of various widths already aligned between electrodes, enabling efficient device fabrication and electron transport measurements.[19] In addition to oxygen plasma etching, hydrogen plasma has also been used to etch away the exposed graphene after lithographic patterning.[20] This methodology, however, does not provide atomic control over the edge structure of the ribbons and the harsh reaction conditions often lead to GNRs with many defects.

Tapasztó and coworkers were able to improve upon this methodology by combining the scanning tunneling microscopy (STM) techniques of surface modification and atomic resolution imaging to engineer GNRs with greater control of the edge structure. They were able to cut single graphene sheets by applying a high constant bias potential while simultaneously moving the STM tip. This method, however, is not scalable in the production of bulk GNRs and still result in some edge disorder in the ribbons.[21] In addition to using e-beam lithography and STM lithography, helium ion beam lithography has also been employed but is not widely used due to the destructive nature of the ion beam (Figure 1.3a and c).[18] Nanowire masks have also been utilized as physical protection masks during oxygen plasma etching as an alternative to lithography to achieve sub-10 nm width GNRs (Figure 1.3b and d).[22]

Unzipping CNTs

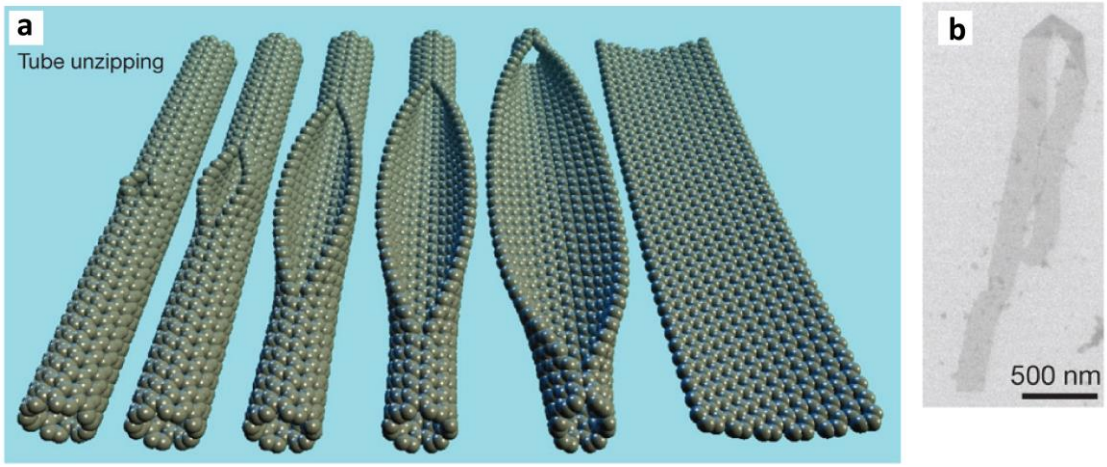

Figure 1.4 Unzipping of CNTs to form GNRs. (a) Schematic representation of unzipping a CNT to form a GNR. (b) SEM image of a folded, 4-μm-long single-layer nanoribbon on a silicon surface. Both images reproduced from *Nature* **458,** 872–876 (2009).[23]

Bulk samples of GNRs can be produced by unzipping CNTs. Various chemical reagents have been used to longitudinally unzip both single and multi-walled CNTs (Figure 1.4). These methods include oxidation of CNTs with concentrated sulfuric acid followed by treatment with $KMnO_4$,[23] intercalation of Li^+ in liquid NH_3,[24] and treatment with catalytic Ni or Co nanoparticles.[25] CNTs have also been unzipped by plasma etching,[26] high-current pulse burning,[27] and mild gas-phase oxidation step followed by sonication in organic solvents.[28] The edge structure and width of the resulting GNRs is directly correlated to the chirality of the CNTs used initially. As a result, these methods often produce a mixture of various types and width of GNRs since most

CNTs are a mixture of different widths and chirality. Additionally, these very harsh reaction conditions often lead to GNRs with many defect sites and edge oxidation.

Sonication of Graphene

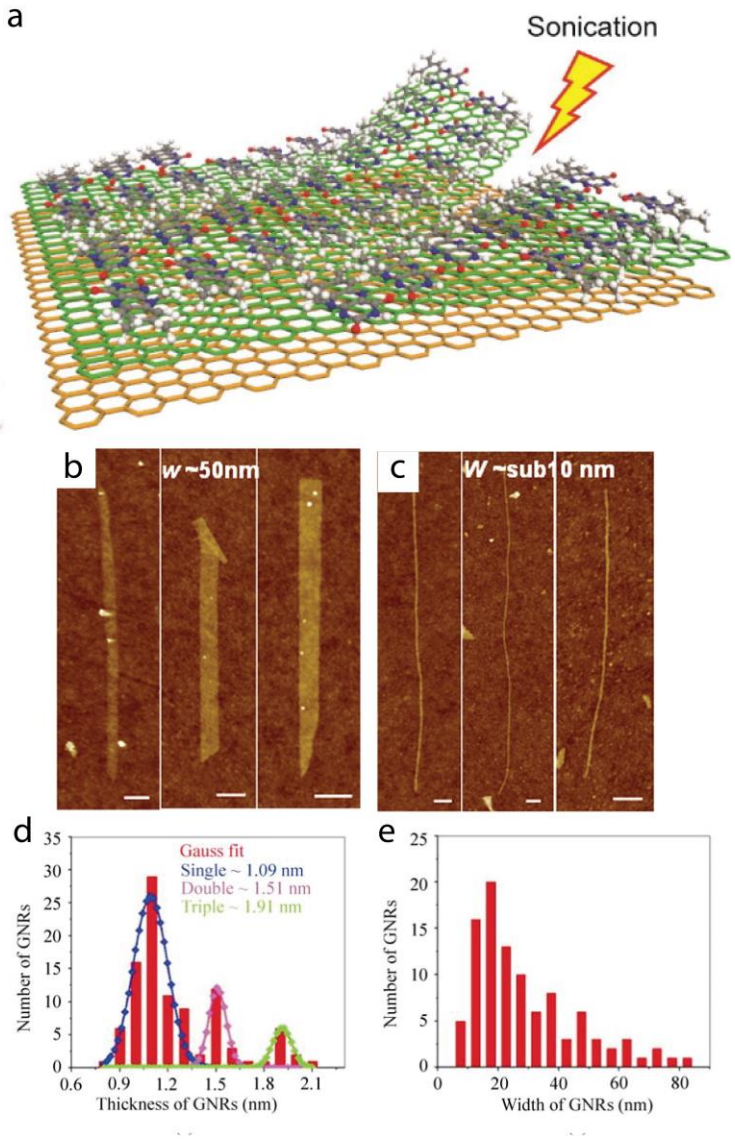

Figure 1.5 (a) Pictorial illustration of graphene unzipping into graphene nanoribbons upon sonication after templating with flavin mononucleotide. Imaged reproduced from *Carbon* **81**, 629–638 (2015).[30] (b) and (c) AFM images of selected GNRs with widths in the 50-nm and sub-10-nm regions, respectively, synthesized by sonochemical cutting of graphite flakes templated with PmPV. Images reproduced from *Science* **319**, 1229–32 (2008).[11] (d) and (e) The thickness and width distributions of 100 individual GNRs, respectively, of GNRs synthesized by sonochemical cutting of graphene sheets with PVP and sodium dodecyl sulfate. Images reproduced from *Nano Res* **3,** 16–22 (2010).[29]

An alternative method to synthesize GNRs takes advantage of naturally occurring defects in exfoliated graphite and graphene surfaces by sonochemical cutting of graphite flakes. This process usually involves dispersing exfoliated graphite flakes or graphene sheets with templating reagents and often surfactants, such as poly(m-phenylenevinylene-co-2,5-dioctoxy-p-phenylenevinylene) (PmPV),[11] mixtures of polyvinylpyrrolidone (PVP) and sodium dodecyl sulfate,[29] and flavin mononucleotide and its analogue,[30] followed by strong sonication (Figure 1.5a–c). In the case where PVP and sodium dodecyl sulfate were used, hydrazine hydrate was added after sonication and the reaction mixture was stirred at reflux for 36 hours to remove the oxygen-containing groups and to partially restore the extended conjugated sp^2 network of resulting GNRs.[29] All the methods then centrifuged the samples to remove larger particles and bundles and collected the supernatant to isolate the GNRs.

Sonochemical cutting of graphene has the advantage of using widely available graphite as the source material and is able to produce bulk samples of GNRs with edge roughness well below ribbon width. The drawbacks, however, are the resulting GNRs are often a mixture of various widths and lengths and often lead to GNR bundles of up a few stack layers due to the strong π-π stacking interaction between ribbons (Figure 1.5d and e).[29]

1.2.2 Bottom up Synthesis

Since the atomic structure of the GNRs is dependent upon its properties and any defects will also affect the electronic properties of the ribbon, atomic precision and rational design are key requirements for dialing-in desired electronic properties into the GNR. Unlike the previously described top down approaches which failed in this endeavor, bottom up synthesis which utilizes small molecule precursors as GNR building blocks has the powerful capability of both rational design and atomic control. Since these precursors will define the resulting GNR structure, including width, edge structure, geometry, and dopant positions, the properties of the resulting GNRs are predetermined by the monomer design. Bottom up syntheses employ a three step strategy: design of a molecular precursor, polymerization to a GNR polymer precursor, and finally cyclodehydrogenation to access the fully graphitized GNR. This strategy can be used to synthesize GNRs on metal surfaces in ultra-high vacuum (UHV) or in solution.

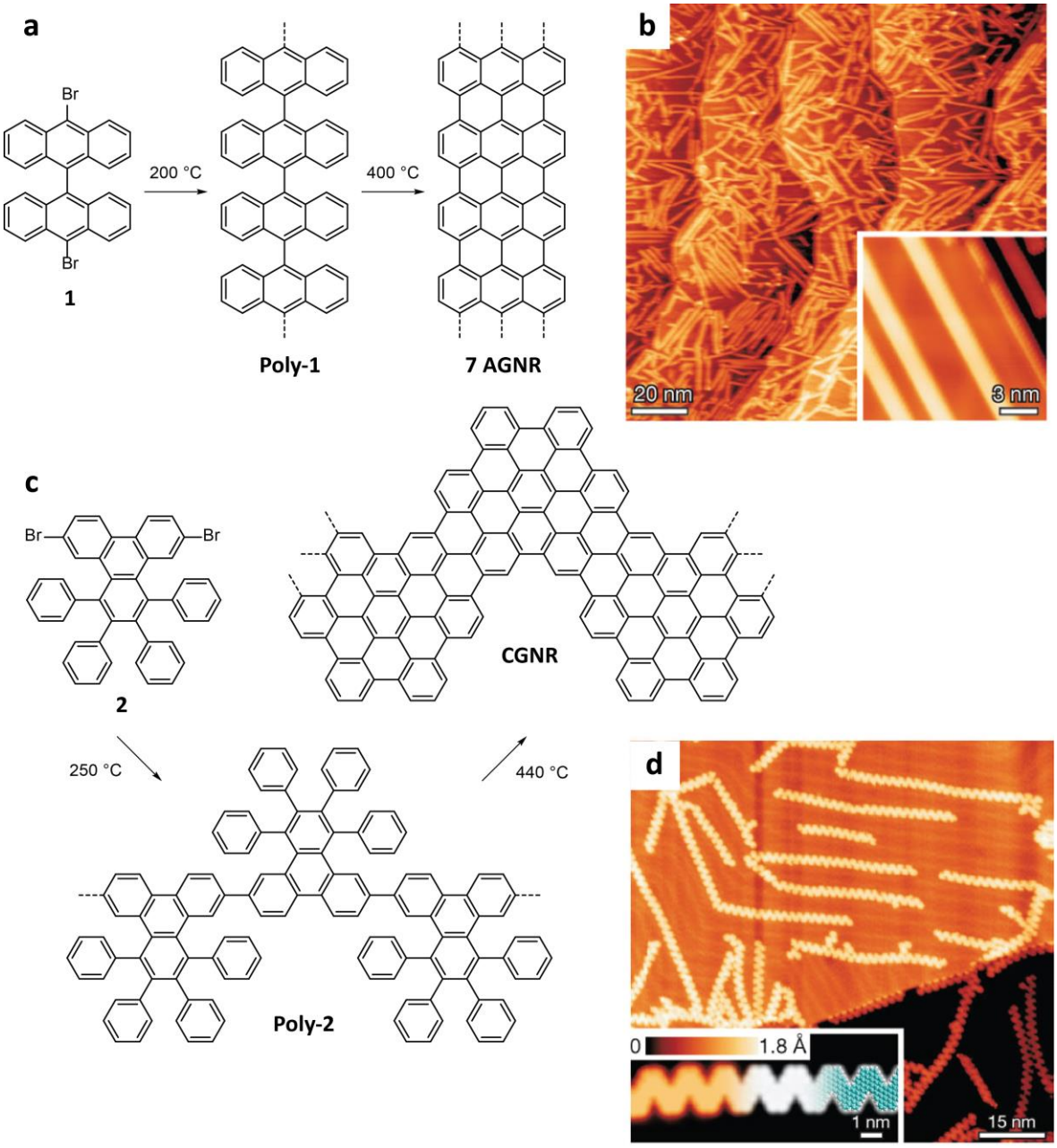

Figure 1.6 Surface synthesis of 7-AGNR and CGNRs. (a) Reaction scheme from **1** to 7-AGNRs. (b) Overview STM image of straight N = 7 GNRs on Au(111). The inset shows a higher-resolution STM image. (c) Reaction scheme for **2** to CGNRs. (d) Overview STM image of CGNRs on Au(111). The inset shows a higher resolution STM image with DFT-based simulation of the STM image partly overlaid. STM images in (b) and (d) reproduced from *Nature* **466,** 470–3 (2010).[31]

Surface-Assisted Synthesis of GNRs

Pioneering work on bottom up synthesized GNR was started by Müllen, Fasel and coworkers in 2010 when they first synthesized both N = 7 AGNRs (where N is the width of the

ribbon in number of carbon atoms) and chevron type GNRs on Au (111) in UHV (Figure 1.6).[31] They deposited 10,10'-dibromo-9,9'-bianthryl (DBBA, **1**) on Au(111) via sublimation. Annealing the surface to 200 °C caused surface catalyzed homolytic bond cleavage, resulting in diradical species, which then diffuse along the metal surface and recombine in step growth polymerization. Further annealing to 400 °C induced intramolecular cyclodehydrogenation of the polymer chain to yield 7-AGNRs on the surface (Figure 1.7). Similarly, starting with 6,11-dibromo-1,2,3,4-tetraphenyltriphenylene (**2**) as a GNR precursor afforded CGNRs on the surface.

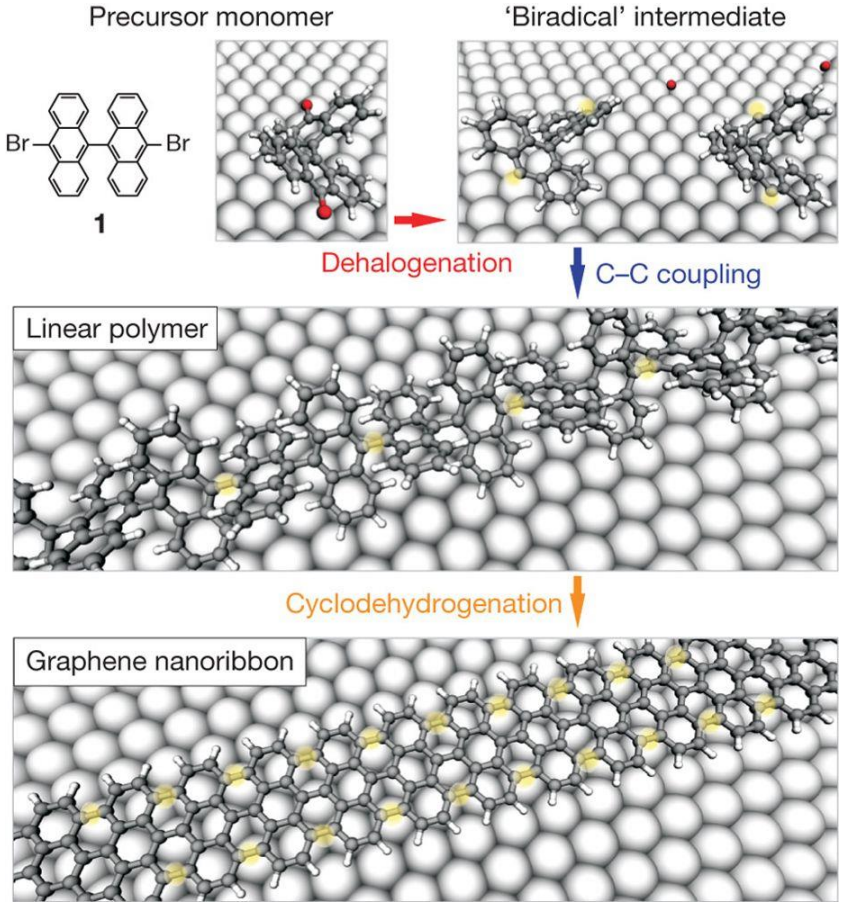

Figure 1.7 Schematic representation for the basic steps of surface-assisted GNR synthesis. Image reproduced from *Nature* **466,** 470–3 (2010).[31]

Since the publication of this initial precedent report on the surface assisted bottom-up synthesis of GNRs, this methodology has been adapted to give access to a number of atomically precise GNRs. Modifying DBBA to have biphenyl substituents (**3**) gave access to 13-AGNRs on the surface (Figure 1.8a and b).[32] Development of new monomers, such as 3′,6′-dibromo-1,1′:2′,1″-terphenyl (**4**), expanded the types of GNRs accessible to 9-AGNRs (Figure 1.8c and d).[33] Besides, designing monomers to alter the width of GNRs, new precursors were synthesized to fabricate GNRs of different edge structures as well. In 2016, Ruffieux and coworkers reported the first bottom-up synthesis of ZGNRs through surface-assisted polymerization and cyclodehydrogenation of a U-shaped monomer (**5**), depicted in Figure 1.9.[34] The importance of

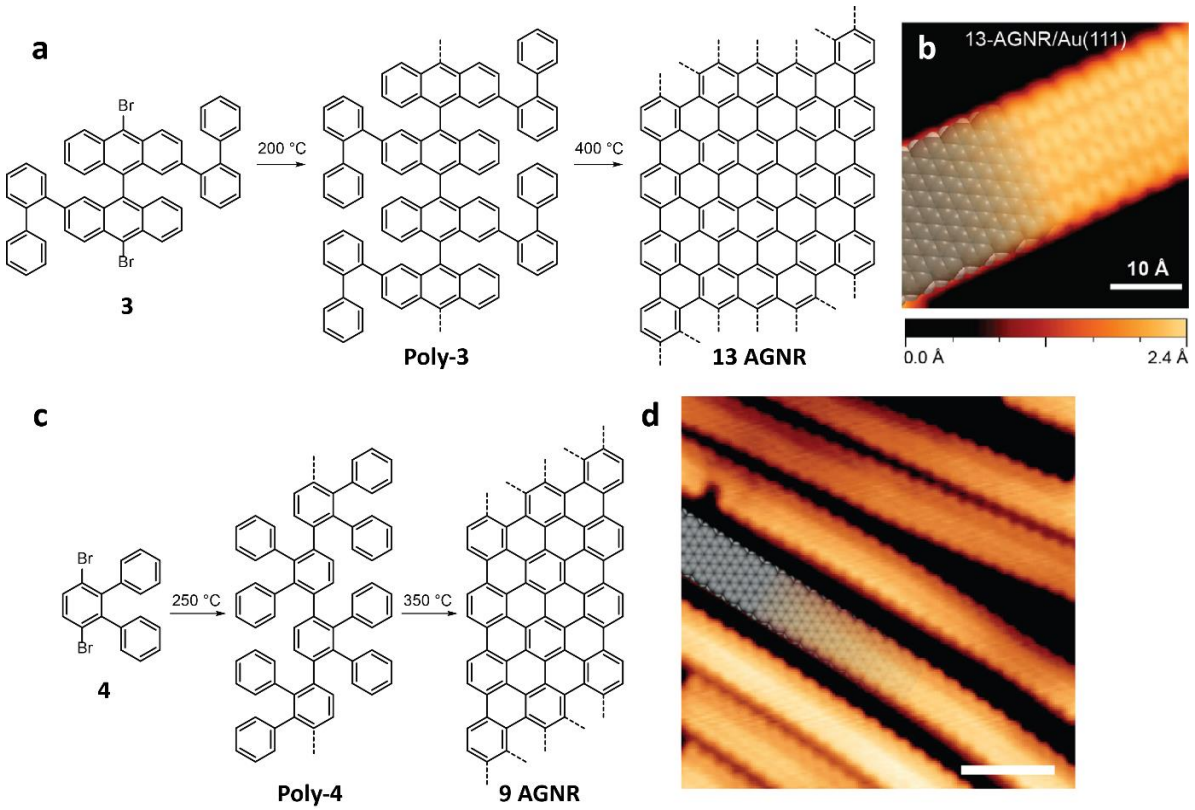

Figure 1.8. Surface-assisted growth of 9- and 13-AGNRs. (a) Reaction scheme from **3** to 13-AGNR. (b) STM image of a 13-AGNR on Au(111). Image reproduced from *ACS Nano* **7,** 6123–6128 (2013).[32] (c) Reaction scheme from **4** to 9-AGNRs. (d) STM image of 9-AGNrs on Au(111). Image reproduced from *ACS Nano* **11,** 1380–1388 (2017).[33]

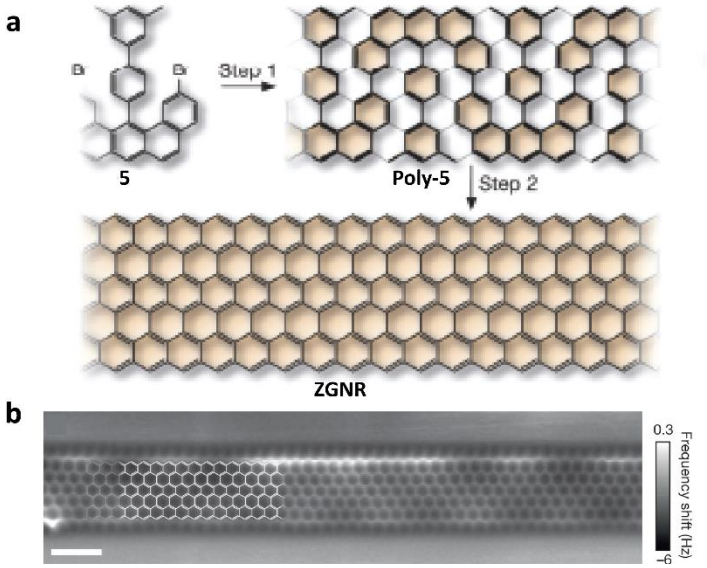

Figure 1.9 Surface synthesis of zGNRs. (a) Reaction scheme from U-shaped monomer **5** to zGNR. (b) nc-AFM image of zGNR. Images reproduced from *Nature* **531,** 489–492 (2016).[34]

these surface grown ZGNRs in UHV is evident when the unstable spin-polarized electronic edge states are considered and as a result attempting to synthesize, isolate, and study ZGNRs in solution would be extremely difficult.

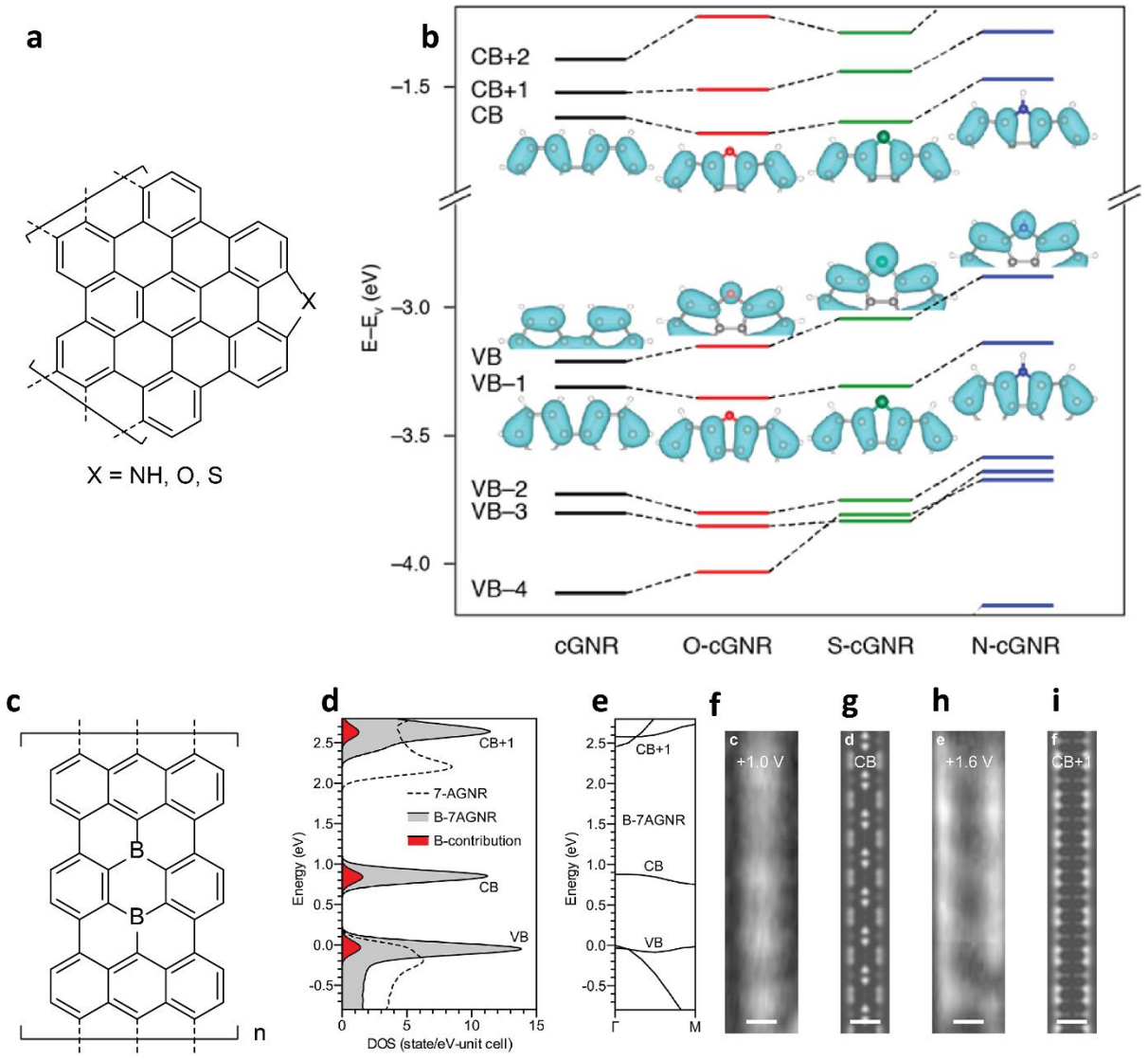

Figure 1.10 Heteroatom doping of GNRs (a) Schematic representation of CGNR with NH, O, and S edge dopants. (b) Calculated energy levels at the Γ point of unsubstituted CGNR (black), O-CGNR (red), S-CGNR (green), and N-CGNR (blue) near the band gap. Image reproduced from *J. Am. Chem. Soc.* **140,** 807–813 (2018).[35] (c) Schematic representain of periodic boron core doping of 7-AGNR. (d) Calculated total DOS for B-7AGNRs (gray) and contribution from B atoms to the DOS (red) using the GW approximation and including screening effects from Au(111) substrate. The total DOS for undoped 7-AGNRs is plotted as a dotted line. (e) Calculated band structure of B-7AGNRs using GW approximation. (f) d*I*/d*V* map at V_s = 1.0 V corresponding to the states in the condution band (CB). (g) Calculated d*I*/d*V* map of states at the CB. (h) d*I*/d*V* map at V_s = 1.6 V corresponding to the states in the CB+1. (i) Calculated d*I*/d*V* map of states at the CB+1. Images in d–i reproduced from *J. Am. Chem. Soc.* **137**, 8872–8875 (2015).[38]

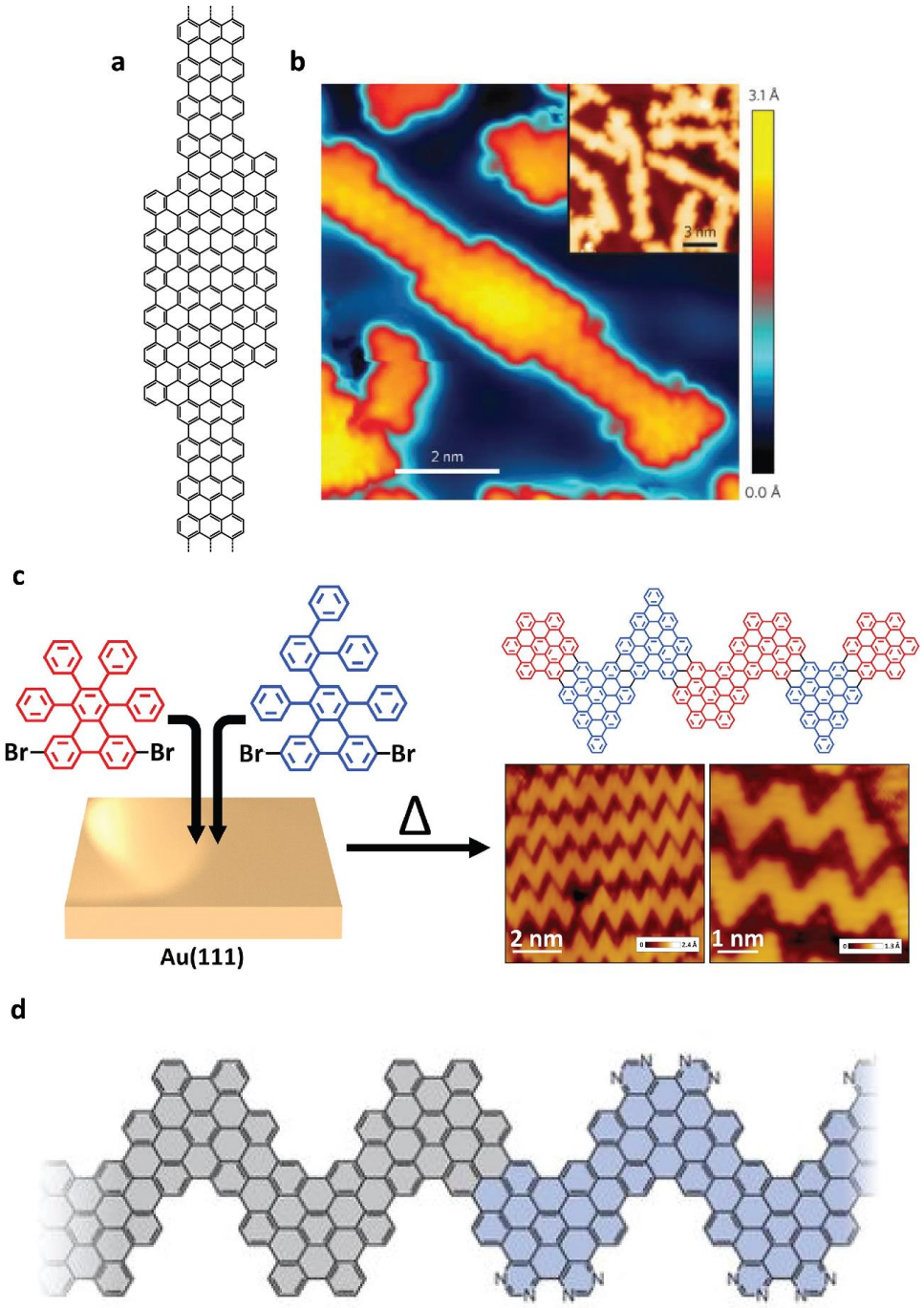

Figure 1.11 GNR heterostructures through random polymerization of two different compatible GNR precursors. (a) Schematic representation of 7–13 AGNR heterojunction. (b) STM topograph of a 7–13 GNR heterojunction on Au(111). Image reproduced from *Nat. Nanotechnol.* **10,** 156–160 (2015).[39] (c) Scheme of GNR heterojunction using chevron precursors of two different widths and STM images of resulting heterojuntions. Image reproduced from *Carbon* **134,** 310–315 (2018).[40] (d) Schematic representioan of heterojuntion between pristine carbon and nitrogen doped CGNRs. Image reproduced from *Nat. Nanotechnol.* **9,** 896–900 (2014).[8]

Doping of GNRs via site selective replacement of carbon atoms with other heteroatoms can also modify the electronic structure of the GNRs. Surface-assisted synthesis has paved the way for atomically precise doped GNRs with regioregular dopant atoms. Several different doped armchair and chevron GNRs have been reported with S, N, and O edge dopants to tune the bandgap (Figure 1.10a and b).[8,35–37] Surface synthesis also gives access to more exotic doped GNRs that could be potentially unstable at ambient conditions or difficult to isolate in solution, such as 7-AGNRs with periodic core boron dopant atoms (Figure 1.10c).[38] Interestingly, unlike edge dopants, these core doped boron atoms have empty p-orbitals in conjugation with the π system, which introduces new electronic dopant states, drastically altering the electronic structure (Figure 1.10d–i).

Access to more complex GNR architectures has also been achieved. GNR heterostructures have been synthesized by random polymerization of two different compatible GNR precursors. This has led the way to heterostructures joining GNRs of various widths, such as 9–13 AGNRs,[39] chevron GNRs of two different widths,[40] and heterojunctions between pristine all carbon CGNRs and nitrogen doped CGNRs (Figure 1.11).[8]

Our group has also developed the fabrication of GNR heterostructures obtained by selective reconstruction of functional groups along the GNR edges starting from one molecular precursor (Figure 1.12).[37,41] In 2016, we showed chevron GNRs with 9-methyl-9H-carbazole units along the edges could undergo thermally induced site-specific ring-expansion that irreversibly converts the 9-methyl-9H-carbazole into a phenanthridine group. The resulting heterostructures had segments of both electron-rich carbazole and electron-deficient phenanthridine units (Figure 1.12a–d).[37] We developed a similar system utilizing fluorenone functionalized CGNRs. After cyclodehydrogenation, excitation of the fluorenone GNRs induced cleavage of carbonyl groups, yielding atomically precise heterojunctions with segments of fluorenone functionalized CGNRs and unfunctionalized CGNRs (Figure 1.12e and f).[41] Our group has also reported the first controlled heterostructure synthesis via hierarchical growth by capitalizing on difference in the bond dissociation energy of carbon-iodine bonds and carbon-bromine bonds.[42]

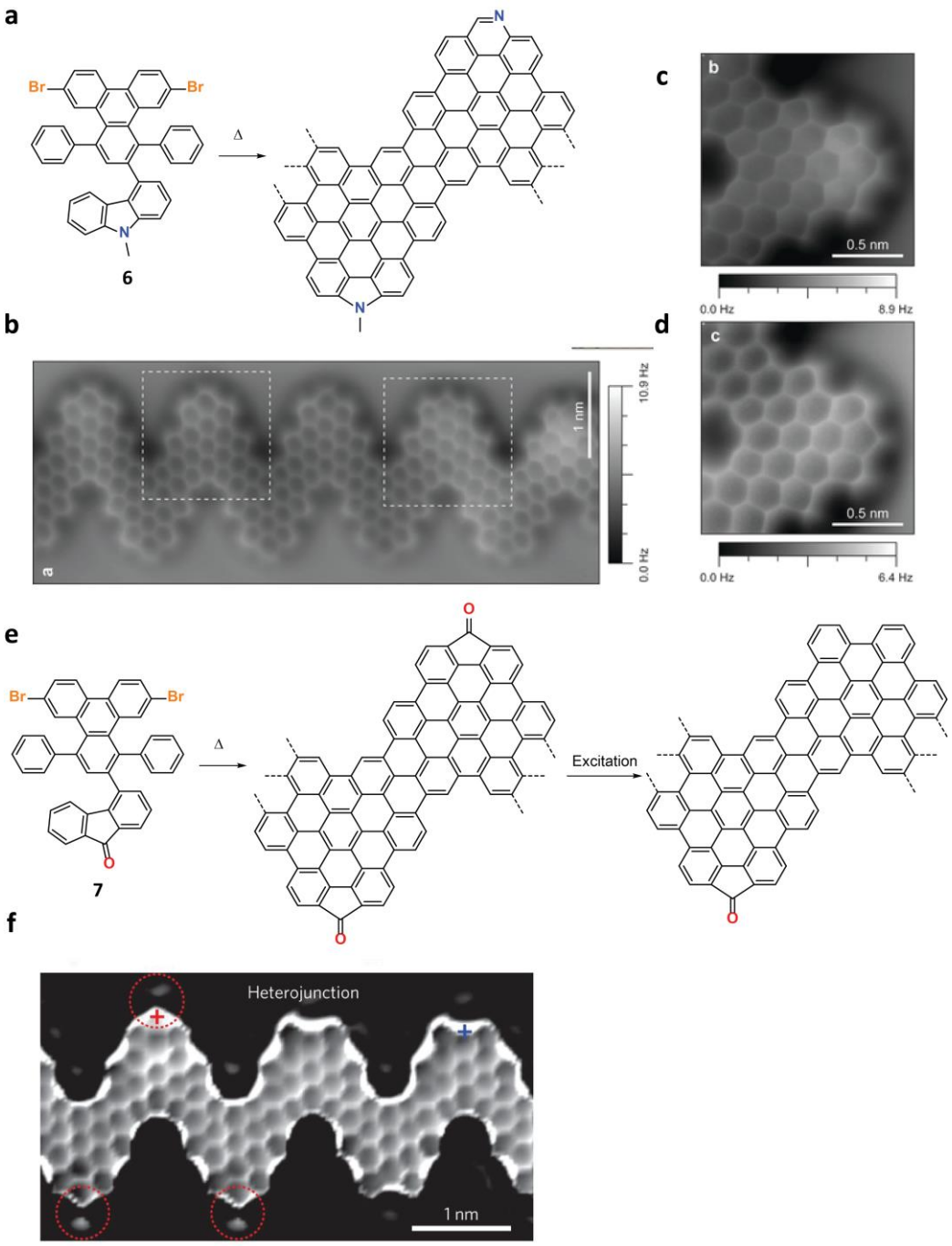

Figure 1.12 Heterojunction through edge reconstruction. (a) Reaction scheme for the synthesis of GNR heterojunction with phenanthridine and carbazole units from chevron precursor **6**. (b) nc-AFM image of CGNR heterostructure on Au(111) featuring segments of fused phenanthridine and carbazole groups. (c) nc-AFM image of phenanthridine-fused GNR segment. (d) nc-AFM image of carbazole-fused GNR segment. Images b–d reproduced from *Chem. - A Eur. J.* **22,** 13037–13040 (2016).[37] (e) Reaction scheme for the synthesis of fluorenone/unfunctionalized chevron GNR heterojunction from a single precursor, **7**. (f) BRSTM image of a fluorenone/unfunctionalized chevron heterojunction. Red circles indicate positions with carbonyl groups. Image reproduced from *Nat. Nanotechnol.* **12,** 1077–1082 (2017).[41]

Solution Phase Synthesis

While surface-assisted synthesis has the powerful capability of fabricating atomically precise GNRs that can be directly characterized *in situ* by high-resolution STM, atomic force microscopy (AFM) and scanning tunneling spectroscopy (STS), it is limited in its ability to synthesize large quantities of GNRs. Furthermore, GNRs synthetized on conductive metal surfaces cannot be directly used for device fabrication and electrical testing and thus need to be transferred to a dielectric substrate. In contrast, solution synthesis enables bulk scale production of GNRs, does not require expensive and sensitive equipment, does not need UHV, and does not require a metal surface. Solution synthesis relies on step-growth polymerization such as *Diels-Alder* polymerization, *Yamamoto* polymerization, or *Suzuki* polymerization, to access a polyphenylene precursor. This polyphenylene must be designed such that when it is planarized, the resulting GNR does not have defects and thus requires rationally designed, tailor-made monomers. Intramolecular oxidative cyclodehydrogenation, usually via the iron chloride mediated *Scholl* reaction, affords the GNR. Unfortunately, one disadvantage of solution synthesis is the resulting GNRs tend to form aggregates and bundles due to the π-stacking interactions between the ribbons. As a result, many solution synthesized GNRs have solubilizing groups along the backbone and these aggregates must be disrupted before any single ribbon experiments can be performed.

In 2014, the group of Müllen synthesized the first example of a liquid-phase-processable cove-type graphene nanoribbons which had alkyl chains along the periphery to enhance the dispersibility of the resulting GNRs as well as sterically hinder undesired conformations.[43] They designed monomer **8** consisting of a substituted cyclopentadienone as the conjugated diene, and a terminal alkyne group as the dienophile and successfully subjected it to an AB-type *Diels-Alder* polymerization. Subsequent oxidation via iron chloride mediated *Scholl* oxidation afforded long, dispersible, alkylated cGNRs (Scheme 1.1).[43] Since then, this basic monomer design has been modified to afford cGNRs of various widths and functionalities.[44–47]

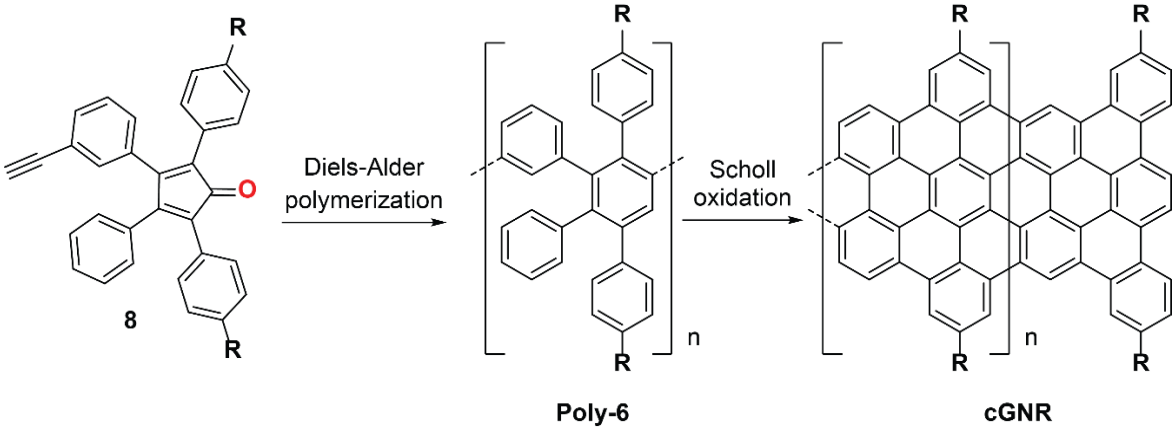

Scheme 1.1 General synthetic scheme for the solution synthesis of cove-type GNRs first reported by Müllen and coworkers.[43]

Armchair ribbons of various widths have also been synthesized in solution. Müllen and coworkers first synthesized 9-AGNRs in solution via A_2B_2-type *Suzuki-Miyaura* polymerization

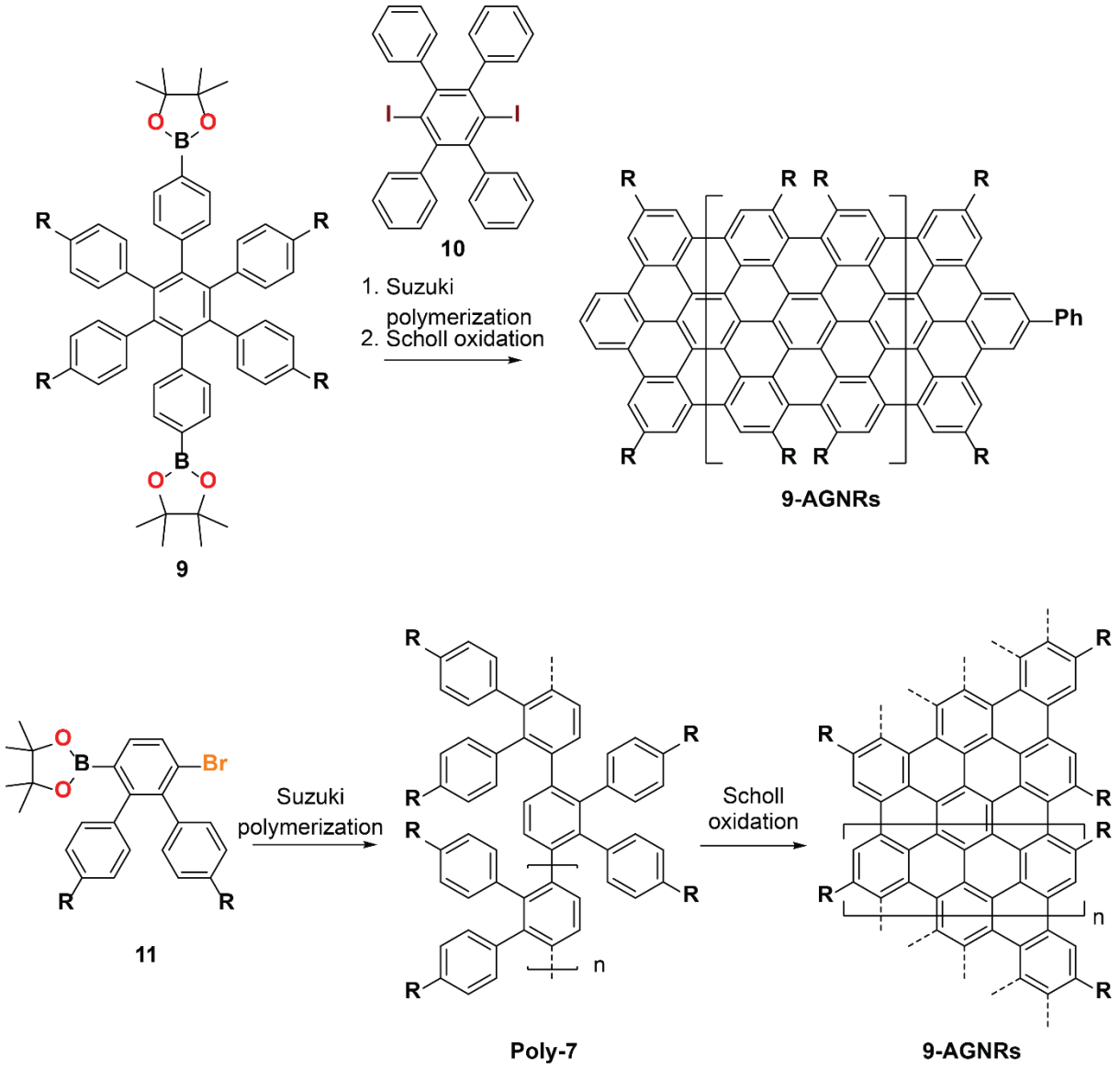

Scheme 1.2 Synthesis of 9-AGNRs developed by Müllen and coworkers (top)[48] and Li and coworkers (bottom).[49]

of a diborylated hexaphenylbenzene, **9**, with 1,4-diiodo-2,3,5,6-tetraphenylbenzene, **10**, followed by cyclodehydrogenation (Scheme 1.2 top).[48] Achieving high molecular weight polymers was challenging due to the use of sterically congested penta- and hexaaryl monomers that hampered the efficacy of the polymerization. Furthermore, A_2B_2-type polymerizations are never as efficient as AA- or AB-type polymerizations, and also lead to lower molecular weight polymers. In 2016. Li *et al.* reported the solution synthesis of 9-AGNRs starting with an alkylated triaryl monomer.[49] They designed a sterically less-hindered AB-type monomer, namely a substituted 2,3-bisarylated-4-bromophenylboric acid ester, **11**. AB-type *Suzuki-Miyaura* polymerization of **11**, afforded high molecular weight polymers, and subsequent oxidation afforded long alkylated 9-AGNRs.[49] N=18 AGNRs have also been synthesized in solution via a *Yamamoto* polymerization of a modified hexaphenyl benzene, and subsequent *Scholl* oxidation.[50]

Other edge structures, such as chevron GNRs have also been synthesized in solution (Figure 1.3). The 6,11-dibromo-1,2,3,4-tetraphenyltriphenylene monomer, **2**, used for surface growth, can also be polymerized in solution via the *Yamamoto* polymerization. Subsequent iron chloride mediated cyclodehydrogenation yielded CGNRs in solution.[51] This monomer design has since been modified to give rise to nitrogen doped GNRs in solution as well as laterally extended GNRs.[14,52,53]

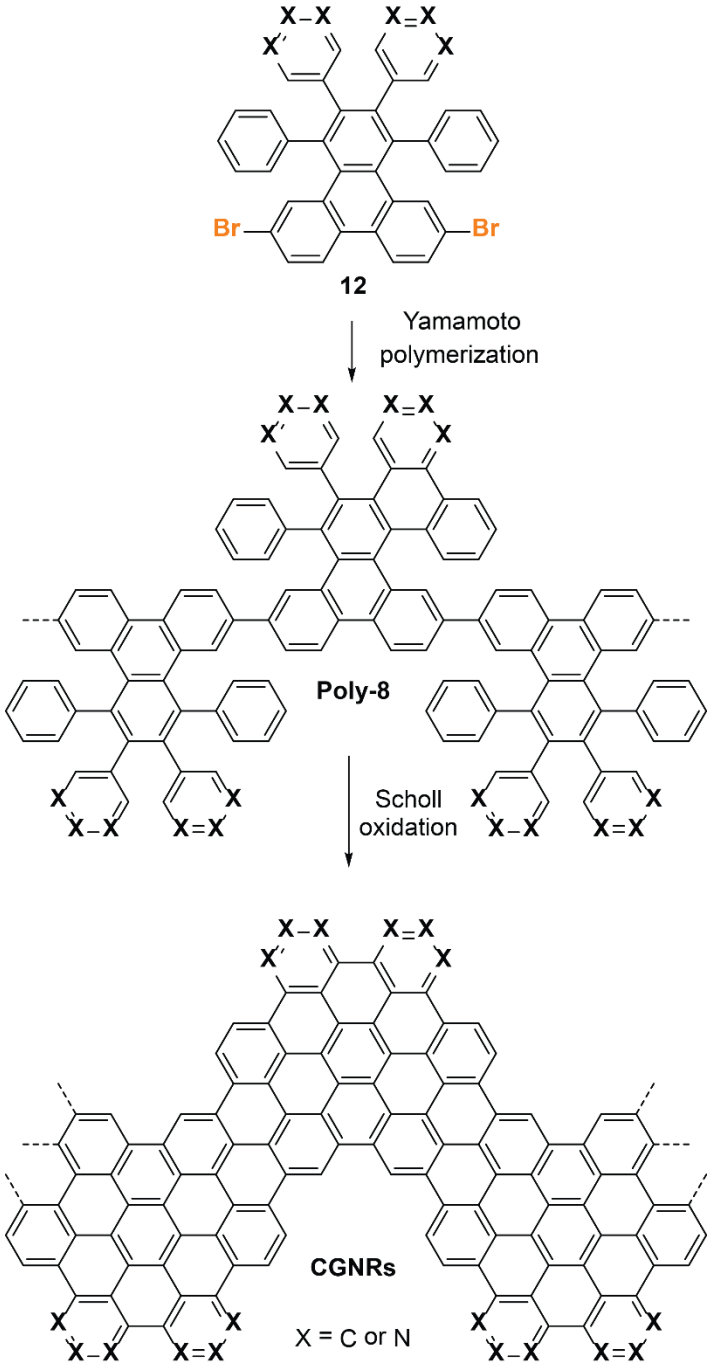

Scheme 1.3 Solution synthesis of CGNRs.

1.2.3 Late Stage Functionalization of GNRs

As described in the previous section, the GNR structure is directly correlated to the monomer design for bottom up synthesized GNRs. As a result, desired functional groups are often incorporated into the monomer design. However, since solution synthesized GNRs usually require polymerization reactions at high temperatures or with reactive catalysts followed by harsh oxidative cyclodehydrogenation reactions, the types of functionalities that can be incorporated onto the GNR backbone are limited by the parameters of synthesis. Late stage functionalization, however, offers the powerful capability to introduce functionality after graphitization to fabricate the GNR. As a result, a variety of different, modified GNRs can be accessed from one precursor and more exotic and labile functional groups can thus be incorporated.

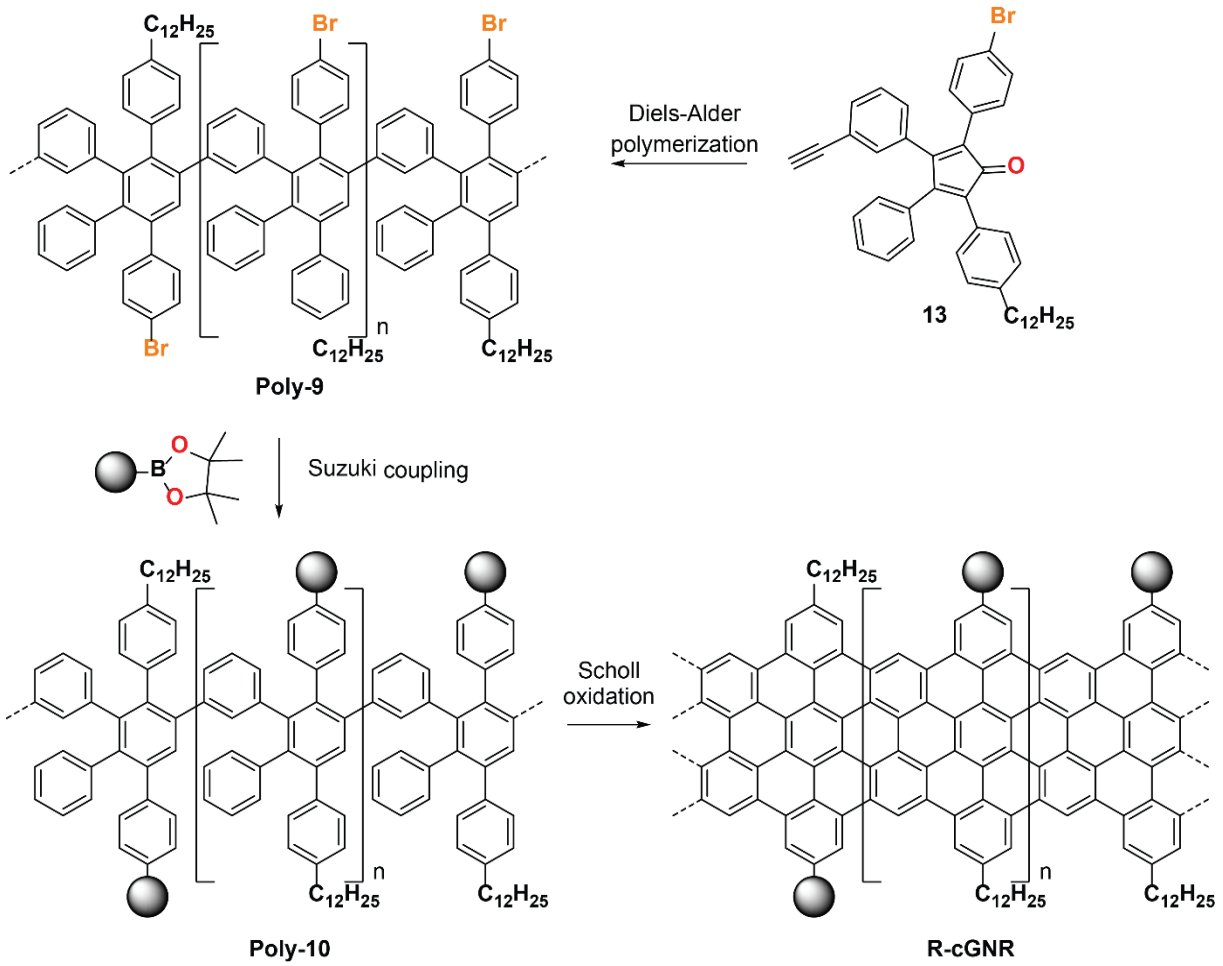

Scheme 1.4 Late stage functionalization of polymer precursor via Suzuki coupling developed by Müllen and coworkers.[55]

Thus far, there have been only few examples of late stage derivatization of GNRs. In 2013, the group of Müllen showed that edge chlorination of cove-type GNRs could be accomplished by subjecting cGNRs to ICl with catalytic $AlCl_3$ in CCl_4. The resulting chlorinated cGNRs had a lower band gap and were more processible compared to the pristine cGNRs.[54] More recently, they

have developed a methodology for edge functionalization of cGNRs through a Suzuki coupling of polyphenylene precursors bearing bromine groups, prior to the intramolecular oxidative cyclo-dehydrogenation (Scheme 1.4). Unfortunately, this strategy limits the types of functionalities that can be incorporated to those that would survive the Scholl reaction.[55]

1.3 Characterization of GNRs

An added benefit of surface assisted growth of GNRs in UHV is the integration with atomically resolved scanning probe imaging techniques, capable of probing the electronic structure and providing atomic scale resolution of isolated, single, immobilized ribbons. AFM, non-contact AFM (nc-AFM), and bond-resolved STM (brSTM) enable bond resolved imaging of GNRs. STM and nc-AFM can accurately measure the apparent height and width of the GNRs and the precursor polymers.[31,41] Thus, these tools are able to provide atomically precise information regarding the planarity, edge structure, periodicity, and sometimes positions of dopant atoms within the GNRs.[31,37,41,56] Additionally, the electronic structures of the GNRs can be directly probed by STS, and can even identify the valence and conduction bands. STS is also able to provide information regarding where these electronic states are localized within a GNR through dI/dV mapping.[32,56]

Unfortunately, scanning probe microscopy (SPM) does require very delicate, expensive instrumentation and is very time intensive. Additionally, attempting to locate and image solution synthesized GNRs using these techniques is extremely difficult. Since solution synthesis produces GNR bundles and aggregates, attempting to locate and image single GNRs that have been deposited on a surface using SPM is challenging. Furthermore, depositing solution synthesized GNRs on a surface for imaging results in contamination with solvent molecules and other impurities, adding to the difficulty of imaging via SPM.

GNRs have very characteristic Raman signatures. Both surface and solution synthesized GNRs can be analyzed by Raman spectroscopy, making this a fundamental tool in GNR characterization. GNRs, like all graphitic materials, exhibit a G peak around 1600 cm^{-1}, which corresponds to the high frequency E_{2g} phonon at Γ.[57,58] For GNRs, the G peak does not show any splitting as seen with CNTs and thus can be used as a characteristic feature to distinguish between GNRs and CNTs.[58] All graphitic materials also feature a D peak around 1300 cm^{-1}, which corresponds to the breathing modes of six atom rings and requires a defect or edge for its activation.[57,58] Since GNRs are laterally confined, they exhibit a strong D peak regardless of structural defects due to the confinement of π-electrons into finite sized domains.[31] The D peak dispersion is also unique to different allotropes of carbon and can be used to differentiate GNRs from other graphitic structures.[58] The radial breathing-like mode, RBLM, is a third distinguishing signature in the Raman spectrum of GNRs. The RBLM is created by the vibration of the outer atoms, while the center atoms are almost static.[59] The RBLM is found in the lower frequency region, but the actual peak position in dependent upon the GNR width, with wider ribbons having lowering frequency RBLM.[57–59] Besides the RBLM, GNRs exhibit a Raman fingerprint in the lower frequency regime (> 1000 cm^{-1}) resulting from the relative motion of the GNR plane and are very sensitive to edge morphology and functionalization.[58]

1.4 Application of GNRs

Due to their remarkable electronic properties, GNRs have been a sought after material for a variety of different applications, ranging from next generation electronic devices,[60–62] chemical sensors[10,14] and catalytic support materials.[44,63] As previously mentioned, they share many of the same extraordinary properties of graphene, with the exception of a tunable band gap. Since graphene is gapless, it cannot be used in devices that require switching. In contrast, GNRs, with their tunable electronic properties, are ideal candidates for such devices.

The integration of single GNRs into next generation electronics, such as FETs, is still a major challenge. GNRs grown on metal surfaces must be transferred to dielectrics. Unfortunately, many transfer processes result in contamination that degrade the electrical performance of the devices, rendering large-scale integration of such GNRs into devices challenging. Furthermore, attempting to locate and image transferred individual GNRs via AFM or STM haven proven to be difficult. Initial work by Cai *et al.* transferred GNRs onto SiO_2 through mechanical contact of the gold substrate with intact GNRs and the SiO_2, or "chip-to-chip press" method.[31] This transfer method, however, has been found to be unreliable. Our group, in collaboration with the Crommie and Bokor group, has developed a more reliable transfer process to fabricate GNR FETs, depicted in Figure 1.13a.[61] Starting with GNRs grown on Au on mica, poly-methyl methacrylate (PMMA) was deposited onto the GNRs, to form a PMMA/GNR/Au/mica stack. The resulting stack was then floated on concentrated hydrofluoric acid to delaminate the mica layer, followed by removal of the gold with a gold etchant to leave GNRs on PMMA. The PMMA/GNR stack was transferred onto a SiO_2/Si substrate by fishing. The PMMA was washed off with acetone and Pd contacts were deposited onto the surface to yield a three terminal transistor device (Figure 1.13b). Raman spectroscopy was used to confirm the integrity of the ribbons after the transfer process. Since the ribbons were not very long (30–40 nm, with an average length of 10–15 nm), and the transfer process randomly deposited the ribbons on the target substrate, the resulting devices had GNRs arranged randomly under the contacts with many GNRs not even spanning the source and drain contacts, leading to low device yield. The resulting GNR FETs did have a remarkable I_{on}/I_{off} of 3.6×10^3 at a source-drain voltage of V_{sd} = 1V. Unfortunately, transport was largely dominated by the Schottky junction due to the mismatch in band alignment of the GNR and Pd contacts and short channel lengths.[61] More recently, FETs have been fabricated with N = 9 and 13 AGNRs with a slightly modified deposition process.[62] For both the N=9 and N=13 GNR FETs, on-current (I_{on}) of ~1μA per ribbon was observed, a 1000X improvement compared to the N=7 GNRFETs. The increase in I_{on} was attributed to two factors. First, the reduction in bandgap resulted in a proportional decrease in the barrier height. Second, these devices were fabricated in an improved process with much thinner gate dielectric. This provided improved electrostatic gate control, leading to a significant reduction in the Schottky barrier width. The combination provided the 1000X reduction in contact resistance. However, these devices were still dominated by contact resistance and showed tunneling behavior in the I_D-V_D characteristics.[62]

While solution synthesis enables bulk production of ultra-long GNRs, their integration into electronic devices is hampered by their processability, visualization and localization on surfaces by SPM. As previously mentioned, wet chemical synthesis leads to GNR bundles and aggregates,

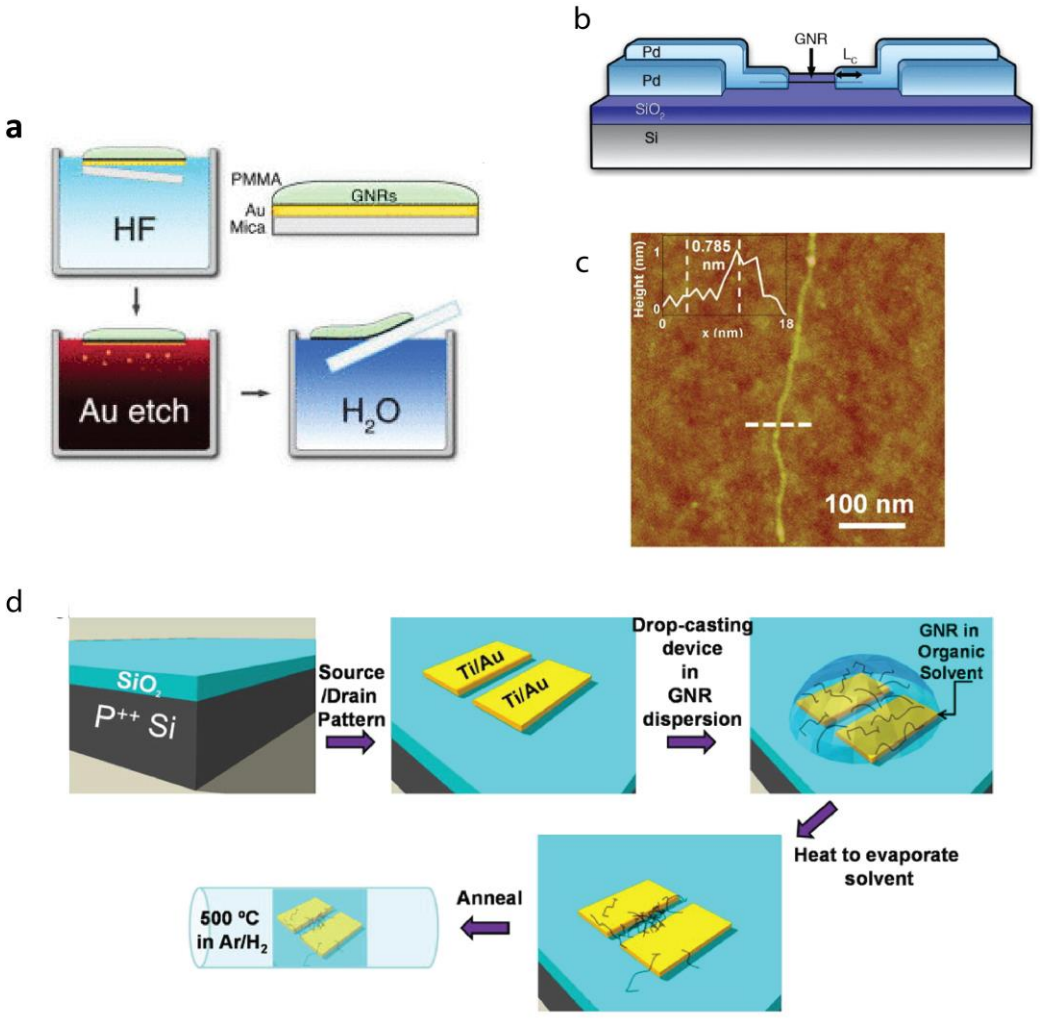

Figure 1.13 Device fabrication methods from bottom up synthesized GNR. (a) Wet transfer method developed Bennet *et al.* to transfer surface grown GNRs from gold to dielectric substrates. (b) Representative GNR FET device. Images a and b reproduced from *Appl. Phys. Lett.* **103,** 253114 (2013).[61] (c) AFM image of deposited solution synthesized GNR with length >500 nm. (d) Scheme of GNR thin-film device fabrication for NO_2 sensor. Images c and d reproduced from *J. Am. Chem. Soc.* **136.** 7555–8 (2014).[10]

making it difficult to isolate, image and integrate single GNRs into devices. In 2014, Abbas *et al.* initially reported the deposition and visualization of individual solution synthesized alkylated cGNRs and films on Si/SiO_2 and their application as devices and chemical sensors.[10] They successfully dispersed GNRs in 1-cyclohexyl-2-pyrrolidone and deposited it on dodecyltriethoxysilane functionalized Si/SiO_2 wafers. Raman spectroscopy and AFM confirmed the presence of a single ribbon (Figure 1.13c). They also patterned two Ti/Pd electrodes on the individual GNR using e-beam lithography and were able to measure conductance metal angle deposition with a channel length of ~20 nm. They also fabricated a GNR thin-film device by drop casting GNR dispersions from chlorobenzene or THF onto SiO_2 on doped silicon substrates with pre-patterned gold electrodes. Annealing the device to 400-500 °C removed the alkyl side chains on the GNRs (Figure 1.13d). They used their device as an NO_2 gas sensor and found exceptional

NO_2 sensing performance and sensitivity as low as 50 ppb of NO_2.[10] Laterally extended chevron GNR films have also been used in gas sensors and an electrical nose system which showed improved responsivities to low molecular weight alcohols compared to other similar systems.[14]

In 2015, Zschieschang *et al.* fabricated FETs by dispersing GNRs in SDS solutions of water, depositing the GNRs onto an insulting substrate, and patterning Ti/AuPd contacts by e-beam lithography.[60] The researchers used AFM to confirm the presence of a single GNR, but the measured width ribbon was 50 nm which they attributed to limited lateral resolution of AFM limited by the tip radius. Thus, they used the height of the GNR, found to be 2 nm, as the width. As a result, they claimed they could not rule out the possibility of having an agglomerated GNRs in their transistor channel instead of the desired single GNR. The GNR FET exhibited a large drain current of 70 μA, good charge injection from the metal source and drain contacts, and current saturation at larger drain-source voltages. Unfortunately, they observed a small I_{on}/I_{off} of 2, which they attributed to either the unfavorable transistor geometry or the unintentional agglomeration of two or more GNRs in the channel.

While the electronic properties of GNRs have elevated them to sought after materials of next-generation electronics, their unique properties also make them good candidates as catalytic support materials. Although other graphitic materials, such as graphene, graphene oxide, reduced graphene oxide and CNTs, have been investigated as support materials, they lack rational tunability and atomic precision. In comparison, deterministic bottom up synthesized GNRs have structural and electronic tunability, high mechanical flexibility, and a high aspect ratio, making them attractive candidates as nanoparticle supports. Recently, our group has investigated employing GNRs as catalytic nanoparticle support materials for a variety of different applications ranging from CO_2 reduction to hydrogen storage.[44,63]

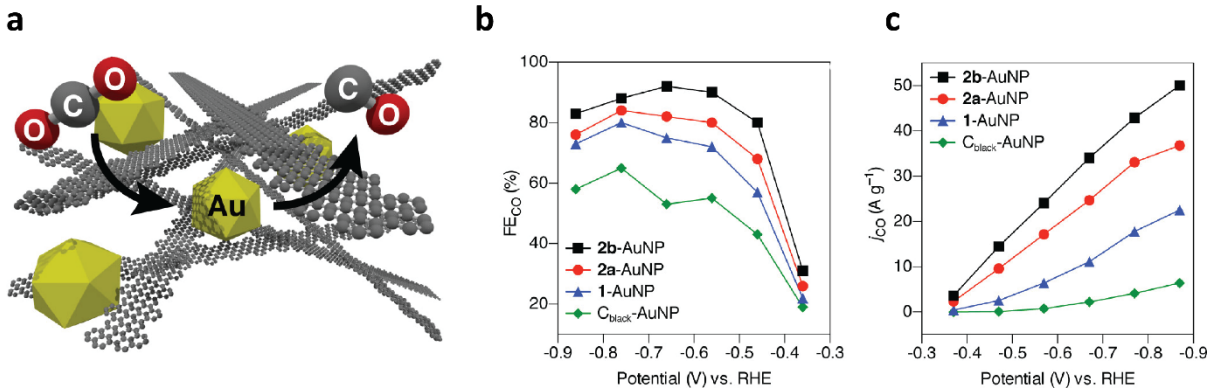

Figure 1.14 Enhancement of electrocatalytic CO_2 reduction with AuNP embedded in functional GNR matrix. (a) Schematic representation of AuNP embedded in GNR matrix. (b) Faradaic efficiencies for CO production by various GNR-AuNP composite materials (blue, red, and black) and carbon black-AuNP (green) composite. (c) Partial current for CO production (j_{CO}) by various GNR-AuNP composite materials (blue, red, and black) and carbon black-AuNP (green) composite. Images reproduced from *J. Am. Chem. Soc* **139,** 14 (2017).[44]

Previous work in our group utilized GNRs as support materials for the electrocatalytic reduction of CO_2 by gold nanoparticles (AuNP) (Figure 1.14a).[44] Rogers and coworkers found that using rationally designed functionalized GNRs as supports lead to increases in key performance parameters, such as activity, selectivity, and stability. They observed increased Faraday efficiency (FE_{CO} > 90%), lowered requisite CO_2 reduction overpotential by hundreds of millivolts, and increased partial current (j_{CO}) for CO_2 reduction to CO when GNRs were used as supports compared to carbon black (Figure 1.14b and c). Furthermore, embedding the nanoparticles in a GNR matrix increased the AuNP electrochemically active surface area. Capitalizing on the tunability of bottom up synthesized GNRs, they also synthesized functionalized cGNRs with ester groups and observed that this increased functionality enhanced the catalytic properties even more. Interestingly, electrochemical studies indicated that the enhanced performance of GNR-AuNP composites arose from a change in mechanism, illustrating the drastic influence GNRs have as support materials.[44]

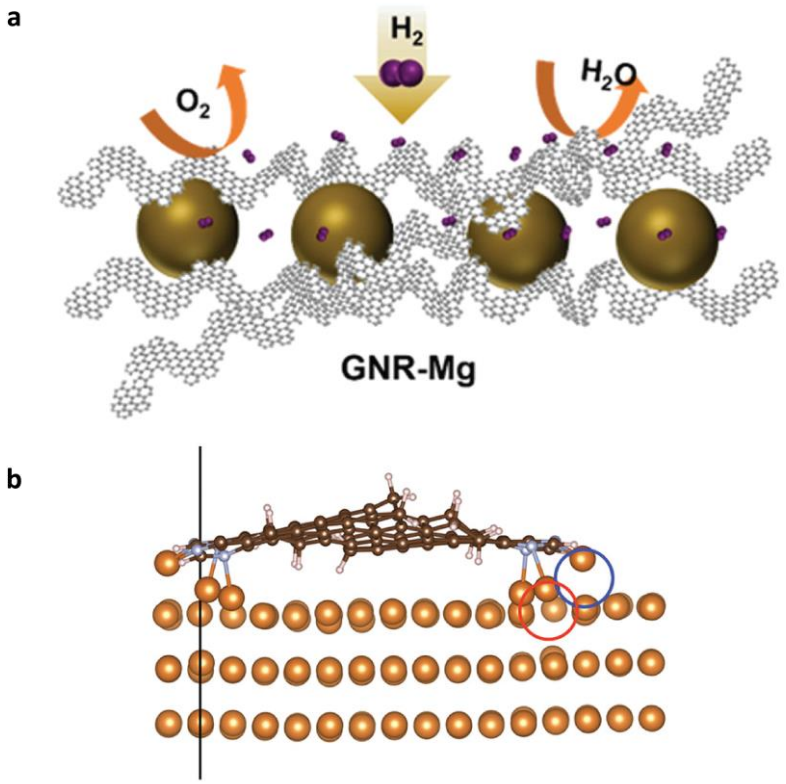

Figure 1.15 MgNP-GNR composite for Hydrogen storage. (a) Schematic representation of MgNP-GNR composite material (b) Calculated optimized 4N-GNR–Mg interfacial structure (side view) showing the formation of a chemical bond between Mg and the pyridinic nitrogens. Images reproduced from *Chem. Mater.* **31,** 2960–2970 (2019).[63]

Recently, our group in collaboration with the Urban and Prendergast groups, investigated magnesium nanoparticles (MgNP) encapsulated in a variety of edge functionalized GNRs for hydrogen storage (Figure 1.15a).[63] They observed that encapsulation of the nanoparticles led to increased long term air stability of at least 6 months, the highest hydrogen storage capacity for

Mg-based hydride materials measured to date with values ranging from 7.10 – 7.29 wt%, and excellent reversibility between hydriding and dehydriding. Faster reaction kinetics were observed for hydriding and dehyrididing when a 4N and fluorenone GNR were used as support materials. First principle calculations imply the edge-functional groups helped reduce the kinetic barriers for the surface hydrogen reactions the at the MgNP-GNR interface with the GNR stabilizing surface defects. For the 4N-GNR, calculations showed the formation of a chemical bond between Mg and the pyridinic N, thus causing the Mg atom to be dragged out of the plane of the Mg surface to create a vacancy (Figure 1.15b). Calculations imply that these vacancies lower the activation barrier and promote H_2 dissociation on the Mg surfaces and H_2 recombination on the MgH_2 surfaces.[63] Both of these examples illustrate the powerful capability GNRs have as tunable support materials. However, to date, there have been no examples of GNR as support materials for homogenous molecular catalysts, which would essentially heterogenize homogenous catalysts and bridge the gap between homogeneous and heterogeneous catalysis.

1.5 Conclusion and Outlook

Due to the poor reproducibility and limited control over the structure of GNRs, top down fabrication methods are unreliable in synthesizing atomically precise GNRs required for their applications in devices, sensors, and catalysis. The high reliability and structural perfection obtained from deterministic bottom up methods, however, lead to GNRs with uniform and predicable electronic properties. Furthermore, late stage functionalization of these GNRs enables a variety of novel functionalized GNRs to be accessed from one GNR precursor.

The remainder of this dissertation will focus on late stage functionalization of solution synthesized GNRs and development of GNR precursors for surface growth of novel GNRs using a modular synthesis. Late stage modification of GNRs is key in accessing GNRs with exotic functionalities that would not survive the harsh reaction conditions required during GNR fabrication. With very few examples of installing functionality after graphitization, we investigated late stage functionalization methods of GNRs. In Chapter 2 we have developed a method for late stage functionalization of alkyled cove-type GNRs through click chemistry and its subsequent imaging with super resolution imaging as an alternative to traditional SPM techniques. In Chapter 3, late stage edge modification of GNRs via condensation chemistry and subsequent metalation and its application in catalysis is discussed. We present the first examples of heterogenization of homogenous catalyst by placing them in direct conjugation with the GNR backbone. Challenges still remain in accessing atomically precise low bandgap GNRs for device applications. As alluded to earlier, low bandgap GNRs are required to reduce the Schottky barrier height to yield GNR FETs with promising device performance.[62] Chapter 4 addresses this issue and focuses on the development of novel precursors for the surface synthesis of low band gap GNRs using a modular synthesis.

Chapter 2

Clickable GNR Functionalized with Photoswitchable Dyes for Super Resolution Imaging

Parts of this chapter have been published in Joshi, D.; Hauser, M.; Veber, G.; Berl, A.; Xu, K.; Fischer, F. R. *J. Am. Chem. Soc.* **2018**, *140*, 9574-9580.

In this chapter, we introduce the late stage functionalization of GNRs through click chemistry. We also discuss the challenges of integrating solution synthesized GNRs into next generation electronic devices and the need for a more efficient method for localizing and imaging GNRs. Here we report the design and synthesis of ultralong (~10 μm) cove-type GNRs (cGNRs) featuring azide groups along the edges that can serve as a universal handle for late-stage functionalization with terminal alkynes. Copper-catalyzed click-chemistry with Cy5 fluorescent dyes gives rise to cGNRs decorated along the edges with fluorescent tags detectable by optical microscopy. We then successfully imaged individual dye-functioanlzied cGNRs using super-resolution microscopy in collaboration with Megan Hauser and Ke Xu.

2.1 Introduction

The solution synthesis of GNRs all rely on polymerization, usually at high temperatures, followed by cyclodehydrogenation via the harsh oxidative Scholl reaction. Due to these extreme conditions, the functionalities that can be incorporated into the GNR backbone are limited to chemical groups that are oxidatively stable.[43,44,64] Therefore, accessing GNRs with more exotic functionalities is very challenging. Additionally, most functionalities require early stage introduction, usually installed during monomer synthesis, and thus new synthetic approaches are required for each novel GNR. A post graphitization modification would allow for a wide range of GNRs to be accessed from one common GNR intermediate and would allow for the incorporation of various functional groups compatible with the late stage modification methodology.

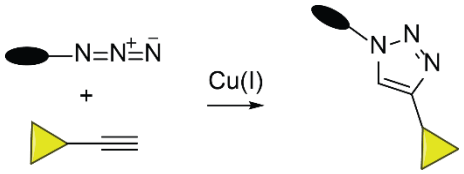

Figure 2.1 Schematic illustrating the 1,3-dipolor cycloaddition of azides and alkynes to form triazoles (Click reaction; black oval represents the GNR).

Due to the insolubility of GNRs, the late stage functionalization reaction must be efficient and high yielding. Click chemistry, namely the 1,3-dipolor cycloaddition of azides and alkynes to form triazoles, is widely used in biological applications to efficiently and reliably functionalize large biomolecules (Figure 2.1). It is envisioned that adapting this approach for nanomaterials allows for reliable and efficient modification. Thus, a clickable azide functionalized GNR, **N_3-cGNR**, provides a route in which any functional group can be incorporated after graphitization by reacting with the appropriate alkyne of choice.

2.2 Application in Imaging of GNRs

While bottom up synthesized GNRs grown on a catalytically active metal surface can be imaged with atomically-resolved scanning probe microscopy (SPM), an imaging technique capable of resolving the detailed atomic and electronic structure of individual, immobilized GNRs, this advanced tool is not scalable to bulk processing. Additionally, because surface growth requires a metallic substrate, the GNRs must be transferred onto an insulating substrate in order to integrate them into single-ribbon electronic devices.[61,62] These transfer processes, however, are difficult, unreliable, and can introduce contamination into the device architecture resulting in poor performance.

In comparison, solution-based approaches relying on either *Diels-Alder* or transition-metal catalyzed *Yamamoto* polymerizations followed by oxidative cyclodehydrogenation reactions have yielded bulk samples of cove- and chevron-type GNRs, yet critical challenges remain toward the incorporation of solution-synthesized GNRs into device architectures such as field effect transistors (FETs).[10] The solution-processing of GNR dispersions, for example, is limited by the inherent insolubility and the tendency of GNRs to aggregate into bundles driven by non-covalent

stacking interactions along the extended π-conjugated backbone.[65] While flakes of single-layer graphene can be readily visualized on SiO_2 and transparent substrates by optical microscopy,[66,67] the spatial localization of narrow solution-processed GNRs on insulating substrates required for aligning lithographic masks used in device fabrication remains a daunting challenge. Traditional imaging techniques like atomic force microscopy (AFM),[9,37] transmission electron microscopy (TEM),[28] scanning electron microscopy (SEM),[9,28] and scanning tunneling microscopy (STM)[9,31,32,37] are either restricted to atomically flat substrates (e.g., mica, graphite), require the sample to be suspended on a fragile, atomically thin support, or are restricted to conductive surfaces incompatible with electronic device architectures.

Optical microscopy provides an attractive alternative for its ease of use, ambient operating conditions, as well as its general applicability to nonconductive, simple substrates such as glass. Although the resolution of optical microscopy was traditionally limited by the diffraction of light to ~300 nm, this limit has been overcome in the past decade with the advent of super-resolution microscopy (SRM).[68,69] SRM encompasses many new fluorescence microscopy techniques that overcome the diffraction limit of light by reinventing how the fluorescence signal is generated, detected and processed.[70] Many of these techniques rely on the complex temporal behavior of photoswitchable fluorophores and take advantage of the fact that these dyes emit light at separate times, allowing them to be resolvable in time despite being close to another in space.[71] The most common SRM techniques, including STORM (Stochastic optical reconstruction microscopy), PALM (photo activated localization microscopy) and FPALM (fluorescence photo activated localization microscopy) rely on single molecule localization methods which require photoswitchable dyes that stochastically switch between on and off states.[71] Super resolution is then achieved by isolating emitters in time and fitting their images with their point spread functions (Figure 2.2).[71]

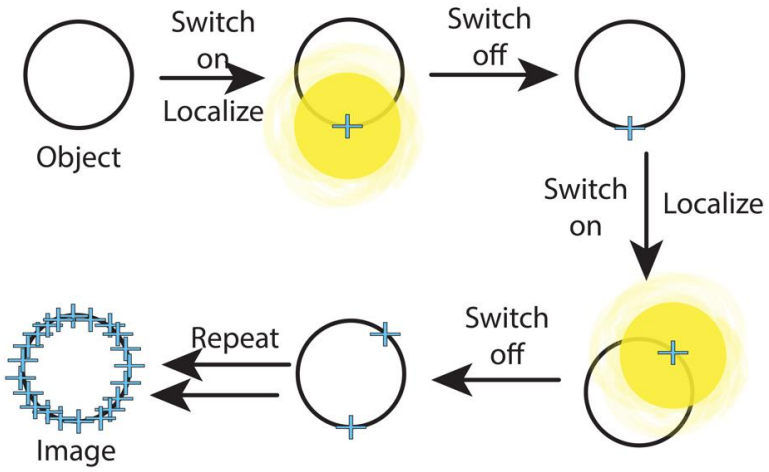

Figure 2.2 Schematic illustrating single molecule localization methods used in SRM.

While the primary application of SRM has been toward elucidating nanoscopic structures and interactions in biological specimens, its application to materials systems is beginning to be explored.[72–76] For carbon-based nanomaterials, SRM imaging of the quenching effect of graphene on a fluorescent substrate has enabled high-resolution characterization of the outlines of graphene flakes.[73] However, highly specialized substrates are still required, and the negative signal due to quenching limits image contrast.

By developing new strategies to directly functionalize GNRs with SRM-compatible fluorescent dyes, we can optically resolve and characterize the structure of single GNRs on insulating substrates at ~50 nm resolution through SRM. However, the photoswitchable dyes required for SRM, such as carbocyanine dyes (Figure 2.3), would not survive the harsh reaction conditions associated with the GNR synthesis, and thus must be installed after graphitization.

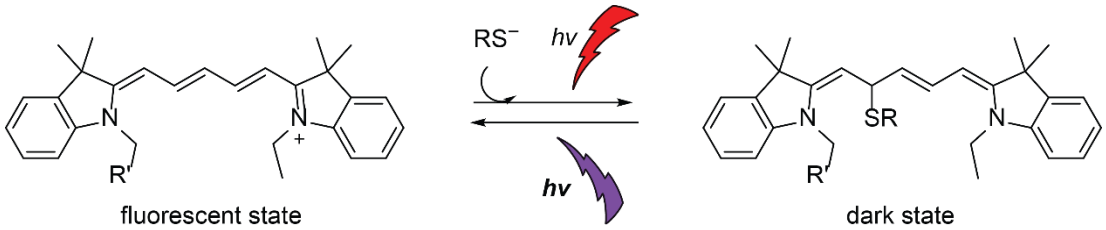

Figure 2.3 Switching mechanism of the carbocyanine dye (Cy5) that we envision clicking onto the GNR[113].

2.3 Synthetic Strategy

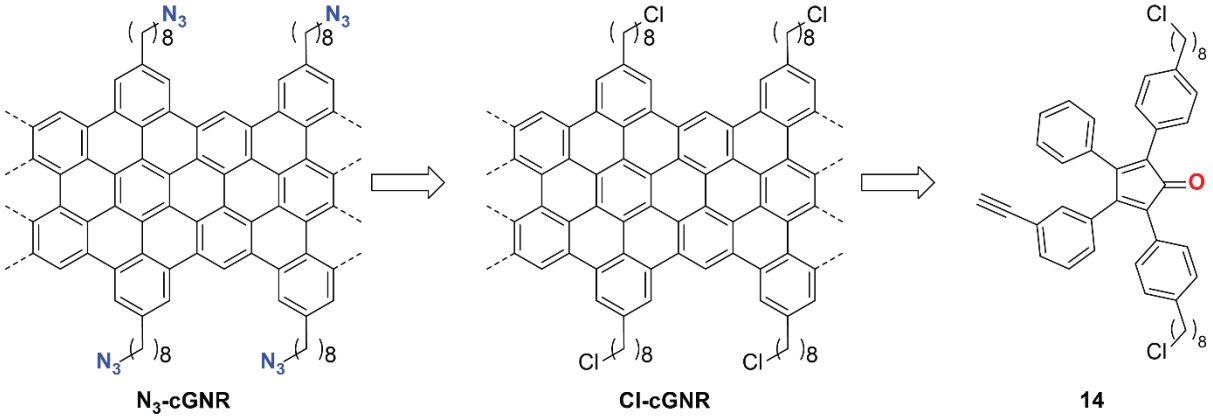

Scheme 2.1 Retrosynthesis of clickable **N_3-GNR**.

The synthetic route follows a similar path as previous cove-type solution synthesized GNRs; first requiring the synthesis of a monomer, which is then polymerized via a *Diels-Alder* polymerization, followed by oxidation (Scheme 2.1). Since the azide group required for the click-chemistry is not compatible with the harsh reaction conditions associated with the oxidative cyclodehydrogenation of the GNR precursor polymers, a synthetic route with a late-stage functional group interconversion was developed. In order to probe which functional handles would survive the oxidative cyclodehydrogenation, we did test reactions by subjecting a solubilized hexaphenylbenzene to the Scholl oxidation with oleylamine, heptylamine, and 6-chloro-1-hexanol. We were unable to recover the amines but could recover 6-chloro-1-hexanol, implying that the alkyl chloride groups survived the oxidation and thus chose chlorides as our leaving group. The *Diels-Alder* monomer, **14**, was designed to have alkyl chloride side chains to allow for late stage installation of the azide moiety after graphitization via a nucleophilic substitution of an alkyl

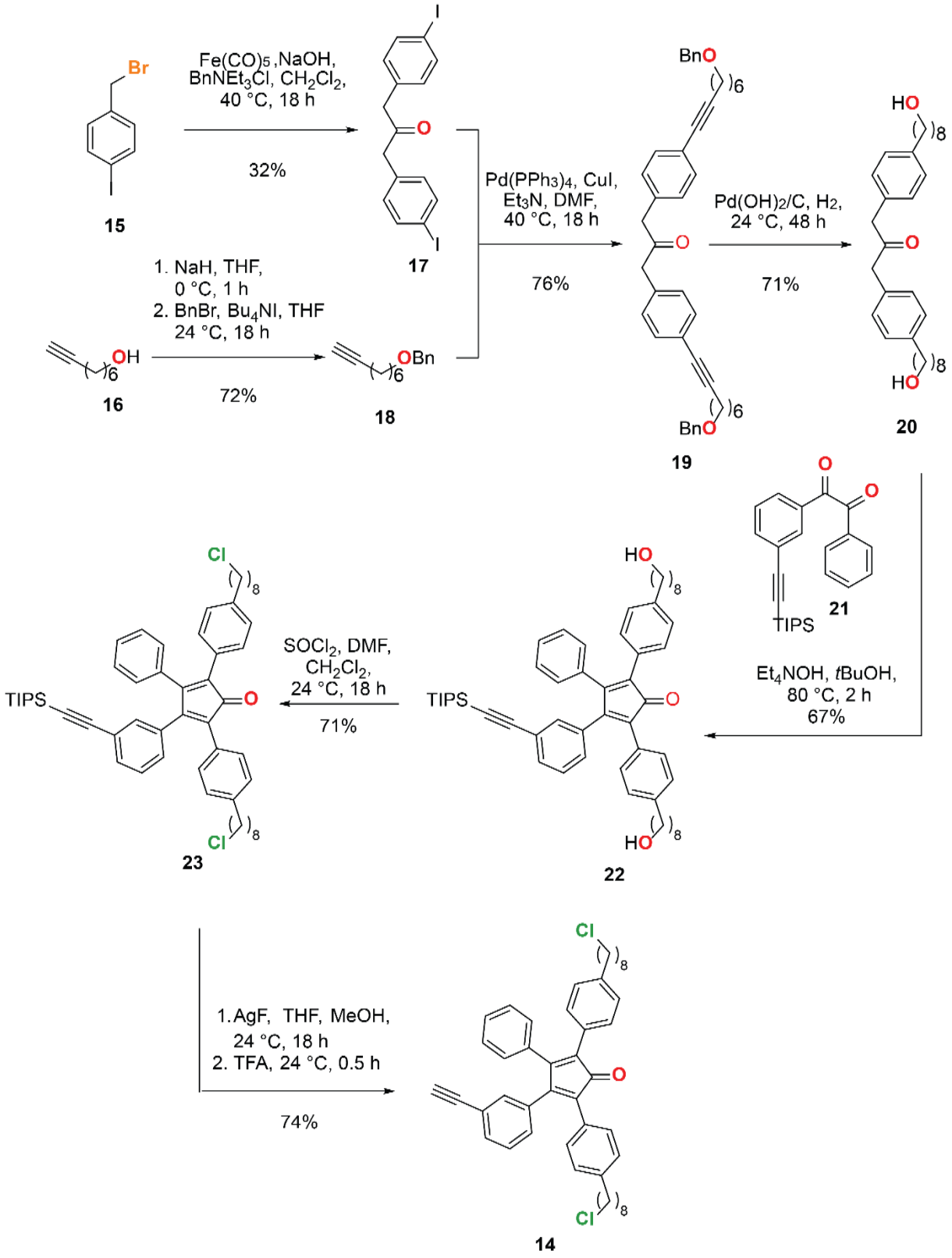

Scheme 2.2 Synthesis of *Diels-Alder* monomer **14**.

chloride with an azide. Additionally, post graphitization functionalization requires the GNRs to be well dispersed for efficient conversion. Thus, the monomer has long alkylated side groups to help as solubilizing groups.

The synthesis of monomer **14** is depicted in Scheme 2.2. An $Fe(CO)_5$ mediated coupling of 1-(bromomethyl)-4-iodobenzene afforded 1,3-bis(4-iodophenyl)propan-2-one, **17**, in 32 % yield. *Sonogashira* coupling of ketone **17** with an unprotected 7-octyn-1-ol resulted in very low yields, but was readily improved with the protection of the alcohol with a benzyl group. Hydrogenation with Pearlman's catalyst reduces the alkynes and removes the benzyl protecting group to yield ketone **20** in 71% yield. *Knoevenagel* condensation of ketone **20** with TIPS-protected benzil **21** yielded cyclopentadienone **22** in 67% yield. Treatment of cyclopentadienone **22** with $SOCl_2$ yielded chlorinated cyclopentadienone **23** and subsequent deprotection of the TIPS protected alkyne with AgF gave **14**, our target monomer for the *Diels-Alder* polymerization, in moderate yield. Initial deprotection attempts of the alkyne with TBAF resulted in many byproducts compared to AgF, making purification of the monomer difficult.

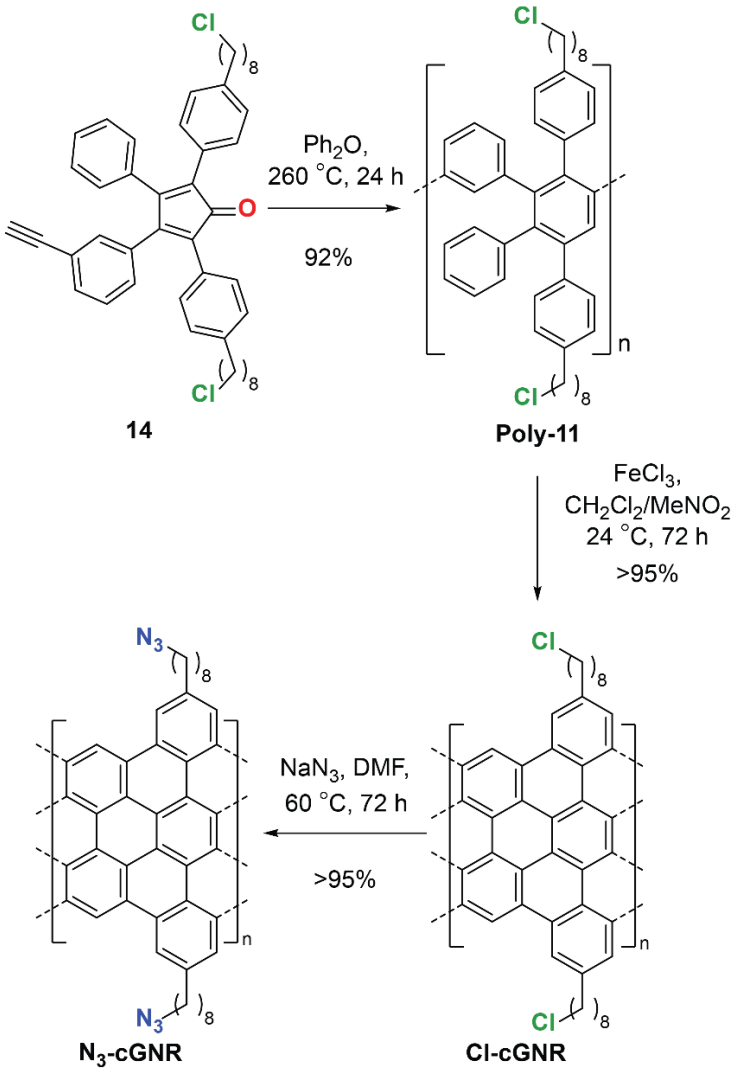

Scheme 2.3 Synthesis of **N_3-cGNR**.

With monomer **14** in hand, the subsequent polymerization and oxidation sequence gives access to the fully graphitized material. The bottom up synthesis of a clickable azide functionalized GNR is depicted in Scheme 2.3. *Diels-Alder* polymerization and decarbonylation of cyclopentadienone **14** gave polyphenylene intermediate **poly-11** in 92% yield. Oxidative cyclodehydrogenation via the Scholl oxidation of **poly-11** yielded structurally homogeneous cGNRs (**Cl-cGNR**) featuring solubilizing 8-chlorooctyl side chains along the protrusions of the cove-edges. Nucleophilic substitution of the primary chlorides in the solubilizing side chains of **Cl-cGNR** with sodium azide gave the clickable cGNRs (**N_3-cGNR**) in > 90% yield. In order to achieve high conversion of the alkyl chlorides to the alkyl azides, the reaction mixture was sonicated for at least 2 hours every day over 3 days to help keep the GNRs dispersed. With the **N_3-GNR** in hand, we now have GNR with the ability to undergo copper-catalyzed Huisgen 1,3-dipolar cycloaddition with any functionalized terminal alkyne.

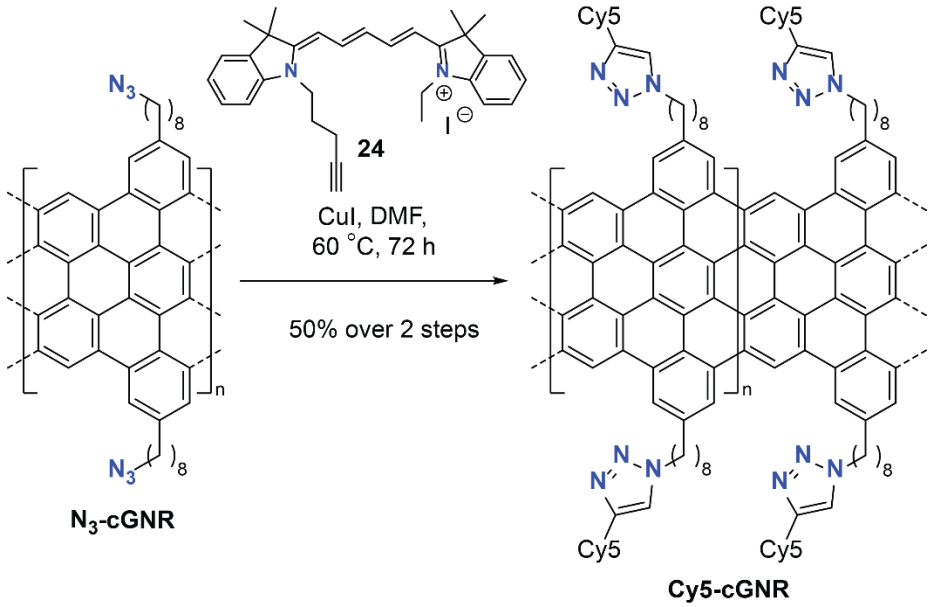

Scheme 2.4 Click reaction between **N_3-cGNR** and alkyne functionalized Cy5 dye **24**.

Copper-catalyzed Huisgen 1,3-dipolar cycloaddition between **N_3-cGNRs** and a Cy5 dye bearing a terminal alkyne, **24**, gave the dye-functionalized **Cy5-cGNRs** in ~ 50% yield over two steps (Scheme 2.4). Once again, in order to achieve high conversion, the reaction mixture was sonicated for at least 2 hours every day over 3 days to help keep the GNRs well dispersed.

2.4 Structural Analysis

Due to the insolubility of graphene nanoribbons, traditional characterization methods such as solution NMR and mass spectrometry are extremely challenging. Thus, we utilized characterization methods, such as Raman and IR spectroscopy, to elucidate the structure of the GNRs. We are able to determine and control the lengths of the GNRs by controlling the polymer length of **poly-11**.The polymer lengths were controlled by the concentration of the *Diels Alder* polymerization and the longest polymers were isolated using a concentration of 1:1 monomer **14**

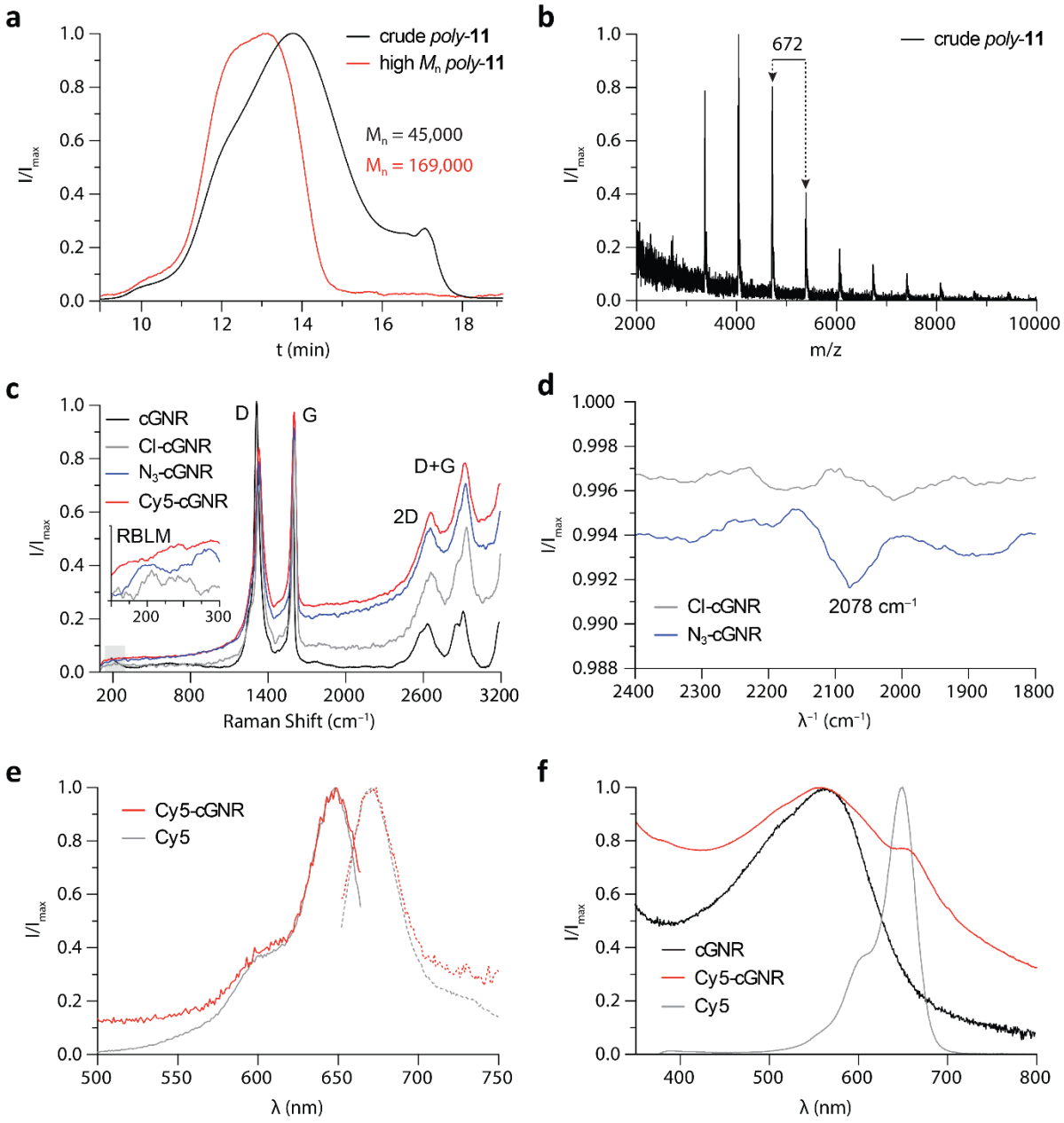

Figure 2.4 (a) Size exclusion chromatography (SEC) trace of crude **poly-11** (black) and the high molecular weight fraction (red) isolated by preparative SEC. (b) MALDI mass spectrum of crude **poly-11** showing the characteristic family of molecular ions. The spacing corresponds to the mass of the polymer repeat unit. (c) Raman spectrum (λ_E = 514 nm) of bulk samples of alkylated cGNRs, **Cl-cGNRs**, **N_3-cGNRs**, and **Cy5-cGNRs**. Inset shows a magnification of the spectral region associated with the RBLM. (d) IR spectrum of **Cl-cGNRs** and **N_3-cGNRs** showing the characteristic peak associated with the azide stretching mode. (e) Fluorescence excitation (solid lines) and emission (dotted lines) spectra of free Cy5 and dye-functionalized **Cy5-cGNRs**. (f) UV-Vis absorption spectra of free Cy5, dye-functionalized **Cy5-cGNRs** and alkylated cGNRs.

to diphenyl ether. The molecular weight dispersity, $Đ_M$, of **poly-11** using this concentration derived from size exclusion chromatography (SEC, calibrated to polystyrene standards) ranges from 2.5 to 3.9 with a number average molecular weight M_n of 45 kg mol^{-1} (Figure 2.4a). Preparative SEC yielded a high molecular weight fraction of **poly-11** with $Đ_M$ = 1.7 and a M_n of 169 kg mol^{-1} that was carried on through the remainder of the synthesis. MALDI mass spectrometry (Figure 2.4b) shows the characteristic family of molecular ions separated by the mass of the decarbonylated monomer (ΔM = 672 g mol^{-1}).

Raman spectroscopy (λ_E = 532 nm) of the **Cl-cGNR** shows the characteristic signatures for the radial breathing like mode (RBLM) (232 cm^{-1}; FWHM = 83 cm^{-1}), the D (1334 cm^{-1}; FWHM = 56 cm^{-1}) and G (1607 cm^{-1}; FWHM = 26 cm^{-1}) peaks with a ratio of $I_{D/G}$ = 0.76 along with higher order 2D and D+G peaks (Figure 2.4c), which is in agreement with the reported spectrum of an unsubstituted alkylated cGNR.[43,45,58]

After the nucleophilic substitution of the primary chlorides, a comparison of the infrared spectra of **Cl-cGNR** and **N_3-cGNR** (Figure 2.4d) reveals the appearance of a characteristic absorption peak (λ^{-1} = 2078 cm^{-1}) assigned to the azide linear stretching mode.[77] The Raman spectrum of **N_3-cGNR** shows no significant change in the RBLM, D and G peak position/ratio, consistent with the selective attack of the azide on the ancillary alkyl chloride side chain rather than a functionalization of the conjugated backbone of the cGNRs.

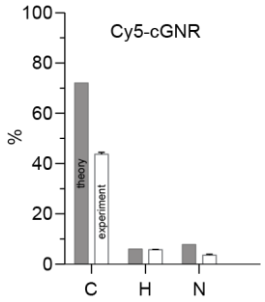

Figure 2.5 Elemental CHN analysis of **Cy5-cGNRs.**

Elemental analysis was utilized to determine the yield for the conversion of the **Cl-cGNR** to the **Cy5-GNR** over two steps (Figure 2.5). As observed previously for carbon-rich graphitic nanomaterials, the combustion of **Cy5-cGNRs** does not go to completion at 1000 °C leaving behind a residue of amorphous carbon that is reflected in the difference between theoretical and experimental carbon content.[78] The experimental hydrogen content largely associated with the aliphatic side chains instead is commensurate with the expected values.[10,64] The combustion analysis of **Cy5-cGNRs** accounts for ~50% of the expected nitrogen. Based on these results we estimate that on average only every second side chain on the cGNR has been successfully functionalized with Cy5 dye. Fluorescence and UV-Vis spectroscopy show the successful integration of the dye with the cGNRs (Figure 2.4e and f). The fluorescence excitation and emission spectra of **Cy5-cGNRs** are almost indistinguishable from the spectra of free Cy5, indicating that the alkyl spacers between the dye and the extended π-system of the cGNR effectively prevent quenching of excited states. The excitation (emission) maxima are found at 649 nm (674 nm) and 648 nm (671 nm) for the **Cy5-GNRs** and Cy5, respectively. While free Cy5

shows a maximum UV-Vis absorption at λ_{max} = 650 nm the corresponding transition in the dye-functionalized **Cy5-GNRs** is slightly red-shifted and appears as a shoulder around λ = 663 nm.

2.5 SRM Imaging of Cy5-GNR

Samples of dye-functionalized GNRs for fluorescence imaging were prepared by spin-coating dilute suspensions (0.1 mg mL^{-1}) of **Cy5-cGNRs** in acetone onto silanized glass coverslips. In order to achieve stable enough suspensions of the GNRs in acetone, the samples were probe sonicated for 30 to 60 minutes. **Cy5-GNR** dispersions in other better solubilizing solvents, such as THF and toluene, caused large GNR aggregations and drying rings to form upon spin coating, indicating a solvent with a lower boiling point, such as acetone, was required. Additionally, spin coating onto unsilanized glass resulted in inhomogeneous coverage of only a few large bundled GNRs and very few single GNRs on the surface. By controlling the suspension concentration, spin rate, and solvent, isolated GNRs were well-spread across the silanized glass surface. Raman mapping of the G peak intensity reveals a homogeneous coverage of the surface with **Cy5-cGNRs** with only minimal aggregation into larger bundles when 0.1 mg mL^{-1} suspensions in acetone and silanized glass was used (Figure 2.6)

.

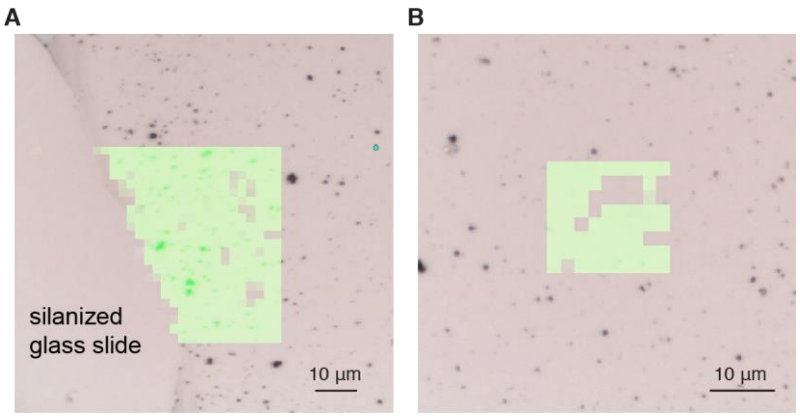

Figure 2.6 Figure S2. Raman maps of spin-coated **Cy5-cGNRs** on silanized glass slides. (A) Raman map of the G peak intensity of spin-coated **Cy5-cGNRs** on a silanized glass slide. The bare area of the slide was covered with Scotch tape during spin-coating. Prior to Raman imaging, Scotch tape was peeled off to reveal the bare glass slide. (B) Raman map of the G peak intensity of spin-coated **Cy5-cGNRs** on a silanized glass slide.

Conventional, diffraction limited fluorescence microscopy (laser λ_{Ex} = 647 nm; 2 $mWcm^{-2}$) of **Cy5-cGNRs** on glass coverslips reveals isolated fluorescent strings and larger bundles with typical apparent lengths in the range 5−15 μm (Figure 2.8A–C insets). Cross-sectional fluorescence intensity profiles of individual GNRs show apparent FWHM widths of ~300 nm (gray circles and lines in Figure 2.8D–F), comparable to the diffraction limit of our system given the relatively long emission wavelength of Cy5 (λ_{Em} = 671 nm). While conventional fluorescence microscopy of **Cy5-cGNRs** clearly reveals the position of dye-functionalized cGNRs even on an

insulating nonplanar substrate, the resolution is insufficient to unambiguously distinguish between single **Cy5-cGNRs** and larger bundles.

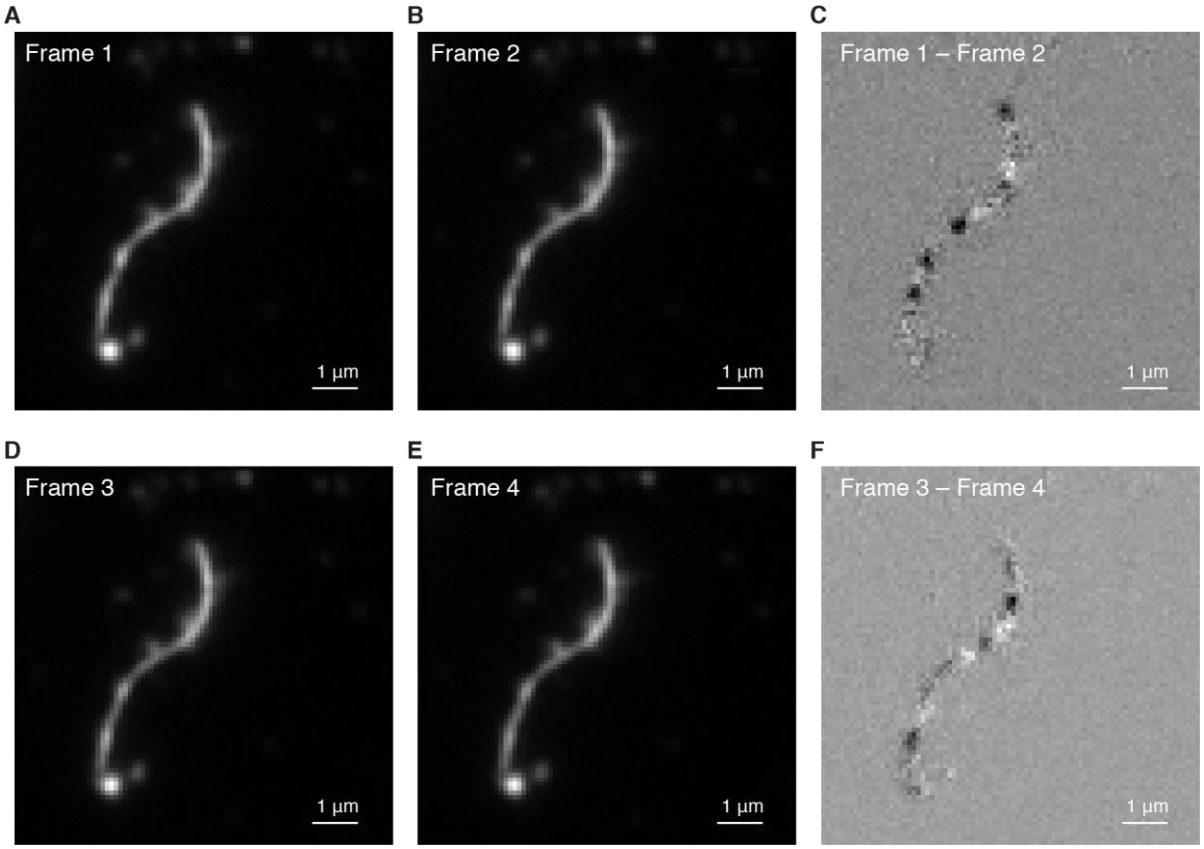

Figure 2.7 Representative imaging frames recorded as part of the SRM imaging of **Cy5-cGNRs**. (A,B) Two sequential frames of the SRM raw data obtained for a **Cy5-cGNR**, showing fluctuations in local fluorescence but not full fluorescence switch-off. (C) Subtraction of the fluorescence intensity of the two consecutive frames, highlighting local fluctuations in intensity, which enabled the use of SRRF algorithms to reconstruct SRM images. (D–F) Results from two other frames. Reconstructed SRRF SRM image from 4,000 frames is shown in Figure 2.8.

To increase the lateral resolution and to identify the number and the arrangement of cGNRs in a specific sample, we imaged the same structures using SRM. The sample slide was immersed in an imaging buffer containing 2-aminoethanethiol to assist the photoswitching of Cy5 dyes, and the laser power was increased to 2 kW cm^{-2}. Ideally, these routine STORM (stochastic optical reconstruction microscopy) SRM conditions should switch a majority of the labeled Cy5 molecules into a non-fluorescent dark state, so that the remaining emitting molecules are sparsely distributed across the view to avoid spatial overlap of fluorescence signal, as routinely achieved in SRM of biological samples.[16-18] Unexpectedly, although the measured bulk fluorescence excitation and emission spectra of **Cy5-GNR** were nearly identical to that of free Cy5 (Figure 2.4E), photoswitching characteristics of single molecules were quite different for the conjugated Cy5. Most molecules could not be efficiently switched to a dark state, even at the highest concentration of thiol quencher (100 mM). Figure 2.7 shows representative frames recorded as part of the STORM imaging of **Cy5-cGNRs**. Figure 2.7 A,B and D,E shows two sequential frames of the STORM raw data obtained for a Cy5-cGNR, respectively, showing fluctuations in local

fluorescence but not full fluorescence switch-off. As a result, heavy overlapping of the emission from different individual Cy5 molecules always occurred along the GNRs, preventing us from performing single-molecule localization analysis as in STORM. We hypothesize that this effect is caused by a combination of the unusually high density of dyes along the edge of the cGNR (~1–2 Cy5 dyes nm^{-1}) compared to traditional dye concentrations used in biological samples and the hydrophobic local environment of the cGNRs that limits the local concentration of the polar thiol quencher.

Although we did not attain single-molecule switching required for STORM, substantial temporal fluorescence intensity fluctuations were achieved along the length of the **Cy5-GNR**s, evident in Figure 2.7 C and F which shows the subtraction of the fluorescence intensity of the two consecutive frames, highlighting local fluctuations in intensity. This allowed us to realize SRM

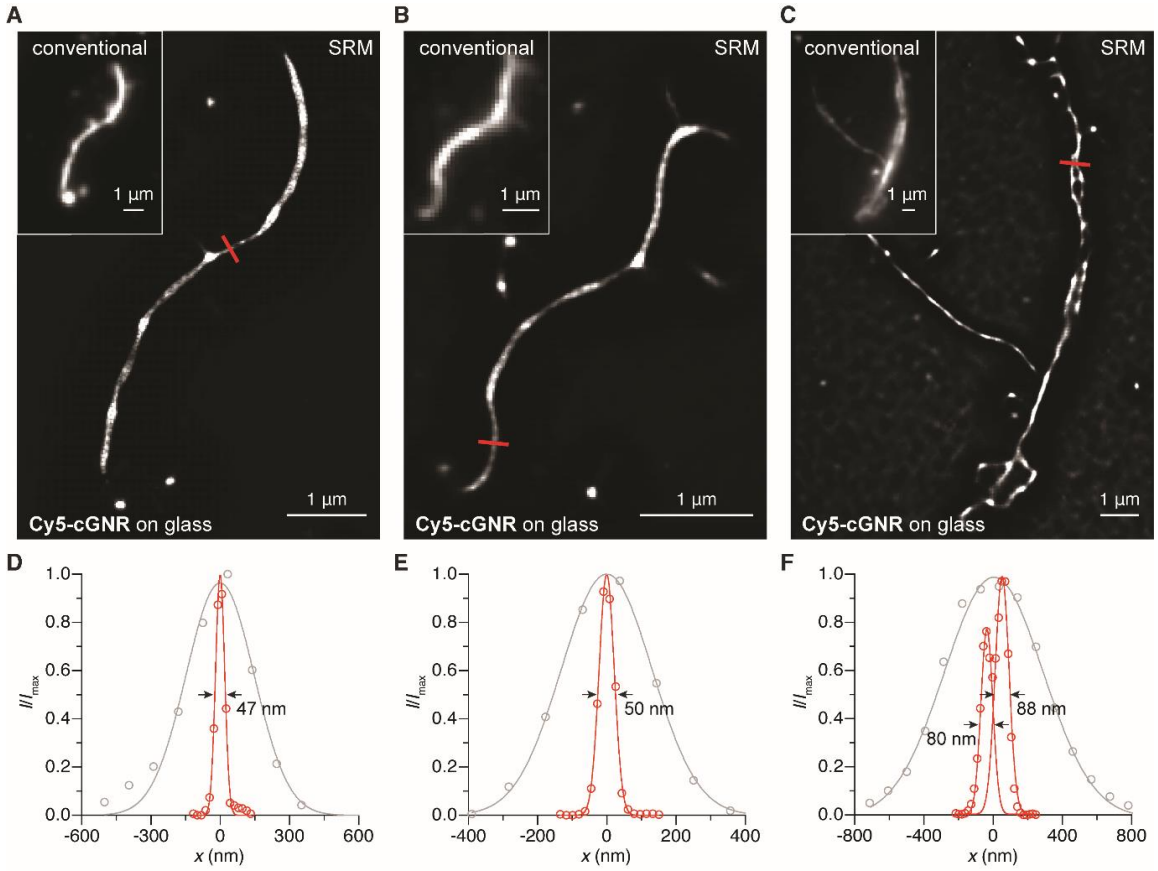

Figure 2.8 Comparison between conventional fluorescence and super-resolution microscopy of dye-functionalized **Cy5-cGNRs**. (A−C) SRM (SRRF) fluorescence images of samples of **Cy5-cGNRs** on silanized glass coverslips. Figure insets show conventional diffraction-limited microscopy of the same area of the sample. (D−F) Fluorescence intensity cross-section profiles at positions highlighted (red lines) in A−C in conventional diffraction-limited fluorescence microscopy (gray) and SRM (SRRF) images (red) (circles: experimental data, lines: Gaussian fits). The SRM data in (F) are fitted by two Gaussian peaks with a 98 nm peak-to-peak distance.

through analysis methods that leverage the temporal correlation of images collected in different frames, e.g. super-resolution optical fluctuation imaging (SOFI)[19] and super-resolution radial

fluctuations (SRRF).[20] SOFI requires the fluorophores to have fluctuating fluorescence properties that can be recorded. This includes fluorescence intensity and dye molecules that switch between bright and dim states but do not necessarily switch off.[79] SRRF is an analytical approach similar to SOFI, however SRRF analysis does not require emitting fluorophores to be sparsely distributed, is able to provide a super resolution reconstruction without detecting and localizing individual fluorophores and provides a significant reduction in reconstruction artefacts. Thus SRRF is still able to distinguish between two spatially close emitters and is a more robust SRM analysis method for images with overlapping fluorophores.[80,81]

Figures 2.8A,B show SRRF images of the two distinct **Cy5-cGNRs** corresponding to the diffraction-limited images depicted in the figure insets. Intensity cross-section profiles show an apparent FWHM of 47–50 nm for both dye-functionalized cGNRs. Assuming the backbone of the cGNRs adsorbs planar and parallel to the surface, the theoretically predicted width of **Cy5-cGNRs** is expected to range between 7–10 nm. The uniform apparent width of ~50 nm observed across numerous different **Cy5-cGNRs** samples (see Figure 2.9 for additional images) suggests that single isolated **Cy5-cGNRs** can be resolved with an apparent width close to the reported theoretical resolution limit of SRRF.

SRRF imaging of dye-functionalized **Cy5-cGNRs** not only represents a ~10-fold improvement over the resolution of diffraction-limited fluorescence microscopy images (Figure 2.8A–C insets) but further provides a reliable tool to analyze structures comprised of entangled cGNR bundles and potentially even more complex functional arrays. Figure 2.8C shows both a conventional fluorescence image and a SRRF image of a **Cy5-cGNR** bundle comprised of entangled cGNRs. The fluorescence intensity cross-section profile for a region of the diffraction-limited image shows a single unresolved broad peak with a FWHM of 670 nm. In contrast, the corresponding SRRF image reveals two parallel cGNRs. The intensity cross-section profile shows two well-separated peaks at 98 nm center-to-center distance with FWHMs of 80 nm and 88 nm respectively. This example demonstrates that SRRF imaging of dye-functionalized GNRs can resolve structural details well below the resolution limit imposed by the diffraction of light.

While non-destructive SRM imaging of dye-functionalized cGNRs on glass coverslips serves as a proof of concept, the greater challenge lies in transferring this tool to more relevant substrates like bare Si or Si/SiO_2 wafers traditionally used in electronic device fabrication. SRM imaging on these opaque substrates was achieved by inverting the sample geometry and imaging through an opposing coverslip. Representative images of linear strings and small bundles of **Cy5-cGNRs** spin-coated from acetone dispersions onto silanized Si and Si/SiO_2 wafers are depicted in Figure 2.10A,B and Figure 2.10C,D, respectively. Fluorescence intensity cross-section profiles of SRRF images on both bare Si and SiO_2 show a FWHM of 60–68 nm (Figure 2.10E–H) reminiscent of the apparent width of **Cy5-cGNRs** on glass slides. This work demonstrates that SRM (SRRF) of dye-functionalized cGNRs can be used as a non-destructive, high-throughput, high-resolution imaging tool to localize individual isolated ribbons in the very dilute samples required for the targeted deposition of lithographic contacts in the fabrication of experimental electronic device architectures.

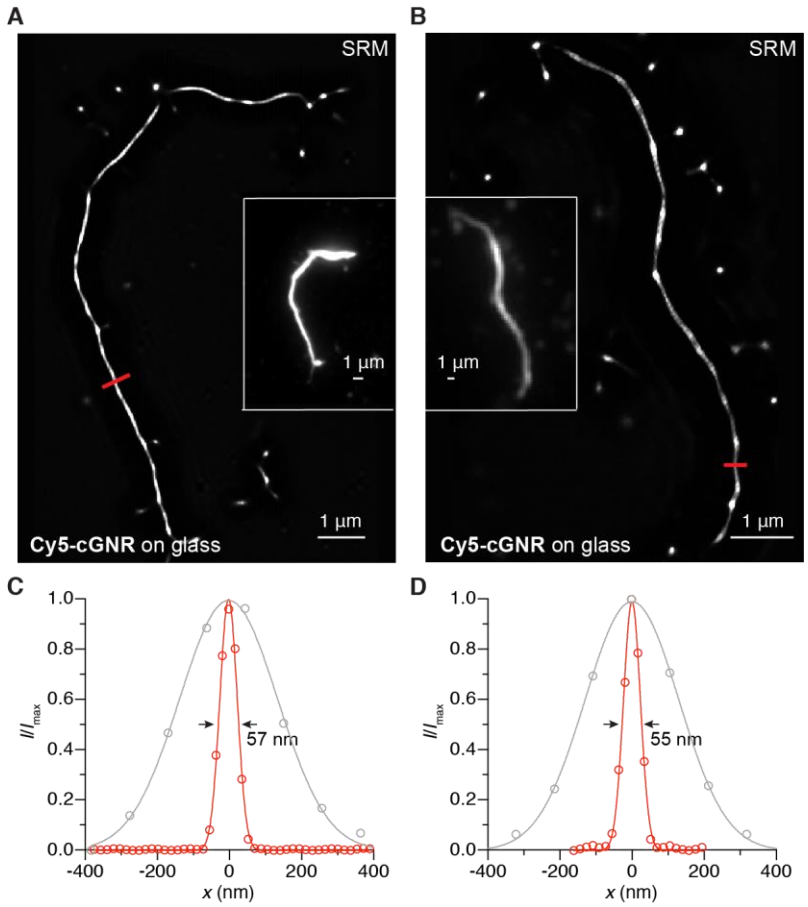

Figure 2.9 Additional examples of comparison between conventional fluorescence and super-resolution microscopy of **Cy5-cGNRs**. (A–B) SRM (SRRF) fluorescence images of samples of **Cy5-cGNRs** on silanized glass coverslips. Figure insets show conventional diffraction-limited microscopy of the same area of the sample. (C–D) Fluorescence intensity cross-section profiles at positions highlighted (red lines) in (A–B) using conventional diffraction-limited fluorescence microscopy (gray) and SRM (SRRF) image processing (red). (circles: experimental data, lines: Gaussian fits).

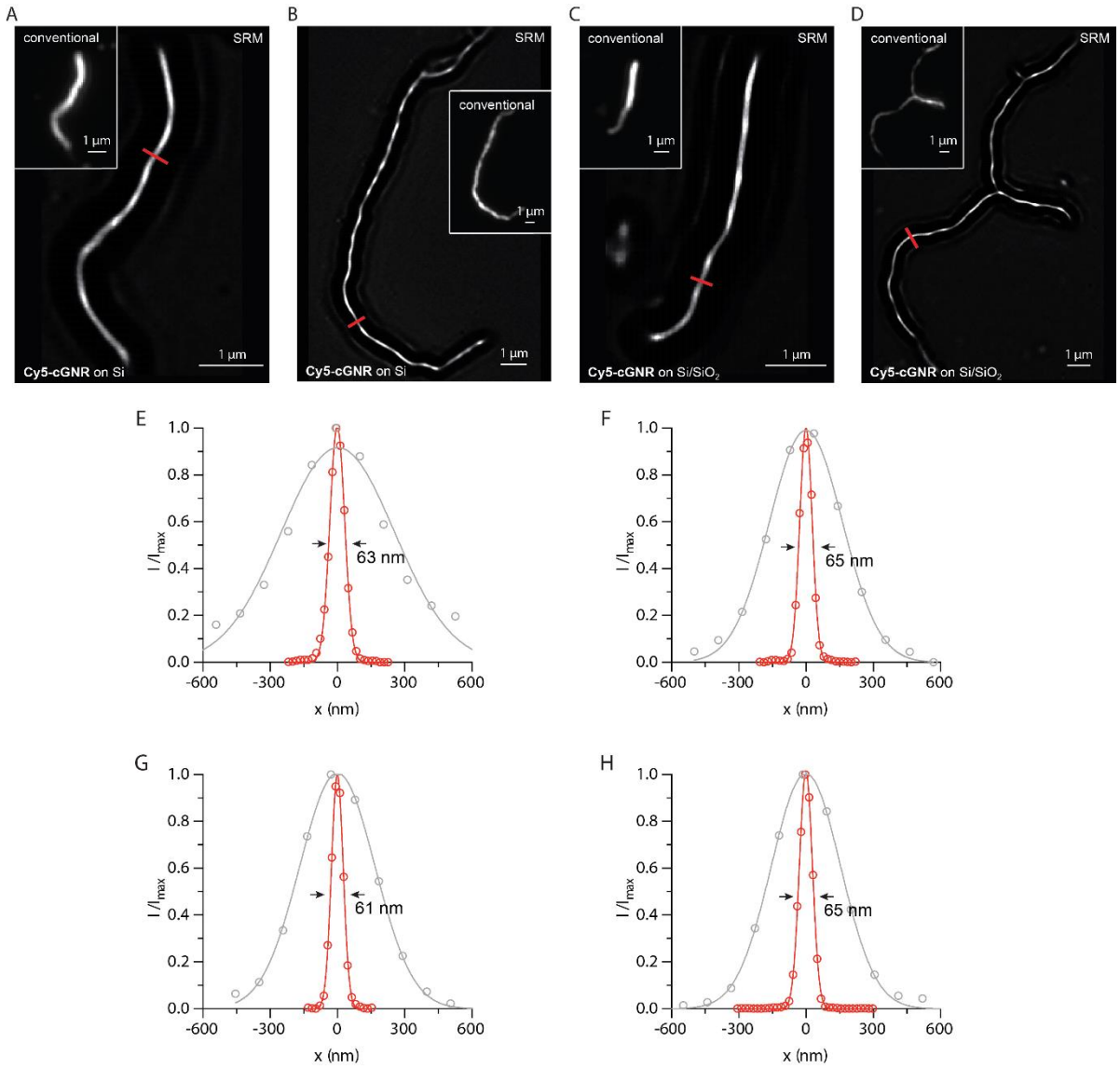

Figure 2.10 Comparison between conventional fluorescence and super-resolution microscopy of dye functionalized **Cy5-cGNRs** on Si and Si/SiO_2 wafers and their corresponding fluorescence intensity cross-section profiles. (A–B) SRM (SRRF) fluorescence images of samples of **Cy5-cGNRs** on silanized Si wafers. Figure insets show the conventional diffraction-limited microscopy of the same area of the sample. (C–D) SRM (SRRF) fluorescence images of samples of **Cy5-cGNRs** on silanized Si/SiO2 wafers (SiO_2 thickness ~ 300 nm). Figure insets show the conventional diffraction-limited microscopy of the same area of the sample. (E–H) Fluorescence intensity cross-section profiles at positions highlighted (red lines) in A–D. Diffraction limited fluorescence microscopy (gray) and SRM (SRRF) image processing (red). (circles: experimental data, lines: Gaussian fit)

2.6 Model System with Cy5-CNT

In an effort to corroborate the apparent width of **Cy5-cGNRs** derived from SRRF analysis to the real dimensions of the ribbon we selected single wall carbon nanotubes (SWCNTs) as a reference standard that could be independently verified by atomic force microscopy (AFM) (we were unable to resolve cGNRs on glass directly as the surface roughness of glass coverslips is greater than the apparent height of individual graphene nanoribbons). Due to their tubular structure, CNTs are slightly more processable than GNRs because they have reduced aggregation. Additionally, due to their more rigid structure compared to GNRs and their long lengths (1 to 5 μm), they made ideal model systems for SRM. Thus, a cyanine labeled SWCNT, **Cy5-CNT** was prepared (Scheme 2.5).

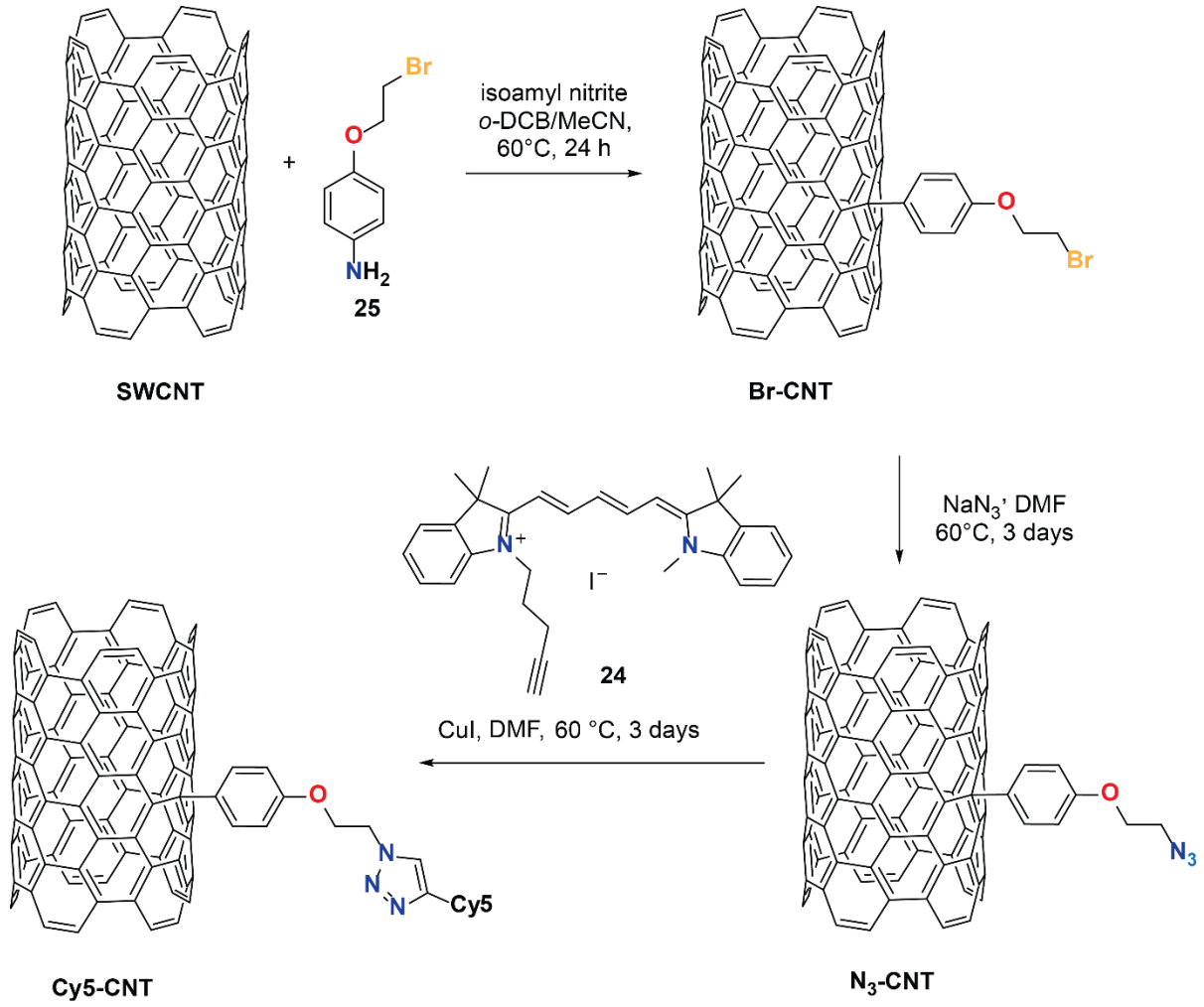

Scheme 2.5 Synthesis of **Cy5-CNT**.

Following a procedure developed by the Tour group, SWCNTs were modified with the in situ formation of aryl diazonium species formed 4-(2-bromoethoxy)-aniline and isoamyl nitrite to yield **Br-CNT**[82]. Nucleophilic substitution of the primary bromides of **Br-CNT** with sodium azide afforded the clickable SWCNT (**N_3-CNT**). Copper-catalyzed *Huisgen* 1,3-dipolar cycloaddition of **N_3-CNT** with *N*-pentynyl-Cy5, **24**, gave the corresponding dye-functionalized SWCNTs, **Cy5-**

CNT. This synthesis confirms the generality and versatility of our approach of using an azide functionalized carbon nanomaterial for late stage functionalization via click chemistry.

Infrared spectroscopy indicates the presence of azide moieties for the **N_3-CNT** from the emergence of a new peak corresponding to the azide stretch at 2092 cm^{-1} (Figure 2.11A).[77] Raman spectroscopy of the **Br-CNT**, **N_3-CNT**, and **Cy5-CNT** all have strong G peaks, associated with CNTs, as well as a smaller D peak, indicative of functionalization onto the CNT backbone (Figure 2.11B). UV-Vis spectroscopy and fluorescence spectroscopy clearly show the successful

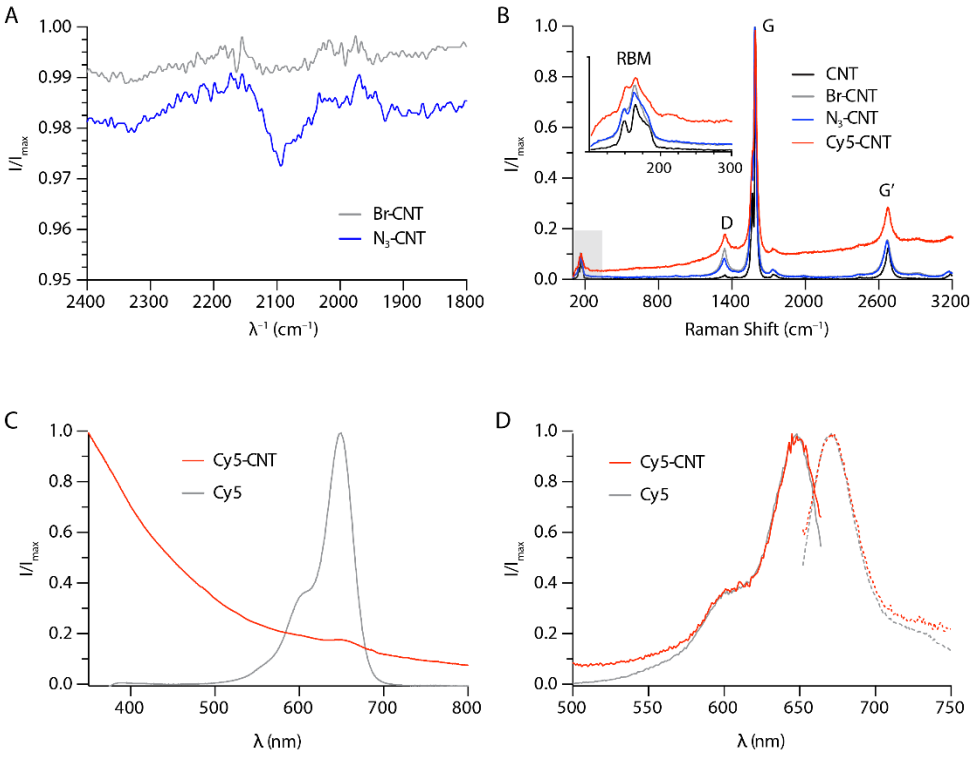

Figure 2.11 Characterization of dye-functionalized single-walled carbon nanotubes (**Cy5-CNTs**). (A) IR spectrum of **Br-CNTs** and **N_3-CNTs** showing the characteristic peak associated with the azide stretching mode. (B) Raman spectrum (λ_E = 532 nm) of bulk samples of SWCNTs, **Br-CNTs**, **N_3-CNTs**, and **Cy5-CNTs**. Inset shows a magnification of the spectral region associated with the radial breathing mode (RBM). (C) UV-Vis absorption spectra of free Cy5 and dye-functionalized **Cy5-CNTs**. (D) Fluorescence excitation (solid lines) and emission (dotted lines) spectra of free Cy5 and dye-functionalized **Cy5-CNTs**.

functionalization of the CNTs with Cy5 via the Click reaction (Figure 2.11 C and D). The free Cy5 has a maximum UV-Vis absorbance at 649.5 nm. When covalently linked to the SWCNTs, the absorption of the dye is slightly red shifted as seen by the shoulder around 653.0 nm for the **Cy5-CNT**. The fluorescence excitation and emission spectra of **Cy5-CNT** correlate well that of free **Cy5**.

Figure 2.12A shows conventional fluorescence and SRRF microscopy images of **Cy5-CNTs** spin-cast from dilute aqueous dispersions onto unfunctionalized, hydrophilic glass coverslips. The fluorescence intensity cross-section profile reveals an apparent width of 52–82 nm for individual carbon nanotubes. Analogous to our studies on **Cy5-cGNRs**, nanotubes within larger aggregates

or bundles can be resolved by SRRF when separated by distances greater than the apparent width of a **Cy5-CNT** (Figure 2.12A,B). A correlation of structures imaged by SRM with AFM height profiles recorded at the same position (Figure 2.12C,D) reveals that the ~50 nm wide features resolved in our SRRF SRM images indeed correspond to individual SWCNTs.

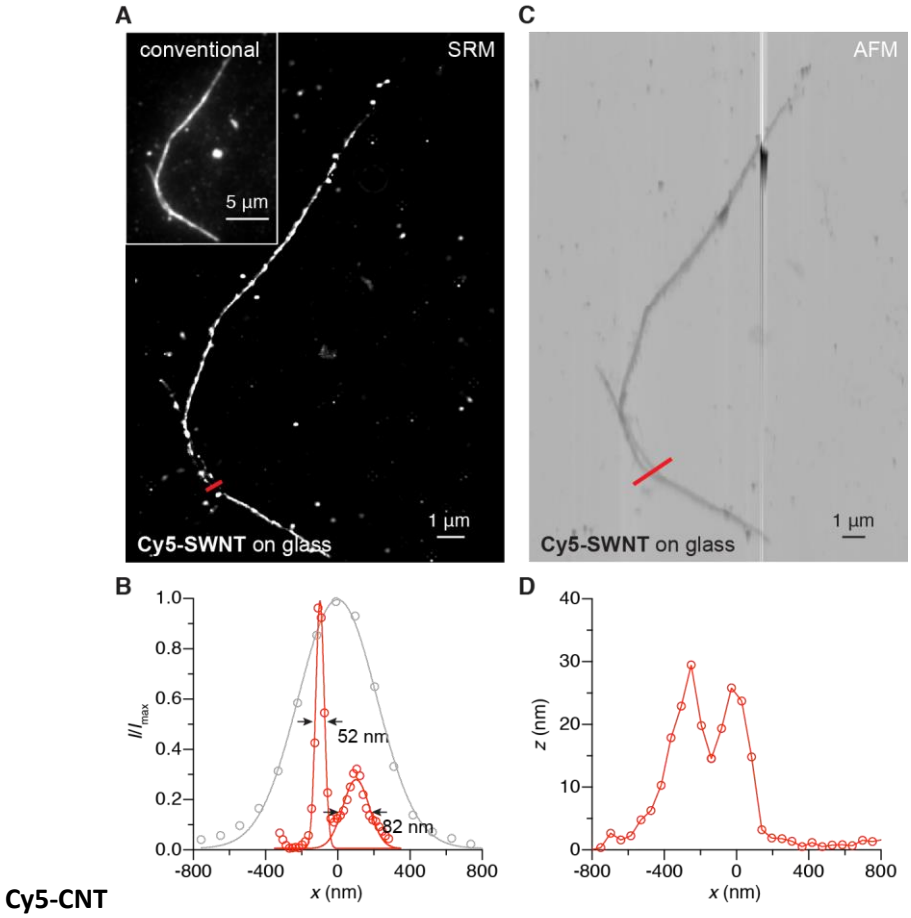

Figure 2.12 Conventional fluorescence, super-resolution, and atomic force microscopy of dye-functionalized **Cy5-CNTs**. (A) SRM (SRRF) fluorescence image of **Cy5-CNTs** on a glass coverslip. Figure inset shows conventional diffraction-limited microscopy of the same area of the sample. (B) Fluorescence intensity cross-section profiles at positions highlighted (red lines) in (A) in the conventional diffraction-limited fluorescence microscopy (gray) and SRM (SRRF) (red) images (circles: experimental data, lines: Gaussian fits). (C) AFM image of the same area of the sample depicted in (A). (D) AFM height profile of **Cy5-CNTs** at the position highlighted (red line) in (C).

2.6 Conclusion and Outlook

In conclusion, we have developed a solution-based synthesis of a new class of cGNRs functionalized with reactive azide groups along the edges that can undergo Cu-catalyzed click-reactions with a wide variety of functional groups and molecules bearing a terminal alkyne. Our N_3-cGNR opens the door to synthesizing previously inaccessible functionalized GNRs. We have demonstrated that conjugation of these clickable cGNRs with fluorescent dyes derived from Cy5 allows the imaging of dilute dispersions of cGNRs spin-coated onto glass, Si, or Si/SiO_2 substrates using not only conventional fluorescence but also super-resolution microscopy (SRM). While the apparent width of individual ribbons imaged by SRM is well below the diffraction limit of light and allows the unambiguous distinction between isolated ribbons and larger bundles on the surface, a statistical analysis of the length of **Cy5-cGNRs** reveals that the exceptionally efficient *Diels-Alder* polymerization of cGNR monomers can give rise to graphene nanoribbons ranging in length from 6–10 μm. This work not only describes the development of a highly versatile and modular material based on azide-functionalized GNRs, but also demonstrates that one of the critical challenges in the exploration and exploitation of the exotic properties of GNRs in electronic devices, the non-destructive imaging of dilute samples on opaque dielectric substrates, can be accomplished using super-resolution fluorescence imaging techniques derived from cell biology.

The development of an azide functionalized GNR also paves the way to access a variety other novel GNRs. For instance, the **N_3-cGNR** could be functionalized with DNA for the self-assembly of GNR through DNA origami. The **N_3-cGNR** could also be immobilized onto an alkyne functionalized surface via click chemistry. In both cases, the resulting GNRs could be pre-patterned onto a surface for more efficient device integration. Since click chemistry is such a versatile reaction, known to provide high yielding functionalization of supermolecular structures, and synthesizing alkyne functionalized moieties of interest are known chemistries, the applications of the **N_3-cGNR** are numerous.

Chapter 3

Conjugating Molecular Catalysts onto Graphene Nanoribbons

In chapter 2 late stage functionalization of GNRs was discussed in which we successfully "clicked" on terminal alkynes to an azide functionalized **N_3-GNR** through a 1,3-dipolor cycloaddition. This **N_3-GNR**, however, has an insulating alkyl tether between the functional groups and GNR backbone. In contrast, late stage edge modification via condensation chemistry would directly place the desired functional group in conjugation with the GNR backbone. We have developed a quinone functionalized GNR (**q-CGNR**) which can react with various diamines. Successful condensation 1,10-phenanthroline-5,6-diamine onto the **q-CGNR** gave rise to a **Phenanthroline-CGNR** (**Phen-CGNR**), which has bidentate ligand sites along the edge to which various metals can be coordinated. We have additionally developed a **2N-CGNR** which also contains ligand sites along the edges. By using this strategy, we were able to access metallated GNRs with known CO_2 and hydrogen activation catalysts and were able to study the kinetics for hydrogen activation with our system. H_2/D_2 exchange kinetic studies were carried out in collaboration with Lennie Klebanoff and Don Cowgill at Sandia National Laboratories.

3.1 Introduction

Immobilizing homogenous catalysts on various solid supports makes the molecular catalysts insoluble in the reaction solution, essentially heterogenizing the homogenous catalyst. This combines the benefit of both types of catalysis, namely ease of separation and recovery of the catalysts from the reaction mixture, while still having distinct reaction sites with high selectivity and known reactions mechanisms. Additionally, by immobilizing molecular catalysts, deactivation pathways by bimolecular reactions, such as dimerization of metal complexes, can be prevented, thereby increasing catalyst efficiency.[83,84] Many examples have immobilized molecular catalysts on solid supports such as silica or polymeric beads consisting of polyethylene or polystyrene.[85–87] Besides the above stated advantages of immobilizing molecular catalysts, using a tunable and electronically relevant support, such as graphene nanoribbons, could further improve the catalytic performance and provide increased stability and selectivity.

There are only a few selected reports of graphitic supports in the literature to enhance performance of electrochemical and photochemical catalysts. In 2016, the Surendranath group showed graphite conjugated rhenium catalysts for the electrochemical reduction of CO_2 to CO with increased efficiency and turnover frequencies compared to the molecular analogue.[88] This system, however, did not use a molecularly defined support, nor did it have precise control of the resulting hybrid material. In 2017, the Li group demonstrated the same rhenium catalyst with increased efficiency for the electrochemical reduction of CO_2 to CO when supported with a nanographene ligand.[89] They showed that the nanographene ligand was an integral part of the catalyst and found that electron delocalization over the nanographene ligand and the metal ion significantly decrease the electrical potential required for the CO_2 reduction. They also hypothesized that using larger nanographene ligands would further decrease the reduction over potentials needed for the CO_2 reduction due to size dependent electrochemical properties of nanographenes.[89] We envision that using graphene nanoribbons as solid support ligands for such systems would bridge the gap between these two examples by providing a graphitic solid support that is atomically precise and laterally extended with tunable electronic properties.

A graphene nanoribbon with quinone or 1,2-dione functionalities along the edges is not only interesting on its own due to potential redox activity, but it could also be used as a handle for late stage edge-functionalization. The quinone handles can be further transformed by numerous different pathways, including condensation chemistry. Condensation with 1,10-phenanthroline-5,6-diamine gives rise to a phenanthroline- GNR, which has bidentate ligand sites conjugated onto the edge of the GNR and can coordinate various metals.

3.2 Quinone-CGNR (q-CGNR)

3.2.1 Synthesis of q-CGNR

Two different synthetic approaches could be followed to access the quinone functionalized GNR precursor **26** (Scheme 3.1). In route A, the key step is the *Diels-Alder* with cyclopentadienone **27** and the quinone functionalized alkyne **28**. Alternatively, in route B the key transformation is a final oxidation of **29**, which can be accessed from a *Diels-Alder* with cyclopentadienone **27** and 4-ethynylphenanthrene **30**.

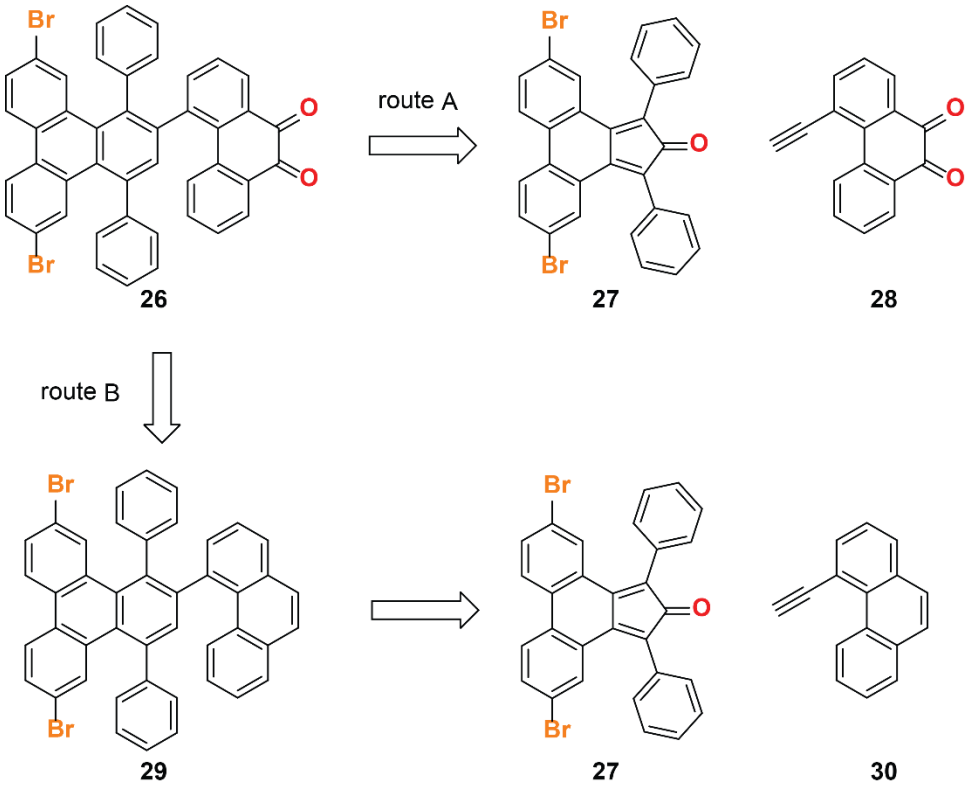

Scheme 3.1 Retrosynthesis of quinone GNR monomer **23**.

The first synthetic route followed (route A) is depicted in Scheme 3.2 and begins with a *Suzuki* coupling of 2-bromobenzaldehyde with (2-methoxyphenyl)boronic acid to give aldehyde functionalized biphenyl **33** in 86% yield. Treatment of biphenyl **33** with TMS diazomethane and LDA converts the aldehyde to a terminal alkyne to give **34** in 94% yield. Next a $PtCl_2$ mediated cyclization affords 4-methoxyphenanthrene **35** in 68% yield. Subjecting **35** to an oxidation with $RuCl_3$ and $NaIO_4$ yielded a complex mixture of products. Even after subjecting the crude material to a silica gel column, the fractions with desired product eluted with several other byproducts. The desired quinone **36**, however, could be isolated by crystallization from hot toluene after a silica get column in 17% yield.

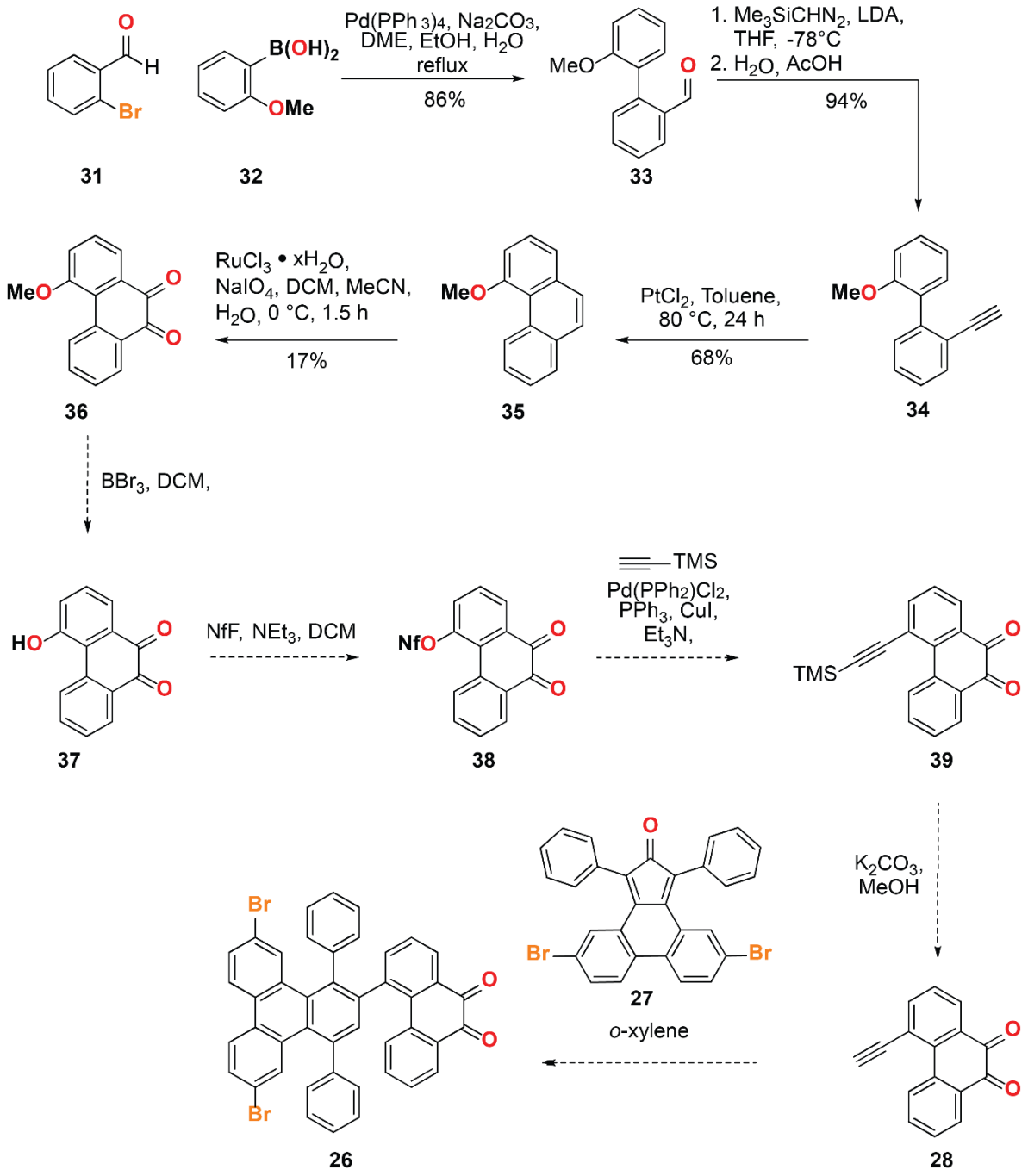

Scheme 3.2 Initial synthetic route towards quinone GNR monomer **26**.

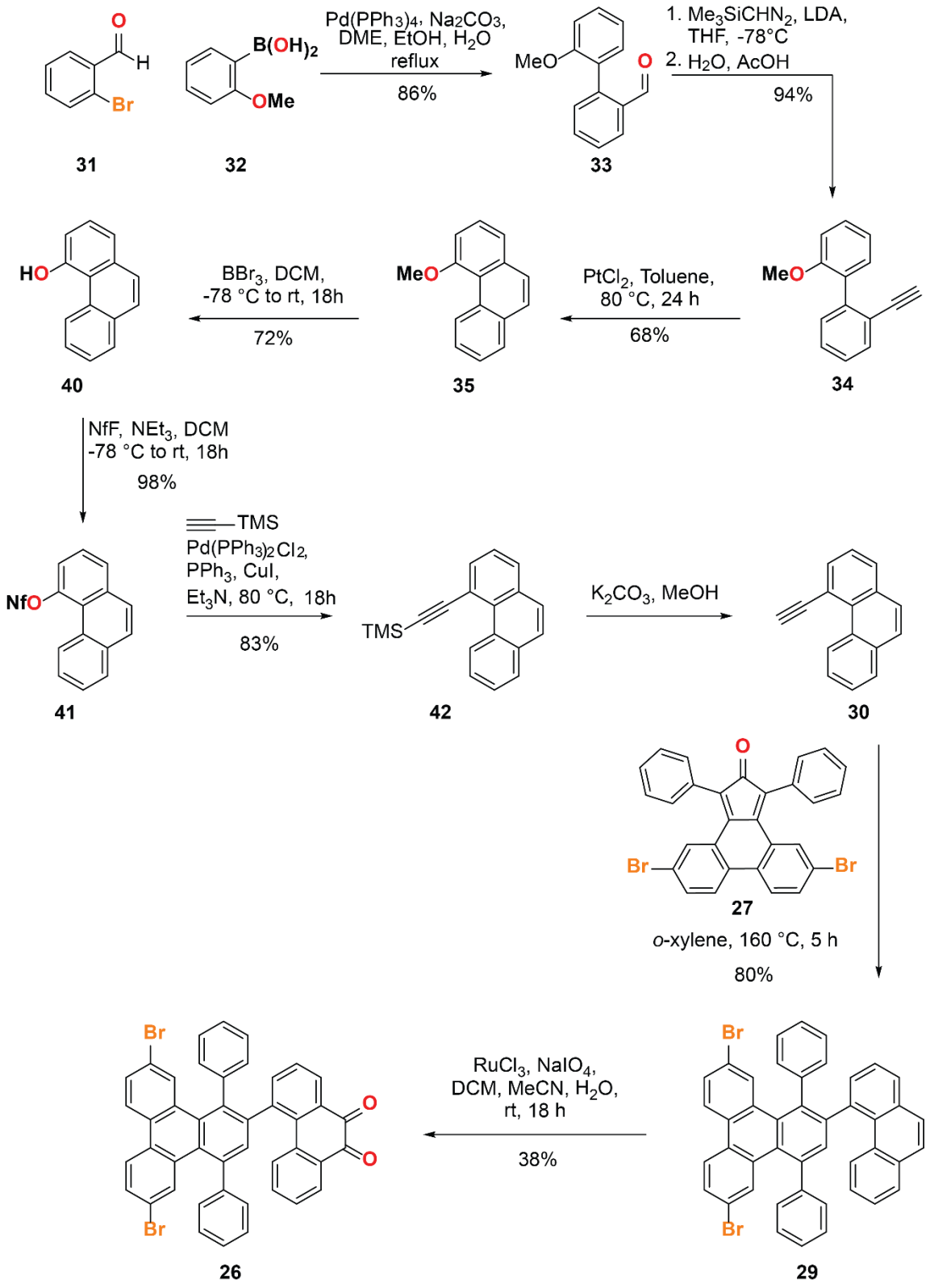

Scheme 3.3 Synthesis of quinone GNR monomer **26**.

Due to this low yielding oxidation, we decided to pursue route B outlined in Scheme 3.1, where the last step would be the oxidation (Scheme 3.3). Subjecting 4-methoxyphenanthrene **35** to a deprotection with BBr_3 gave 4-hydroxyphenanthrene **40** in 72% yield. Treatment of **40** with trimethylamine and perfluorobutanesulfonyl fluoride gave nonaflate functionalized phenanthrene **41** in 98% yield. A *Sonogashira* coupling with TMS acetylene and subsequent deprotection yielded 4-ethynylphenanthrene **30**. A *Diels-Alder* of **30** and cyclopentadienone **27** afforded the un-oxidized monomer **29** in 80% yield. A final oxidation with $RuCl_3$ and $NaIO_4$ yielded the desired monomer **26** in 38% yield after a silica gel column with 10-20% impurities which could be removed by recrystallization from layered MeOH and CH_2Cl_2. At this stage **26** could be sublimed onto gold surface for the surface assisted growth of quinone functionalized GNRs since the chevron monomer is both solution and surface growth compatible.

Copper mediated *Yamamoto* polymerization of **26** proved to be unsuccessful and no polymer was isolated and instead we only observed dimers and trimers by MALDI. We hypothesize that the quinone functionality is acting as an oxidant, causing the catalytic species to become oxidized and no longer active in the coupling of aryl-bromine bonds. As a result, we decided to protect the quinone group. Instead of directly protecting **26** with ethylene glycol, which would have resulted in a difficult purification, we decided to protect the quinone wing. We designed an alternative, more scalable synthesis, which is depicted in Scheme 3.4

Commercial 2,2′-dibromobiphenyl **43** was lithiated with nBuLi in THF at −78 °C. Subsequent quenching with DMF yielded aldehyde **44** in 97% yield. Conversion of the aldehyde to alkyne **45** was performed with an *in situ* formed diazomethane species from TMS diazomethane and LDA in THF. Next, cyclization with $PtCl_2$ afforded 4-bromophenanthrene **46** in 54% yield. An oxidation with slow addition of CrO_3 in AcOH gave quinone **47** in 44% yield. Protection of **47** with ethylene glycol and catalytic *p*-toluenesulfonic acid afforded the protected quinone **48** in 92% yield. A *Sonogashira* coupling with TMS acetylene and subsequent deprotection yielded terminal alkyne **50**. A *Diels-Alder* of **50** with cyclopentadienone **27** gave the desired protected monomer **51** in 76% yield.

The solution synthesis of **q-CGNR** from precursor **51** is depicted in Scheme 3.5. Copper mediated *Yamamoto* polymerization of **48** yielded protected quinone polymer, **Poly-12**. The ketal protecting groups were then removed with $HClO_4$ to give the quinone polymer, **Poly-13**. Before oxidizing the polymer directly, we performed test reactions on monomer **26** to find the best conditions for the Scholl oxidation. However, oxidation with $FeCl_3$ did not yield the fully cyclized monomer based on MALDI mass spectrometry, but using harsher oxidation conditions with DDQ and TfOH in CH_2Cl_2 afforded the desired fully cyclized monomer. Applying these *Scholl* oxidation conditions to **Poly-13** then yielded the quinone GNR.

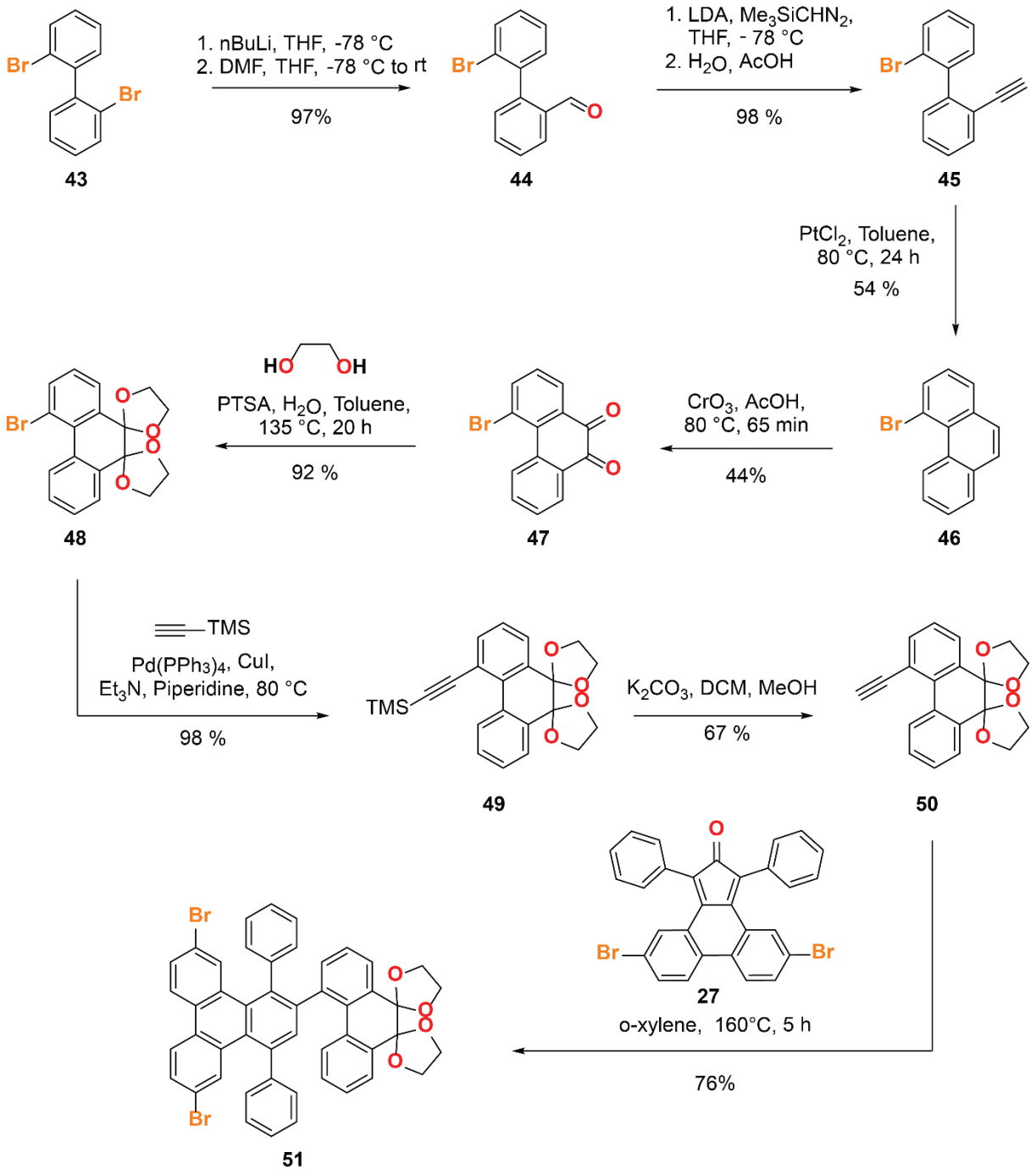

Scheme 3.4 Synthesis of protected quinone monomer **51**.

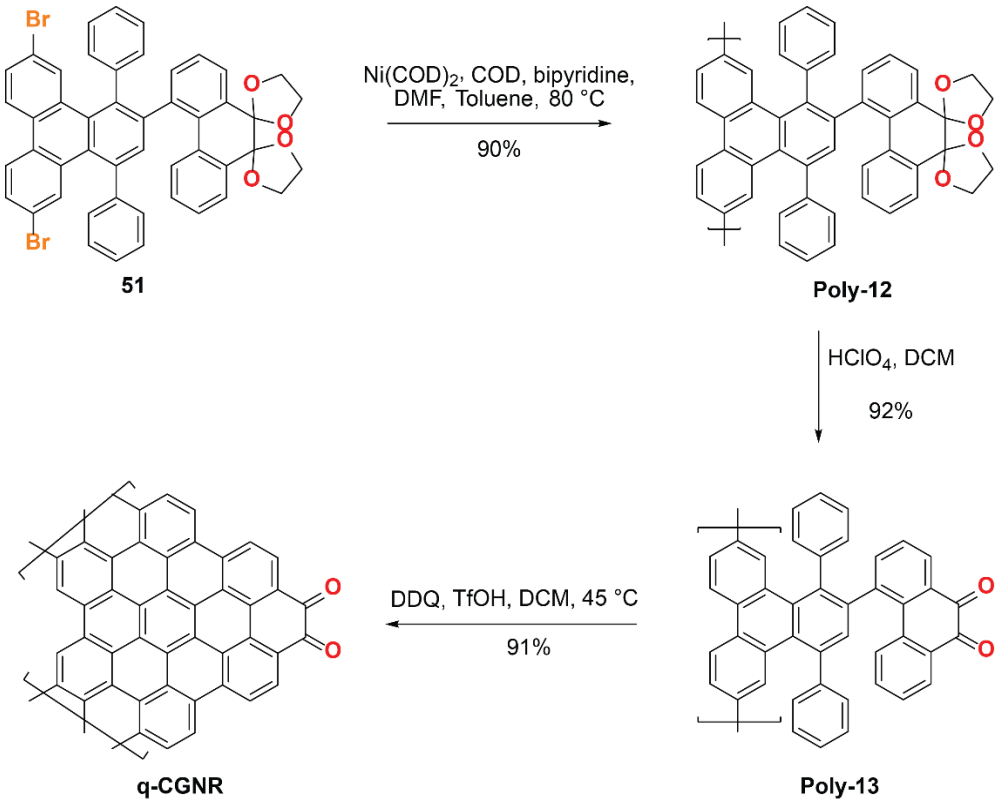

Scheme 3.5 Solution synthesis of **q-CGNR**.

3.2.2 Structural Analysis of q-CGNR

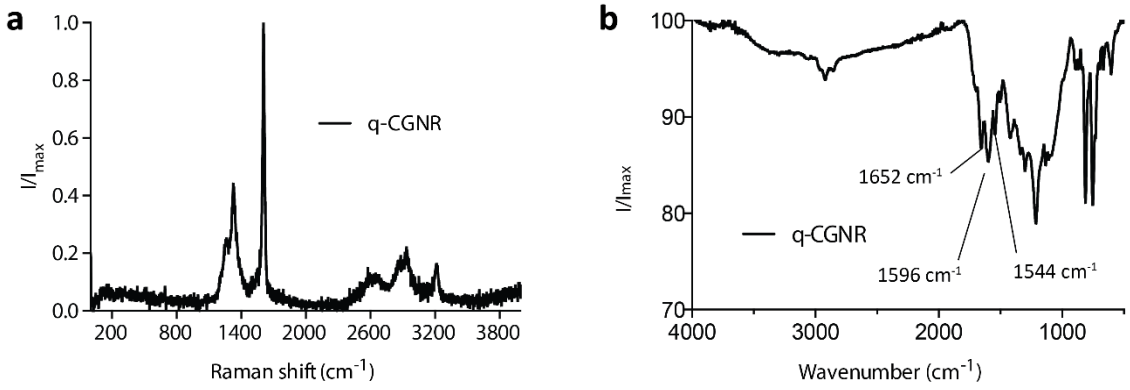

Figure 3.1 Raman spectrum (a) IR spectrum (b) of **q-CGNR**.

Raman spectroscopy of **q-CGNR** shows the characteristic signatures for D and G peaks that are consistent with the formation of extended chevron GNRs (Figure 3.1a).[9] In order to probe the edge functionalities, we used IR spectroscopy. Carbonyl groups have very distinctive IR frequencies and thus we were able to confirm the presence of the 1,2-dione groups via IR

spectroscopy.[90] The three peaks at 1652, 1596 and 1544 cm^{-1} indicate the presence of carbonyls along the edges of the GNRs (Figure 3.1b)

3.3 Phenanthroline-GNR (Phen-CGNR)

3.3.1 Synthesis of Phen-CGNR

Late stage condensation of the **q-CGNR** with diamine **52** in 1:1 degassed EtOH/chloroform at 70 °C afforded the phenanthroline GNR (**Phen-CGNR**) (Scheme 3.6). In order to achieve high conversion, the reaction was run for 3 days and was sonicated every day for 1-2 hours to help keep the GNRs dispersed. Unfortunately, these reaction conditions proved to be irreproducible and the successful transformation of **q-CGNR** to **Phen-CGNR** could not be achieved. Changing the reaction conditions to use dry pyridine as a solvent and a reaction temperature of 120 °C, however, provided a more reliable and reproducible method for this transformation.

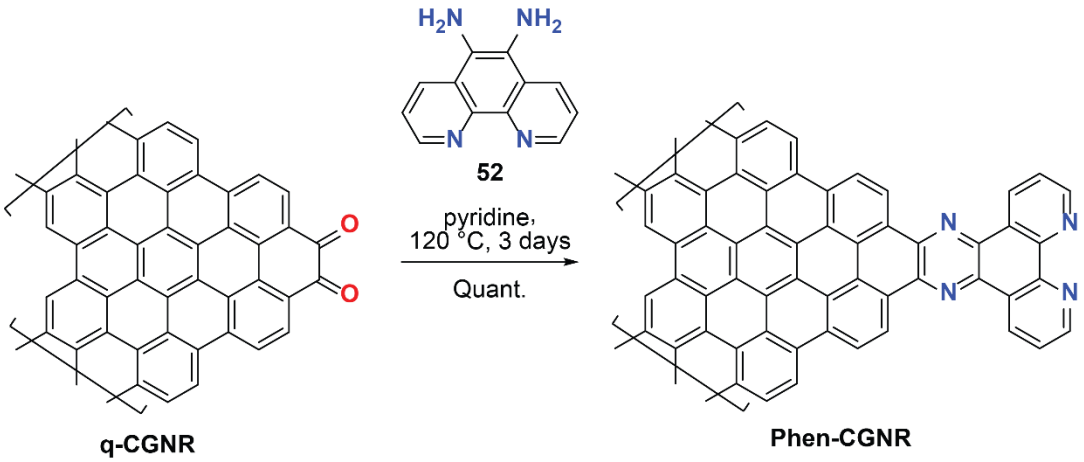

Scheme 3.6 Late stage synthesis of **Phen-CGNR**.

3.3.2 Structural Analysis of Phen-CGNR

The Raman spectrum of **Phen-CGNR** shows no significant change in the D and G peak position and ratio, consistent with condensation of the diamine with the 1,2-dione edge functionalization of the **q-CGNR** to yield the **Phen-CGNR** with an intact backbone (Figure 3.2a). After the condensation of diamine **52**, a comparison of the infrared spectra of **q-CGNR** and **Phen-CGNR** (Figure 3.2b) reveals the attenuation or complete loss of the peaks at 1652, 1596 and 1544 cm^{-1}, associated with presence of carbonyls along the edges of the GNRs, and the appearance of new peaks at 1385, 1372, 1129, and 1088 cm^{-1}. In order to further confirm that these new peaks arose from the phenanthroline moieties along the GNR backbone, we synthesized dibenzo[*a*,*c*]dipyrido[3,2-*h*:2',3'-j]phenazine (**53**) as a model system (Figure 3.8b).

A comparison of the infrared spectra the model compound with **Phen-CGNR** is shown in Figure 3.3a. Reproducible IR stretches are observed in both spectra. For instance, the 1385 and 1372 cm^{-1} stretches in the **Ir-CGNR** correspond to the 1392 and 1370 cm^{-1} stretches present in the model system. Similarly, the 1129 and 1088 cm^{-1} stretches in the infrared spectrum of the **Ir-CGNR** correspond to the 1131 and 1091 cm^{-1} stretches present in the model system.

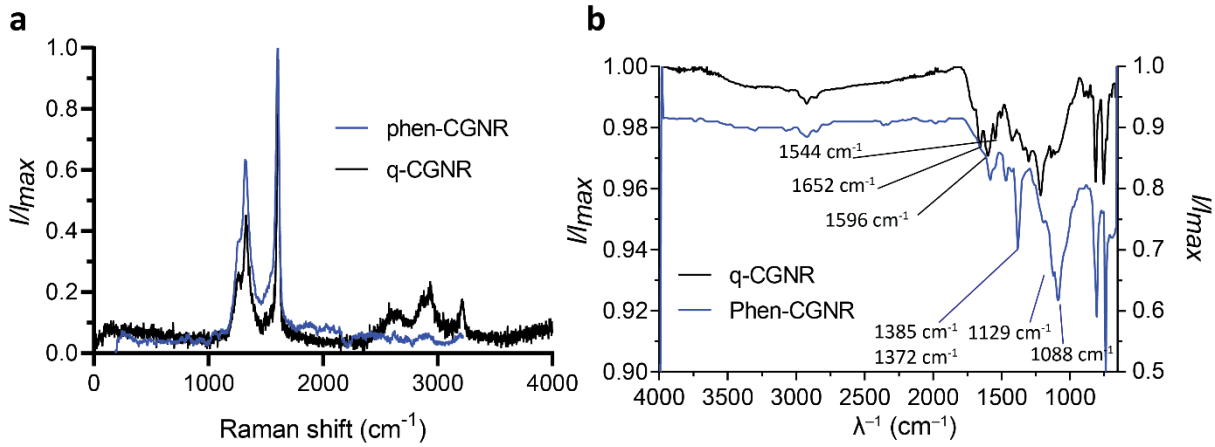

Figure 3.2 Comparison of Raman (a) and IR spectra (b) of **q-CGNR** and **phen-CGNR**.

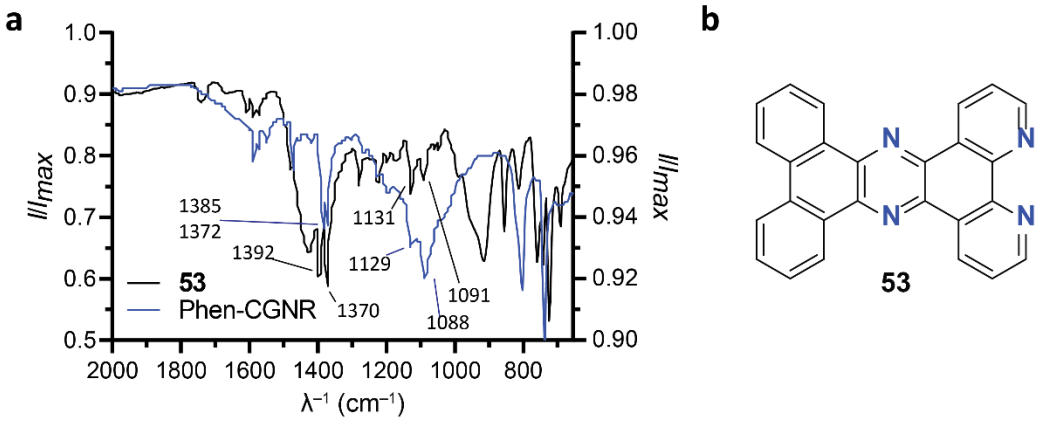

Figure 3.3 (a) IR spectra of model compound **53** and **Phen-CGNR**. (b) model compound **53**.

X-ray photoelectron spectroscopy (XPS) also confirms the successful transformation of the **q-CGNR** to the **Phen-CGNR (**Figure 3.4**)**. By high resolution XPS, we determined the atomic percent carbon to be 84.88 %, atomic percent nitrogen to be 4.86 % and atomic percent oxygen to be 10.25 %. This indicates that some of the 1,2-dione functionality did not react in the condensation, since the expected nitrogen percentage is 7.52%. The high oxygen content in the sample could be due to adsorbed oxygen containing species. Additionally, XPS revealed a small percentage (0.39%) of chlorine present in the sample, mostly likely due to impurity present in the sample or slight chlorination of the GNR edge during oxidation. XPS also detected a silicon signal from contamination of the SiO_2 substrate.

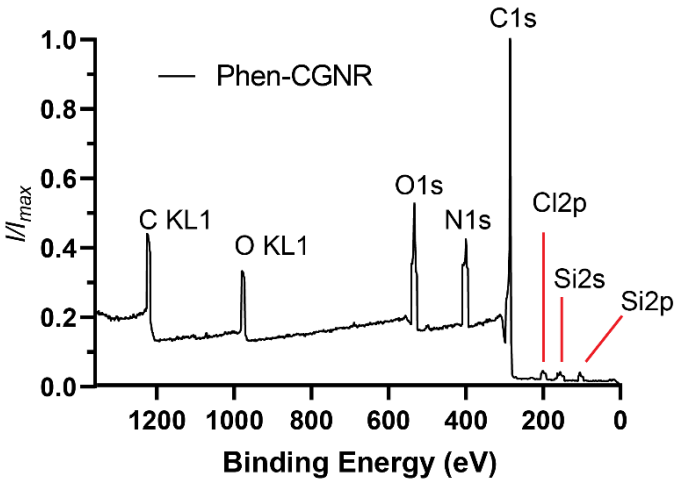

Figure 3.4 XPS spectrum of **Phen-CGNR**.

3.4 Re-CGNR

Extending upon the work by the Surendranath group on graphite conjugated rhenium catalysts and the work by the Li group on a well-defined nanographene–rhenium complex for CO_2 reduction, we developed a GNR conjugated rhenium catalyst, **Re-CGNR**. This system filled a gap between the bulk conjugated catalyst system developed by Surendranath *et al.* and the molecular system developed by Li *et al*.

3.4.1 Synthesis of Re-CGNR

The **Re-CGNR** was synthesized by treating **Phen-GNR** with $Re(CO)_5Cl$ in refluxing degassed toluene for 3 days (Scheme 3.7). In order to keep the GNRs well dispersed, the reaction mixture was sonicated every day for at least one hour. The resulting black powder was washed with hot toluene, hot DMSO, EtOH, acetone, CH_2Cl_2, ethyl acetate, and hexane.

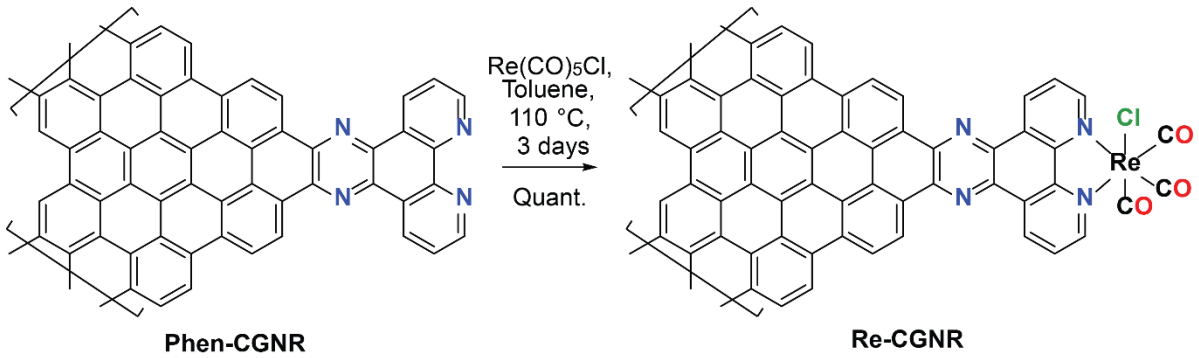

Scheme 3.7 Synthesis of **Re-CGNR**.

3.4.2 Structural Analysis of Re-CGNR

As expected, the Raman spectrum of **Re-CGNR** showed no significant change in the D and G peak position and ratio, consistent with the backbone of the GNR being intact after metalation (Figure 3.5). Infrared spectroscopy confirmed the successful metalation of the **Phen-CGNR** with rhenium. Comparing the infrared spectra of the **Phen-CGNR** and **Re-CGNR**, the appearance of new IR stretches at 2015, 1892 and 1752cm^{-1} are consistent with the three CO ligands (2009, 1887, and 1764 cm^{-1}) in the metal complex, **54** (Figure 3.6). These samples are still awaiting testing for the electrochemical reduction of CO_2 to CO.

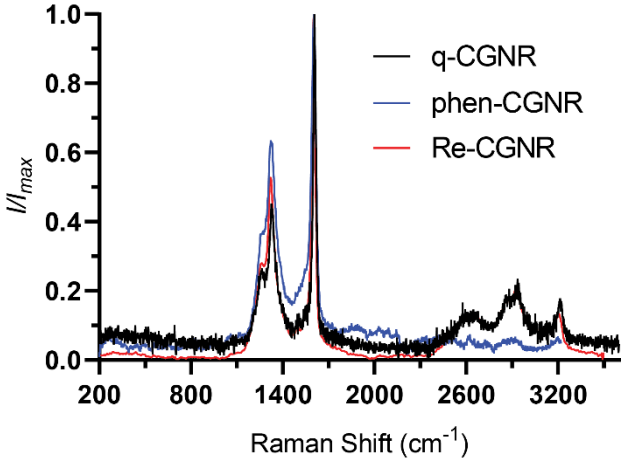

Figure 3.5 Comparison of Raman spectra for **q-CGNR**, **phen-CGNR and Re-CGNR**.

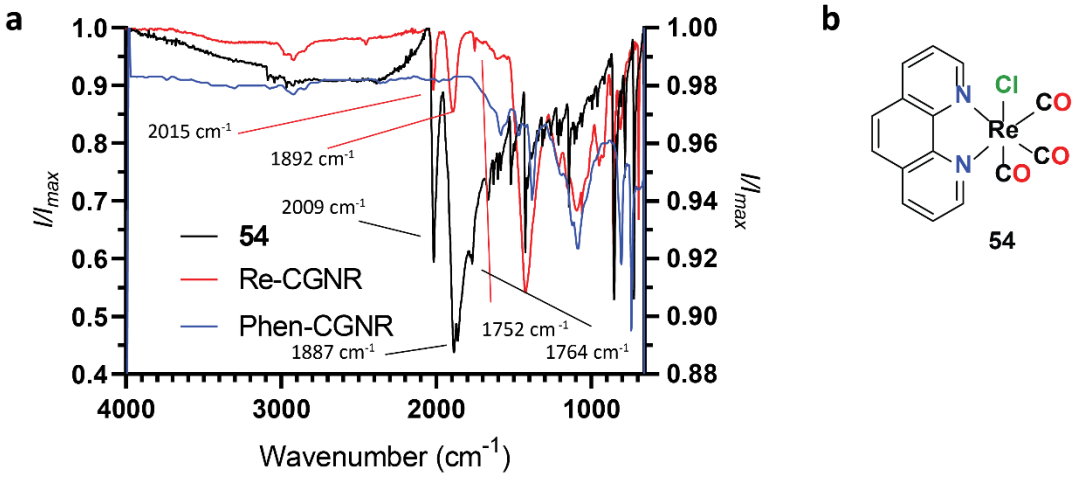

Figure 3.6 (a) Comparison of infrared spectra of **54**, **Re-CGNR**, and **Phen-CGNR**. (b) molecular analogue **54**.

3. 5 Ir-GNR

Hydrogen has been heralded as a zero-emission, clean energy source.[91] However, adapting hydrogen as the main source of fuel in an economical and efficient manner in vehicles has many challenges yet to overcome. Technologies still need to be developed in hydrogen infrastructure and hydrogen storage to allow for fast H_2 storage capacity but also efficient thermodynamics and kinetics, i.e. fast hydriding and dehydriding, at reasonable operating conditions.[92,93] Many hydrogen storage systems, such as MgH_2, require high temperatures and pressures to chemically store and release hydrogen and have sluggish kinetics.[94]

In order to address these issues, we hypothesized that introducing molecular hydrogen activation catalysts into the system would reduce the barrier for hydriding and dehydriding kinetics, enabling lower operating temperatures and pressures. Since this catalysis occurs at the solid – gas interface, we designed a system where molecular catalysts were dispersed in a GNR matrix, thus allowing the separation of reaction centers and more open catalytic sites. Our only requirements for catalyst choice was to use a catalyst with a bidentate nitrogen ligand, such as bipyridine or phenanthroline, which could be replaced by our **Phen-GNR**. We identified [phenIrCp*OH_2]$(OTf)_2$, **55**, as a promising candidate since it catalyzes the hydrogenation of carboxylic acids (Figure 3.7).[95]

3.5.1 Synthesis of Ir-CGNR

The reported synthesis of the **55** stirred [Cp*$IrCl_2$]Cl_2 with phenanthroline in methanol to yield **58** and subsequent treatment with AgOTf in water gave the desired catalyst (Scheme 3.8).[95] Unfortunately, this last step formed AgCl as a byproduct. When working with the water soluble molecular catalyst, the AgCl was removed by filtration. However, this purification method could not be used for the insoluble **Ir-CGNR**. As a result, we had to redesign the catalyst synthesis to enable purification of the **Ir-CGNR** without the need to separate the AgCl from the GNR (Scheme 3.9). Our redesigned synthetic route treated [Cp*$IrCl_2$]Cl_2 with AgOTf in water to give the tris aqua complex **59** and AgCl as a byproduct. Subsequent ligand exchange of **59** with phenanthroline yielded the desired catalyst **55**. In order to access the **Ir-CGNR**, we treated the tris aqua complex **59** with the **Phen-CGNR** (Scheme 3.10). The resulting black powder was filtered and washed with water, ether, and hexanes.

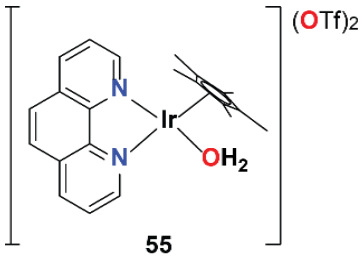

Figure **3.7** Iridium catalyst **55**.

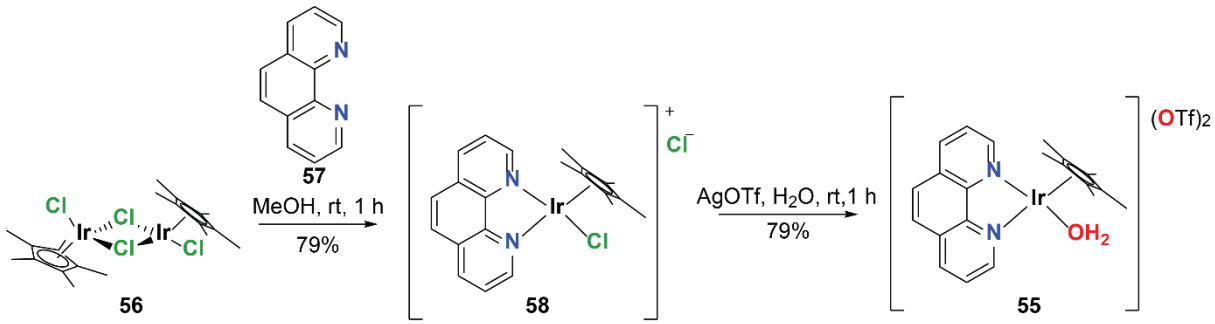

Scheme 3.8 Reported synthesis of **55**.

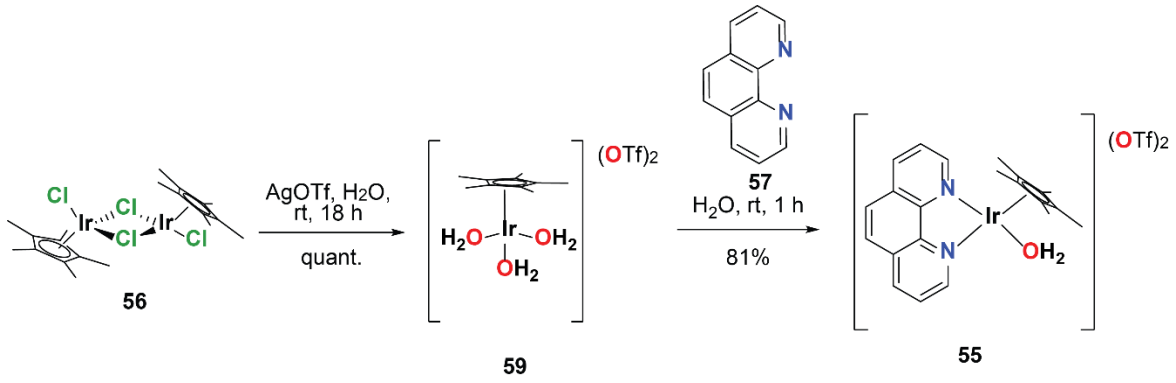

Scheme 3.9 Redesigned synthesis of **55**.

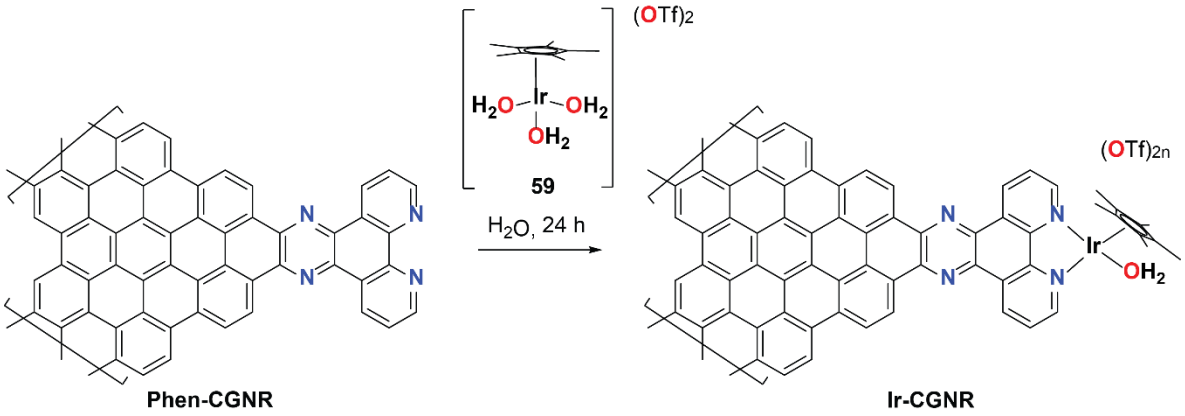

Scheme 3.10 Synthesis of **Ir-GNR.**

3.5.2 Structural Analysis of Ir-CGNR

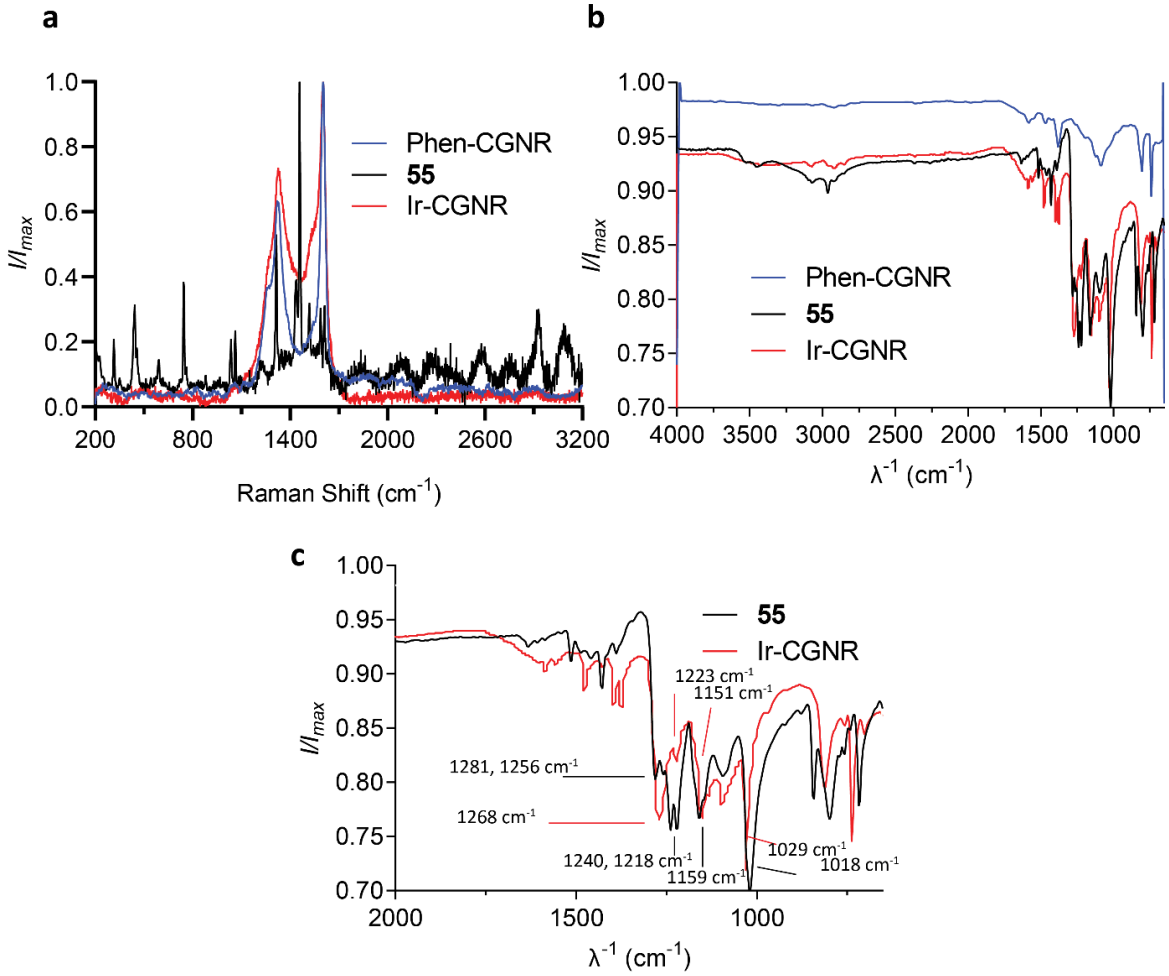

Figure 3.8 Comparison of Raman (a) and IR spectra (b) of **Phen-CGNR**, **55**, and **Ir-CGNR**. (c) Zoomed in IR spectra of **55** and **Ir-CGNR**

The Raman spectrum of the **Ir-CGNR** showed a broad D and G peak (Figure 3.8a). This broadening could be due to contribution of the iridium catalyst to the Raman spectrum since the molecular analogue **55** has Raman shifts between 1100 and 1700 cm^{-1} which overlap with the D and G peak of the GNR backbone. A comparison of the infrared spectra of **Phen-CGNR** and **Ir-CGNR** confirms the successful metalation of the GNR with the rise of new stretches at 1268, 1223, 1151, and 1029 cm^{-1}, which correspond to IR frequencies present in the molecular catalyst at 1281, 1256, 1240, 1218, 1159 and 1018 cm^{-1} (Figure 3.8b and c).

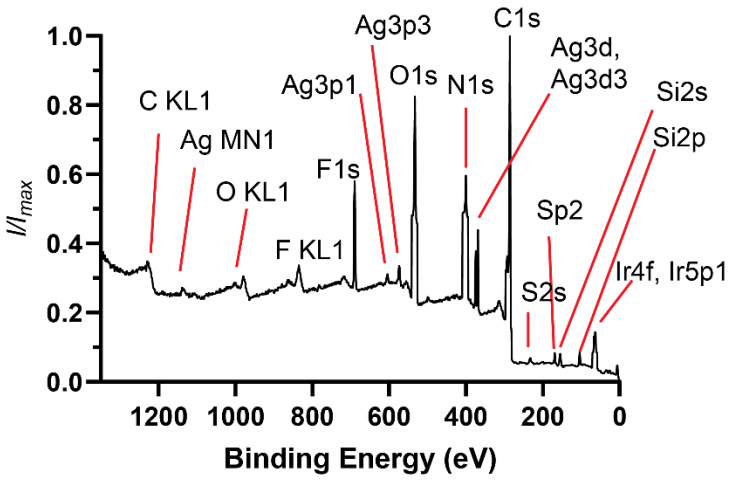

Figure 3.9 XPS spectrum of **Ir-CGNR**.

XPS analysis also confirmed the successful metalation of the **Phen-CGNR** (Figure 3.9). We were unable to quantify the atomic composition due to detection of signal from the underlying substrate (Ag tape on SiO_2), which may also contain carbon and oxygen in the adhesive. However, the peak at 61.66 eV corresponds to the Ir4f transition, confirming the successful metalation of **Phen-CGNR**. XPS also revealed fluorine and sulfur peaks associated with the triflate anion. The silver and silicon peaks are caused by the silver tape used to mount the sample and SiO_2 substrate

3.6 Kinetic Study of H_2/D_2 Exchange

H_2/D_2 exchange experiments were performed to test the catalytic activity of the **Ir-CGNR** compared to the **Phen-CGNR** and **55**. H_2 and D_2 were passed over the samples at a constant pressure and the formation of HD was measured at various time points. A plot of the reaction quotient, Q, versus time reveals that, as expected, the **Phen-CGNR** shows no activity for the exchange of H_2 and D_2 (Figure 3.10). The molecular catalyst **55** at 23, 50 and 80 °C shown in red, orange and pink, respectively, all have K values that range between 0.01 and 0.1. In comparison, the **Ir-CNGR** is highly active with K values over an order of magnitude greater than the molecular catalyst. Furthermore, the **Ir-CGNR** approaches equilibrium faster than the molecular catalyst as seen by the steep slope of the curves within the first 25 minutes. The **Ir-CGNR** scrambling behavior shows a temperature dependence, with the samples reaching equilibrium faster and with greater K values at higher temperatures.

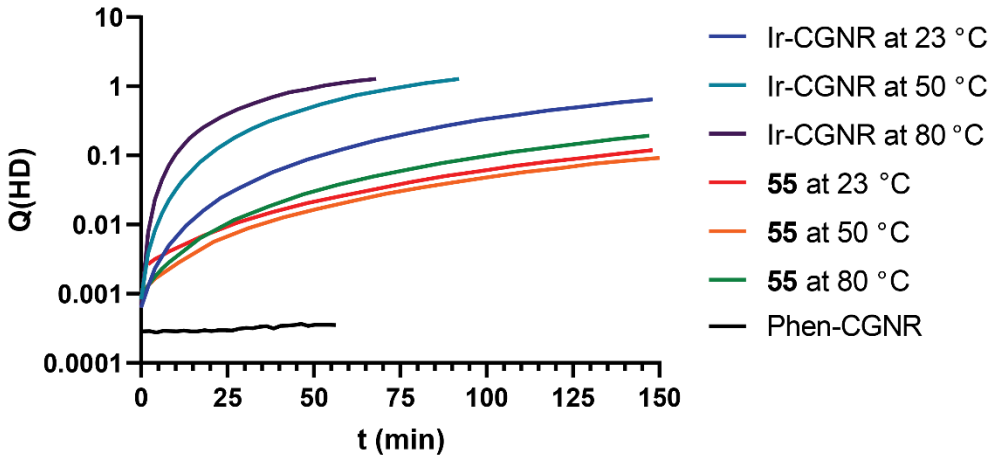

Figure 3.10 Plot of reaction quotient, Q, defined as Q(KD) = $[HD]^2/[H_2][D_2]$ versus time for H_2/D_2 scrambling experiments.

Resubjecting the **Ir-CGNR** to the same scrambling experiments after heating to 80 °C, revealed a loss of activity (Figure 3.11). In contrast, repeating the experiment for the molecular catalyst at 80 °C showed very little change, indicating the molecular catalyst is not deactivated or

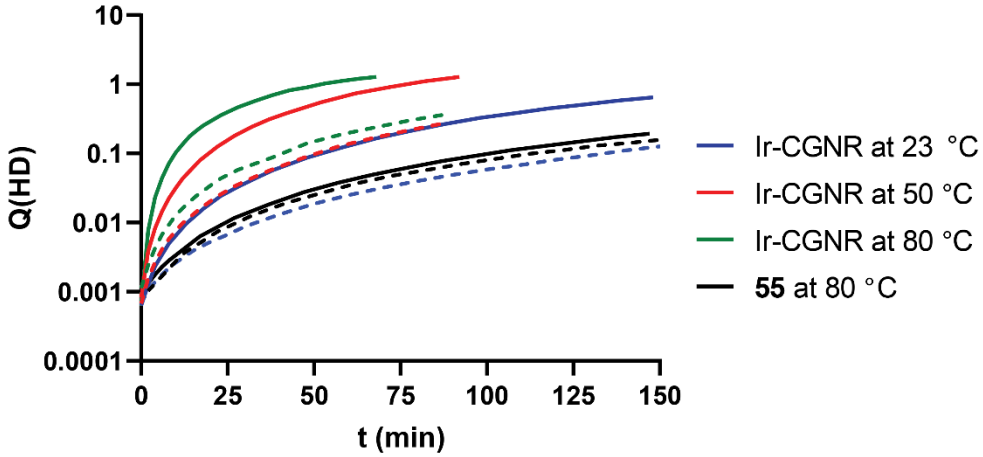

Figure 3.11 Plot of reaction quotient, Q, defined as Q(KD) = $[HD]^2/[H_2][D_2]$ versus time for H_2/D_2 scrambling experiments performed twice. Solid lines are the first set of experiments. Dotted lines are resubjected samples after being exposed to 80 °C during round 1 experiments.

decomposed upon heating. We hypothesize the slower kinetics observed with the **Ir-CGNR** arises from migration of the iridium center to the C-N binding site, the more thermally favorable binding position (Figure 3.12a). However, molecular catalyst **60** with a phenylpyridine ligand, instead of a phenathroline ligand, is inactive for the hydrogenation of carboxylic acids.[95] Thus, migration of the iridium centers on the GNR to this undesired position, could lead to catalyst deactivation, and thus

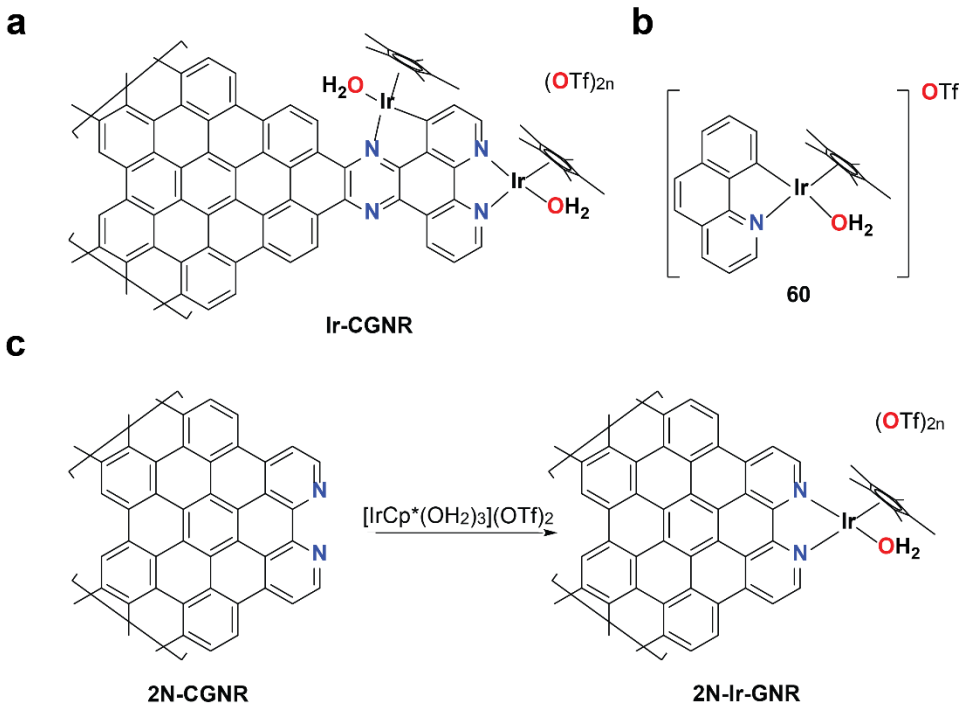

Figure 3.12 (a) Hypothesized undesired migration of iridium center upon heating leading unproductive catalyst binding. (b) phenylpyridine analogue **60** of molecular catalyst which has been reported to not catalyze the hydrogenation of carboxylic acids. (c) **2N-CGNR** with only one possible binding site.

result in lower performance. This could be prevented by redesigning the GNR to only have one possible binding site (Figure 3.12c)

3.7 2N-CGNR

3.7.1 Synthesis of 2N-CGNR

Due to the decrease in catalytic efficiency, we synthesized a novel chevron GNR functionalized with two nitrogen atoms to form a bipyridine moiety along the edge. This GNR would only have one possible binding site for metal centers. It also has the added advantage of the bipyridine functionality being installed at the monomer stage, and thus we have more atomic control of the GNR and only need one late stage functionalization step to access a metallated version of this GNR. In contrast, the **Ir-CGNR** requires two late stage functionalization steps: condensation of the diamine to yield the **Phen-CGNR** and subsequent metalation. Since these two steps do not always proceed with 100% yield and the synthesis of **Phen-CGNR** has proven to be challenging, we do not have complete atomic control of the resulting structure

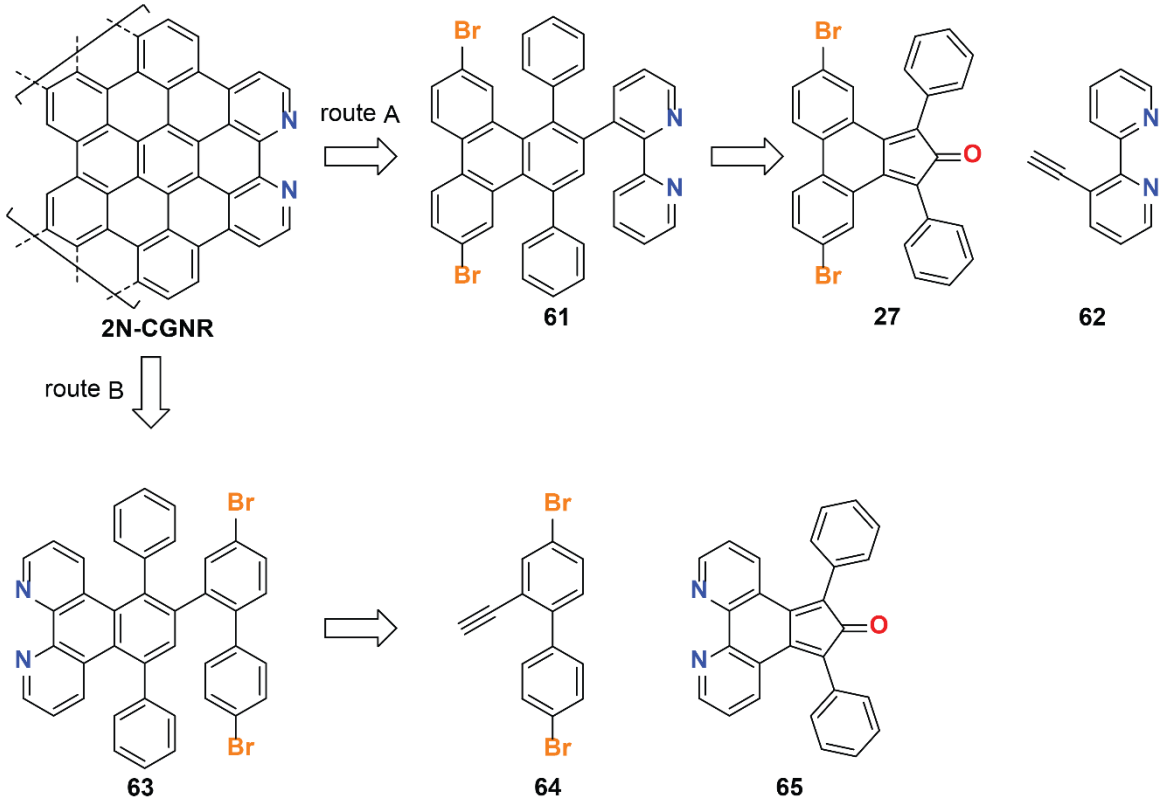

Scheme 3.11 Retrosynthesis of **2N-CGNR**.

The key step in the synthesis of the **2N-CGNR** precursor is the *Diels-Alder* reaction. Two different *Diels-Alder* coupling partners can be used at this stage (Scheme 3.11). In the first route, a *Diels-Alder* with an alkyne functionalized bipyridine **62** and cyclopentadienone **27** gives monomer **61**, which is structurally similar to most chevron GNR monomers (Route A). We could, however, use a nitrogen doped cyclopentadienone (**65**) and 4,4'-dibromo-2-ethynyl-1,1'-biphenyl (**64**) to access monomer **63** which would now polymerize through the biphenyl wing.

Starting with route A, the bipyridine wing could be synthesized in 4 steps (Scheme 3.12). 3-Bromo-2,2'-bipyridine **68** was synthesized according to a procedure from Zucker and coworkers in two steps.[96] First a palladium catalyzed direct halogenation of bipyridine N-oxide gave brominated bipyridine N-oxide **67** in 75% yield. Removal of the N-oxide with PBr_3 in chloroform at 80 °C afforded 3-bromo-2,2'-bipyridine **68** in 87% yield. *Sonogashira* coupling with TMS acetylene resulted in a complex mixture of products and no desired product could be isolated. Since bipyridines are known to complex palladium, we decided to pursue coupling with stoichiometric amounts of the copper acetylide, synthesized from TIPS acetylene. The best results were obtained with DMSO at 100 °C for only 1 hour. Longer reactions times caused a significant decrease in yield. Deprotection of **69** with tetrabutylammonium fluoride (TBAF) afforded several byproducts and the desired terminal alkyne could not be isolated. While other deprotection conditions could be tried, we decided to pursue the alternative route that did not require synthesizing an alkyne functionalized bipyridine.

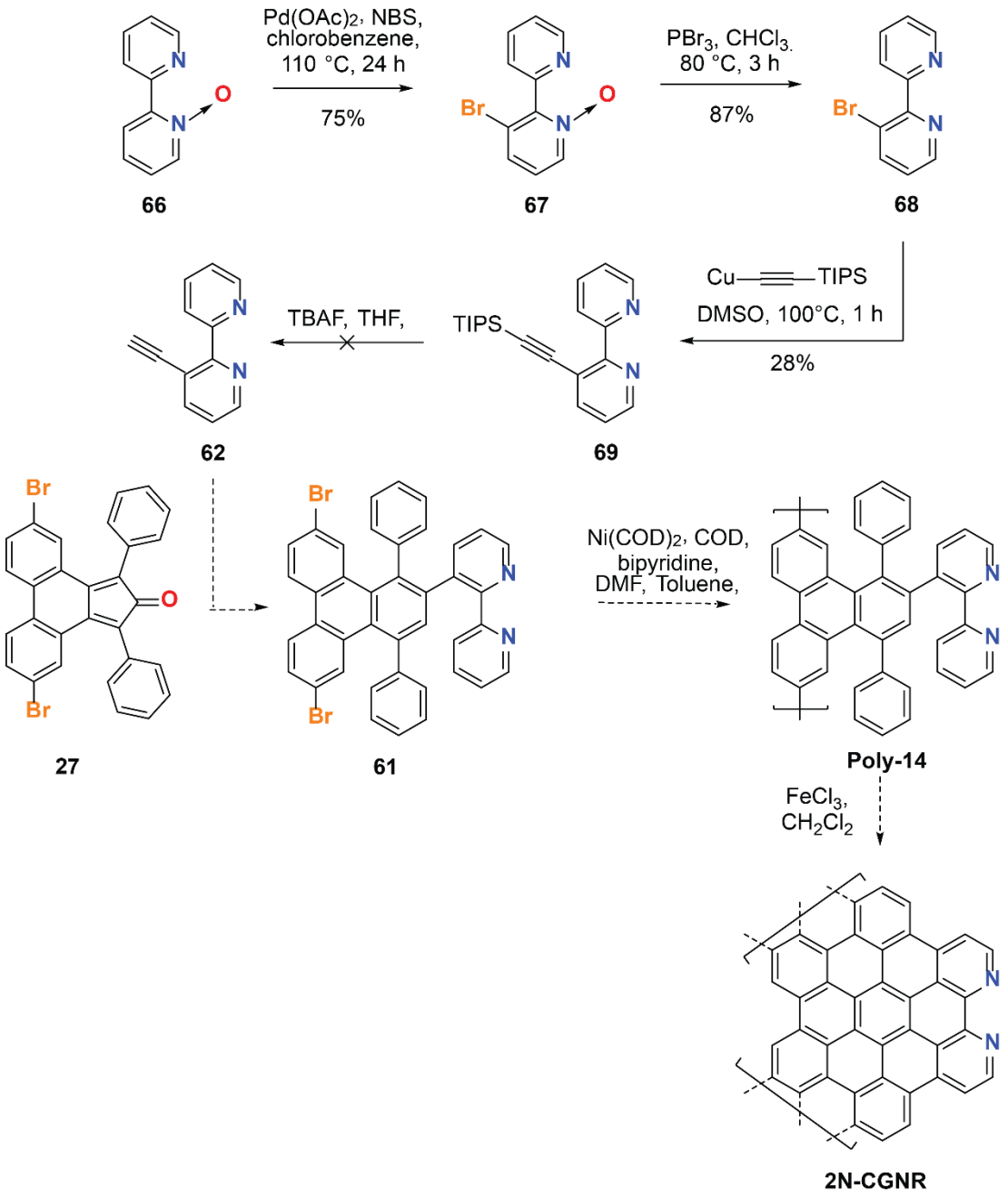

Scheme 3.12 Synthetic route towards **2N-CGNR** monomer via route A.

Route B required synthesizing terminal alkyne **64** and cyclopentadienone **65** (Scheme 3.13). Terminal alkyne **64** was accessed in two steps starting with a *Suzuki* coupling of commercially available 5-bromo-2-iodobenzaldehyde and (4-bromophenyl)boronic acid to give biphenyl **72** in 51% yield. It is important to note that since boronic acid **71** can couple with itself, and excess **71** can couple with the desired product, we only used 1.2 equivalents of the boronic acid. We still obtained a variety of different undesired products which could be removed by silica gel column chromatography with a slow gradient of CH_2Cl_2 in hexanes. Conversion of the

aldehyde to the alkyne **64** was performed with *in situ* formed diazomethane from TMS diazomethane and LDA in THF. Cyclopentadienone **65** was obtained from a *Knoevenagel* condensation of 1,10-phenanthroline-5,6-dione (**73**) and diphenyl acetone **74** with catalytic DBU. The reaction did not work when stoichiometric or excess DBU was used. In order to isolate pure product, the reaction mixture was rapidly cooled to −20 °C, causing blue-green precipitate to form. The solid was filtered and washed with cold ethanol. A *Diels-Alder* of terminal alkyne **65** and cyclopentadienone **65** gave the desired monomer **63** in 43% yield. Monomer **63** was purified by sonication and filtration from hot hexanes, followed by sonication and filtration from hot MeOH.

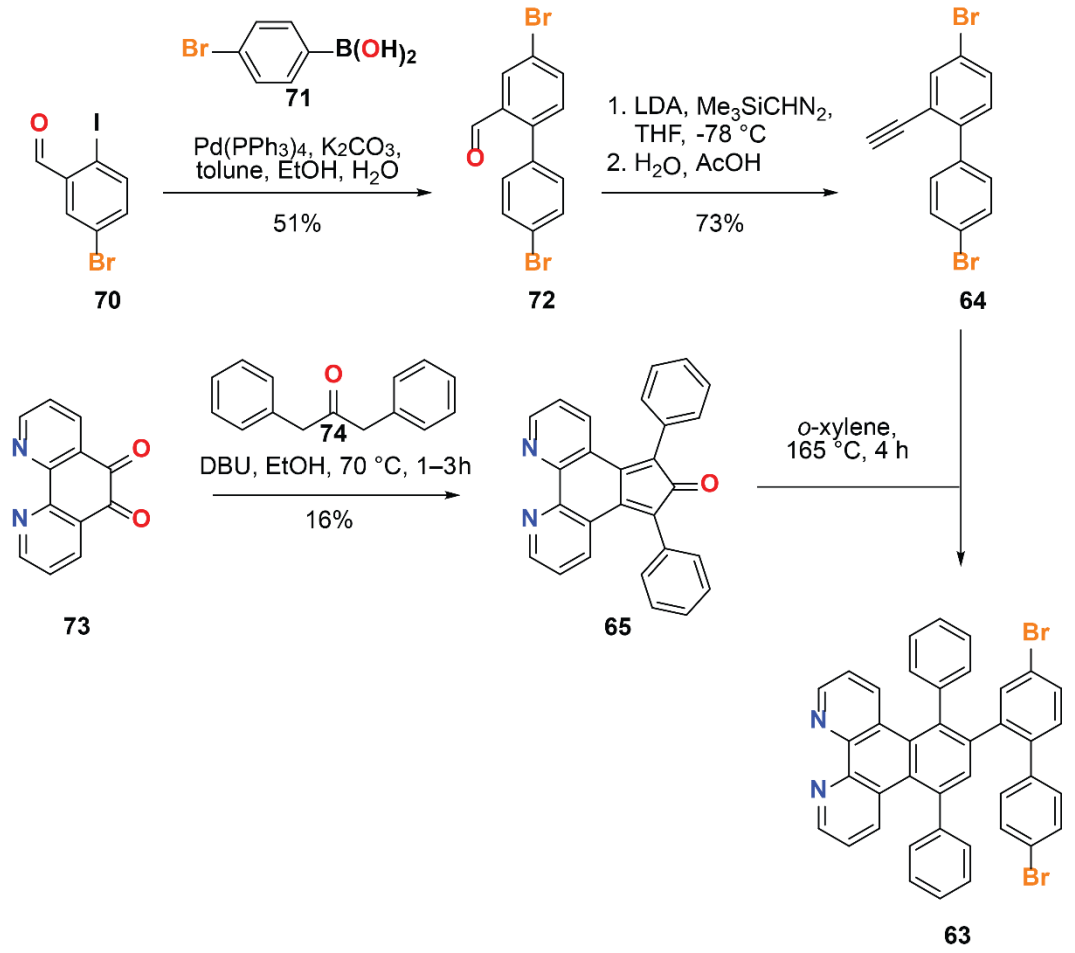

Scheme 3.13 Synthesis of **2N-CGNR** monomer **63** via route B.

Copper mediated *Yamamoto* polymerization of **63** resulted in **poly-15** (Scheme 3.14). Unfortunately, the resulting polymers were very insoluble and thus size exclusion chromatography could not be utilized to determine the average polymer weights or PDI. Matrix Assisted Laser Desorption/Ionization (MALDI) mass spectrometry however revealed long polymers with weights up to 10000 Daltons (Figure 3.13). This is the first example where CGNR precursor polymers we synthesized from the polymerization through the uncyclized biphenyl wing. An $FeCl_3$ mediated *Scholl* oxidation is expected to yield the desired **2N-CGNRs**.

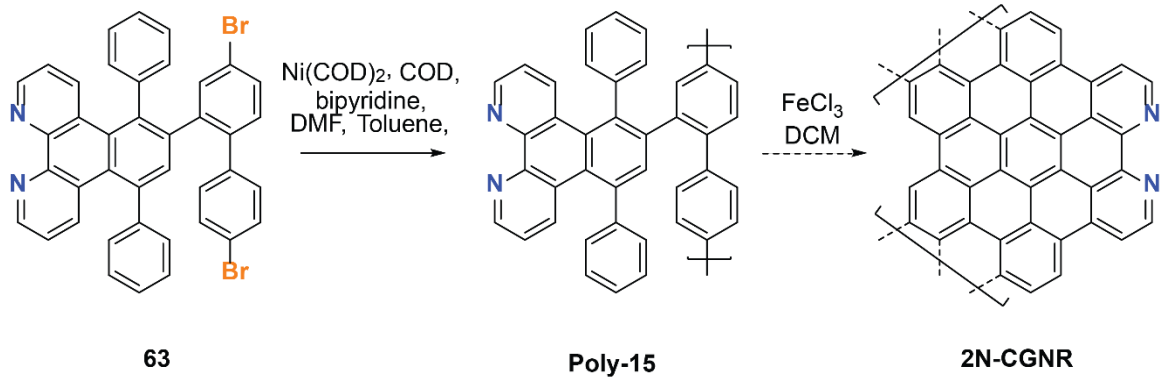

Scheme 3.14 Synthesis of **2N-CGNR**.

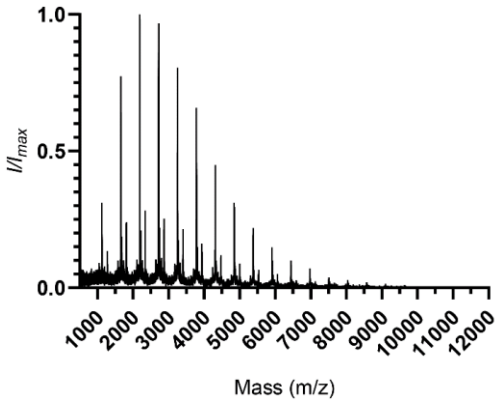

Figure 3.13 MALDI mass spectrometry spectrum of **poly-15**.

3.8 Conclusion and Outlook

Due to the harsh oxidation conditions required to fully cyclize the quinone polymer **poly-12**, we have developed a modified synthetic route with a slightly altered monomer design that could be cyclized with milder conditions such as $FeCl_3$ (Scheme 3.15). Instead of having to cyclize the quinone wing, we designed a monomer where these bonds have already been formed. Our new monomer would now polymerize through an uncyclized biphenyl wing, similar to the synthesis of the **poly-15** via monomer **63**. This new route would start with a *Knoevenagel* condensation of pyrene-4,5-dione with diphenyl acetone to give cyclopentadienone **76**. Subjecting **76** to a *Diels-Alder* with **64** would yield **77**. An oxidation and subsequent protection with ethylene glycol would afford monomer **79**. Compared to the previous route, this synthesis has the added benefit of requiring fewer synthetic steps.

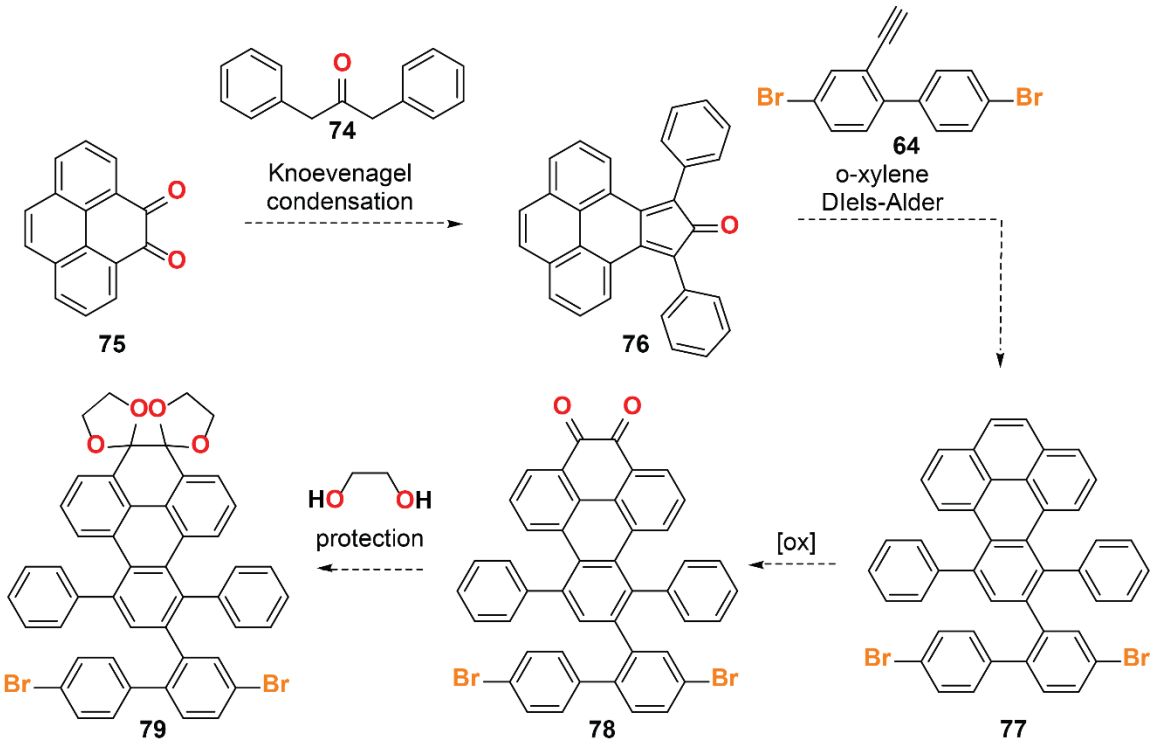

Scheme 3.15 Proposed synthetic route to new **q-GNR** precursor **79**.

In the third chapter of this thesis, late stage functionalization of GNRs through condensation chemistry and metalation was presented. We developed a 1,2-dione edge functionalized GNR, **q-GNR**, and successfully modified it via a late stage condensation with diamine **52**, to access a phenanthroline functionalized GNR, **Phen-GNR**. Successful metalation of the **Phen-CGNR** was achieved through ligand exchange reactions to yield both a **Re-CGNR** and **Ir-CGNR**. Excitingly, we have shown that the **Ir-CGNR** has faster kinetics compared to the molecular catalyst for the gaseous exchange of H_2 and D_2. We did observe slower kinetics after heating the samples, which we hypothesize is due to migration of the iridium metal center. As a result, we have begun synthesizing a **2N-CGNR** with only one possible binding site.

This work is the first example to our knowledge where atomically precise GNRs can be directly conjugated to metal catalyst. It opens up the possibility of extending this research to any catalytic systems that use bidentate nitrogen ligands that are widely used in a variety of catalytic applications, e.g. CO_2 reduction, hydrogen activation, and water splitting.

Chapter 4

Modular Syntheses towards Novel Low Bandgap GNRs

In the fourth chapter of this thesis, a modular synthesis towards low bandgap GNRs is presented. Unlike the previous chapters, this chapter focuses on the synthesis of precursors for surface growth of low bandgap GNR. We report the synthesis of a redesigned, more robust 9-AGNR monomer, its surface growth and its ability to form heterostructures with other GNR precursors. The synthesis of novel, low bandgap 15-AGNR and wide chevron GNR precursors is also reported. The development of a 9-AGNR with pthalimide functional groups with the ability to form hydrogen bonds is also discussed. Surface studies were done in collaboration with Dan Rizzo from the Crommie Group.

4.1 Introduction

Thus far, the previous chapters have focused on solution synthesized graphene nanoribbons. In this chapter, we shift focus to the rational design of monomers for the surface growth of GNRs. As described in chapter 1, controlling the width and edge structure of GNRs allows for the precise control of its electronic properties. To date, one of the most widely studied bottom up synthesized GNR is the N = 7 AGNR. Unfortunately, 7-AGNRs have a large theoretically GW calculated bandgap of 3.7 eV and a measured bandgap of 2.4 eV on Au(111), making it a challenging material for electronic device fabrication.[97,98] Access to atomically defined lower bandgap ribbons is key for their integration into next generation field effect transistors or electronics. Considering the width and edge structure are both crucial factors involved in the bandgap engineering of GNRs, a modular synthesis that allows control of both factors would be greatly desirable. Here we describe the development of a flexible, modular synthesis of low bandgap GNRs from one common intermediate, allowing us to access a variety of different low band GNRs (Figure 4.1).

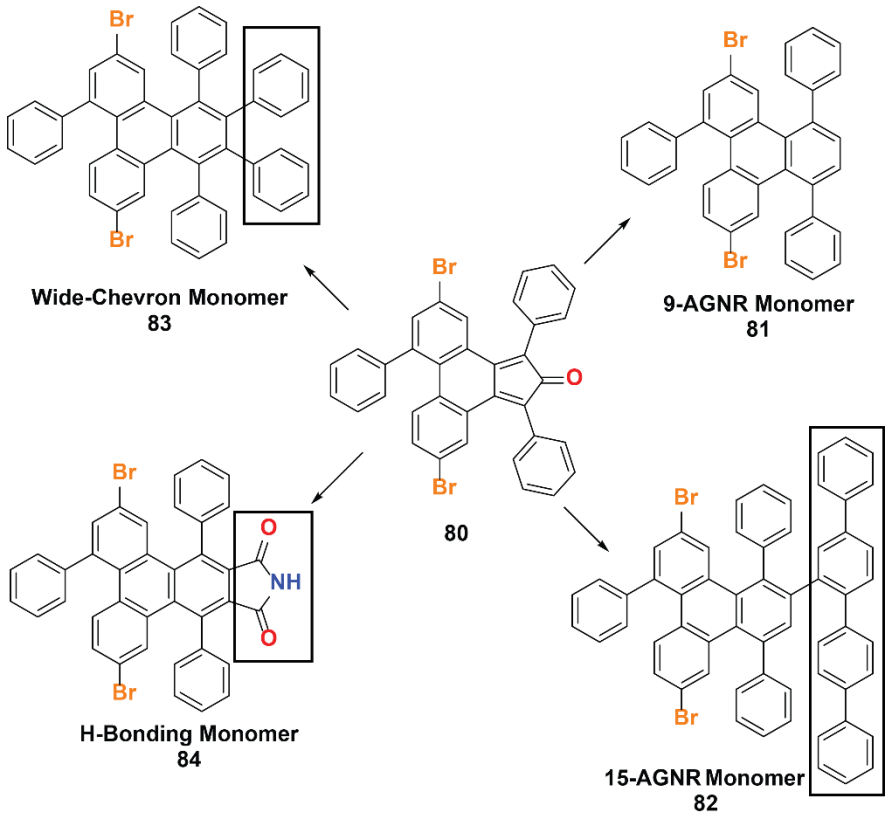

Figure 4.1 Four different new low bandgap GNR precursors from one common intermediate. Differences in monomers highlighted with boxes for clarity.

4.2 N = 9 AGNRs

4.2.1 Introduction to 9-AGNRs

9-AGNRs are known to have a low bandgap, making them ideal candidates for integration into electronic devices. While 9-AGNRs have been synthetized on the surface by Ruffieux in 2017, the 3′,6′-dibromo-1,1′:2′,1″-terphenyl monomer **4** (Figure 4.2) used to grow the ribbons suffers from a high vapor pressure making it difficult to deposit on the surface.[33] Additionally, since monomer **4** is not partially cyclized, the resulting GNRs have significant defect sites, most commonly mouse bites formed from loss of a phenyl ring. In order to address these two issues we redesigned the monomer to be partially fused and similar in sterics to the chevron precursor monomer (Figure 4.2).

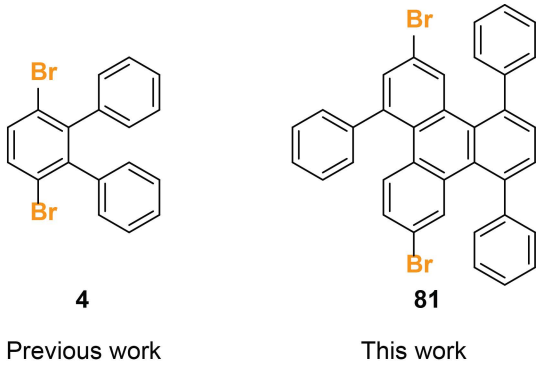

Figure 4.2 3′,6′-dibromo-1,1′:2′,1″-terphenyl, **4**, designed by Ruffieux *et al.* for the synthesis of 9-AGNRs (left). Our redesigned 9-AGNR precursor **81** (right).

Furthermore, creating heterostructures with other GNR molecular precursors can be challenging with the current 9-AGNR monomer **4**. In 2010, Cai *et al.* demonstrated that co-depositing **1**, the monomer precursor to N = 7-AGNRs, and **2**, the precursor to chevron GNRs, did not result in any heterojunctions on the surface and only pure 7-AGNRs and chevron GNRs were observed due to the heteromolecular coupling reaction between the two monomers being sterically hindered (Figure 4.3a,b).[31] However, it has been established that monomers with similar steric interactions do indeed undergo heteromolecular coupling reactions and in 2014, Cai et al. were able to synthesize chevron GNR heterostructures using pristine all carbon and nitrogen doped chevron monomers (Figure 4.3c,d).[8] Additionally, Chen et al. showed that **1** and **3**, the monomer precursor to N = 13 AGNRS, could also undergo heteromolecular coupling to form heterojunctions on the surface since both monomers polymerize via the anthracene units (Figure 4.3e,f).[39] Unfortunately, the current 9-AGNR monomer **4** cannot be used to fabricate GNR heterojunctions via co-deposition of two different monomers, as previously discussed, because no other current GNR monomers have similar steric interactions. However, since our redesigned monomer **81** is sterically similar to the chevron GNR precursors, it has the potential to undergo heteromolecular coupling reactions with other similar monomers to form heterostructures.

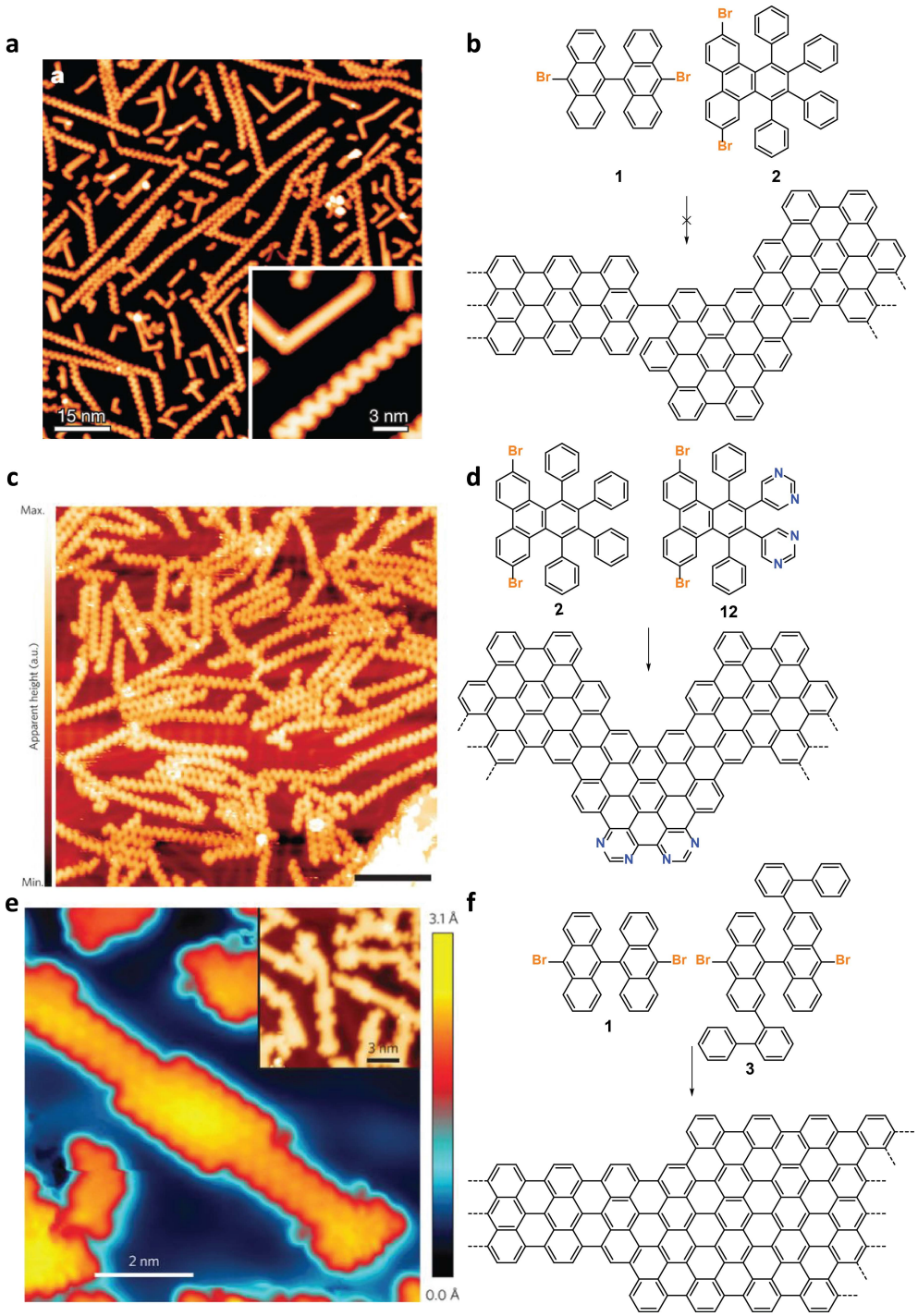

Figure 4.3 (a) STM image of straight N = 7 and chevron-type GNRs sequentially grown on Ag(111). Image reproduced from *Nature* **2010**, *466*, 470–473.[31] (b) Schematic representation of **1** and **2** unable to form heterostructures. (c) STM image of pristine and nitrogen doped chevron GNR heterostructures. Image reproduced from *Nat. Nanotechnol.* 2014, 9, 896–900.[8] (d) Schematic representation of pristine and nitrogen doped chevron GNR heterostructures. (e) High-resolution STM topograph of a 7–13 GNR heterojunction. Image reproduced from *Nat. Nanotechnol.* 2015, 10, 156–160.[39] (f) Schematic representation of 7–13 GNR heterojunction.

4.2.2 Synthesis and Characterization of 9-AGNRs

The initial synthetic route (Scheme 4.1) pursued starts with a *Suzuki* coupling of 4-bromophenanthrene **46** with phenyl boronic acid to give 4-phenylphenanthrene **85** in 76% yield. Oxidation with CrO_3 afforded quinone **86** in 46% yield. Subjecting **86** to a bromination did not yield the desired product **87**, but undesired overbrominated products. As a result, a new synthetic pathway was pursued. In order to avoid bromination, the new synthetic strategy started with already oxidized 9,10-phenanthrenequinone and relied on using nitro groups as functional handles that could later be converted to bromines (Scheme 4.2).

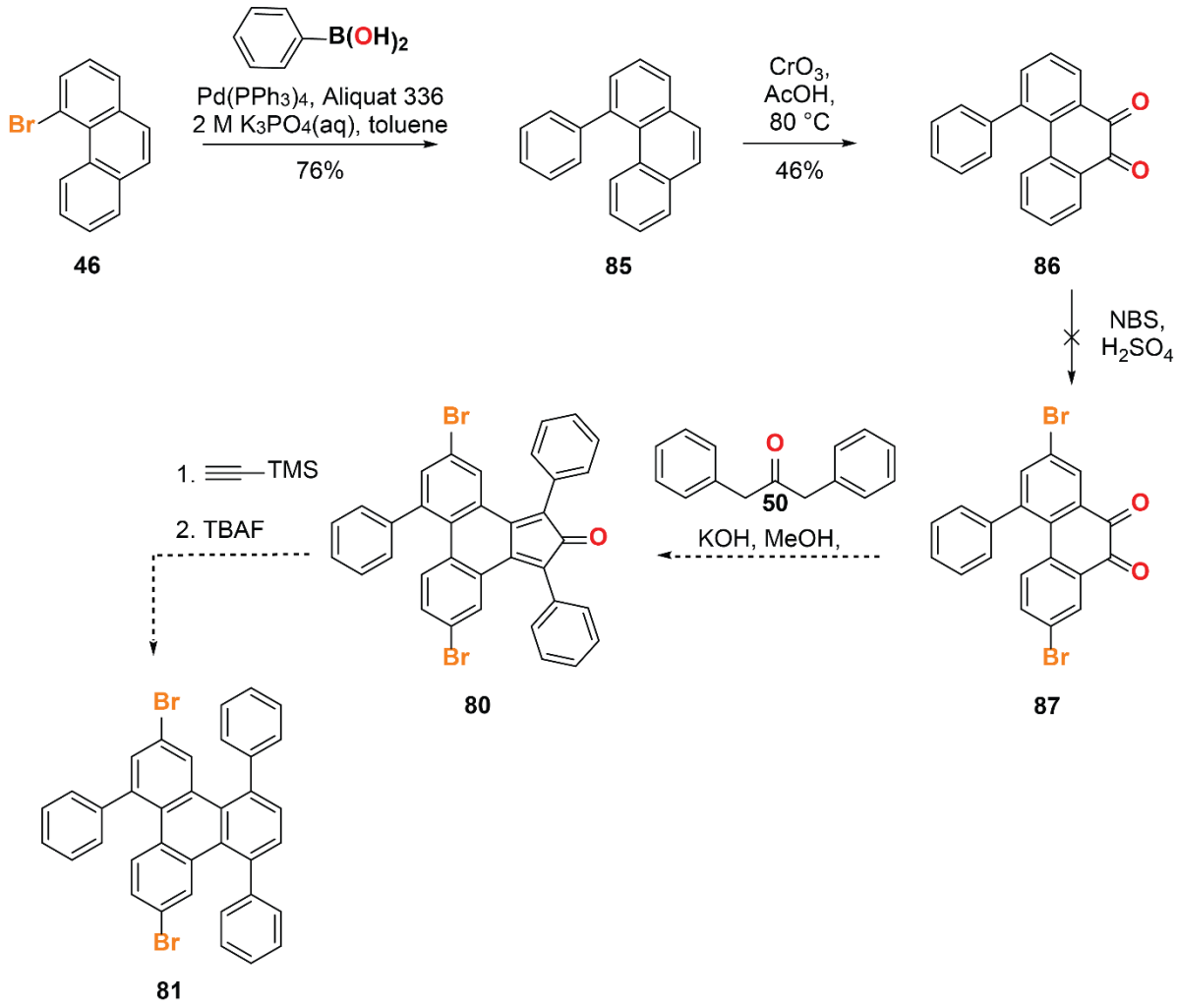

Scheme 4.1 Initial synthetic route towards 9-AGNR precursor **81** starting with 4-bromophenanthrene **46**.

Commercially available 9,10-phenanthrenequinone (**88**) was subjected to a nitration with HNO_3 and H_2SO_4 to yield 2,7-dinitrophenanthrene-9,10-dione **89**. Subjecting **89** to a bromination gave quinone **90** in 65% yield. Because our attempted *Suzuki* coupling reactions directly onto the quinone had not yielded the desired products, we protected **90** with ethylene glycol to afford **91** in 78% yield. Next, a *Suzuki* coupling with phenylboronic acid gave the desired product **92** in 87% yield. Reduction of the nirtro groups with iron in acetic acid and ethanol did not yield the desired

diamine. Subjecting **92** to a $Na_2S_2O_4$ reduction yielded the desired diamine **93** in 42% yield. However, the yield for this reduction was drastically improved when hydrogenation with Pd/C was used as the hydrogenation catalyst, and afforded **93** in quantitative yield. Next, a *Sandmeyer* reaction converted the amines to bromines to give **94** in 73% yield. Subsequent deprotection with $HClO_4$ afforded the desired quinone **87** in 96% yield. The synthetic route to **87** proved to be very scalable with purification of the intermediates optimized to require three column chromatography

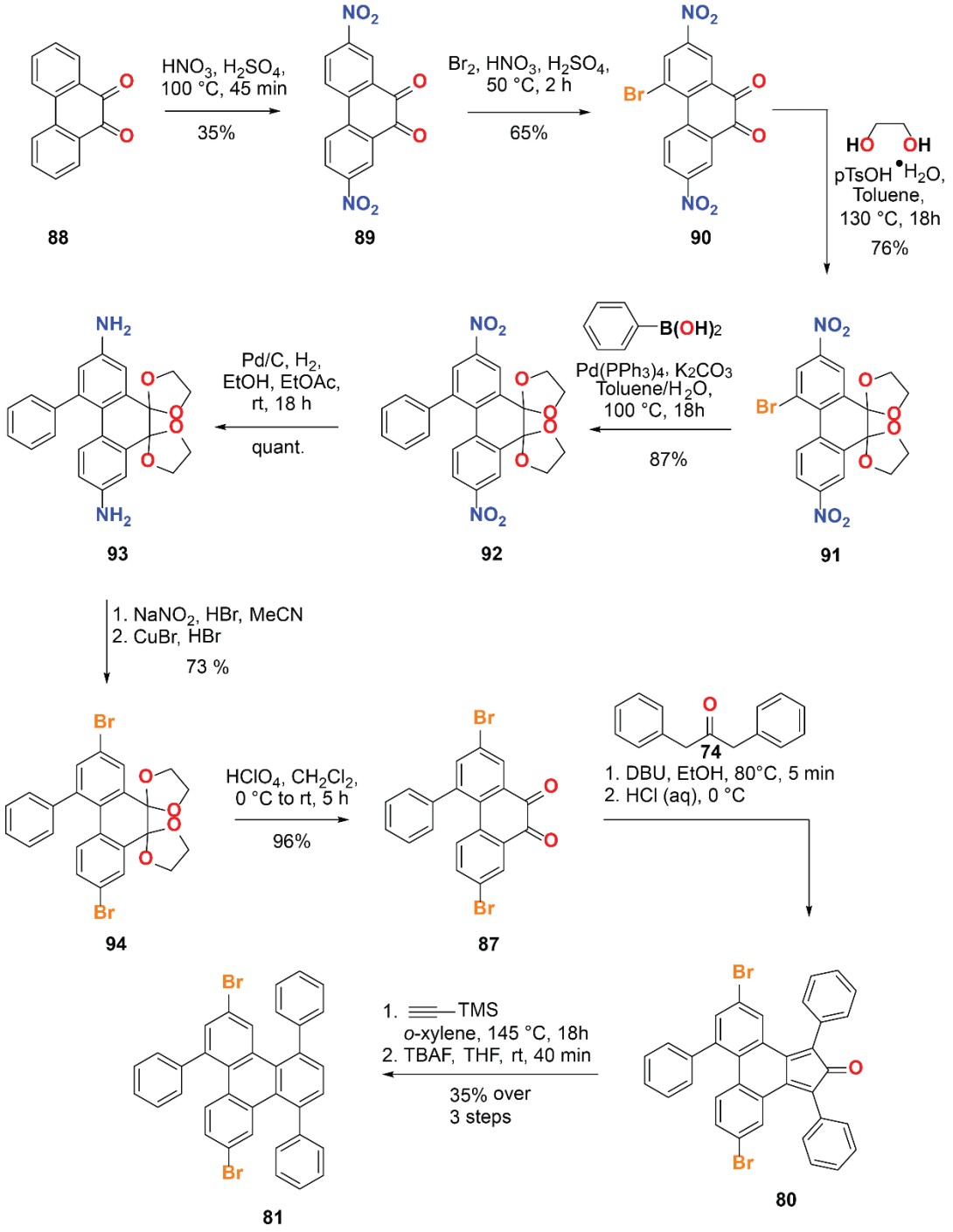

Scheme 4.2 Redesigned synthetic route towards **81** starting with 9,10-phenanthrenequinone.

purification in order to isolate **92**, **94**, and **87.**

Knoevenagel condensation of **87** with diphenyl acetone **74** and isolation of the resulting cyclopentadienone **80** proved to be difficult. Due to the instability of **80**, the best results were observed when a bulkier, non-nucleophilic base such as DBU was used instead of KOH. Additionally, it was found that the best results were achieved with a reaction time of 5 minutes, followed by immediate quenching with 2M HCl at -20 °C, which causes a green precipitate to form. Filtration and washing with water yielded the crude material as a green solid which was then used immediately without further purification to prevent decomposition. Allowing the reaction to run longer than 5 minutes usually resulted in the dark green reaction mixture turning red over time. Upon addition of 2M HCl, no precipitate was observed and no product could be isolated. Subjecting **80** to a *Diels-Alder* and decarbonylation with TMS acetylene, followed by deprotection with TBAF, gives the desired 9-AGNR monomer **81** in 35% over three steps.

In order to access even longer ribbons, we decided to synthesize an iodinated version of monomer **81**. By utilizing an iodinated monomer instead of a brominated one, we can take advantage of the fact that carbon – iodine bonds have a lower bond dissociation energy (BDE = 272.0 ±4.2 kJ mol^{-1}) compared to carbon – bromine bonds (BDE = 336.4 ±6.3 kJ mol^{-1}).[99] Thus, the iodinated monomer is expected to form radicals on the surface at a lower temperature and will polymerize at a lower temperature, compared to the brominated monomer. As a result, we expect to form longer polymers and GNRs with the iodinated monomer, as seen with other similar systems.[100]

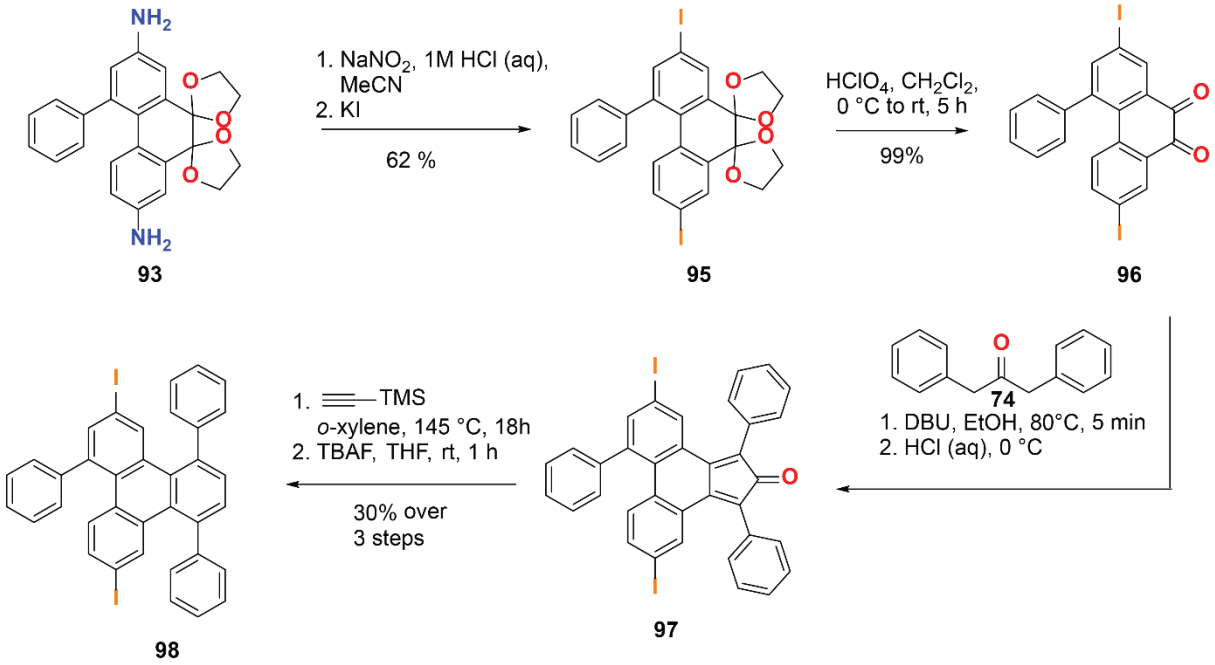

Scheme 4.3 Synthesis of iodinated 9 AGNR monomer **98**.

In order to synthesize an iodinated 9 AGNR monomer, the *Sandmeyer* reaction conditions used to convert diamine **93** to **94** were changed to iodinating conditions (Scheme 4.3). Initially, concentrated H_2SO_4, $NaNO_2$, and KI were used to convert the aryl amines to aryl iodines. Not unexpectedly, the concentrated H_2SO_4 deprotected the quinone *in situ*, resulting in many

byproducts and the deprotected iodinated quinone **96** was isolated in only 40% yield. Using a milder acid, 2M HCl, however prevented undesired deprotection of the quinone. **95** was isolated in 62% yield after purification by silica gel column chromatography. It was later observed that **95** can also be used without further purification. Deprotection of the quinone with $HClO_4$ afforded **96** in quantitate yield. As before, *Knoevenagel* condensation of **96** and diphenyl acetone **74** with DBU in anhydrous ethanol afforded cyclopentadienone **97**, which was immediately converted without further purification. *Diels-Alder* with TMS acetylene and in situ decarbonylation, and subsequent deprotection with TBAF gave the desired 9-AGNR monomer **98** in 30% over three steps.

4.2.2 Surface Studies of 9-AGNRs

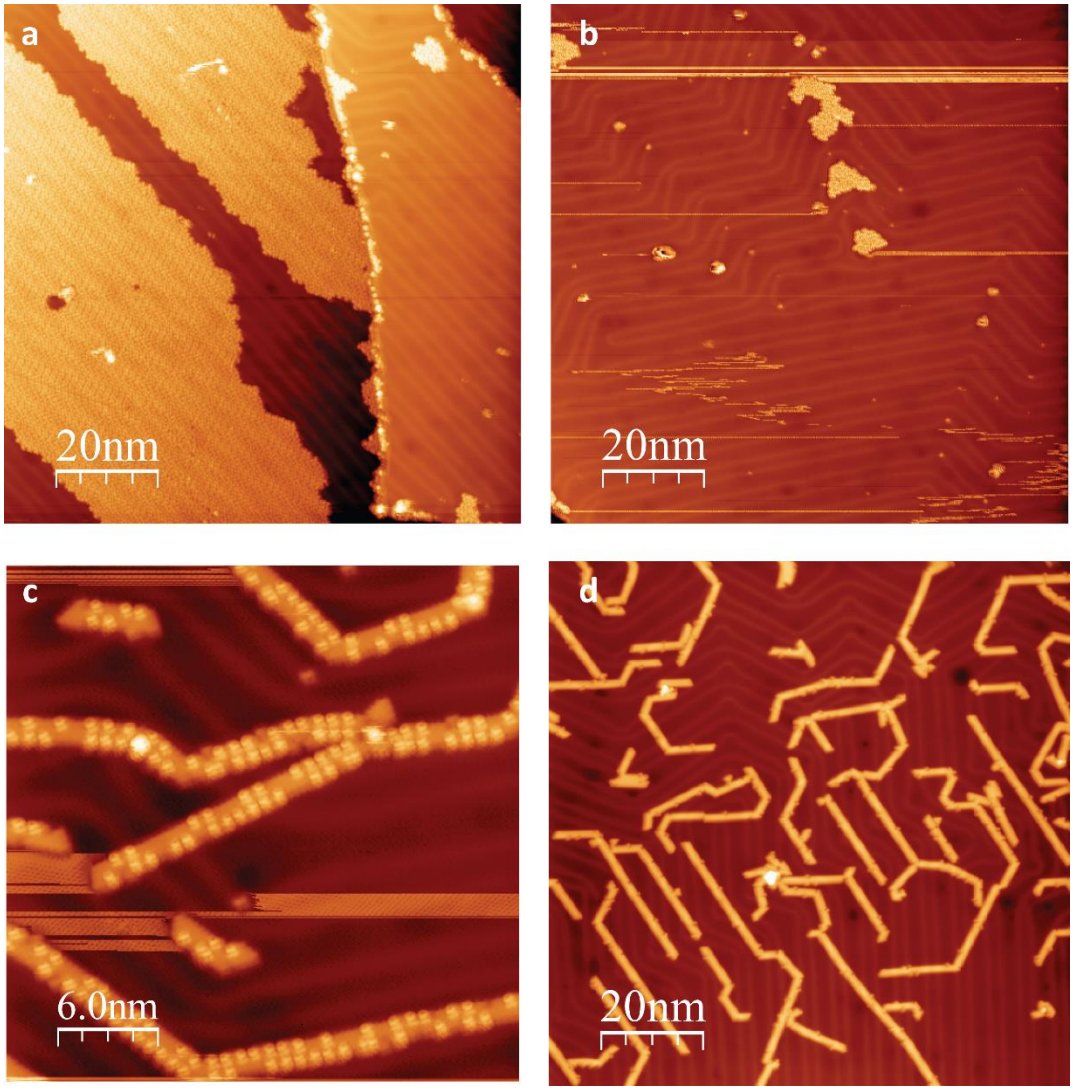

Figure 4.4 (a) STM topography of **81** as deposited on Au(111) (sample bias V_s = 1.5 V, tunneling current I_t = 30 pA) showing areas of large monomer islands. (b) STM topography of **81** as deposited on Au(111) (sample bias V_s = 1.0 V, tunneling current I_t = 30 pA) showing areas with very dilute monomer coverage). (c) Polymers on Au(111) after annealing to 370 °C (sample bias V_s = 1.0 V, tunneling current I_t = 30 pA). (d) Fully cyclized 9-AGNR after annealing to 400 °C (sample bias V_s = 0.5 V, tunneling current I_t = 50 pA).

The N = 9 AGNR precursor monomer **81** was sublimed at 210 °C onto an Au(111) surface in a home-built low temperature (T = 7 K) STM/nc-AFM for 8 minutes. We were able achieve sub-monolayer coverage of **81**, however we observed heterogeneous coverage of the surface, with areas of large monomer islands and areas with only a few small monomer islands (Figure 4.4a, b). The sample was subsequently annealed at 370°C to induce the homolytic cleavage of C–Br bonds followed by radical step-growth polymerization (Figure 4.4c). Further annealing to 400 °C gave fully cyclized N = 9 AGNRs on the surface (Figure 4.4d). Despite the low surface coverage, we were able to form 9-AGNRs, with lengths up to 50 nm long. Unfortunately, we observed sporadic defects periodically along the GNR edges resulting from what appears to be migration of an unfused phenyl ring in the monomer (Figure 4.5).

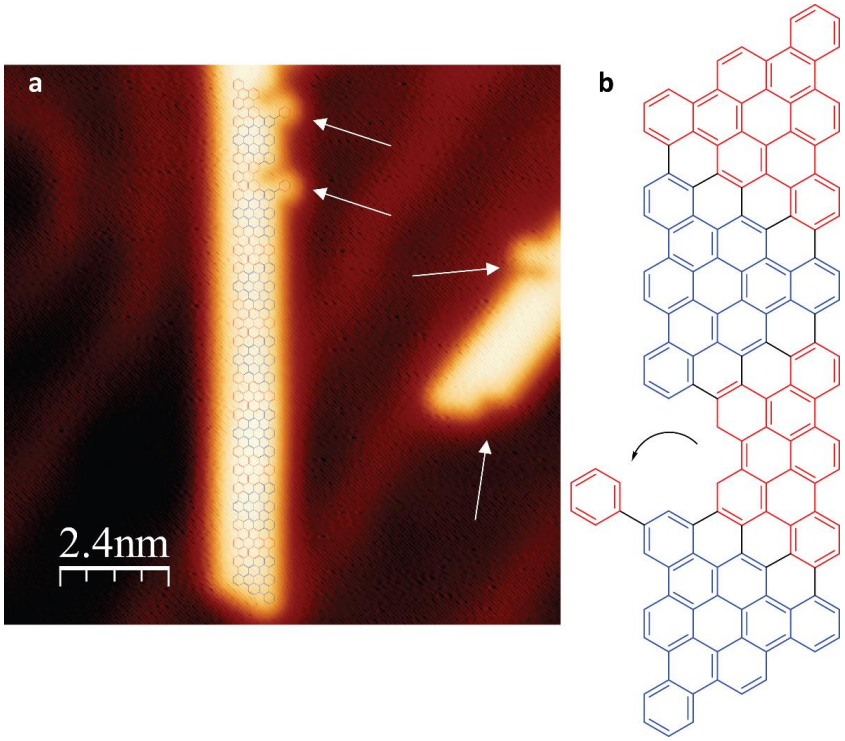

Figure 4.5 (a) STM topography of 9-AGNR on Au(111) with proposed structure overlaid. Arrows point to defects believed to be from phenyl migration (sample bias V_s = 0.2 V, tunneling current I_t = 50 pA). (b) Proposed structure of defect from phenyl migration.

The electronic structure of the 9-AGNRs was analyzed by STS. Figure 4.6b compares dI/dV spectra recorded on the 9-AGNR to spectra recorded on the bare Au(111) substrate, revealing a peak at 1.1 V, corresponding to the empty states of the conduction band, and a small peak at −0.265 V, corresponding to the occupied states of valence band. Thus, the resulting energy gap of the 9-AGNRs is 1.4 eV. These values are in agreement with the STS data obtained by Ruffieux in 2017.[33] dI/dV maps recorded at biases corresponding to the conduction and valence energies in Figure 4.6d and f reveal characteristic, reproducible patterns in the local density of states (LDOS) maps for both bands and correspond well with previously reported calculated LDOS maps (Figure 4.6c, and e).[33]

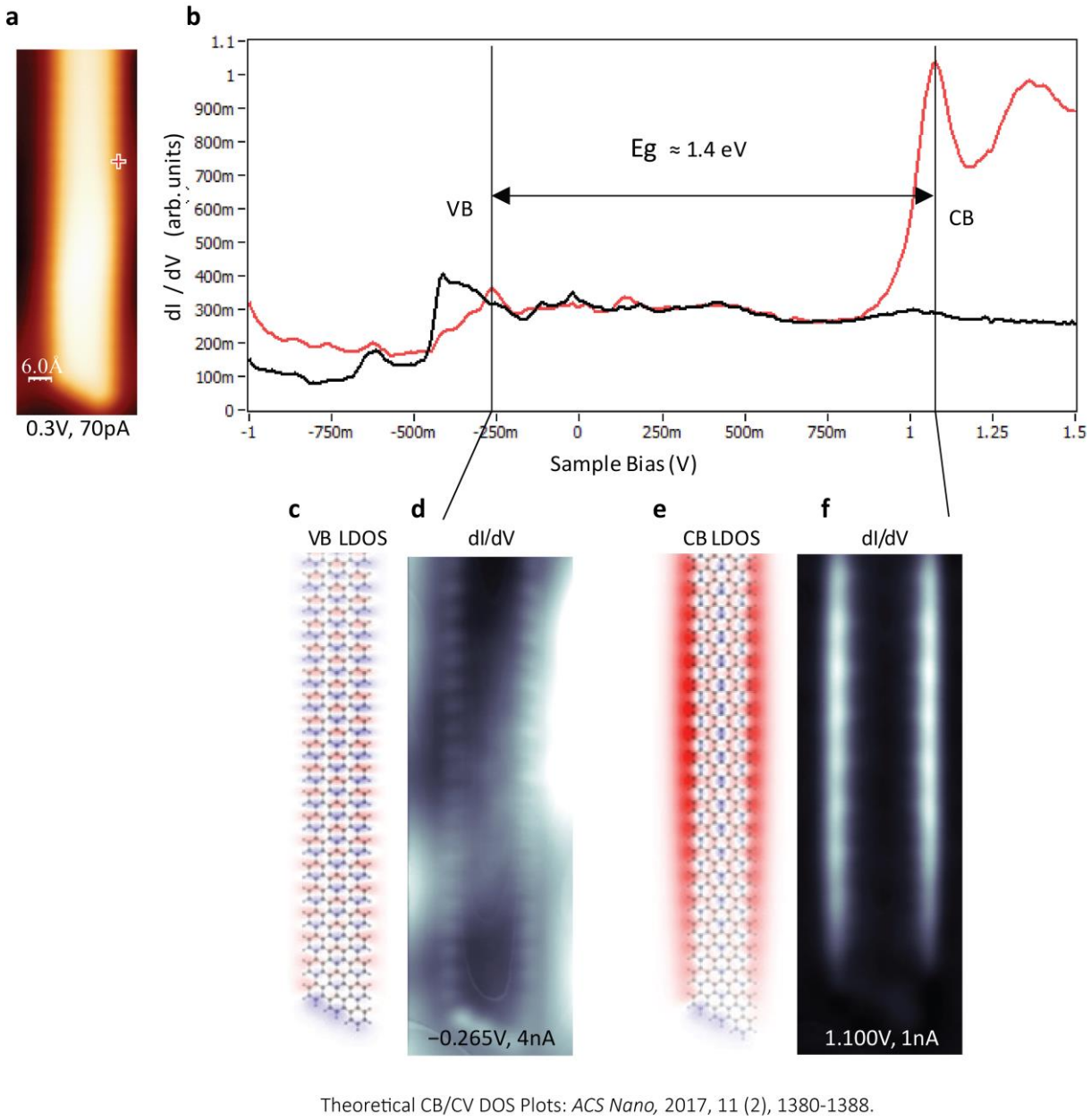

Figure 4.6 (a) STM topography of 9-AGNR ($V_s = 0.30$ V, $I_t = 80$ pA). (b) dI/dV spectra recorded on the edge of a 9-AGNR (red) and on the Au(111) substrate (black). (c) Reported theoretical valence band DOS.[33] (d) Experimental constant-current dI/dV maps obtained at valence band energy ($V = -.0.265$ V, $I_t = 4$ nA). (e) Reported theoretical conduction band DOS.[33] (f) Experimental constant-current dI/dV maps obtained at conduction band energy ($V = 1.100$ V, $I_t = 1$ nA).

4.2.3 9-7-9 Heterojunctions

Only recently has there been a breakthrough in the controlled synthesis of GNR heterojunctions. In 2018, our group reported a controlled heterojunction synthesis using hierarchical growth, taking advantage of the difference in bond dissociation energies of carbon – iodine and carbon – bromine bonds.[42]. An alternative method towards controlled growth of GNR

heterostructures would use the difference in steric interactions between different types of monomers. Recently, researchers in our group developed a linker molecule, **99**, with 7- and 9-AGNR segments (Figure 4.7). With this linker molecule, they were able to polymerize the linker to form a topological GNR super lattice with both regularly spaced 7- and 9-AGNR segments.[101]

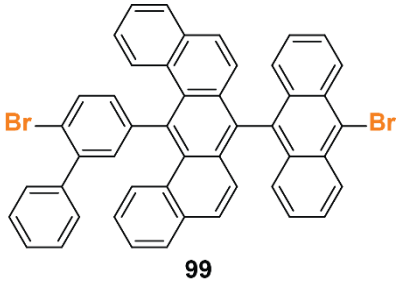

99

Figure 4.7 Linker molecule **99**.

This linker, however, also has the ability to polymerize with DBBA (**1**) and 6,11-dibromo-1,2,3,4-tetraphenyltriphenylene (**2**) to form single and double heterojunctions. However, when **4** was used to grow 9-AGNR segments off the linker, no GNRs or heterojunctions were observed. Since **81** is similar to the chevron monomer in design and steric interactions, we were able to successfully copolymerize it with **99** to form a double heterojunction.

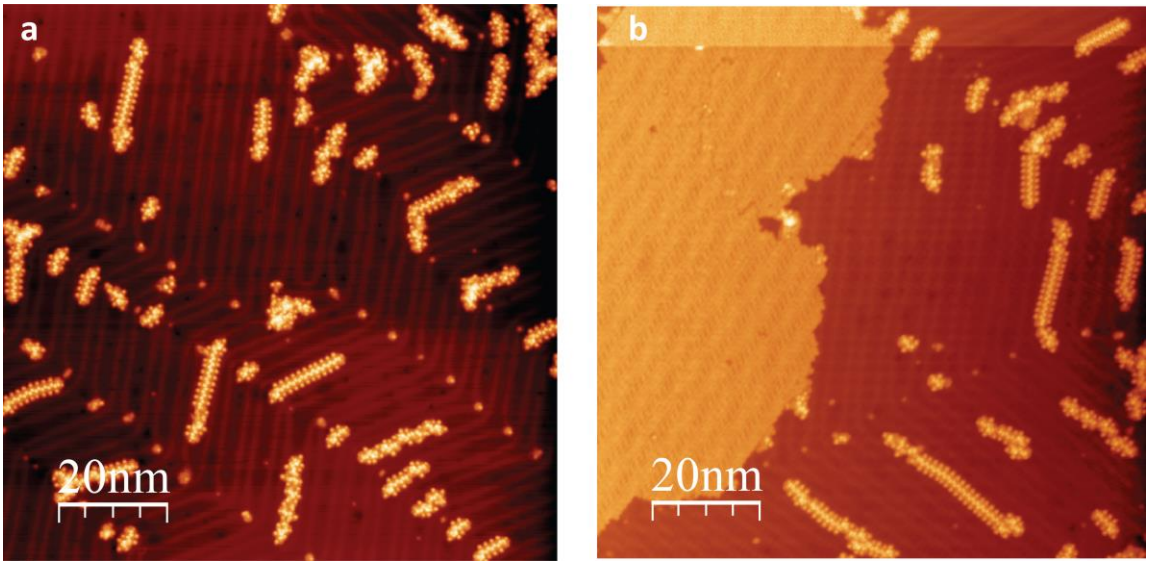

Figure 4.8 (a) STM topography of **99** as deposited on Au(111) (sample bias V_s = 1.0 V, tunneling current I_t = 50 pA). (b) STM topography of **81** and **99** codeposited on Au(111) (sample bias V_s = 1.0 V, tunneling current I_t = 30 pA).

99 was sublimed at 235 °C onto an Au(111) for 80 minutes in a home-built low temperature (T = 7 K) STM/nc-AFM. Figure 4.8a shows a scanning tunneling microscopy (STM) image of a sub-monolayer coverage of **99** on Au(111) at T = 4 K. Then **81** was codeposited by subliming it to 210 °C onto the substrate for 10 minutes. Figure 4.8b shows a STM image of both monomers codepoisted on Au(111) at T = 4 K. The sample was subsequently annealed at 400 °C to form GNRs on the surface. We were able to observe 9-AGNRs and 9-7-9 heterojunctions, in which one linker molecule was incorporated into the GNR to give rise to a small 7-AGNR segment connecting to a long 9-AGNR segment on either side (Figure 4.9). Unfortunately, sporadic defects associated with phenyl migration were still observed.

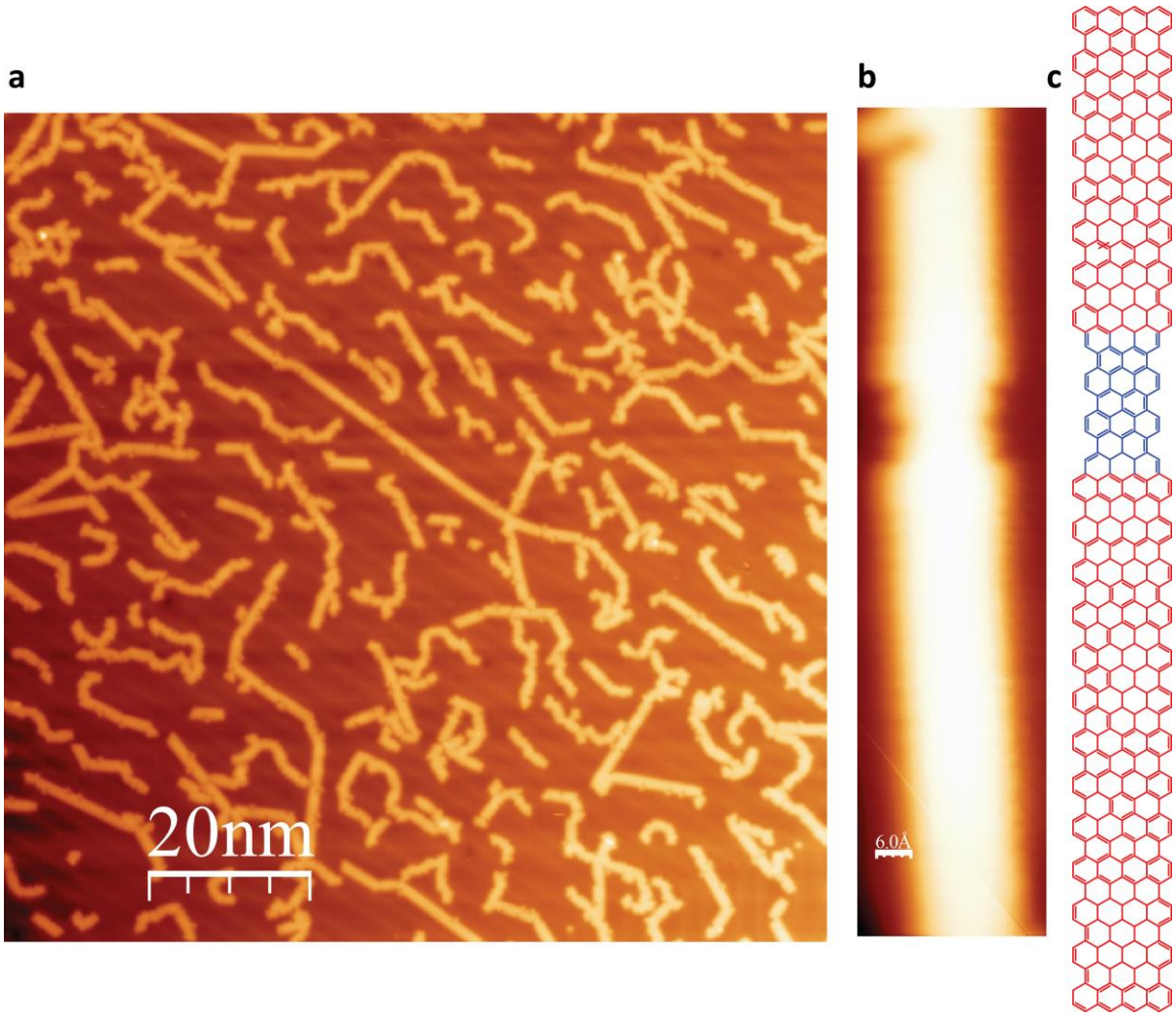

Figure 4.9 (a) STM topography of fully cyclized GNRs on Au(111) (sample bias V_s = 0.5 V, tunneling current I_t = 30 pA). (b) STM 9-7-9 double heterojunction GNR (sample bias V_s = 0.1 V, tunneling current I_t = 100 pA). (c) Schematic representation of 9-7-9 GNR.

4.3 N = 15 AGNRs

While N = 9 AGNRs are of great interest due to their low bandgap, N = 15 AGNRs, also part of the 3p family, have an even lower bandgap. To date, there have been no reported bottom up syntheses of atomically precise 15-AGNRs and the only current reports of 15-AGNRs are due to lateral fusing of narrower GNRs, resulting in a mixture of different GNR widths[102,103] and the attempt as bottom up synthesis through a *para*-oligophenylene based molecular precursor.[104] In 2014 Abdurakhmanova and coworkers attempting to synthesize atomically precise 15-AGNRs from the surface growth of dibromo-*p*-pentaphenyl. Unfortunately, they had to heat the surface to

720 K to obtain fully cyclized structures and the resulting structures were not atomically precise with many defects and very short in length.[104]

Our current synthetic strategy towards the 9-AGNR precursor **81** is very modular and from cyclopentadienone **80** or **97**, a variety of different dienophiles can be used during the *Diels-Alder*. Thus, we can access the 15-AGNR monomer by using alkyne-functionalized quaterphenyl **104** as our dienophile (Scheme 4.5).

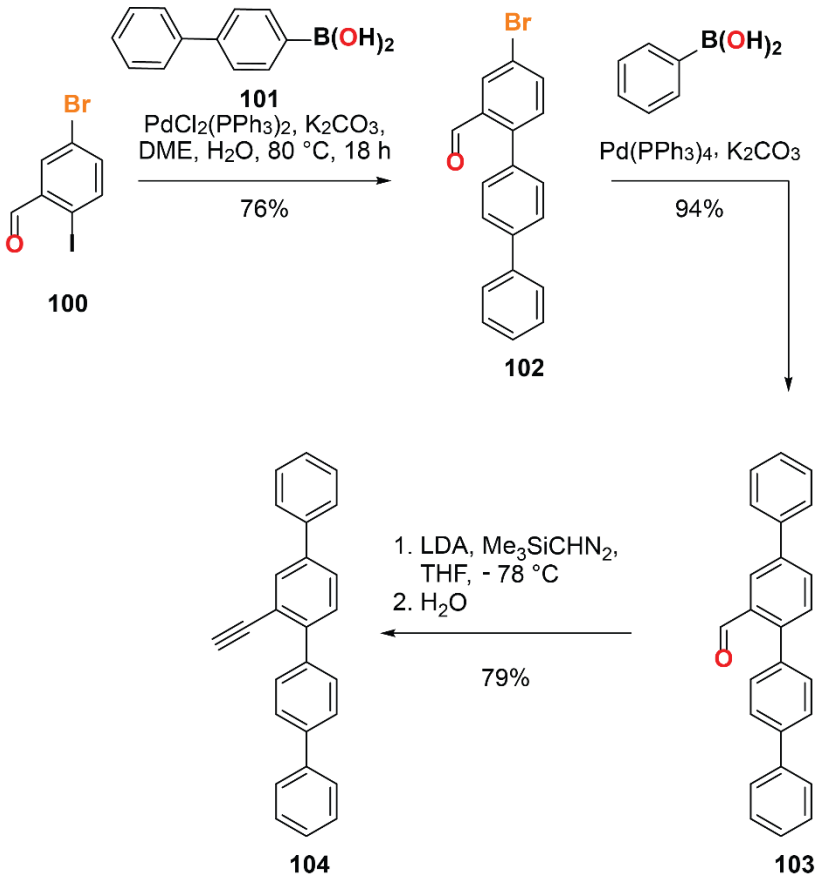

Scheme 4.4 Synthesis of quaterphenyl alkyne wing **104**.

The synthesis of **104**, depicted in Scheme 4.4, starts with a *Suzuki* coupling between 5-bromo-2-iodobenzaldehyde and 4-biphenylboronic acid to afford terphenyl **102** in 76% yield. A subsequent *Suzuki* coupling with phenylboronic acid gave quaterphenyl **103** in 94% yield. Treating **103** with TMS diazomethane and LDA converts the aldehyde to the corresponding alkyne and gave the desired quaterphenyl **104** in 79% yield. The brominated 15-AGNR monomer was accessed via a *Diels-Alder* and subsequent *in situ* decarbonylation with freshly prepared crude **80** to give **82** (Scheme 4.5).

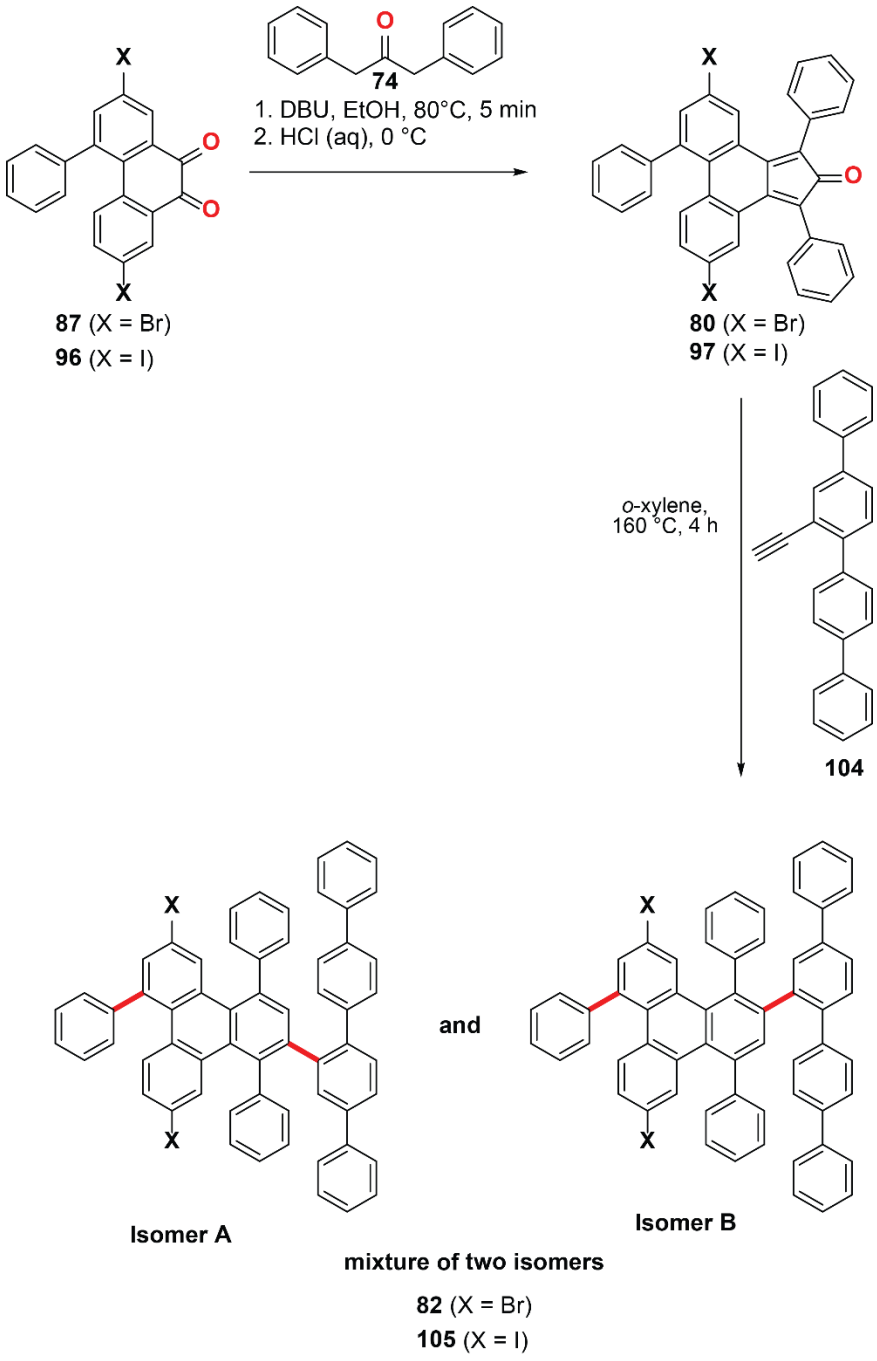

Scheme 4.5 Synthesis of 15 AGNR monomers **82** and **105**.

The products from the *Diels-Alder* were always a mixture of two isomers since the alkyne could approach the cyclopentadienone in two different orientations. Vapor diffusion recrystallization from MeOH/*o*-xylene, preferentially recrystallized isomer **82**A, with small amounts of the other isomer; while recrystallization from layered MeOH/*o*-xylene gave predominately isomer **82**B. We were able to determine which isomer was preferentially isolated via vapor diffusion recrystallization by x-ray crystallography, however the resulting crystal structure was disordered and could not be fully solved (Figure 4.10a). Despite this disorder, a

closer look at the inner fragment clearly shows the bond connectivity associated with isomer **82**A (Figure 4.10b). The stacked ^{1}H NMR spectra of both isolated isomers are depicted in Figure 4.11, while the individual ^{1}H NMR spectra are depicted in Figures 4.12 and 4.13.

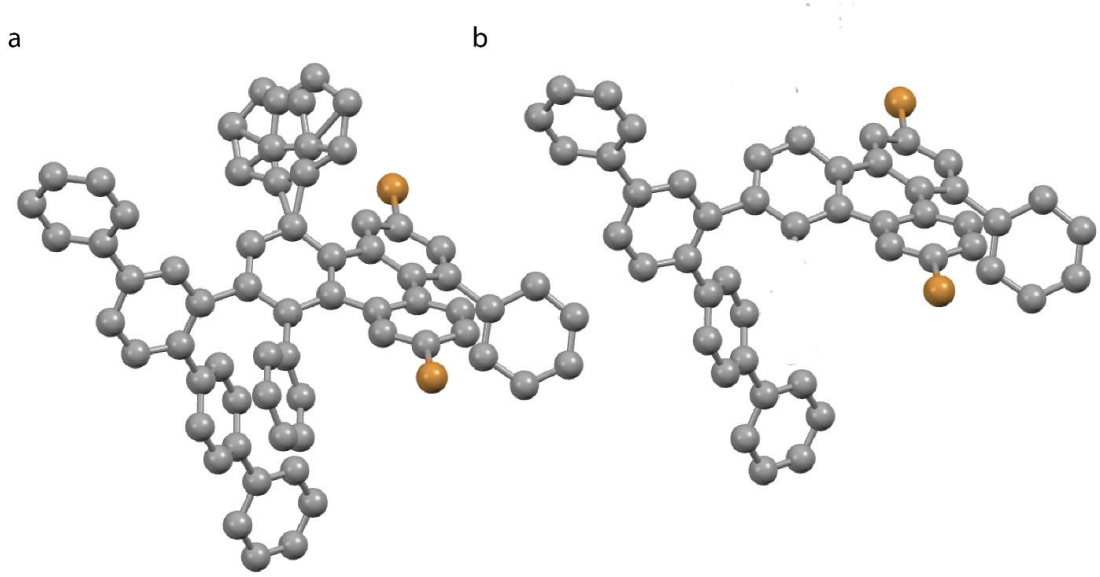

Figure 4.10 (a) Disordered crystal structure of Isomer **82**A. (b) Crystal structure with internal phenyl rings deleted for clarity.

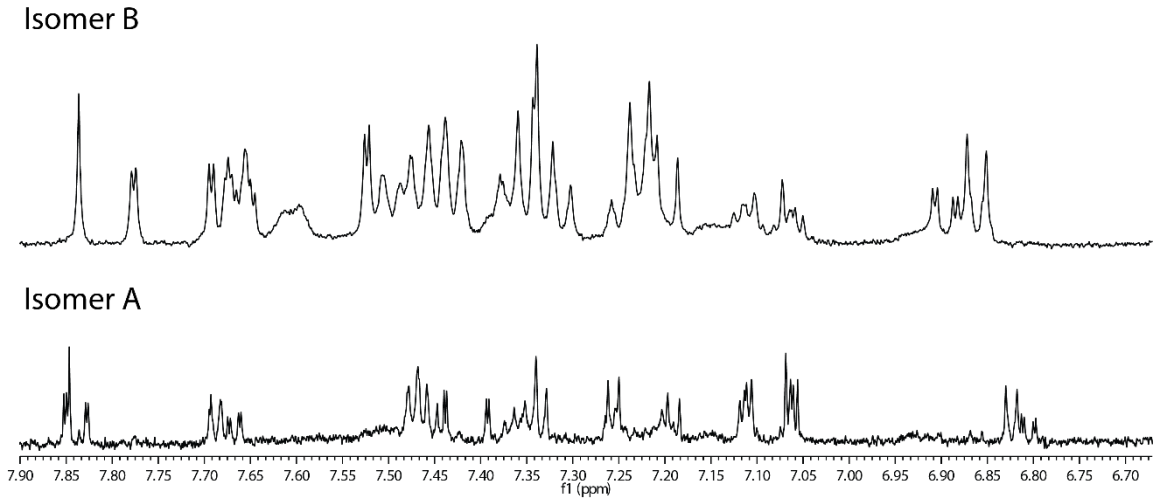

Figure 4.11 Stacked ^{1}H NMR spectra of Isomers **82**A and **82** B.

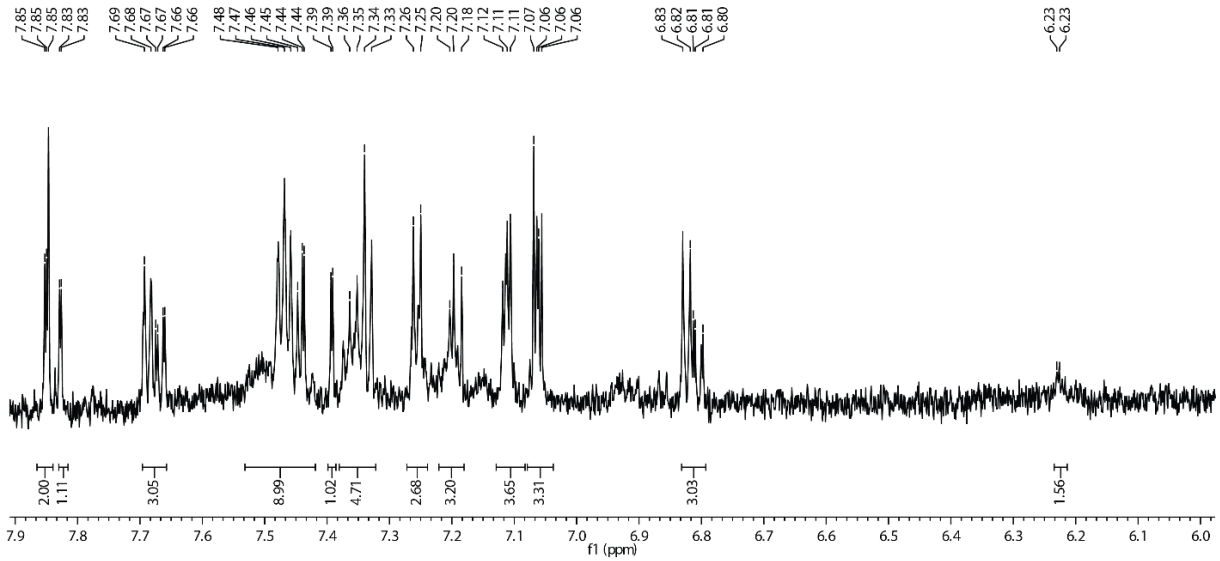

Figure 4.12 [1]H NMR spectrum of Isomer **82**A isolated via vapor diffusion recrystallization from MeOH/*o*-xylene.

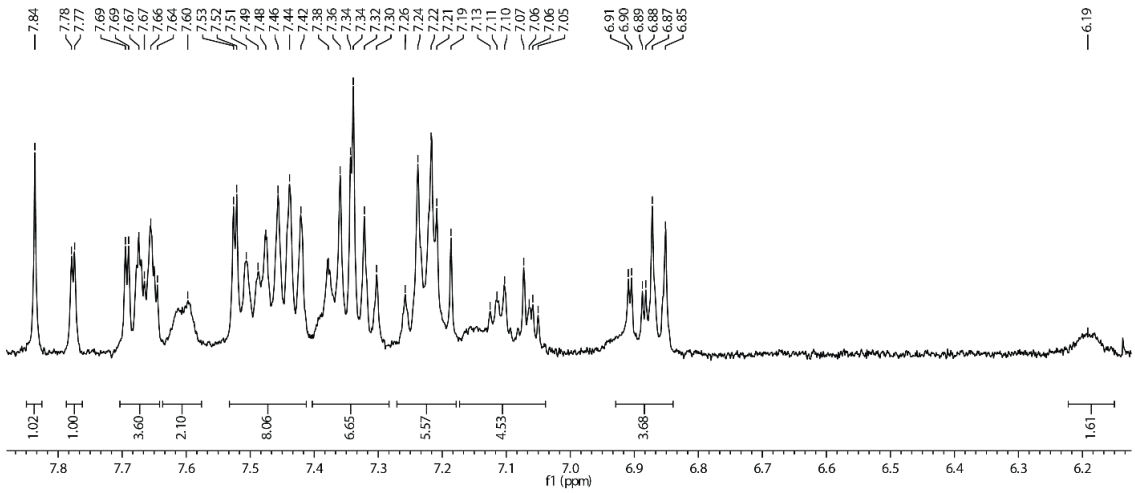

Figure 4.13 [1]H NMR spectra of Isomer **82**B isolated from recrystallization from layered MeOH/*o*-xylene.

Similarly, the iodinated 15-AGNR monomer **105** was obtained from a *Diels-Alder* with cyclopentadienone **97** and alkyne **104**. Recrystallization from hot MeOH/*o*-xylene preferentially recrystallized one of the isomers, with small amounts of the other isomer (Figures 4.14 and 4.15). Integration of two characteristic doublets at 6.84 and 6.83 ppm and 8.05 and 7.90 ppm in the [1]H NMR spectrum confirm that the ratio of the two isomers is 1 to 0.3-0.35, or approximately 3:1 (Figure 4.15). We did not obtain x-ray crystallography quality crystals in order to determine which isomer was isolated, but assume the same isomer **105**B is isolated as the major isomer as seen with the brominated monomer. Vapor diffusion recrystallization from MeOH/*o*-xylene did not result in predominately crystals of one isomer and instead we obtained a 1:2 ratio, determined by

integration of the characteristic of the doublets at 6.84 and 6.83 ppm and the doublets at 8.05 and 7.90 ppm (Figures 4.14 and 4.16).

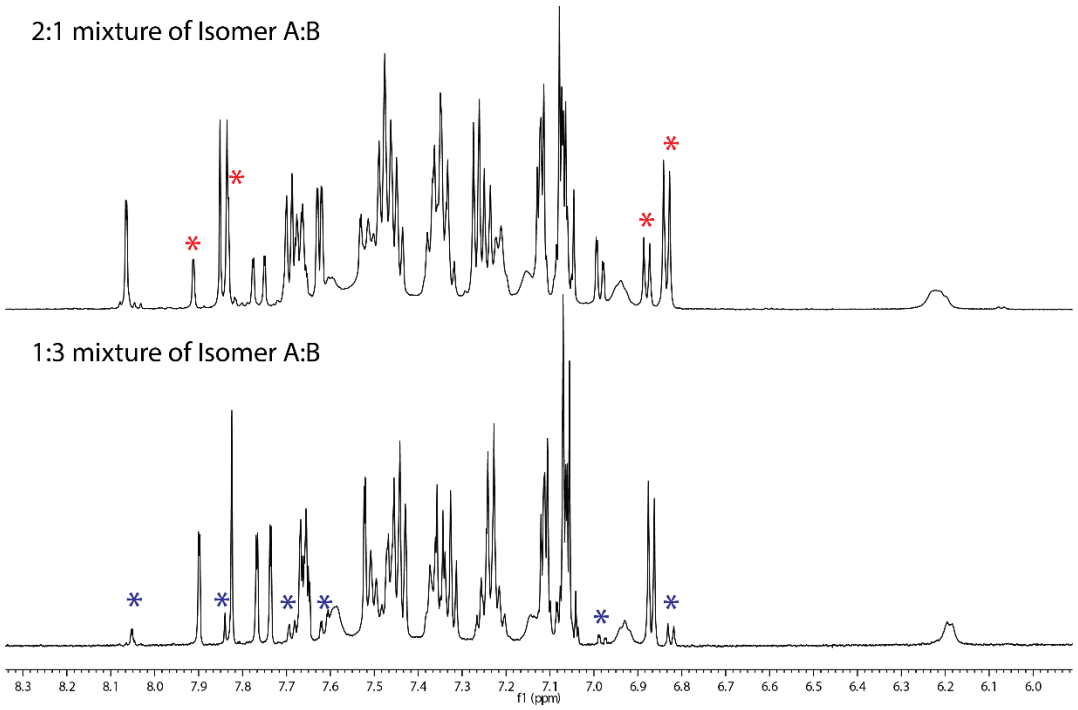

Figure 4.14 Stacked ^{1}H NMR spectra of crystals of **105** obtained from vapor diffusion recrystallization (top) and recrystallization from hot MeOH/o-xylene. Red * signify distinguishable peaks from minor isomer in top spectrum and blue * signify distinguishable peaks from minor isomer in bottom spectrum.

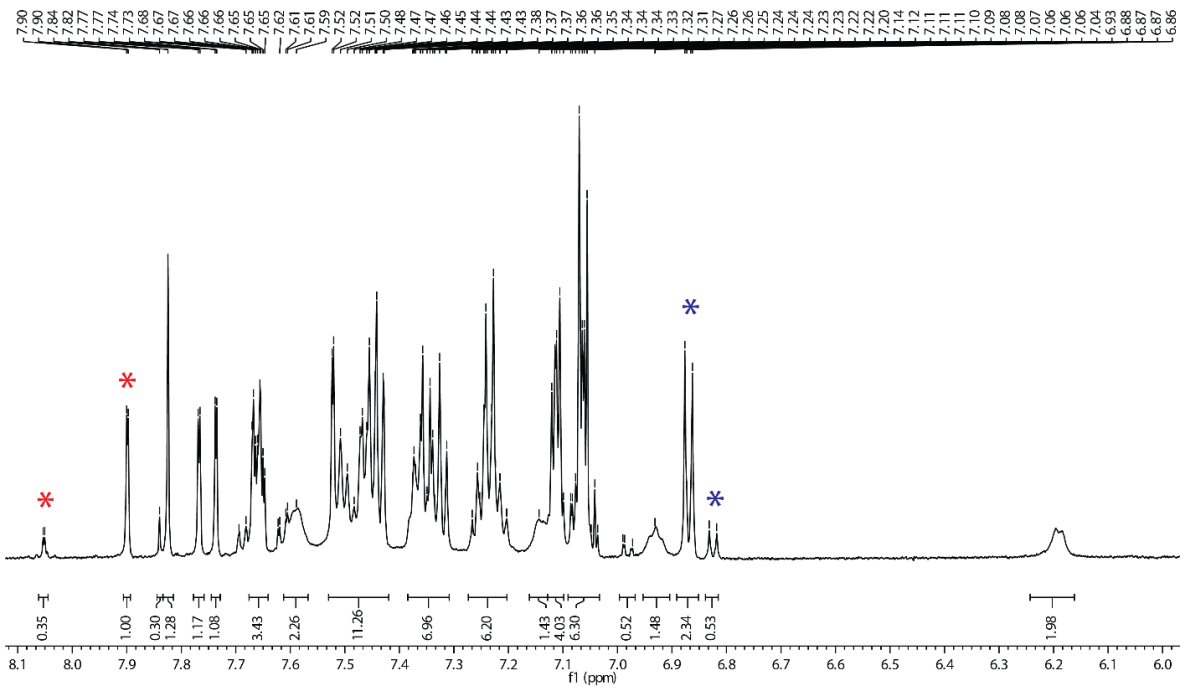

Figure 4.15 ^{1}H NMR spectrum of crystals of **105** obtained from recrystallization from hot MeOH/o-xylene. Isomers A and B were obtained in a 1:3 ratio determined integration of the characteristic of the doublets at 6.84 and 6.83 ppm (blue *) and the doublets at 8.05 and 7.90 ppm (red *).

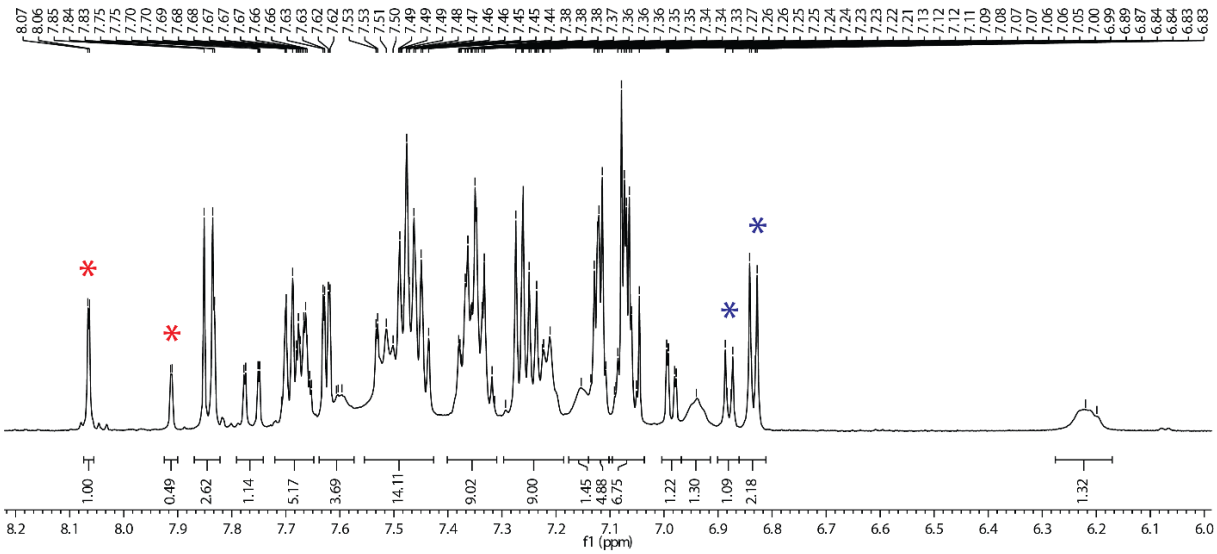

Figure 4.16 ^{1}H NMR spectrum of crystals of **105** obtained from vapor diffusion recrystallization. Isomers A and B were obtained in a 2:1 ratio determined integration of the characteristic of the doublets at 6.84 and 6.83 ppm (blue *) and the doublets at 8.05 and 7.90 ppm (red *).

4.4 Wide Chevron GNRs (w-cGNR)

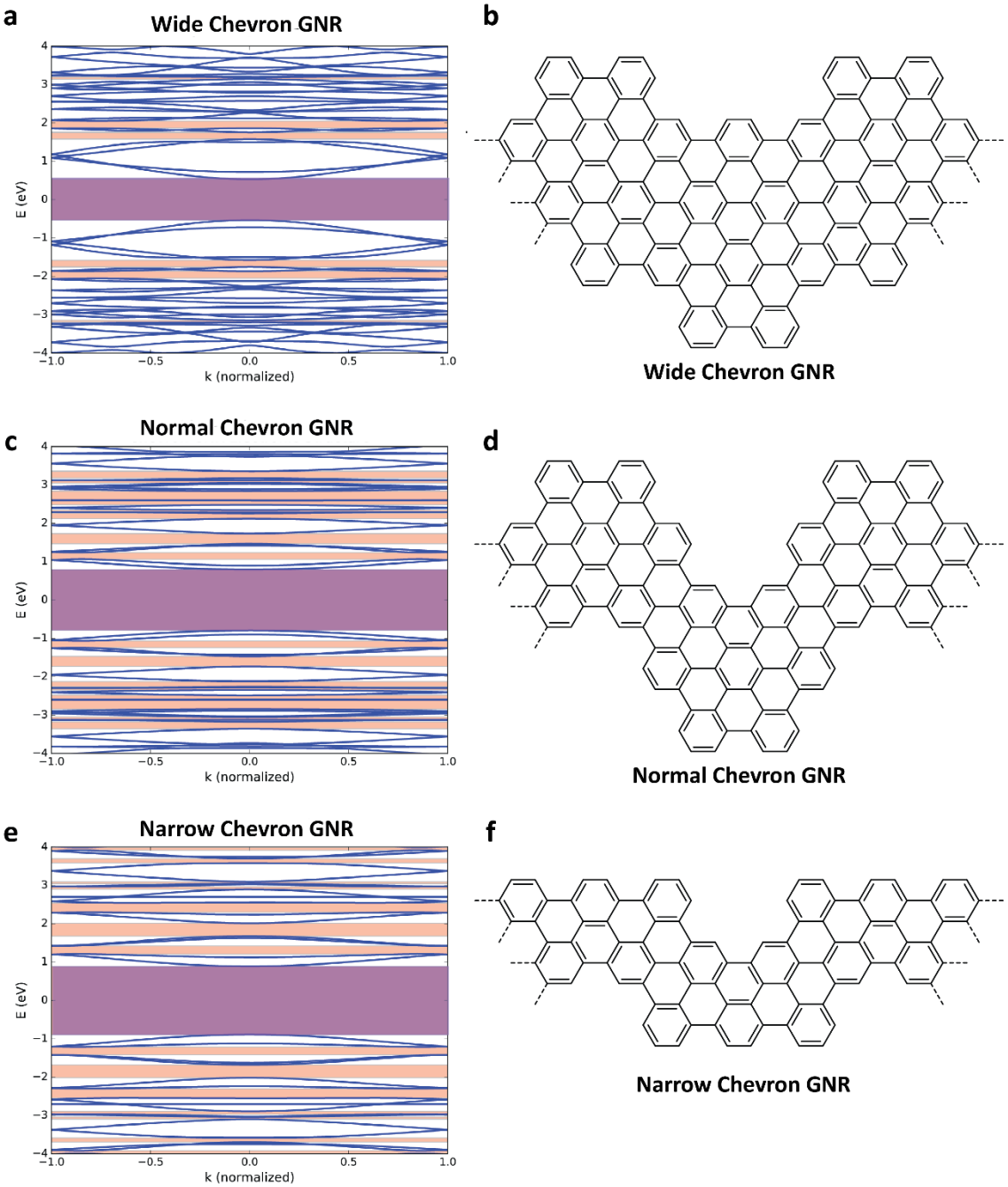

Figure 4.17 Calculated band diagrams of chevron GNRs of various widths. (a) Calculated band diagram and (b) schematic representation of wide chevron GNR (w-CGNR). (c) Calculated band diagram and (d) schematic representation of normal chevron GNR (CGNR). (e) Calculated band diagram and (f) schematic representation of narrow chevron GNR (n-CGNR). Bands shown in blue, bandgap highlighted in purple and mid-gap states highlighted in pink as a visual aid. Images in a, c, and e reproduced from Durr, R. A. (2017). *The rational design and synthesis of graphene nanoribbons and graphene nanoribbon functional nanoarchitectures.*[114]

The bandgap of the chevron GNR is predicted to decrease as the width of the GNRs is increased. In Figure 4.17, the calculated band diagrams for three different chevron GNRs of various widths are plotted. It is very evident, that widening the GNR leads to a lower bandgap and also fewer mid-gap states. Thus engineering the bandgap of chevron GNRs by width, allows us to tune the material to have better electron transport, making it a more suitable material for device fabrication.

For the synthesis of the w-cGNR precursor, the established synthetic route used for the N = 9 and 15 AGNRs could be maintained, diverging at the *Diels-Alder* coupling to the cyclopentaidenone **80** (Scheme 4.6). Whereas commercial TMS acetylene was used in the synthesis of **81** and alkyne **104** was used in the synthesis of **82**, diphenylacetylene **106** was used as the dienophile to afford the desired w-CGNR monomer **83** in 25 % yield over two steps. Since

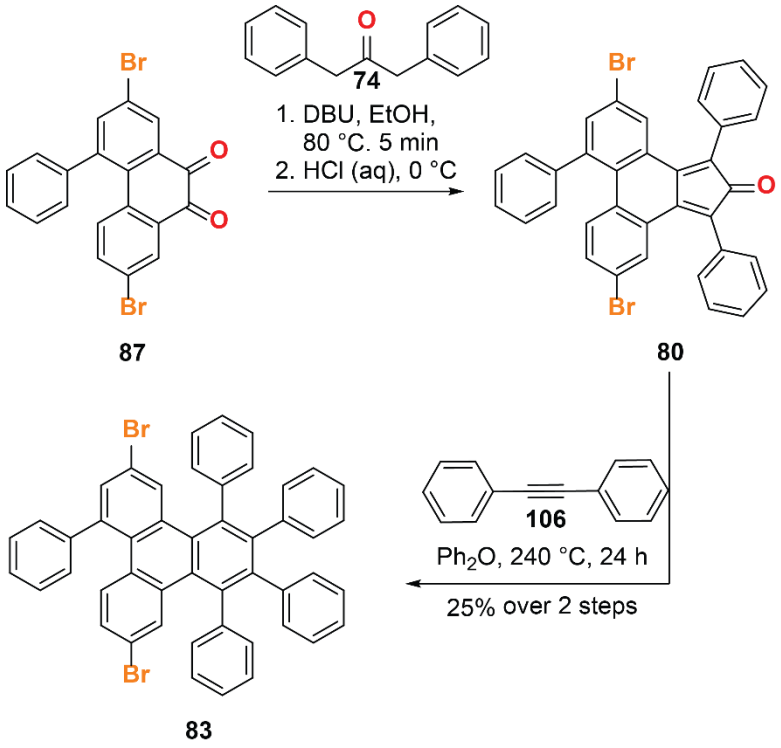

Scheme 4.6 Synthesis of w-CGNR precursor **83**.

this *Diels-Alder* used an internal alkyne as a coupling partner, a high reaction temperature (240 °C) was required compared to *Diels-Alder* with terminal alkynes which only require temperatures of 160 °C. As a result, attempts at isolating an iodinated w-CGNR precursor proved to be difficult since one of the side products was the de-iodinated monomer which was difficult to separate from the desired product by silica gel column chromatography. In order to access an iodinated w-CGNR, biphenyl **107** could be used as the dienophile and subjected to a *Diels-Alder* with **97**. This would lead to an isomeric mixture of w-CGNR precursor **108** (Scheme 4.7).

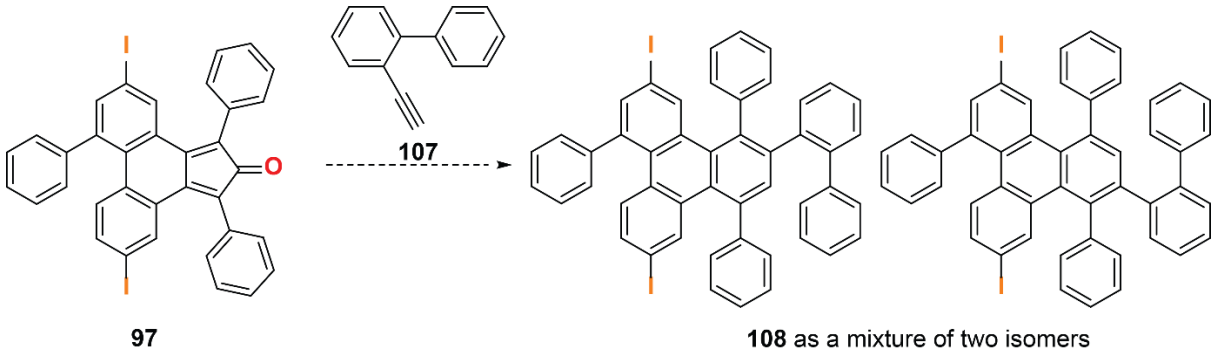

Scheme 4.7 Potential synthetic route to iodinated w-CGNR precursor **108** as mixture of two isomers.

4.5 H-Bonding GNRs

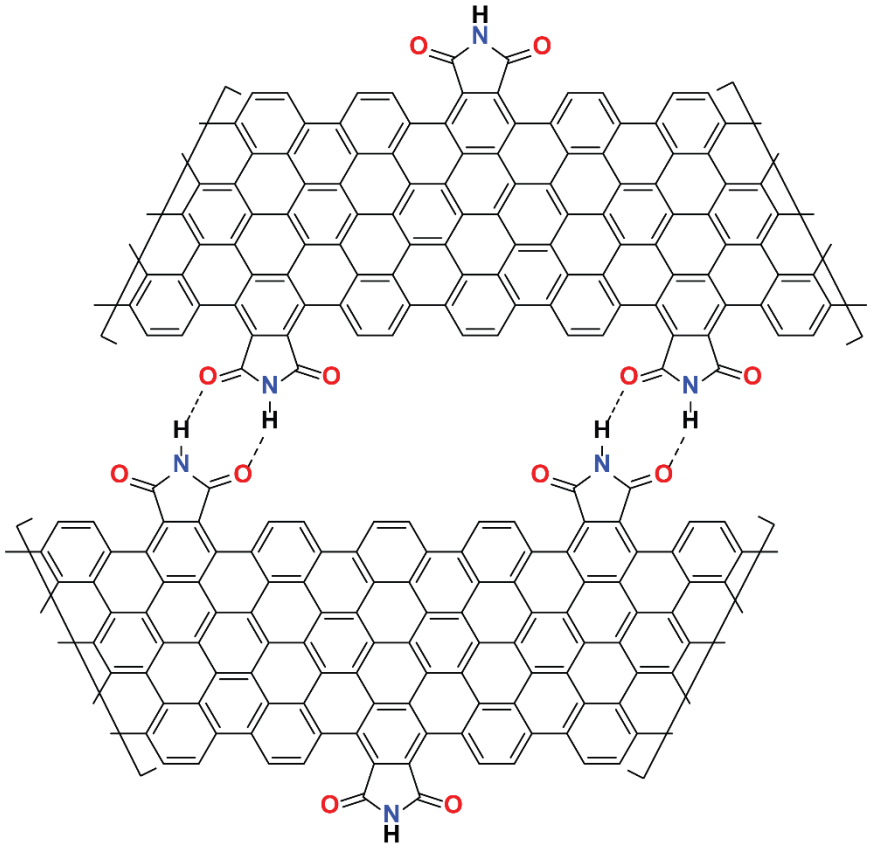

Figure 4.18 Proposed structure of hydrogen bonded GNR with phthalimide groups along the periphery.

One of the biggest challenges in fabricating useful electronic devices from graphene nanoribbons is alignment. Most bottom up syntheses of graphene nanoribbons result in random growth of pristine GNRs at the expanse of global assembly and thus aligning GNRs is still a major

challenge. The current standard to align bottom up synthesized GNRs on a surface is to use a metallic substrate which induces growth in arrays such as Au(788) and Ge(001).[105–107] An alternative method to align GNRs, independent of which crystal face of the metallic surface is used, would be to design GNRs with the ability to self-assembly via intermolecular forces, such as strong hydrogen bonds. The Sinitskii group reported the self-assembly of nitrogen doped chevron GNRs via hydrogen bonding in 2015.[52] However the resulting ordered arrays did not extend beyond a few GNRs at most due to the fact that C-H bonds and C-N bonds are not very strong hydrogen bond donors and acceptors. Herein, we report the synthesis of modified 9AGNR monomers with phthalimide groups along the periphery which would lead to N = 9AGNRs with strong hydrogen bonding groups along the edges (Figure 4.18).

The synthesis of monomer **109** follows a similar path as the N = 9 AGNRs, diverging at the *Diels-Alder* step (Scheme 4.8). Initial attempts used maleimide as the dienophile and cyclopentadienone **97** in DMF at 130 °C. However, this proved to have many byproducts, including the double *Diel-Alder* product. Using nitrobenzene as a solvent and using a higher reaction temperature (210 °C) gave the desired product **109** in 20% over steps. While **109** could be purified by silica gel column chromatography, it could also be purified by sonicating with MeOH and hexane, followed by recrystallization from MeOH/DCM.

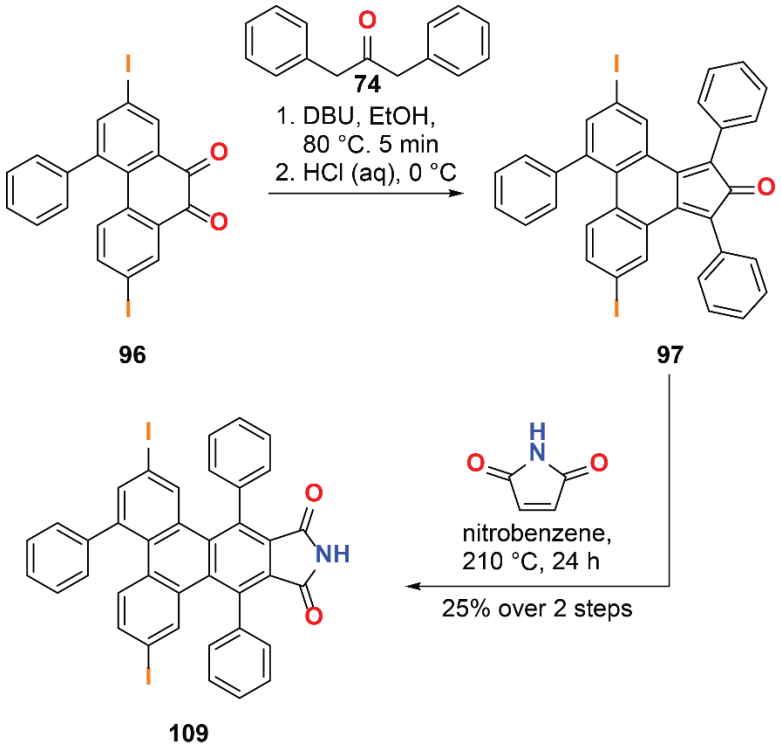

Scheme 4.7 Synthesis of H-Bonding GNR precursor **109**.

4.6 Conclusion

In the fourth chapter of this thesis, the modular synthesis towards low bandgap GNR precursors was presented. The key intermediates, cyclopentadienones **80** and **97**, enabled efficient access to a variety of different GNR monomers in one or two synthetic steps. While N = 9-AGNRs have been reported, we have successfully developed a new, more robust 9-AGNR precursor, with the ability to form heterostructures with other GNRs. Long 9-AGNRs (> 50 nm) were observed on Au(111) and successful heterostructures of N = 9 and 7 GNRs were isolated. While 9-AGNRs have been heralded for their low bandgap, the monomer for 15-AGNRs, an even lower bandgap GNR of the same 3p family, was isolated as a mixture of two isomers and is ready for surface polymerization and STS experiments. In addition to modulating the width of armchair GNRs, we were also able to successfully synthesize w-CGNR precursors.

While access to low bandgap GNRs is a key component to their integration into high performance electronic devices, global alignment is also challenge that needs to be address. Without global alignment of ribbons, the resulting devices would have a random arrangement of GNRs across the electrodes, leading to diminished performance. Using our modular synthetic route, we designed a 9-AGNR with the ability to hydrogen bond through the installation of phthalimide groups along the periphery of the ribbon.

Chapter 5

Summary and Outlook

5.1 Summary

This dissertation discussed the bottom up synthesis of atomically precise functionalized graphene nanoribbons and their applications in a variety of fields. Chapters 2 and 3 focused on the late stage modification of solution synthesized GNRs. In chapter 2, we introduced a "clickable" GNR equipped with azide functionalized alkyl groups that could undergo a 1,3-dipolar cycloaddition with terminal alkynes to install functionality after graphitization. We successfully applied this methodology to synthesize a photoswitchable dye-functionalized GNR that could be imaged via super resolution imaging. This **Cy5-cGNR** could therefore be more efficiently visualized and localized on a surface after deposition, thereby enabling facile integration into next generation electronic devices.

In chapter 3, we developed a late stage functionalization of the GNR backbone via condensation chemistry followed by metalation. First, we synthesized a 1,2-dione functionalized GNR that could undergo condensation chemistry with diamines. We then successfully condensed on 1,10-phenanthroline-5,6-diamine to access a phenanthroline functionalized GNR, **Phen-CGNR**, which has bidentate ligand sites along the backbone to which various metals can be coordinated. Coordination with rhenium and iridium complexes resulted in metallated GNRs with CO_2 reduction and hydrogen activation catalysts, respectively. H_2/D_2 exchange reaction kinetic studies of the **Ir-CGNR** revealed that integrating the molecular catalyst into the GNR matrix resulted in faster kinetics compared to the molecular analogue. This exciting result clearly showed that using a tunable support such as GNRs as solid support materials can greatly improve the catalytic activity of these molecular catalysts. However, we also observed a temperature dependent

deactivation of the **Ir-CGNR** and proposed that this is due to an undesired migration of the iridium metal center to a different binding site along the GNR backbone. In order to prevent this, we are currently synthesizing a **2N-CGNR** with only one possible binding site. These systems are, to our knowledge, the first example where metal catalysts can be directly installed onto atomically precise GNRs, opening the door to various other applications in catalysis, magnetism and spintronic devices.

In chapter 4, the surface synthesis of novel low bandgap GNRs was presented. Due to the low volatility, high defect percentage and inability to copolymerize with other monomers to form heterostructures, we developed a novel precursor to N=9 AGNRs. In collaboration with the Crommie group, long 9-AGNRs and heterostructures were synthesized on a Au(111) surface. The synthetic route developed for the 9-AGNR precursor was designed to be highly modular and thus a variety of other low bandgap GNRs could be accessed from a late-stage intermediate in one step. Using this modular synthesis, we successfully accessed monomers for 15-AGNRs, wide chevron GNRs, and a 9-AGNR with hydrogen bonding groups along the periphery.

The preceding chapters of this thesis have proven the potential of utilizing small molecule precursors as building blocks for atomically precise GNRs. Bottom up synthetic strategies have the powerful capability of "writing-in" desired properties of the resulting GNRs by rational monomer design. In this thesis we have also discussed utilizing modular synthetic strategies to access a variety of different target monomers or GNRs from one sole precursor. In the final chapter, experimental details of relevant compounds and other useful information to the reader are presented.

5.2 Outlook

Looking forward, these late stage modification techniques can be utilized to synthesize atomically precise GNRs with exotic functionalities that are otherwise difficult to access. As a result, the applications of these GNRs are nearly limitless and can range from next generation field effect transistors and spintronic devices to catalysis. With that, the integration of GNRs into next generation electronics still remains a challenge. Low bandgap GNRs are required to fabricate FETs with low Schottky barriers, an issue we have addressed in this dissertation with the synthesis of low bandgap GNR precursors. Surface-assisted synthesized GNRs still need to be transferred from the metallic substrate onto dielectric, a process that is still challenging. Solution synthesized GNRs need to be deposited onto substrates as individual ribbons and subsequently localized and visualized for their integration into devices. While, our development of **Cy_5-cGNR** was a key milestone in the facile localization and visualization of deposited single GNRs, their integration into high performance devices still remains unsolved. However, this idea of late stage functionalization could be applied to other edge and width structures to synthesize Cy_5-labeled low bandgap GNRs better suited for FET applications. Our investigation of conjugating molecular catalysts onto GNRs and previous work in our group on utilizing GNRs as solid supports of nanoparticle catalysis are just the beginning of using functionalized GNRs to enhance catalytic processes. We envision GNRs being applied to enhance the efficiency of a variety of different synthetic transformations.

Chapter 6

Supplementary Information

6.1 Materials and General Methods

Unless otherwise stated, all manipulations of air and/or moisture sensitive compounds were carried out in oven-dried glassware, under an atmosphere of nitrogen. All solvents and reagents were purchased from Alfa Aesar, Spectrum Chemicals, Acros Organics, TCI America, and Sigma-Aldrich and were used as received unless otherwise noted. Organic solvents were dried by passing through a column of alumina and were degassed by vigorous bubbling of N_2 or Ar through the solvent for 20 min. Flash column chromatography was performed on SiliCycle silica gel (particle size 40–63 μm). Thin layer chromatography was carried out using SiliCycle silica gel 60 Å F-254 precoated plates (0.25 mm thick) and visualized by UV absorption. All ^{1}H and ^{13}C NMR spectra were recorded on Bruker AVB-400, AVQ-400, and AV-600 MHz spectrometers, and are referenced to residual solvent peaks ($CDCl_3$ ^{1}H NMR = 7.26 ppm, ^{13}C NMR = 77.16 ppm; CD_2Cl_2 ^{1}H NMR = 5.32 ppm, ^{13}C NMR = 54.00 ppm, Acetone ^{1}H NMR = 2.05 ppm, ^{13}C NMR = 29.84 and 206.26 ppm). EI mass spectrometry was performed on an Autospec Permier (Waters) sector spectrometer in positive ionization mode. ESI mass spectrometry was performed on a Finnigan LTQFT (Thermo) spectrometer in positive ionization mode. MALDI mass spectrometry was performed on a Voyager-DE PRO (Applied Biosystems Voyager System 6322) in positive mode using a matrix of dithranol. Gel permeation chromatography (GPC) was carried out on a LC/MS Agilent 1260 Infinity set up with a guard and two Agilent Polypore 300 x 7.5 mm columns at 35 °C. All GPC analyses were performed on a 0.2 mg/mL solution of polymer in chloroform. An injection volume of 25 μL and a flow rate of 1 mL/min were used. Calibration was based on narrow polydispersity polystyrene standards ranging from M_w = 100 to 4,068,981. Infrared spectroscopy was conducted with a Bruker ALPHA ATR-FTIR. Raman Spectroscopy is completed on a Renishaw inVia spectrometer with 514 nm excitation laser. A K-Alpha Plus with monochromatic Al x-ray source is used for X-Ray Photoelectron Spectroscopy (XPS) and spectra are analyzed using the Advantage software suite. UV-Vis spectroscopic measurements were conducted in a Varian Cary 50 spectrophotometer (Agilent, USA). FTIR measurements were conducted on a Nicolet 6700 using an attenuated total reflectance measurement on a diamond plate.

6.2 Previously Synthesized Compounds

N-pentynyl-Cy5 (**24**);[108] 5,10-dibromo-1,3-diphenyl-2H-cyclopenta[l]phenanthren-2-one (**27**);[53] 1,10-phenanthroline-5,6-diamine (**52**);[109] [Cp*Ir(phen)OH_2][OTf]$_2$ (**55**);[95] 3-bromo-2,2'-bipyridine (**68**);[96] 2,7-dinitrophenanthrene-9,10-dione (**89**);[110] 4-bromo-2,7-dinitrophenanthrene-9,10-dione (**90**);[111] and 14-(6-bromo-[1,1'-biphenyl]-3-yl)-7-(10-bromoanthracen-9-yl)benzo[m]tetraphene (**99**)[101] were synthesized according literature procedures.

6.3 Synthetic Procedures

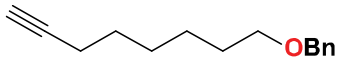

18

((oct-7-yn-1-yloxy)methyl)benzene (**18**) A 100 mL Schlenk flask was charged under N_2 with sodium hydride (95%) (399 mg, 16.6 mmol), and oct-7-yn-1-ol (2.00 g, 15.8 mmol) in dry THF (44 mL). The reaction mixture was cooled to 0 °C, stirred for 30 min, warmed to 24 °C, stirred for an additional 30 min, and then cooled to 0°C. Benzyl bromide (2.85 g, 16.6 mmol) in dry THF (11 mL) was added dropwise. Tetrabutyl ammonium iodide (1.17 g, 3.12 mmol) was added and the reaction mixture was stirred for 18 h at 24 °C. The reaction mixture was poured over an ice bath and exacted with CH_2Cl_2. The organic phases were washed with saturated aqueous NH_4Cl, H_2O, saturated aqueous NaCl, dried over Na_2SO_4, and concentrated on a rotary evaporator Column chromatography (SiO_2; 0–20% EtOAc/hexane) yielded **18** (2.50 g, 11.6 mmol, 73%) as a colorless oil. ^{1}H NMR (400 MHz, CD_2Cl_2, 22 °C) δ = 7.33 (m, 4H), 7.30 – 7.24 (m, 1H), 4.47 (s, 2H), 3.46 (t, *J* = 6.5 Hz, 2H), 2.18 (td, *J* = 7.1, 2.7 Hz, 2H), 1.96 (t, *J* = 2.7 Hz, 1H), 1.64 – 1.57 (m, 2H), 1.55 – 1.49 (m, 2H), 1.42-1.35 (m, 4H) ppm; ^{13}C NMR (101 MHz, CD_2Cl_2, 22 °C) δ = 139.6, 128.8, 128.1, 127.9, 85.2, 73.3, 71.0, 68.5, 30.2, 29.1, 29.1, 26.3, 18.8 ppm; HRMS (EI$^+$) m/z: calcd for $C_{15}H_{19}O$ $[M]^+$ 215.1436, found 215.1434.

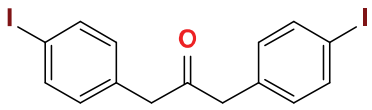

17

1,3-Bis(4-iodophenyl)propan-2-one (**17**) A 100 mL three neck round bottom flask with reflux condenser was charged under N_2 with 1-(bromomethyl)-4-iodobenzne (3.21 g, 10.8 mmol), benzyltriethylammonium chloride (66.8 mg, 0.293 mmol), and NaOH (1.87 g, 46.7 mmol) in H_2O (1.1 mL) and CH_2Cl_2 (26 mL). The reaction mixture was heated to 40 °C. Iron pentacarbonyl (1.10

g, 0.76 mL, 5.61 mmol) was added dropwise and the reaction mixture was stirred for 18 h at 40 °C. The reaction mixture was quenched with a 2 M aqueous HCl solution (20 mL) and filtered through Celite. The product was extracted from the filtrate with CH_2Cl_2, washed with H_2O and saturated aqueous NaCl solution, dried over $MgSO_4$ and concentrated on a rotary evaporator. Column chromatography (SiO_2; 30–50% CH_2Cl_2/hexane) yielded **17** (825 mg, 1.79 mmol, 32%) as a colorless solid. ^{1}H NMR (400 MHz, $CDCl_3$, 22 °C) δ = 7.64 (d, J = 7.9 Hz, 4H), 6.88 (d, J = 7.9 Hz, 4H), 3.66 (s, 4H) ppm; ^{13}C NMR (101 MHz, $CDCl_3$, 22 °C) δ = 204.2, 137.8, 133.3, 131.5, 92.8, 48.6 ppm; FTMS (EI+) m/z: $[C_{15}H_{12}I_2O]^+$ calcd. $[C_{15}H_{12}I_2O]^+$ 461.8978; found 461.8981. Analytical data were in accordance with those previously published.[112]

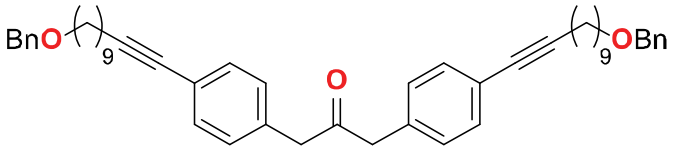

19

1,3-bis(4-(8-(benzyloxy)oct-1-yn-1-yl)phenyl)propan-2-one (**19**) A 100 mL Schlenk flask was charged under N_2 with **17** (1.60 g, 3.46 mmol), CuI (132 mg, 0.693 mmol), and $Pd(PPh_3)_4$ (400 mg, 0.346 mmol) in dry DMF (39 mL) and dry Et_3N (2.2 mL). The reaction mixture was degassed by three freeze-pump-thaw cycles. **18** (2.50 g, 11.43 mmol) in 6 mL degassed dry DMF was added dropwise. The reaction mixture was stirred at 40 °C for 24 h. The reaction mixture was cooled to 24 °C. The reaction mixture was diluted with saturated aqueous NH_4Cl, and extracted with CH_2Cl_2. The combined organic phases were washed with H_2O and saturated aqueous NaCl, dried over $MgSO_4$, and concentrated on a rotary evaporator. Column chromatography (SiO_2; 10% EtOAc/hexane) yielded **19** (1.68 g, 2.63 mmol) as a red oil. ^{1}H NMR (400 MHz, CD_2Cl_2, 22 °C) δ = 7.37 – 7.23 (m, 14H), 7.06 (d, *J* = 8.2 Hz, 4H), 4.47 (s, 4H), 3.71 (s, 4H), 3.48 (t, *J* = 6.5 Hz, 4H), 2.40 (t, *J* = 7.1 Hz, 4H), 1.66 – 1.57 (m, 8H), 1.52 – 1.36 (m, 8H) ppm; ^{13}C NMR (101 MHz, CD_2Cl_2, 22 °C) δ = 205.1, 139.6, 134.1, 132.2, 130.1, 128.8, 128.1, 127.9, 123.4, 91.2, 80.7, 73.3, 71.0, 49.4, 30.3, 29.3, 26.4, 19.9 ppm; HRMS (EI^+) m/z: calcd for $C_{45}H_{50}O_3$ $[M]^+$ 638.3760, found 683.3762.

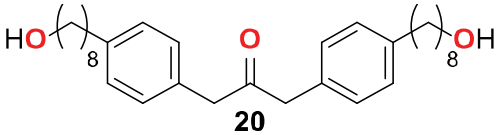

20

1,3-bis(4-(8-hydroxyoctyl)phenyl)propan-2-one (**20**) A 25 mL vial was charged with **19** (1.11 g, 1.74 mmol) and of $Pd(OH)_2$/C (20% wt, 45% wet, 445 mg, 0.349 mmol) in 1:1 EtOAc:EtOH (4 mL). The reaction mixture was degassed with H_2 and stirred under 1 atm H_2 at 24 °C for 48 h. The reaction mixture was filtered over Celite and washed with CH_2Cl_2, EtOAc, EtOH and hot toluene. The filtrate was concentrated on a rotary evaporator. Column chromatography (SiO; 20 – 100%

EtOAc/hexane) yielded **20** (578mg, 1.24 mmol, 71%) as a colorless solid. ^{1}H NMR (400 MHz, CD_2Cl_2, 22 °C) δ = 7.12 (d, *J* = 8.0 Hz, 4H), 7.05 (d, *J* = 8.0 Hz, 4H), 3.67 (s, 4H), 3.62 (t, *J* = 6.6 Hz, 4H), 2.61 – 2.54 (t, *J* = 7.7 Hz, 4H), 1.65 – 1.51 (m, 8H), 1.32 (d, *J* = 2.7 Hz, 16H) ppm; ^{13}C NMR (101 MHz, CD_2Cl_2, 22 °C) δ = 206.5, 141.7, 131.3, 129.5, 128.8, 77.2, 63.1, 48.8, 35.7, 32.9, 31.5, 29.6, 29.5, 29.3, 25.8 ppm; HRMS (ESI-TOF) m/z: $[C_{31}H_{47}O_3]^+$ 467.3520, found 467.3518.

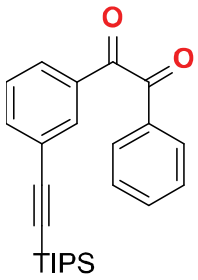

21

3-[(Triisopropylsilyl)ethynyl]benzil (**21**) A 50 mL oven-dried Schlenk flask with reflux condenser was charged under N_2 with 3-Bromobenzil (1.02 g, 3.53 mmol), $Pd(PPh_3)_4$ (127 mg, 0.107 mmol), and CuI (22.0 mg, 0.116 mmol) in degassed THF (10 mL) and Et_3N (10 mL). Triisopropylsilylacetylene (1.95 g, 10.7 mmol) was added dropwise and the reaction mixture was stirred at 80 °C for 14 h. The reaction mixture was filtered through Celite and concentrated on a rotary evaporator. H_2O was added and the product was extracted with CH_2Cl_2. The organic layer was washed with H_2O and saturated aqueous NaCl solution, dried over $MgSO_4$, and concentrated on a rotary evaporator. Column chromatography (SiO_2; 20% CH_2Cl_2/hexane) yielded **21** (1.37 g, 3.51 mmol, 99%) as an orange oil. ^{1}H NMR (400 MHz, $CDCl_3$, 22 °C) δ = 8.10–8.07 (m, 1H), 7.97 (dd, J = 8.2, 1.4 Hz, 2H), 7.90–7.86 (m, 1H), 7.76–7.72 (m, 1H), 7.70–7.64 (m, 1H), 7.56–7.50 (m, 2H), 7.48–7.42 (m, 1H), 1.15–1.10 (m, 21H) ppm; ^{13}C NMR (101 MHz, $CDCl_3$, 22 °C) δ = 194.0, 193.8, 138.2, 135.1, 133.1, 132.9 (2C), 130.0 (2C), 129.7, 129.1 (2C), 129.0, 124.9, 105.3, 93.1, 18.7, 11.3 ppm; FTMS (EI+) m/z: $[C_{25}H_{30}O_2Si]^+$ calcd. $[C_{25}H_{30}O_2Si]^+$ 390.2015; found 390.2018.

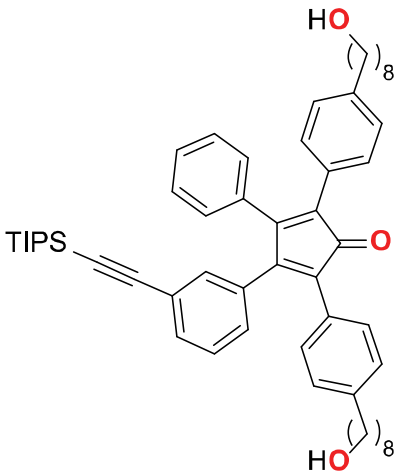

22

2,5-bis(4-(8-hydroxyoctyl)phenyl)-3-phenyl-4-(3-((triisopropylsilyl)ethynyl)phenyl)cyclopenta-2,4-dien-1-one (**22**) A 100 mL three-neck round bottom equipped with a reflux condenser was charged under N_2 with **20** (600 mg, 1.29 mmol) and **21** (502 mg, 1.29 mmol) in *t*BuOH (32 mL). The reaction mixture was warmed to 80 °C. After all the solids had dissolved, tetraethylammonium hydroxide (20% w/v in H_2O, 0.38 mL, 73.2 mg, 0.514 mmol) was added dropwise and the reaction mixture was stirred for 90 min. The reaction mixture was quenched with 2 M aqueous HCl solution (20 mL). The product was extracted with CH_2Cl_2, washed with H_2O and saturated aqueous NaCl solution, dried over $MgSO_4$ and concentrated on a rotary evaporator. Column chromatography (SiO_2; 30-60% CH_2Cl_2/hexane) yielded **22** (724 mg, 0.882 mmol, 67%) as a dark purple foam. ^{1}H NMR (600 MHz, CH_2Cl_2, 22 °C) δ = 7.32 (dt, *J* = 7.7, 1.4 Hz, 1H), 7.28 – 7.23 (m, 1H), 7.23 – 7.18 (m, 2H), 7.15 – 7.04 (m, 9H), 6.99 – 6.91 (m, 4H), 3.58 (td, *J* = 6.7, 1.2 Hz, 4H), 2.56 (td, *J* = 7.9, 5.0 Hz, 4H), 1.54 (m, 12H), 1.32 (m, 16H), 1.06 (m, 21H) ppm; ^{13}C NMR (101 MHz, CD_2Cl_2, 22 °C) δ = 201.3, 154.6, 153.5, 143.4, 143.1, 134.1, 134.0, 133.6, 132.0, 130.5, 129.9, 129.7, 129.0, 128.7, 128.6, 128.6, 128.5, 128.5, 128.5, 126.2, 125.8, 123.7, 107.0, 91.8, 63.4, 36.3, 36.3, 33.4, 31.9, 31.9, 30.0, 29.9, 29.9, 26.3, 19.0, 11.8 ppm; FTMS (ESI-TOF) m/z: $[C_{56}H_{73}O_3Si_1]^+$ calcd. 821.5324; found 821.5315.

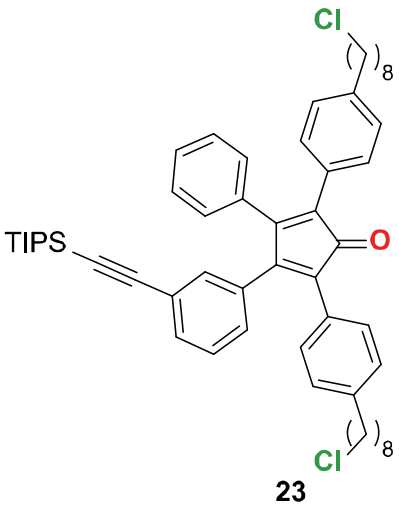

23

2,5-bis(4-(8-chlorooctyl)phenyl)-3-phenyl-4-(3-((triisopropylsilyl)ethynyl)phenyl)cyclopenta-2,4-dien-1-one (**23**) A 10 mL Schlenk flask was charged under N_2 with **22** (300 mg, 0.365 mmol) in anhydrous CH_2Cl_2 (3 mL). The reaction mixture was cooled to 0 °C and $SOCl_2$ (0.1 mL, 1.46 mmol) was added dropwise. Catalytic DMF (0.05 mL) was added to the reaction mixture. The reaction mixture was stirred at 0 °C for 1 hour and then warmed to 24 °C and stirred for 18 h. The reaction mixture was quenched with saturated aqueous $NaHCO_3$ solution (3 mL) and extracted with CH_2Cl_2. The combined organic phases were washed with H_2O, saturated aqueous NaCl solution, dried over $MgSO_4$ and concentrated on a rotary evaporator. Column chromatography (SiO_2; 20 % CH_2Cl_2/hexane) yielded **23** (224 mg, 0.261 mmol, 71 %) as a purple residue. ^{1}H NMR (400 MHz, CH_2Cl_2, 22 °C) δ = 7.32 (dt, *J* = 7.7, 1.4 Hz, 1H), 7.29 – 7.18 (m, 3H), 7.16 – 7.03 (m, 9H), 7.00 – 6.90 (m, 4H), 3.54 (t, *J* = 6.8 Hz, 4H), 2.61 – 2.51 (m, 4H), 1.81 – 1.70 (m, 4H), 1.59 (m, 4H), 1.42 (m, 4H), 1.37 – 1.27 (m, 12H), 1.06 (m, 21H) ppm; ^{13}C NMR (101 MHz, CD_2Cl_2, 22 °C) δ = 200.7, 154.0, 152.9, 142.7, 142.5, 133.5, 133.4, 133.0, 131.4, 129.9, 129.3, 129.2, 128.4, 128.1, 128.1, 128.0, 128.0, 127.9, 127.9, 125.6, 125.2, 123.1, 106.4, 91.2, 45.3, 35.7, 35.7, 32.7, 31.3, 31.2, 29.3, 29.2, 28.8, 26.9, 26.8, 18.4, 11.3 ppm; FTMS (ESI-TOF) m/z: $[C_{56}H_{70}OCl_2NaSi]^+$ calcd. 879.4465; found 879.4473.

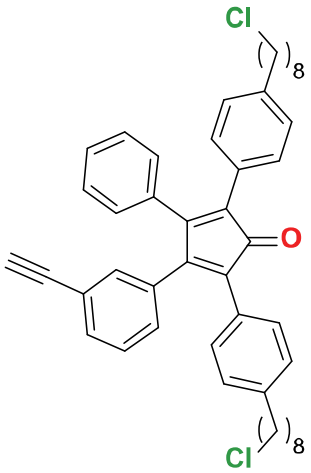

14

2,5-bis(4-(8-chlorooctyl)phenyl)-3-(3-ethynylphenyl)-4-phenylcyclopenta-2,4-dien-1-one (**14**) A 10 mL Schlenk flask was charged under N_2 with **23** (45.0 mg, 0.0524 mmol) in degassed THF (1 mL). AgF (9.98 mg, 0.0787 mmol) was added followed by degassed MeOH (1 mL). The reaction mixture was stirred under N_2 in the dark for 18 h. The reaction mixture was quenched with TFA (1.5 mL) and stirred for 1 hour at 24 °C. The reaction mixture was diluted with ether, washed with H_2O and saturated aqueous NaCl solution, dried over Na_2SO_4 and concentrated on a rotary evaporator. Column chromatography (SiO_2; 0-2 % EtOAc/hexane) yielded **14** (27.1 mg, 0.0386 mmol, 74 %) as a purple residue. ^{1}H NMR (400 MHz, CH_2Cl_2, 22 °C) δ = 7.37 (br d, *J* = 7.7 Hz, 1H), 7.29 – 7.26 (m, 1H), 7.24 – 7.18 (m, 2H), 7.16 – 7.06 (m, 9H), 6.97 – 6.93 (m, 3H), 3.54 (t, *J* = 6.8 Hz, 4H), 3.05 (s, 1H), 2.60 – 2.55 (m, 4H), 1.77 (p, *J* = 6.9 Hz, 4H), 1.67 – 1.56 (m, 4H), 1.47 – 1.38 (m, 4H), 1.37 –1.29 (m, 12H) ppm; ^{13}C NMR (101 MHz, CD_2Cl_2) δ = 201.2, 154.5, 153.4, 143.3, 143.1, 134.5, 133.8, 133.1, 132.4, 130.5, 130.3, 129.8, 129.0, 128.7, 128.7, 128.6, 128.6, 128.4, 126.3, 125.7, 122.5, 83.4, 78.1, 54.5, 54.3, 54.0, 53.8, 53.5, 45.9, 36.2, 33.3, 31.8, 31.8, 30.3, 29.9, 29.8, 29.8, 29.4, 27.4 ppm; FTMS (ESI-TOF) m/z: $[C_{47}H_{50}OCl_2NaSi]^+$ calcd. 723.3131; found 723.3133.

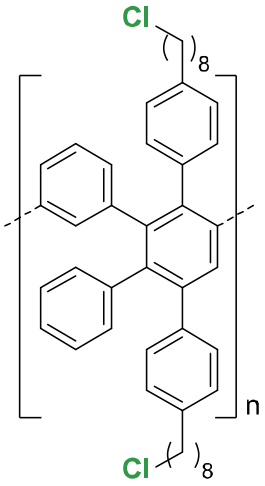

Poly-11

(Poly-1) A 10 mL Schlenk flask was charged under N_2 with **14** (45.3 mg, 0.0645 mmol) in Ph_2O (0.042 mL). The reaction mixture was degassed by three freeze-pump-thaw cycles. The reaction mixture was stirred at 230 °C for 24 h. The reaction mixture was diluted with MeOH and the precipitate was collected via centrifugation. The solid residue was dissolved in THF, triturated with MeOH, and collected via centrifugation to yield **Poly-11** (39.9 mg, 92%) as a colorless solid. The longest polymers were isolated via preparative GPC. ^{1}H NMR (400 MHz, CH_2Cl_2, 22 °C) δ = 7.18 – 6.19 (m, 18H), 3.52 (t, *J* = 6.1 Hz, 4H), 2.68 – 2.30 (m, 4H), 1.81 – 1.68 (m, 4H), 1.64 – 1.08 (m, 20H) ppm.

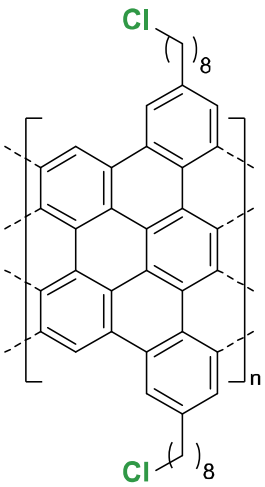

Cl-cGNR

(**Cl-GNR**) A 500 mL Schlenk flask was charged under N_2 with **Poly-11** (10.5 mg) in CH_2Cl_2 (80 mL). A suspension of $FeCl_3$ (212 mg, 1.31 mmol, 7 equiv for one hydrogen to be removed) in $MeNO_2$ (4 mL) was added. The reaction mixture was stirred at 24 °C for 72 h under a continuous stream of N_2. The reaction mixture was quenched with MeOH and filtered. Washing the precipitate

with MeOH (500 mL), 1M HCl (300 mL), H_2O (1000 mL), and THF (500 mL), yielded **Cl-GNR** as a black powder (10.3 mg, 100%). Raman (powder): 1334, 1607, 2654, 2937 cm^{-1}.

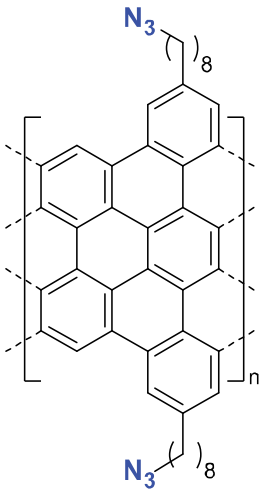

N_3-cGNR

(**N_3-GNR**) A 25 mL vial was charged with **Cl-GNR** (10.6 mg) in DMF (20 mL). The reaction mixture was sonicated for 1.5 hours under N_2. NaN_3 (500 mg, 7.69 mmol) was added and the reaction mixture sonicated for 30 minutes. The reaction mixture was stirred at 60 °C for 18 h under N_2. The reaction mixture was sonicated for 4 hours and stirred at 60 °C for 18 h under N_2. The reaction mixture was sonicated for 1 hour and filtered. Washing the precipitate with H_2O (1000 mL) and THF (500 mL) yielded **N_3-GNR** as a black powder (10.8 mg). Raman (powder): 1329, 1607, 2657, 2934 cm^{-1}.

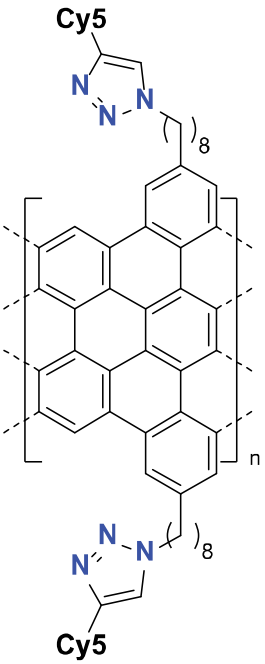

Cy5-cGNR

(**Cy5-GNR**) A 25 mL vial was charged with **N_3-GNR** (5.5 mg), **24** (21.1 mg, 0.0375 mmol), and CuI (60 mg, 0.315 mmol) in DMF (20 mL). The reaction mixture was sonicated for 2 hours and stirred at 60 °C for 18 h under N_2. The reaction mixture was sonicated for 2 hours and stirred for an additional 18 h under N_2. The reaction mixture was sonicated for 2 hours and filtered. The precipitate was washed with acetone (1000 mL), MeOH (1000 ml), H_2O (500 mL), DMF (300 mL), CH_2Cl_2 (300 mL) and THF (500 mL) until the filtrate was completely colorless to yielded **Cy5-GNR** as a black powder (8.5 mg, 59%). Raman (powder): 1329, 1604, 2672, 2928 cm^{-1}.

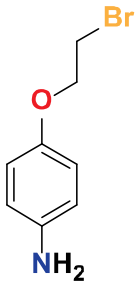

25

4-(2-bromoethoxy)-aniline (**25**) A three neck round bottom flask was charged with 1-(2-bromoethoxy)-4-nitrobenzene (1.21 g, 4.91 mmol), acetic acid (85 mL), and ethanol (85 mL). Iron powder (986 mg, 1.77 mmol) was added and the reaction was stirred at 80 °C for 90 min. The reaction mixture was extracted with CH_2Cl_2. The organic layer was washed with saturated sodium bicarbonate, H_2O, and saturated aqueous NaCl, The crude material was dried over $MgSO_4$, and concentrated on a rotary evaporator. Column chromatography (SiO_2; 40% EtOAc/hexane) yielded **25** (540 mg, 2.50 mmol, 51%) as a light yellow solid. ^{1}H NMR (400 MHz, $CDCl_3$, 22 °C) δ = 6.84 – 6.72 (m, 2H), 6.71 – 6.59 (m, 2H), 4.21 (t, *J* = 6.3 Hz, 2H), 3.59 (t, *J* = 6.3 Hz, 2H); ^{13}C NMR (101 MHz, $CDCl_3$, 22 °C) δ = 151.2 , 140.9 , 116.5 (d, *J* = 4.2 Hz), 69.0 , 29.7; HRMS (ESI-TOF) m/z: $[C_8H_{11}ONBr]^+$ 216.0019, found 216.0017.

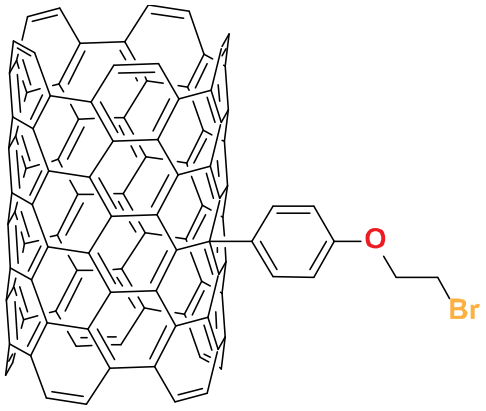

Br-CNT

(**Br-CNT**) Single-walled carbon nanotubes (SWNTs) (6.0 mg, 0.500 mmol) were suspended in ODCB (7.5 mL) and sonicated for 20 min. The reaction mixture was degassed and sonicated for additional 10 min. A degassed solution of **25** (432 mg, 2.00 mmol) in dry CH_3CN (4 mL) was added to the reaction mixture. Isoamyl nitrite (178 mg, 1.50 mmol, 3) was added quickly and the suspension was stirred at 60 °C for 18 h. The reaction was diluted with DMF, filtered, and washed with DMF (500 mL), acetone (300 mL), H_2O (300 mL), hexane (200 mL), EtOAc (200 mL), and CH_2Cl_2 (200 mL) to yield **Br-CNT** as a black powder (7 mg). Raman (powder): 165, 1341, 1589, 1734, 2670 cm^{-1}.

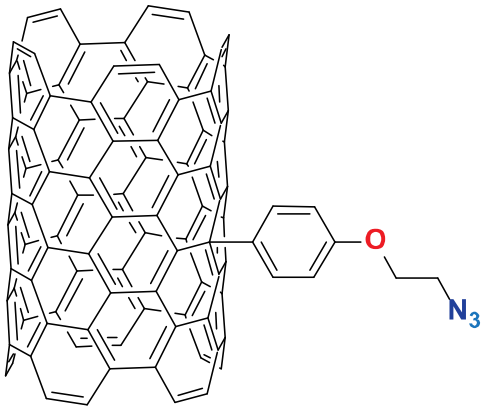

N_3-CNT

(**N_3-CNT**) A 25 mL vial was charged with **Br-CNT** (19.0 mg) in DMF (20 mL) and sonicated for 1 h. NaN_3 (500 mg, 7.69 mmol) was added and the suspension was sonicated for an additional 1 h. The suspension was heated to 60 °C for 18 h. The reaction was sonicated for 5 h and heated to 60 °C for an additional 18 h. The reaction was filtered and washed thoroughly with EtOAc (300

mL), acetone (200 mL), CH_2Cl_2 (200 mL), and hot toluene (100 mL) to yield **N_3-CNT** as a black powder (18.9 mg). Raman (powder): 163, 1339, 1587, 1737, 2665 cm^{-1}.

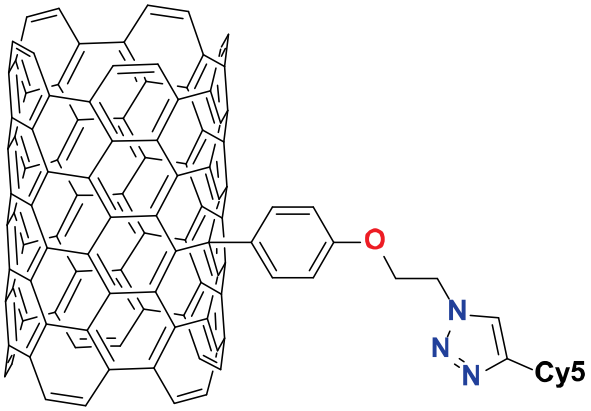

Cy5-CNT

(**Cy5-CNT**) A 25 mL vial was charged with **N_3-CNT** (4.2 mg), **24** (17.0 mg, 0.0323 mmol), and CuI (51.0 mg, 0.268 mmol) in DMF (8 mL) and sonicated for 1 h. The suspension was stirred at 60 °C for 18 h. The reaction was sonicated for 2 hours and stirred at 60 °C for an additional 18 h. The suspension was filtered and washed with EtOAc (300 mL), DMF (300 mL), acetone (200 mL), CH_2Cl_2 (200 mL), and hot toluene (100 mL) to yield **Cy5-CNT** as a black powder (5.0 mg). Raman (powder): 165, 1343, 1587, 1729, 2670 cm^{-1}.

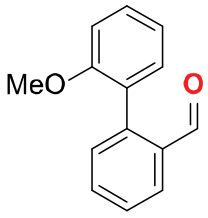

33

2'-methoxy-[1,1'-biphenyl]-2-carbaldehyde (**33**) A 250 mL three-neck round bottom equipped with a reflux condenser was charged under N_2 with 2-bromobenzaldehyde (2.78 g, 15.0 mmol) and $Pd(PPh_3)_4$ (520 mg, 0.45 mmol) in degassed DME (60 mL). A solution of (2-methoxyphenyl)boronic acid (2.81 g, 18.6 mmol) in degassed EtOH (14 mL) was added to the reaction mixture. Then, Na_2CO_3 (3.18 g, 30 mmol) in degassed H_2O (14 mL) was added to the reaction mixture. The reaction mixture was stirred at 92 °C for 18h. The reaction mixture was cooled to 24 °C and diluted with H_2O and extracted with Et_2O. The combined organic phases were washed with saturated aqueous NaCl, dried over Na_2SO_4, and concentrated on a rotary evaporator.

Column chromatography (SiO_2; 20-70 % CH_2Cl_2/hexane) yielded **33** (2.73 g, 12.9 mmol, 86%) as a yellow solid. ^1H NMR (400 MHz, $CDCl_3$, 22 °C) δ = 9.79 (s, 1H), 7.99 (dd, *J* = 7.8, 1.4 Hz, 1H), 7.65 (ddd, *J* = 7.5, 7.5, 1.4 Hz, 1H), 7.48 (dd, *J* = 7.5, 7.5 Hz, 1H), 7.42 (ddd, *J* = 1H), 7.36 (d, *J* = 7.7 Hz, 1H), 7.29 (dd, *J* = 7.4, 1.7 Hz, 1H), 7.09 (dd, *J* = 7..4, 7.4 Hz, 1H), 6.98 (d, *J* = 8.3 Hz, 1H), 3.75 (s, 3H).

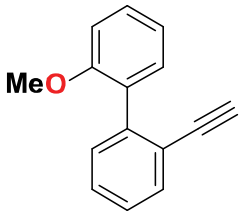

34

2-ethynyl-2'-methoxy-1,1'-biphenyl (**34**) A 25 mL Schlenk flask was charged under N_2 with LDA (2M in THF/n-heptane/ethyl benzene, 3.63 mL, 7.26 mmol) in anhydrous THF (2 mL). The reaction mixture was cooled to −78 °C and Me_3SiCHN_2 (2M in Et_2O, 3.63 mL, 7.26 mmol) was added dropwise. The reaction mixture was stirred at −78 °C for 30 min. **33** (1.27 g, 6.00 mmol) in anhydrous THF (7.5 mL) was added dropwise and the reaction mixture was stirred at 24 °C for 5 hours. The reaction mixture was quenched with H_2O and concentrated AcOH until the reaction mixture stopped bubbling. The reaction mixture was extracted with Et_2O, washed with H_2O and saturated aqueous NaCl, dried over Na_2SO_4, and concentrated on a rotary evaporator. Column chromatography (SiO_2; hexane) yielded **34** (1.17 g, 5.63 mmol, 94%) as a yellow oil. ^1H NMR (600 MHz, $CDCl_3$, 22 °C) δ = 7.60 (d, *J* = 7.67, 1H), 7.42 – 7.33 (m, 3H), 7.33 – 7.28 (m, 2H), 7.03 (ddd, *J* = 8.1, 7.4, 0.9 Hz, 1H), 6.99 (dd, *J* = 8.3, 1.0 Hz, 1H), 3.79 (s, 3H), 2.93 (s, 1H).

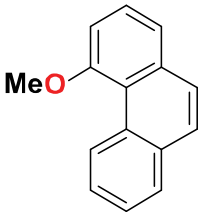

35

4-methoxyphenanthrene (**35**) A 100 mL Schlenk flask was charged under N_2 with **34** (1.59 g, 7.65 mmol) and $PtCl_2$ (203 mg, 0.765 mmol) in anhydrous toluene (38 mL). The reaction mixture was heated to 80 °C and stirred for 24 hours. The reaction mixture was cooled to 24 °C and concentrated on a rotary evaporator. Column chromatography (SiO_2; 10% CH_2Cl_2/hexane) yielded **35** (1.08 g, 5.17 mmol, 68%) as a colorless solid. ^1H NMR (400 MHz, CD_2Cl_2, 22 °C) δ = 9.67 (d, J = 8.5 Hz, 1H), 7.89 (dd, J = 7.7, 1.8 Hz, 1H), 7.83 – 7.68 (m, 2H), 7.68 – 7.49 (m, 4H), 7.20 (dd, J = 7.1, 2.1 Hz, 1H), 4.15 (s, 3H).

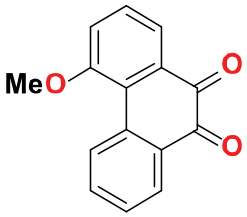

36

4-*methoxyphenanthrene-9,10-dione* (**36**) A 250 mL round bottom flask was charged under N_2 with **35**(677 mg, 3.25 mmol) and $NaIO_4$ (2.30 g, 14.95 mmol) in CH_2Cl_2 and H_2O (34 mL). The reaction mixture was cooled to 0 °C and $RuCl_3 \bullet xH_2O$ (58.9 mg, 0.260 mmol) in MeCN (27 mL) was added dropwise. The reaction mixture was stirred at 0 °C for 1.5 hours. The reaction mixture was diluted with H_2O, extracted with CH_2Cl_2, washed with H_2O and saturated aqueous NaCl, dried over $MgSO_4$ and concentrated on a rotary evaporator. Column chromatography (SiO_2; 50–100% CH_2Cl_2/hexane to 5% EtOAc/CH_2Cl_2) and recrystallization from hot toluene yielded **36** (131 mg, 0.552 mmol, 17%) as orange crystals. ^{1}H NMR (400 MHz, CD_2Cl_2, 22 °C) δ = 8.90 (d, J = 9.0 Hz, 1H), 8.11 (d, J = 7.9 Hz, 1H), 7.79 (d, J = 7.4 Hz, 1H), 7.69 (dd, J = 7.7, 7.7 Hz, 1H), 7.50 – 7.40 (m, 2H), 7.36 (d, J = 8.5 Hz, 1H).

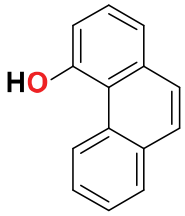

40

phenanthren-4-ol (**40**) A 50 mL Schlenk flask was charged under N_2 with **35** (604 mg, 2.90 mmol) in anhydrous CH_2Cl_2 (18 mL). The reaction mixture was cooled to −78 °C and BBr_3 (0.56 mL, 5.80 mmol) was added dropwise. The reaction mixture was stirred at 24 °C for 18 hours. The reaction mixture was cooled to −78 °C and quenched with slow addition of MeOH (7 mL) with a vent needle. The reaction mixture stirred at 24 °C for 15 minutes and concentrated on a rotary evaporator. Column chromatography (SiO_2; 20% EtOAc/hexane) yielded **40** (404 mg, 2.08 mmol, 72%) as a colorless solid. ^{1}H NMR (400 MHz, CD_2Cl_2, 22 °C) δ = 9.73 – 9.65 (m, 1H), 7.90 (dd, *J* = 7.7, 1.8 Hz, 1H), 7.79 – 7.58 (m, 4H), 7.52 (dd, *J* = 7.8, 1.3 Hz, 1H), 7.45 (dd, *J* = 7.7, 7.7 Hz, 1H), 7.06 (ddd, *J* = 7.6, 1.4, 1.4 Hz, 1H), 6.69 – 6.32 (m, 1H, OH).

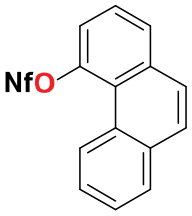

41

phenanthren-4-yl 1,1,2,2,3,3,4,4,4-nonafluorobutane-1-sulfonate (**41)** A 25 mL Schlenk flask was charged under N_2 with **40** (320 mg, 1.65 mmol) in anhydrous CH_2Cl_2 (9.6 mL) and anhydrous Et_3N (3.5 mL). The reaction mixture was cooled to −78 °C and perfluorobutanesulfonyl fluoride (0.37 mL, 1.98 mmol) was added dropwise. The reaction mixture was stirred at −78 °C for 30 minutes and then warmed to 24 °C and stirred for an 18 hours. The reaction mixture was quenched with H_2O, extracted with CH_2Cl_2, washed with H_2O and saturated aqueous NaCl, dried over $MgSO_4$ and concentrated on a rotary evaporator. Column chromatography (SiO_2; 0-10% EtOAc/hexane) yielded **41** (768 mg, 1.62 mmol, 98%). ^{1}H NMR (400 MHz, CD_2Cl_2, 22 °C) δ = 9.22 – 9.14 (m, 1H), 8.00 – 7.92 (m, 2H), 7.85 (d, *J* = 8.8 Hz, 1H), 7.78 (d, *J* = 8.8 Hz, 1H), 7.75 – 7.68 (m, 2H), 7.67 – 7.60 (m, 2H).

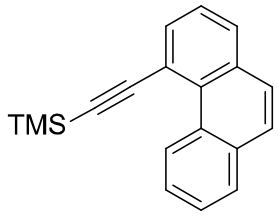

42

trimethyl(phenanthren-4-ylethynyl)silane (**42**) A 50 mL Schlenk flask was charged under N_2 with **41** (900 mg, 1.89 mmol), $Pd(PPh_3)_2Cl_2$ (16 mg, 0.023 mmol), PPh_3 (6 mg, 0.023 mmol), and CuI (4.3 mg, 0.023 mmol) in Et_3N (26 mL). The reaction mixture was degassed by three freeze-pump-thaw cycles. Ethynyltrimethylsilane (0.46 mL, 3.31 mmol) was added. The reaction mixture was stirred at 80 °C for 18 hours. The reaction mixture was cooled to 24 °C and concentrated on a rotary evaporated. Column chromatography (SiO_2; 0–4% EtOAc/hexane) and recrystallization from EtOH yielded **42** (430 mg, 1.57 mmol, 83%) as a colorless solid. ^{1}H NMR (400 MHz, $CDCl_3$, 22 °C) δ = 10.51 – 10.45 (m, 1H), 7.98 – 7.86 (m, 3H), 7.79 – 7.69 (m, 2H), 7.69 – 7.62 (m, 2H), 7.56 – 7.50 (m, 1H), 0.42 (d, *J* = 1.7 Hz, 9H).

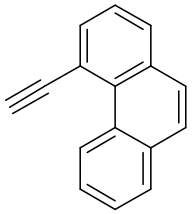

30

4-ethynylphenanthrene (**30**) A 50 mL Schlenk flask was charged under N_2 with **42** (337 mg, 1.23 mmol) in MeOH (34 mL). The reaction mixture was degassed by sparging with N_2 for 20 minutes. K_2CO_3 (689 mg, 4.84 mmol) was added and the reaction mixture was stirred at 24 °C for 16 hours. The reaction was quenched with H_2O, extracted with CH_2Cl_2, washed with saturated aqueous NaCl, dried over $MgSO_4$ and concentrated on rotary evaporator. Recrystallization from EtOH yielded **30** (143 mg, 0.706 mmol, 58%) as off-white crystals. ^{1}H NMR (500 MHz, CD_2Cl_2, 22 °C) δ = 10.37 – 10.32 (m, 1H), 7.97 – 7.90 (m, 3H), 7.82 – 7.72 (m, 2H), 7.70 – 7.64 (m, 2H), 7.56 (dd, *J* = 7.9, 7.3 Hz, 1H), 3.78 (s, 1H).

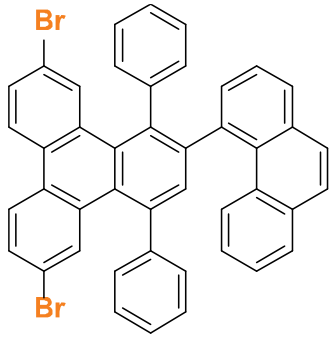

29

6,11-dibromo-2-(phenanthren-4-yl)-1,4-diphenyltriphenylene (**29**) A 25 mL reaction tube was charged under N_2 with **27** (381 mg, 0.706 mmol) and **30** (143 mg, 0.706 mmol) in 2.4 mL degassed *o*-xylene. The reaction mixture was stirred at 160 °C for 4.5 hours. The reaction mixture was cooled to 24 °C and concentrated on a rotary evaporator. Column chromatography (SiO_2; 0-5% EtOAc/hexane) yielded **29** (398 mg, 0.558 mmol, 79%) as an off-white solid. ^{1}H NMR (400 MHz, CD_2Cl_2, 22 °C) δ = 8.31 (dd, *J* = 8.8, 6.4 Hz, 2H), 8.03 (d, *J* = 8.6 Hz, 1H), 7.90 (d, *J* = 2.0 Hz, 1H), 7.81 (dd, *J* = 7.8, 1.5 Hz, 1H), 7.77 ((dd, *J* = 7.8, 1.3 Hz, 1H), 7.73 (s, 1H), 7.71 – 7.63 (m, 3H), 7.60 (dd, *J* = 8.7, 2.0 Hz, 1H), 7.55 – 7.33 (m, 9H), 7.10 (ddd, *J* = 8.6, 7.0, 1.5 Hz, 1H), 7.05 – 6.94 (m, 3H), 6.77 – 6.69 (m, 2H).

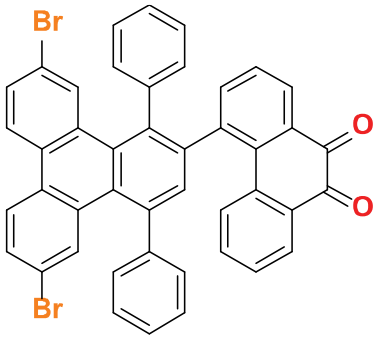

26

4-(6,11-dibromo-1,4-diphenyltriphenylen-2-yl)phenanthrene-9,10-dione (**26**) A 25 mL three-neck round bottom was charged under N_2 with **29** (100 mg, 0.140 mmol) in CH_2Cl_2 (1.3 mL). $NaIO_4$ (163 mg, 0.763 mmol) in H_2O (1.3 mL) was added to the reaction mixture. $RuCl_3$●xH_2O (3.5 mg, 0.015 mmol) in MeCN (0.95 mL) was added to the reaction mixture. The reaction mixture was stirred at 24 °C for 18 hours. The reaction mixture was extracted with CH_2Cl_2, washed with H_2O and saturated aqueous NaCl, dried over $MgSO_4$ and concentrated on rotary evaporator. Column chromatography (SiO_2; 50-100% CH_2Cl_2/hexane) yielded **26** (39 mg, 0.053 mmol, 38%) as an orange solid. Recrystallization from layered MeOH/CH_2Cl gave analytically pure crystals for surface experiments. ^{1}H NMR (400 MHz, CD_2Cl_2, 22 °C) δ = 8.28 (d, *J* = 8.8 Hz, 1H), 8.25 (d, *J* = 8.7 Hz, 1H), 8.02 (dd, *J* = 7.7, 1.5 Hz, 1H), 7.91 (d, *J* = 2.3 Hz, 2H), 7.79 (dd, *J* = 7.6, 1.5 Hz, 1H), 7.74 (dd, *J* = 7.6, 1.5 Hz, 1H), 7.71 – 7.33 (m, 9H), 7.15 (td, *J* = 7.4, 1.2 Hz, 1H), 7.11 – 7.03

(m, 3H), 7.03 – 7.00 (m, 1H), 6.91 (d, *J* = 7.1 Hz, 1H), 6.77 (t, *J* = 7.0 Hz, 1H), 6.08 (d, *J* = 7.7 Hz, 1H).

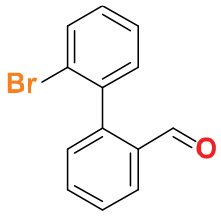

44

2'-bromo-[1,1'-biphenyl]-2-carbaldehyde (**44**) A 250 mL Schlenk flask was charged under N_2 with 2,2'-dibromo-1,1'-biphenyl (4.46 g, 14.3 mmol) in dry THF (86 mL). The reaction mixture was cooled to –78 °C. n-BuLi (2.5M in hexanes, 5.7 mL, 14.3 mmol) was added dropwise over 15 minutes and the reaction mixture was stirred for 15 minutes at -78 °C. DMF (2.6 mL 33.7 mmol) in dry THF (13 mL) was then added dropwise. The reaction mixture was warmed to 24 °C and stirred for 18 h. The reaction mixture was quenched with saturated aqueous NH_4Cl (100 mL) and extracted with CH_2Cl_2. The combined organic phases were washed with H_2O and saturated aqueous NaCl, dried over $MgSO_4$, and concentrated on a rotary evaporator. Column chromatography (SiO_2; 0-2% EtOAc/Hexanes) yielded **44** (3.64 g, 13.9 mmol, 97%) as a colorless viscous oil that solidified into a colorless solid over time. ^{1}H NMR (400 MHz, $CDCl_3$, 22 °C) δ = 9.77 (d, *J* = 0.8 Hz, 1H), 8.00 (dd, *J* = 7.7, 1.5 Hz, 1H), 7.74 – 7.65 (m, 2H), 7.57 (dddd, *J* = 7.6, 7.6, 1.1, 1.1 Hz, 1H), 7.44 (ddd, *J* = 7.5, 7.5, 1.2 Hz, 1H), 7.38 – 7.30 (m, 3H) ppm; ^{13}C {^{1}H} NMR (101 MHz, $CDCl_3$, 22 °C) δ = 191.8, 144.9, 139.5, 134.3, 134.2, 133.2, 132.2, 131.4, 130.3, 129.1, 128.0, 127.8, 124.3, 54.5, 54.3, 54.0, 53.7, 53.5 ppm. FTMS (EI+) m/z: $[C_{13}H_9OBr]^+$ calcd. $[C_{13}H_8OBr]^+$ 258.9759; found 258.9757

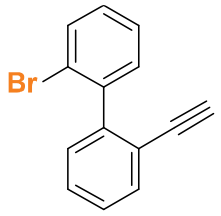

45

2-bromo-2'-ethynyl-1,1'-biphenyl (**45**) A 100 mL Schlenk flask was charged under N_2 with LDA (2 M in THF/n-heptane/ethyl benzene, 8.4 mL, 16.7 mmol) in dry THF (7.2 mL). The reaction mixture was cooled to -78 °C and Me_3SiCHN_2 (2 M in diethyl ether, 8.4 mL, 16.7 mmol) was

added dropwise. The reaction mixture was stirred at – 78 °C for 30 min. **44** (3.64 g, 13.9 mmol) in dry THF (17 mL) was added dropwise and the reaction mixture was stirred at 24 °C for 5 h. The reaction mixture was quenched with H_2O and AcOH until bubbling stopped, and extracted with CH_2Cl_2. The combined organic phases were washed with H_2O and saturated aqueous NaCl, dried over $MgSO_4$, and concentrated on a rotary evaporator. Column chromatography (SiO_2; 0-2 % CH_2Cl_2/hexanes yielded **45** (3.51 g, 13.7 mmol, 98%) as a colorless oil. ^{1}H NMR (400 MHz, $CDCl_3$, 22 °C) δ = 7.68 (dd, *J* = 8.0, 1.3 Hz, 1H), 7.62 (dd, *J* = 7.8, 1.4 Hz, 1H), 7.47 – 7.36 (m, 3H), 7.33 (dd, *J* = 7.6, 1.9 Hz, 1H), 7.30 – 7.24 (m, 2H), 3.01 (s, 1H) ppm; ^{13}C {^{1}H} NMR (101 MHz, $CDCl_3$, 22 °C) δ = 144.20, 141.49, 133.02, 132.72, 131.35, 129.89, 129.28, 128.59, 127.83, 127.07, 123.47, 121.84, 82.28, 80.49 ppm; FTMS (EI+) m/z: $[C_{14}H_9Br]^+$ calcd. $[C_{14}H_9Br]^+$ 255.9888; found 255.9889.

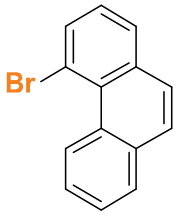

46

4-bromophenanthrene (**46**) A 50 mL Schlenk flask was charged under N_2 with **45** (1.16 g, 4.51 mmol) and $PtCl_2$ (120 mg, 0.451 mmol) in dry toluene (22 mL). The reaction mixture was stirred at 80 °C for 24 h. The reaction was cooled to 24 °C and concentrated on a rotary evaporator. Column chromatography (SiO_2; hexanes) yielded **46** (623 mg, 2.42 mmol, 54 %) as a colorless solid. ^{1}H NMR (400 MHz, $CDCl_3$, 22 °C) δ = 10.07 – 10.01 (m, 1H), 8.01 (dd, *J* = 7.6, 1.4 Hz, 1H), 7.95 – 7.90 (m, 1H), 7.88 (dd, *J* = 7.8, 1.4 Hz, 1H), 7.77 (d, *J* = 8.8 Hz, 1H), 7.72 – 7.64 (m, 3H), 7.41 (dd, *J* = 7.7, 7.7 Hz, 1H); ^{13}C NMR (101 MHz, CD_2Cl_2, 22 °C) δ = 135.74, 135.26, 133.96, 130.22, 129.48, 129.08, 128.99, 128.72, 127.70, 127.63, 127.25, 127.15, 125.90, 119.91. (EI+) m/z: $[C_{14}H_9Br]^+$ calcd. $[C_{14}H_9Br]^+$ 255.9888; found 255.9892.

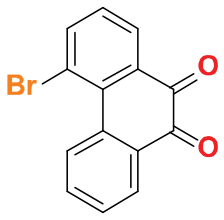

47

4-bromophenanthrene-9,10-dione (**47**) A 100 mL three-neck round bottom equipped with a reflux condenser was charged under N_2 with **46** (360 mg, 1.40 mmol) in AcOH (32 mL). The reaction

mixture was heated to 80 °C. CrO_3 (560 mg, 5.60 mmol) in 80% AcOH (5.4 mL) was added dropwise over 45 minutes. The reaction mixture was stirred at 80 °C for 20 minutes. The reaction mixture was poured into ice water, filtered, and washed with water. Column chromatography (SiO_2; 50-70 % CH_2Cl_2/hexane) yielded **47** (178 mg, 0.621 mmol, 44%). ^{1}H NMR (400 MHz, $CDCl_3$, 22 °C) δ = 8.83 (d, *J* = 8.2 Hz, 1H), 8.12 (dd, *J* = 7.6, 1.4 Hz, 2H), 8.00 (dd, *J* = 8.0, 1.5 Hz, 1H), 7.75 (ddd, *J* = 8.9, 7.6, 1.6 Hz, 1H), 7.52 (ddd, *J* = 7.5, 7.5, 1.1 Hz, 1H), 7.31 (dd, *J* = 7.8, 7.8 Hz, 1H). ^{13}C NMR (101 MHz, $CDCl_3$, 22 °C) δ = 182.05, 181.99, 142.93, 136.00, 135.47, 135.08, 132.97, 131.23, 130.01, 129.96, 129.83, 129.60, 129.35, 120.65. FTMS (EI+) m/z:

$[C_{14}H_7BrO_2]^+$ calcd. $[C_{14}H_7BrO_2]^+$ 285.9633; found 285.9629.

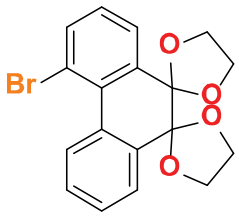

48

4'-bromodispiro[[1,3]dioxolane-2,9'-phenanthrene-10',2''-[1,3]dioxolane] (**48**) A 25 mL round bottom equipped with a Dean-Stark trap was charged with **47** (111 mg, 0.386 mmol), *p*-toluenesulfonic acid monohydrate (11 mg, 0.06 mmol), and ethylene glycol (0.9 mL, 16.1 mmol) in toluene (15 mL). The reaction mixture was stirred at 135 °C for 20 hours. The reaction mixture was cooled to 24 °C and extracted with EtOAc, washed with H_2O, and saturated aqueous NaCl, dried over Na_2SO_4 and concentrated on rotary evaporator. Column chromatography (SiO_2; 60% CH_2Cl_2/hexane with 1% EtOAc) yielded **48** (134 mg, 0.0356 mmol, 92%) as a colorless foamy solid. ^{1}H NMR (500 MHz, CD_2Cl_2, 22 °C) δ = 8.58 – 8.53 (dd, *J* = 7.8, 1.6 Hz, 1H), 7.77 (dd, *J* = 7.9, 1.3 Hz, 1H), 7.72 – 7.70 (m, 2H), 7.51 – 7.44 (m, 2H), 7.26 (dd, *J* = 7.8, 7.8 Hz, 1H), 4.46 – 3.79 (m, 4H), 3.75 – 3.25 (m, 4H).

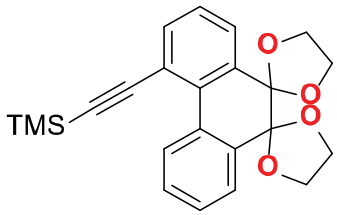

49

(dispiro[[1,3]dioxolane-2,9'-phenanthrene-10',2''-[1,3]dioxolan]-4'-ylethynyl)trimethylsilane (**49**) A 24 mL Schlenk flask was charged with **48** (133 mg, 0.354 mmol) and CuI (6.7 mg, 0.035 mmol), in piperdine (2.2 mL) and Et_3N (6.6 mL). The reaction mixture was degassed by three freeze-pump-thaw cycles. $Pd(PPh_3)_4$ (41 mg, 0.035 mmol) was added and the reaction mixture was stirred for15 minutes. Ethynyltrimethylsilane (0.06 mL, 0.432 mmol) was added dropwise and the

reaction mixture was stirred at 80 °C for 16 hours. The reaction mixture was cooled to 24 °C and filtered over Celite. The filtrate was concentrated on a rotary evaporator. Column chromatography (SiO_2; 20% EtOAc/hexane) yielded **49** (136 mg, 0.346 mmol, 98%) as a brown foamy solid. ^1H NMR (600 MHz, CD_2Cl_2, 22 °C) δ = 9.01 – 8.97 (m, 1H), 7.73 – 7.69 (m, 2H), 7.65 (dd, *J* = 7.7, 1.5 Hz, 1H), 7.46 – 7.42 (m, 2H), 7.35 (dd, *J* = 7.7, 7.7 Hz, 1H), 4.28 – 4.05 (m, 4H), 3.64 – 3.43(m, 4H), 0.26 (s, 9H).

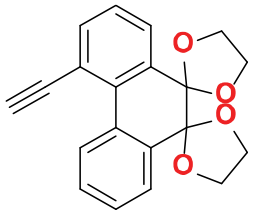

50

4'-ethynyldispiro[[1,3]dioxolane-2,9'-phenanthrene-10',2''-[1,3]dioxolane] (**50**) A 100 mL three neck round bottom was charged with **49** (136 mg, 0.346 mmol) in 1:1 CH_2Cl_2/MeOH (20 mL). The reaction mixture was degassed by sparging with N_2 for 15 minutes. K_2CO_3 (71.7 mg, 0.519 mmol) was added and the reaction mixture was stirred at 24 °C for 2 hours. The reaction mixture was quenched with H_2O and extracted with CH_2Cl_2, washed with saturated aqueous NaCl, dried over Na_2SO_4 and concentrated on rotary evaporator. Column chromatography (SiO_2; 20% EtOAc/hexane) yielded **50** (74.7 mg, 0.233 mmol, 67%) as a colorless foamy solid. ^1H NMR (600 MHz, CD_2Cl_2, 22 °C) δ = 8.95 – 8.91 (m, 1H), 7.76 – 7.68 (m, 3H), 7.49 – 7.44 (m, 2H), 7.37 (dd, *J* = 7.7, 7,7 Hz, 1H), 4.27 – 4.05 (m, 4H), 3.63 – 3.45 (m, 4H), 3.43 (s, 1H).

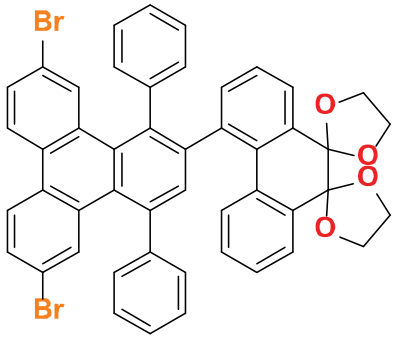

51

4'-(6,11-dibromo-1,4-diphenyltriphenylen-2-yl)dispiro[[1,3]dioxolane-2,9'-phenanthrene-10',2''-[1,3]dioxolane] (**51**) A 5 mL sealable reaction tube was charged under N_2 with **27** (121 mg, 0.224 mmol) and **50** (71.7 mg, 0.224 mmol) in *o*-xylene. The reaction mixture was degassed, sealed under N_2 and stired at 160 °C for 4 hours. The reaction mixture was cooled to 24 °C and concentrated on rotary evaporator. Column chromatography (SiO_2; 1:1:8 CH_2Cl_2/EtOAc/hexane) yielded **51** (141.7 mg, 0.170 mmol, 76%) as a yellow solid. ^1H NMR (400 MHz, CD_2Cl_2, 22 °C)

δ = 8.26 (d, *J* = 8.8 Hz, 1H), 8.23 (d, *J* = 8.7 Hz, 1H), 7.93 – 7.67 (m, 3H), 7.64 (dd, *J* = 7.7, 1.6 Hz, 2H), 7.60 – 7.25 (m, 10H), 7.12 – 7.00 (m, 3H), 6.98 – 6.89 (m, 2H), 6.87 – 6.66 (m, 3H), 4.30 – 4.09 (m, 3H), 3.86 (s, 2H), 3.61 – 3.44 (m, 3H), 3.30 (s, 2H).

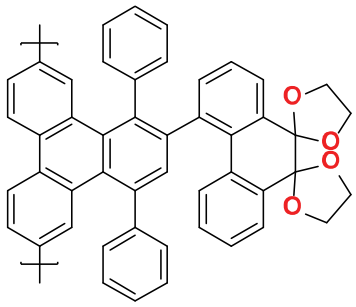

Poly-12

(**Poly-12**)A 25 mL sealable reaction tube was charged with $Ni(COD)_2$ (31.5 mg, 0.093 mmol), bipyridine (14.5 mg, 0.093 mmol), and COD (0.017 mL, 0.093 mmol) in anhydrous DMF (1 mL) in an Ar glovebox. The reaction mixture was stirred at 55 °C for 30 minutes under Ar. **51** (20.0 mg, 0.025 mmol) in anhydrous toluene (4 mL) was added to the reaction mixture under Ar and stirred at 80 °C for 2 days. The reaction mixture was cooled to 24 °C and quenched with excess MeOH (10 mL). The reaction mixture was filtered and washed with MeOH, H_2O, 1M NaOH, and 1:1 1M NaOH/MeOH. The solid was washed with $CHCl_3$ and the filtrate was concentrated on rotary evaporator to yield a yellow solid. The polymer was further purified by precipitation from 1:2 $CHCl_3$/MEOH to yield **Poly-12** (14.6 mg, 0.020 mmol, 90%) as a yellow solid. ^1H NMR (400 MHz, $CDCl_3$, 22 °C) δ = 8.53 – 7.27 (m, 12H), 7.27 – 6.18 (m, 12H), 4.48 – 2.95 (m, 8H).

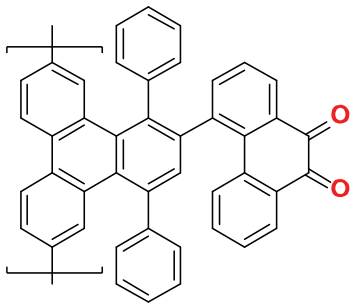

Poly-13

(**Poly-13**) A 20 mL vial was charged with **Poly-12** (14.6 mg, 0.02 mmol) in CH_2Cl_2 (5 mL). The reaction mixture was cooled to 0 °C and 70% $HClO_4$ (0.2 mL) was added dropwise to the reaction mixture. The reaction mixture was stirred at 0 °C for 2 hours. CH_2Cl_2 (2 mL) was added after 30 minutes to help with solubility. The reaction mixture was quenched with H_2O and extracted with CH_2Cl_2, washed with saturated aqueous NaCl and concentrated on a rotary evaporator. The solid residue was dissolved in CH_2Cl_2, triturated with MeOH, and collected via centrifugation to yield

Poly-3 (10.4 mg, 0.018 mmol, 89%) as a foamy orange solid. ^{1}H NMR (400 MHz, $CDCl_3$, 22 °C) δ = 8.51 – 7.31 (m, 12H), 7.28 – 5.59 (m, 12H).

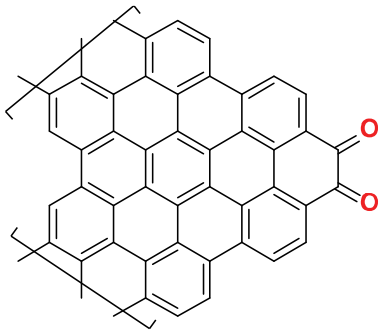

q-CGNR

(**q-CGNR**) A 50 mL Schlenk flask was charged under N_2 with **Poly-13** (9.7 mg, 0.016 mmol) and DDQ (30.5 mg, 0.13 mmol) in anhydrous CH_2Cl_2 (17 mL). TfOH (0.14 mL, 1.65 mmol) was added to the reaction mixture dropwise at 24 °C. The reaction mixture was stirred at 45 °C for 2 days. The reaction mixture was cooled to 24 °C and quenched with saturated aqueous K_2CO_3 and filtered. The black precipitate was washed with H_2O, MeOH, CH_2Cl_2, 2M HCl, acetone, and hexane. The black precipate was suspended in $CHCl_3$/toluene via sonication and filtered again. The solid was washed with $CHCl_3$, toluene, NMP, and acetone to yield **q-CGNR** (8.3 mg, 91%) as a black solid. Raman (powder) 1317, 1602, 2627, 2944, 3211 cm^{-1}.

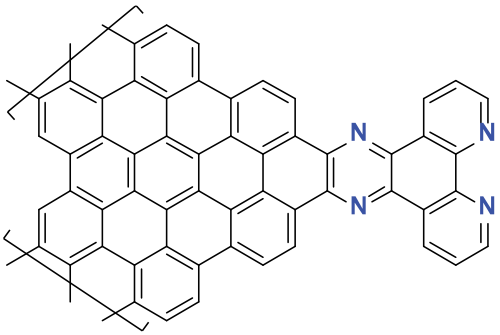

Phen-CGNR

(**Phen-CGNR**) A 3-neck round bottom equipped with a reflux condenser was charged under N_2 with **q-CGNR** (18 mg) in anhydrous pyridine (5 mL). The reaction mixture was sonicated for 1 hour under N_2 and degassed by sparging with N_2 for 30 minutes. **52** (180 mg, 0.85 mmol) in anhydrous pyridine (15 mL) was added to the reaction mixture. The reaction mixture was degassed by sparging for 30 minutes and sonicated under N_2 for 1 hour. The reaction mixture was stirred at 120 °C for 18 hours under N_2. The reaction mixture was sonicated for 2 hours under N_2 and stirred at 120 °C for 18 hours under N_2. The reaction mixture was sonicated for 2 hours under N_2 and stirred at 120 °C for an additional 18 hours under N_2. After 3 days, the reaction mixture was cooled to 24 °C and filtered. Washing the precipitate with hot DMSO, pyridine, hot DMF, MeCN, MeOH,

EtOH, 1M HCl, 1M KOH, H_2O, THF, CH_2Cl_2, EtOAc, Acetone, and hexane yielded a black powder. The solid was suspended in DMSO via sonication and filtered and washed with hot DMSO, pyridine, hot DMF, MeCN, MeOH, EtOH, 1M HCl, 1M KOH, H_2O, THF, CH_2Cl_2, EtOAc, Acetone, and hexane to yield **Phen-CGNR** (22.9 mg, 98%) as a black powder. Raman (powder) 1323, 1603 cm^{-1}.

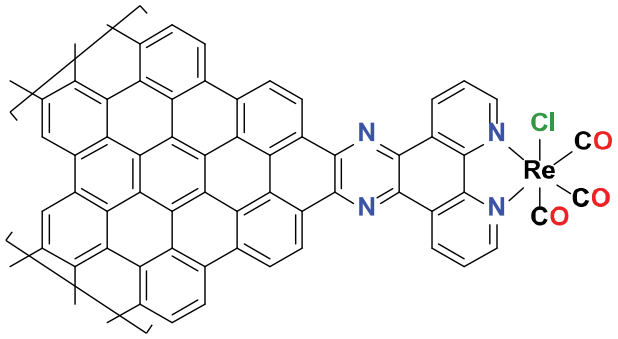

Re-CGNR

(**Re-CGNR**) A three neck round bottom flask equipped with a reflux condenser was charged with **Phen-CGNR** (9.7 mg) in toluene (20 mL). The reaction mixture was sonicated for 1.5 hours. Then $Re(CO)_5Cl$ (100 mg, 0.276 mmol) in toluene (10 mL) was added to the reaction mixture. The reaction mixture was degassed by sparging with N_2 for 30 minutes. The reaction mixture as sonicated for 30 minutes and stirred at 110 °C for 18 hours. The reaction mixture was sonicated for 2 hours and stirred at 110 °C for an additional 18 hours. The reaction mixture was cooled to 24 °C, filtered, and washed with hot toluene, hot DMSO, hot EtOH, CH_2Cl_2, Acetone, EtOAc, and hexane to yield **Re-CGNR** (13 mg, 95%) as a black powder. Raman (powder) 1313, 1607, 2613, 2913, 3200 cm^{-1}.

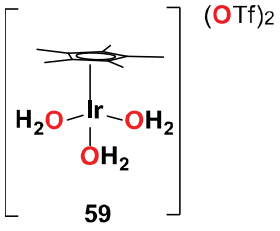

59

$[IrCp^*(OH_2)_3](OTf)_2$ (**59**) A 25 mL vial was charged under N_2 with pentamethylcyclopentadienyliridium(III) chloride dimer (34.5 mg, 0.043 mmol) and AgOTf (56 mg, 0.217 mmol) in degassed H_2O (1.75 mL). The reaction mixture was stirred at 24 °C for 18 hours. The reaction mixture was filtered and the filtrate was evaporated to dryness to yield **59** (70 mg, > 100% due to H_2O residue) as a yellow solid which was used without further purification.

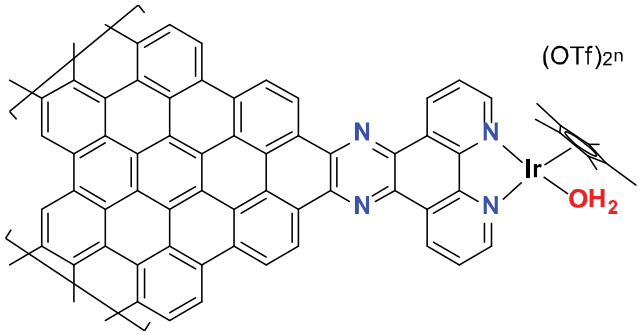

Ir-CGNR

(**Ir-CGNR**) A 100 mL Schlenk flask was charged with **Phen-CGNR** (19 mg) in H_2O (40 mL). The reaction mixture as sonicated for 30 minutes and degassed by sparging with N_2 for 30 minutes. Then **59** (185 mg, 0.267 mmol) in degassed H_2O (5 mL) was added to the reaction mixture. The reaction mixture was degassed for an additional 30 minutes by sparging with N_2 and sonicated for 1 hour under N_2. The reaction mixture was stirred at 24 °C for 18 hours under N_2. The reaction mixture was sonicated for 1 hour under N_2 and stirred at 24 °C for 18 hours. The reaction mixture was filtered and the solid was washed with H_2O, diethyl ether, and hexane to yield **Ir-CGNR** (18.5 mg, lost material during transfer off filter paper) as a black powder. Raman (powder) 1325, 1605 cm^{-1}.

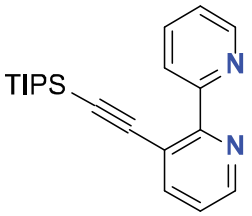

69

3-((triisopropylsilyl)ethynyl)-2,2'-bipyridine (**69**) A 50 mL round bottom flask was charged with **68** (250mg, 1.06 mmol) in DMSO (15 mL). ((triisopropylsilyl)ethynyl)copper (651 mg, 2.66 mmol) was added and the reaction mixture was stirred at 100 °C for 30 minutes. The reaction mixture was quenched by pouring into ice water. The product was extracted with CH_2Cl_2, washed with saturated aqueous NH_4Cl, H_2O, and saturated aqueous NaCl, dried over $MgSO_4$ and concentrated on a rotary evaporator. Column chromatography (SiO_2; 10% EtOH/hexane) yielded as a dark green oil. The product was then sonicated in hexane and filtered. The filtrate was concentrated on a rotary evaporator. The product was then stirred in diethyl ether and EDTA with concentrated aqueous NH_3 to remove copper contamination and extracted with diethyl ether, washed with 2M NaOH, H_2O, and saturated aqueous NaCl, dried over Na_2SO_4 and concentrated on a rotary evaporator to yield **69** (111 mg, 0.330 mmol, 31%). ^1H NMR (300 MHz, CD_2Cl_2, 22 °C) δ = 8.67 (dd, J = 4.9, 1.8, 1H), 8.61 (dd, J = 4.8, 1.7 Hz, 1H), 7.96 – 7.86 (m, 2H), 7.78 (ddd,

J = 7.7, 7.7, 1.8 Hz, 1H), 7.36 – 7.24 (m, 2H), 1.05 (m, 21H). FTMS (ESI-TOF) m/z: $[C_{21}H_{29}N_2Si]^+$ calcd. 337.2095 found 337.2098.

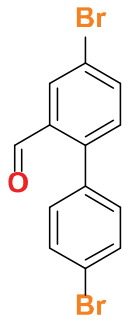

72

4,4'-dibromo-[1,1'-biphenyl]-2-carbaldehyde (**72**) A 100 mL 3-neck round bottom flask equipped with a reflux condenser was charged under N_2 with 5-bromo-2-iodobenzaldehyde (500 mg, 1.61 mmol), 4-bromophenylboronic acid (388 mg, 1.93 mmol), $Pd(PPh_3)_4$ (56 mg, 0.048 mmol), and K_2CO_3 (445 mg, 3.22 mmol) in degassed 8:1:1 toluene/H_2O/EtOH (64 mL). The reaction mixture was stirred at 100 °C for 18 h. The reaction mixture was quenched with H_2O, extracted with CH_2Cl_2, washed with H_2O, saturated aqueous NH_4Cl and saturated aqueous NaCl, dried over $MgSO_4$ and concentrated on a rotary evaporator. Column chromatography (SiO_2; 0-40% CH_2Cl_2/hexane) yielded **72** (284 mg, 0.834 mmol. 52%) as a colorless solid. ^{1}H NMR (300 MHz, $CDCl_3$, 22 °C) δ = 9.88 (s, 1H), 8.13 (d, *J* = 2.2 Hz, 1H), 7.75 (dd, *J* = 8.2, 2.2 Hz, 1H), 7.65 – 7.57 (m, 2H), 7.30 (d, *J* = 8.2 Hz, 1H), 7.25 – 7.20 (m, 2H).

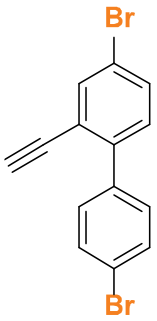

64

4,4'-dibromo-2-ethynyl-1,1'-biphenyl (**64**) A 10 mL Schlenk flask was charged under N_2 with LDA (2M in THF/ n-heptane/ethyl benzene, 0.47 mL, 0.941 mmol) in anhydrous THF (1.3 mL). The reaction mixture was cooled to -78 °C and Me_3SiCHN_2 (2 M in diethyl ether, 0.47 mL, 0.941 mmol) was added dropwise. The reaction mixture was stirred at – 78 °C for 30 min. **72** (267 mg, 0.784 mmol) in dry THF (4 mL) was added dropwise and the reaction mixture was stirred at 24

°C for 5 h. The reaction mixture was quenched with H_2O and AcOH until bubbling stopped, and extracted with CH_2Cl_2. The combined organic phases were washed with H_2O and saturated aqueous NaCl, dried over $MgSO_4$, and concentrated on a rotary evaporator. Column chromatography (SiO_2; hexane) yielded **64** (192 mg, 0.57 mmol, 73%) as a colorless solid. ^{1}H NMR (300 MHz, CD_2Cl_2, 22 °C) δ = 7.76 (d, *J* = 2.1 Hz, 1H), 7.60 – 7.53 (m, 3H), 7.48 – 7.41 (m, 2H), 7.24 (d, *J* = 8.3 Hz, 1H), 3.17 (s, 1H). FTMS (EI+) m/z: $[C_{14}H_8Br_2]^+$ calcd. $[C_{14}H_8Br_2]^+$ 335,8972; found 335.8973.

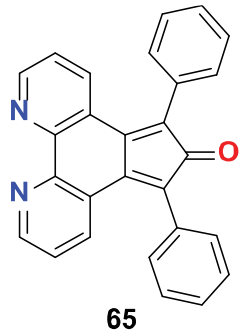

65

5,7-diphenyl-6H-cyclopenta[f][1,10]phenanthrolin-6-one (**65**) A 10 mL Schlenk flask was charged under N_2 with 1,10-phenanthrene-5,6-dione (105 mg, 0.5 mmol) and 1,3-diphenylacetone (105 mg, 0.5 mmol) in anhydrous EtOH (5 mL). The reaction mixture was heated to 70 °C and then one drop of DBU was added. The reaction mixture was stirred at 70 °C for 3 hours. The reaction mixture was then rapidly cooled to −20 °C for 1 hour causing a blue/green solid to precipate out. The reaction mixture was filtered and washed with cold EtOH to yield **65** (31 mg, 0.08 mmol, 16%) as a blue/green solid. The product was immediately used in the next step without further purification. ^{1}H NMR (600 MHz, CD_2Cl_2, 22 °C) δ = 8.61 (dd, *J* = 4.5, 1.7 Hz, 2H), 7.78 (dd, *J* = 8.1, 1.7 Hz, 2H), 7.50 – 7.42 (m, 6H), 7.39 – 7.35 (m, 4H), 6.99 (dd, *J* = 8.1, 4.6 Hz, 2H).

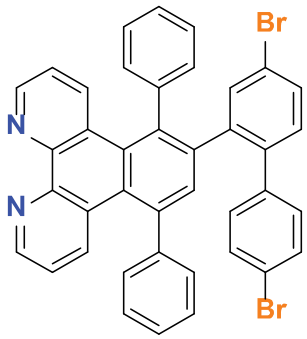

63

6-(4,4'-dibromo-[1,1'-biphenyl]-2-yl)-5,8-diphenylbenzo[f][1,10]phenanthroline (**63**) A 25 mL sealable reaction tube was charged under N_2 with **64** (53 mg, 0.156 mmol) and **65** (55 mg, 0.142

mmol) in degassed *o*-xylene (2 mL).The reaction mixture was stirred at 165 °C for 4 hours under N_2. The reaction mixture was concentrated on a rotary evaporator, sonicated in hot hexanes and filtered. The resulting solid was sonicated in hot MeOH and filtered to yield **63** (42 mg, 0.061 mmol, 43%) as a light tan solid. ^{1}H NMR (600 MHz, CD_2Cl_2, 22 °C) δ = 8.88 (dd, *J* = 4.3, 1.6 Hz, 1H), 8.76 (dd, *J* = 4.2, 1.6 Hz, 1H), 8.05 (dd, *J* = 8.5, 1.6 Hz, 1H), 7.77 (d, *J* = 2.1 Hz, 1H), 7.75 (s, 1H), 7.57 (dd, *J* = 8.6, 1.6 Hz, 2H), 7.52 – 7.42 (m, 3H), 7.42 – 7.26 (br m, 1H), 7.25 – 7.11 (m, 4H), 7.11 – 7.03 (m, 3H), 7.00 (d, *J* = 8.3 Hz, 1H), 6.90 (dd, *J* = 8.6, 4.2 Hz, 1H), 6.82 (t, *J* = 7.5 Hz, 1H), 6.52 – 6.43 (m, 2H), 5.95 (d, *J* = 7.6 Hz, 1H). ^{13}C NMR (151 MHz, CD_2Cl_2, 22 °C) δ = 149.9, 149.4, 147.9, 147.8, 143.8, 142.0, 140.4, 139.7, 139.5, 139.1, 138.9, 138.0, 137.2, 137.0, 135.1, 134.5, 132.4, 131.6, 131.4, 131.3, 131.3, 131.1, 131.1, 123.0, 129.6, 129.4, 128.7, 128.4, 128.2, 127.4, 121.8, 121.8, 121.4, 121.2. FTMS (EI+) m/z: $[C_{40}H_{24}N_2Br_2]^+$ calcd. $[C_{40}H_{24}N_2Br_2]^+$ 692.0286; found 692.0298.

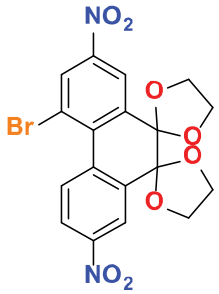

91

4'-bromo-2',7'-dinitrodispiro[[1,3]dioxolane-2,9'-phenanthrene-10',2''-[1,3]dioxolane] (**91**) A 100 mL round bottom was charged under N_2 with **90** (1.30 g, 3.46 mmol) in toluene (23 mL). Ethylene glycol (3.87 mL, 69.27 mmol) and *p*TsOH●H_2O (98.5 mg, 0.518 mmol) was added and the reaction mixture was refluxed at 130 °C for 18 h with a Dean-Stark trap. The cooled reaction mixture was filtered and washed with cold MeOH and the solids were collected. In order to increase the yield, the filtrate was concentrated on a rotary evaporator. The crude material was diluted with CH_2Cl_2 and washed with H_2O and saturated aqueous NaCl solution, dried over $MgSO_4$ and concentrated on a rotary evaporator. Column chromatography (SiO_2; 20 % EtOAc/hexane) yielded **91**. The products were combined to give **91** (1.23 g, 2.64 mmol, 76%) as a colorless solid. ^{1}H NMR (400 MHz, $CDCl_3$, 22 °C) δ = 8.81 (d, *J* = 8.8 Hz, 1H), 8.69 – 8.59 (m, 3H), 8.37 (dd, *J* = 8.9, 2.5 Hz, 1H), 4.60 – 3.98 (m, 4H), 3.74 – 3.30 (m, 4H). ^{13}C NMR (151 MHz, $CDCl_3$, 22 °C) δ = 148.68, 148.03, 138.03, 137.46, 136.44, 135.88, 131.59, 130.67, 123.75, 122.01, 121.42, 121.00, 91.54, 90.99, 63.49 (br), 59.71 (br). HRMS (EI^+) *m/z*: $[C_{18}H_{13}BrN_2O_8]^+$ calcd for $[C_{18}H_{13}BrN_2O_8]^+$ 463.9855; found 463.9856.

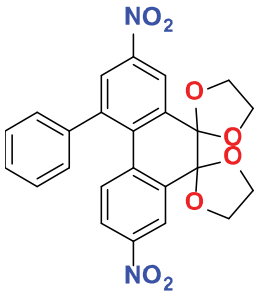

92

2',7'-dinitro-4'-phenyldispiro[[1,3]dioxolane-2,9'-phenanthrene-10',2''-[1,3]dioxolane] (**92**) A 250 mL three-neck round bottom equipped with reflux condenser was charged under N_2 with **91** (1.59 g, 3.42 mmol), phenylboronic acid (1.25 g, 10.26 mmol), K_2CO_3 (1.42 g, 10.26 mmol), and $Pd(PPh_3)_4$ (197 mg, 0.171 mmol) in degassed toluene (80 mL) and degassed H_2O (20 mL). The reaction mixture was stirred at 100 °C for 18 h. The reaction mixture was diluted with CH_2Cl_2 and washed with H_2O and saturated aqueous NaCl solution, dried over $MgSO_4$, and concentrated on a rotary evaporator. Column chromatography (SiO_2; (70 % CH_2Cl_2/hexane) yielded **92** (1.38 g, 2.99 mmol, 87%) as a pale yellow solid. ^{1}H NMR (400 MHz, CD_2Cl_2, 22 °C) δ = 8.59 (d, *J* = 2.5 Hz, 1H), 8.53 (d, *J* = 2.5 Hz, 1H), 8.31 (d, *J* = 2.5 Hz, 1H), 7.79 (dd, *J* = 8.8, 2.5 Hz, 1H), 7.71 – 7.08 (m, 6H), 4.27 (br s, 4H), 3.60 (br s, 4H). ^{13}C NMR (101 MHz, $CDCl_3$, 22 °C) δ = 148.2, 147.8, 143.0, 140.2, 137.5, 137.2, 136.0, 135.9, 131.9, 129.6, 128.9, 128.0, 123.1, 121.9, 121.1, 91.7, 91.3, 61.4. HRMS (EI^+) *m/z*: $[C_{24}H_{18}N_2O_8]^+$ calcd for $[C_{24}H_{18}N_2O_8]^+$ 462.1063; found 462.1065.

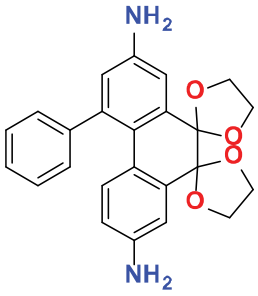

93

4'-phenyldispiro[[1,3]dioxolane-2,9'-phenanthrene-10',2''-[1,3]dioxolane]-2',7'-diamine (**93**) A 100 mL round bottom was charged with **92** (500 mg, 1.08 mmol) and Pd/C (10% Pd, 230 mg, 0.216 mmol) in 1:1 EtOAc:EtOH (30 mL). The reaction was degassed with H_2 and stirred under 1 atm H_2 at 24 °C for 24 h. The reaction mixture was filtered over Celite and washed with CH_2Cl_2, EtOAc, EtOH and hot toluene. The filtrate was concentrated on a rotary evaporator. The crude material was sonicated in a minimum amount of CH_2Cl_2 (3-4 mL), filtered and washed with hexanes to yield **93** (416 mg, 1.03 mmol, 96%) as an orange solid. ^{1}H NMR (300 MHz, $CDCl_3$, 22 °C) δ = 7.40-7.26 (m, 5H), 7.09 (d, *J* = 2.6 Hz, 1H), 7.00 (d, *J* = 2.6 Hz, 1H), 6.66 (d, *J* = 2.6 Hz, 1H), 6.56 (d, *J* = 8.6 Hz, 1H), 6.24 (dd, *J* = 8.6, 2.7 Hz, 1H), 4.17 (br s, 4H), 3.69 (br s, 4H). ^{13}C NMR (151 MHz, CD_2Cl_2, 22 °C) δ = 146.0, 145.7, 144.3, 141.0, 135.0, 133.9, 131.0, 127.3,

124.1, 123.2, 120.1, 115.0, 112.1, 112.0, 93.5, 93.0. HRMS (ESI-TOF) *m/z*: $[C_{24}H_{22}N_2O_4]^+$ calcd for $[C_{24}H_{23}N_2O_4]^+$ 403.1652; found 403.1648

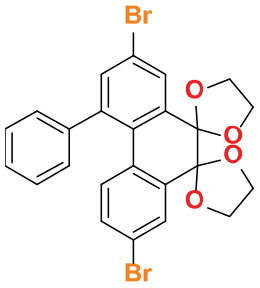

94

2',7'-dibromo-4'-phenyldispiro[[1,3]dioxolane-2,9'-phenanthrene-10',2''-[1,3]dioxolane] (**94**) A 25 mL vial was charged with **93** (393 mg, 0.976 mmol) in 48% HBr (0.98 mL) and MeCN (0.20 mL). The reaction mixture was cooled to −5 °C and $NaNO_2$ (168 mg, 2.44 mmol) in H_2O (0.45 mL) was added dropwise. The reaction mixture was stirred at −5 °C for 40 minutes and was then added dropwise to a solution of CuBr (560 mg, 3.91 mmol) in 48% HBr (7.7 mL) at −5 °C. The reaction mixture was stirred at −5 °C for 1 hour, stirred at 24 °C for 2 hours, stirred at 50 °C for 1 hour and at 24 °C for 18 hours. The reaction mixture was quenched by pouring into an ice bath and concentrated aqueous NH_4OH was added until the pH was 10. The reaction mixture was filtered and washed with H_2O. Column chromatography (SiO_2; 0 – 4% EtOAc/hexane) yielded **94** (379 mg, 0.714 mmol, 73%) as a colorless solid. ^{1}H NMR (300 MHz, CD_2Cl_2, 22 °C) δ = 7.87 (d, *J* = 2.2 Hz, 1H), 7.79 (d, *J* = 2.3 Hz, 1H), 7.55 (d, *J* = 2.2 Hz, 1H), 7.50 - 7.09 (m, 5H), 7.05 (dd, *J* = 8.7, 2.3 Hz, 1H), 6.73 (d, *J* = 8.6 Hz, 1H), 4.18 (m, 4H), 3.59 (m, 4H). ^{13}C NMR (151 MHz, CD_2Cl_2, 22 °C) δ = 142.8, 141.9, 136.6, 136.5, 135.8, 132.3, 131.8, 131.7, 130.6, 129.5, 129.1, 128.3, 122.7, 122.5, 92.6, 92.1, 62.3, 60.8. HRMS (EI^+) *m/z*: $[C_{24}H_{18}Br_2O_4]^+$ calcd for $[C_{24}H_{18}Br_2O_4]^+$ 527.9572; found 527.9573.

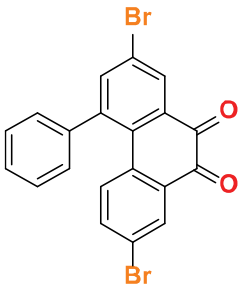

87

2,7-dibromo-4-phenylphenanthrene-9,10-dione (**87**) A 100 mL two-neck round bottom was charged with **94** (370 mg, 0.698 mmol) in CH_2Cl_2 (48 mL). The reaction mixture was cooled to 0 °C and 70% $HClO_4$ (3.4 mL) was added dropwise. The reaction mixture was gradually warmed to 24 °C over 2 hours. The reaction mixture was stirred at 24 °C for 3 hours and monitored by TLC.

The reaction mixture was quenched with H_2O, extracted with CH_2Cl_2, and washed with H_2O and saturated aqueous NaCl solution, dried over $MgSO_4$, and concentrated on a rotary evaporator. Column chromatography (SiO_2; benzene) yielded **87** (309 mg, 0.698 mmol, 99%) as an orange solid. ^{1}H NMR (400 MHz, CD_2Cl_2, 22 °C) δ = 8.25 (d, *J* = 2.3 Hz, 1H), 8.13 (d, *J* = 2.3 Hz, 1H), 7.78 (d, *J* = 2.3 Hz, 1H), 7.50 – 7.42 (m, 3H), 7.37 – 7.27 (m, 3H), 6.86 (d, *J* = 8.7 Hz, 1H). ^{13}C NMR (101 MHz, $CDCl_3$, 22 °C) δ = 180.3, 180.3, 143.6, 142.2, 140.4, 137.5, 134.7, 132.8, 132.8, 132.7, 132.4, 132.0, 129.8, 128.9, 123.6, 123.6, 77.5, 77.2, 76.8. HRMS (EI$^+$) *m/z*: $[C_{20}H_{10}Br_2O_2]^+$ calcd for $[C_{20}H_{10}Br_2O_2]^+$ 439.9048; found 439.9054.

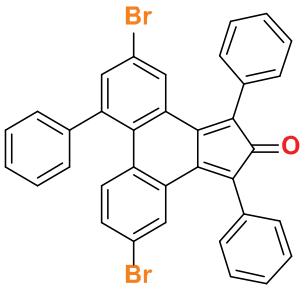

80

5,10-dibromo-1,3,7-triphenyl-2H-cyclopenta[l]phenanthren-2-one (**80**) A 10 mL Schlenk flask was charged under N_2 with **87** (50.0 mg, 0.113 mmol) and diphenylacetone (20.0 mg, 0.0951 mmol) in anhydrous EtOH (2.2 mL). DBU (7.4 µL) was added dropwise and the reaction mixture was stirred at 80 °C for 5 minutes. The reaction mixture was rapidly cooled to 0 °C and 2 M aqueous HCl was added. The reaction mixture was filtered and washed with H_2O and dried under vacuum to yield **80** (60.5 mg) as a green solid. The product was used immediately without further purification. FTMS (MALDI) m/z: $[C_{35}H_{20}Br_2O]^+$, calcd. $[C_{35}H_{20}Br_2O]$ 613.9803; found 614.1481.

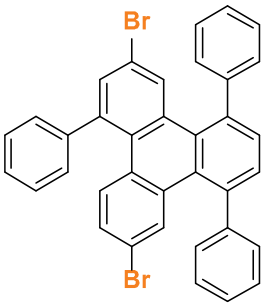

81

3,10-dibromo-1,5,8-triphenyltriphenylene (**81**) A 5 mL sealable tube was charged under N_2 with **80** (35 mg) and ethynyltrimethylsilane in degassed *o*-xylene (0.5 mL). The reaction mixture was stirred 145 °C for 18 h. The reaction mixture was concentrated on a rotary evaporator. Column chromatography (SiO_2; 20% CH_2Cl_2/hexane) yielded the TMS-functionalized product **81*** (23 mg, 0.34 mmol) as an orange solid.

A 10 mL Schlenk flask was charged under N_2 with **81*** (23 mg, 0.34 mmol) in anhydrous THF (1 mL). TBAF (1 M in THF, 0.1 mL) was added dropwise and the reaction mixture was stirred at 24 °C for 40 minutes. The reaction mixture was quenched with MeOH and concentrated on a rotary evaporator. Column chromatography (SiO_2; 20% CH_2Cl_2/hexane), followed by sonication in MeOH and filtration yielded **81** (10.2 mg, 0.0166 mmol, 35% over 3 steps) as a colorless solid. Recrystallization from CH_2Cl_2/MeOH gave analytically pure crystals for surface experiments. ^{1}H NMR (400 MHz, CD_2Cl_2, 22 °C) δ = 7.79 (d, *J* = 2.1 Hz, 1H), 7.63 (dd, *J* = 4.1, 2.4 Hz, 3H), 7.59 – 7.54 (m, 2H), 7.54 – 7.33 (m, 14H), 7.26 (d, *J* = 8.8 Hz, 1H), 6.91 (dd, *J* = 8.8, 2.1 Hz, 1H). ^{13}C NMR (151 MHz, CD_2Cl_2, 22 °C) δ = 144.1, 143.6, 143.4, 142.2, 139.6, 139.0, 134.2, 134.0, 133.7, 132.5, 131.7, 131.6, 131.5, 131.3, 131.2, 131.0, 130.3, 130.0, 129.9, 129.8, 129.7, 129.6, 129.1, 128.6, 128.2, 128.1, 127.9, 120.1, 120.0. HRMS (EI$^+$) *m*/*z*: $[C_{36}H_{22}Br_2]^+$ calcd for $[C_{36}H_{22}Br_2]^+$ 612.0088; found 612.0083.

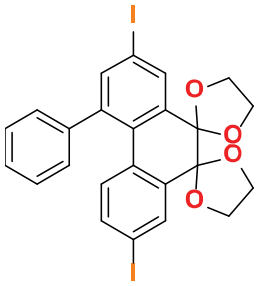

95

2',7'-diiodo-4'-phenyldispiro[[1,3]dioxolane-2,9'-phenanthrene-10',2''-[1,3]dioxolane] (**95**) A 25 mL vial was charged with **93** (200 mg, 0.497 mmol) in HCl (2 M, 6 mL) and MeCN (6 mL). The reaction mixture was cooled to −5 °C and $NaNO_2$ (88 mg, 1.25 mmol) in H_2O (2.4 mL) was added dropwise. The reaction mixture was stirred at −5 °C for 30 minutes. KI (1.98 g, 11.93 mmol) was slowly added to the reaction mixture. The reaction mixture was stirred at 24 °C for 18 hours. The reaction mixture was extracted with CH_2Cl_2, washed with saturated aqueous $Na_2S_2O_3$, H_2O, and saturated aqueous NaCl solution, dried over $MgSO_4$, and concentrated on a rotary evaporator. Column chromatography (SiO_2; 5– 10% EtOAc/hexane) yielded **95** (191 mg, 0.306 mmol, 62%) as a pale yellow solid. ^{1}H NMR (300 MHz, CD_2Cl_2, 22 °C) δ = 8.11 (d, *J* = 2.0 Hz, 1H), 8.04 (d, *J* = 2.0 Hz, 1H), 7.81 (d, *J* = 2.0 Hz, 1H), 7.62 – 6.99 (m, 6H), 6.65 (d, *J* = 8.5 Hz, 1H), 4.23 (m, 4H), 3.65 (m, 4H). ^{13}C NMR (151 MHz, CD_2Cl_2, 22 °C) δ = 142.6, 142.5, 141.6, 137.6, 136.4, 135.7, 135.5, 135.0, 132.5, 132.3, 131.2, 129.6 (br), 129.6 (br), 94.3, 94.0, 92.4, 91.9, 62.0 (br). HRMS (EI$^+$) *m*/*z*: $[C_{24}H_{18}I_2O_4]^+$ calcd for $[C_{24}H_{18}I_2O_4]^+$ 623.9295; found 623.9298.

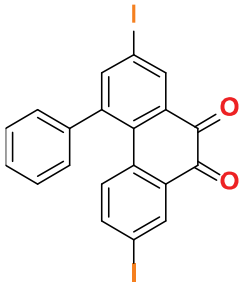

96

2,7-diiodo-4-phenylphenanthrene-9,10-dione (**96**) A 100 mL two-neck round bottom was charged with **95** (191 mg, 0.306 mmol) in CH_2Cl_2 (21 mL). The reaction mixture was cooled to 0 °C and 70% $HClO_4$ (2.2 mL) was added dropwise. The reaction mixture was gradually warmed to 24 °C over 2 hours and monitored by TLC. The reaction mixture was quenched with H_2O, extracted with CH_2Cl_2, and washed with H_2O and saturated aqueous NaCl solution, dried over $MgSO_4$, and concentrated on a rotary evaporator. Column chromatography (SiO_2; 5 – 10 % EtOAc/hexane) yielded **96** (162 mg, 0,303 mool, 99%) as a red-orange solid. ^1H NMR (600 MHz, CD_2Cl_2, 22 °C) δ = 8.45 (d, *J* = 2.1 Hz, 1H), 8.33 (d, *J* = 2.1 Hz, 1H), 8.00 (d, *J* = 2.1 Hz, 1H), 7.51 – 7.45 (m, 4H), 7.35 – 7.31 (m, 2H), 6.72 (d, *J* = 8.6 Hz, 1H). ^{13}C NMR (151 MHz, $CDCl_3$, 22 °C) δ = 180.2, 180.1, 148.1, 143.4, 143.3, 140.3, 138.8, 138.4, 135.3, 133.4, 132.6, 132.6, 131.9, 129.7, 128.9, 128.8, 95.0, 95.0, 77.4, 77.2, 76.9. HRMS (EI^+) *m/z*: $[C_{20}H_{10}I_2O_2]^+$ calcd for $[C_{20}H_{10}I_2O_2]^+$ 535.8770; found 535.8774.

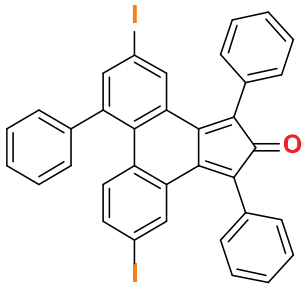

97

5,10-diiodo-1,3,7-triphenyl-2H-cyclopenta[l]phenanthren-2-one (**97**) A 10 mL Schlenk flask was charged under N_2 with **96** (60.6 mg, 0.113 mmol) and diphenylacetone (20.0 mg, 0.0951 mmol) in anhydrous EtOH (2.2 mL). DBU (0.02 mL) was added dropwise and the reaction mixture was stirred at 80 °C for 5 minutes. The reaction mixture was rapidly cooled to 0 °C and 2 M aqueous HCl was added. The reaction mixture was filtered and washed with H_2O and dried under vacuum to yield **97** (71.2 mg) as a green solid. The product was used immediately without further

purification. FTMS (MALDI) m/z: $[C_{35}H_{20}I_2O]^+$, calcd. $[C_{35}H_{20}I_2O + C_9H_{16}N_2]$ 862.0916; found 862.5525.

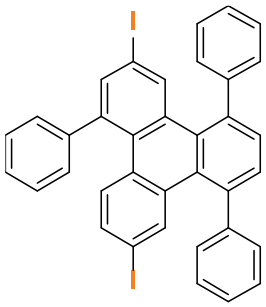

98

3,10-diiodo-1,5,8-triphenyltriphenylene (**98)** A 5 mL sealable tube was charged under N_2 with **97** (71 mg, 0.100 mmol) and ethynyltrimethylsilane (0.6 mL, 4.33 mmol) in degassed *o*-xylene (1.5 mL). The reaction mixture was stirred 145 °C for 18 h. The reaction mixture was concentrated on a rotary evaporator. Column chromatography (SiO_2; 20% CH_2Cl_2/hexane) yielded the TMS-functionalized product **98*** (39 mg, 0.055 mmol) as an orange solid.

A 10 mL Schlenk flask was charged under N_2 with **98*** (39 mg, 0.055 mmol) in anhydrous THF (1.5 mL). TBAF (1 M in THF, 0.2 mL) was added dropwise and the reaction mixture was stirred at 24 °C for 1 h. The reaction mixture was quenched with MeOH and concentrated on a rotary evaporator. Column chromatography (SiO_2; 10 – 20% CH_2Cl_2/hexane), followed by sonication in MeOH and filtration yielded **98** (24.1 mg, 0.0.340 mmol, 30% over 3 steps) as a colorless solid. Recrystallization from $CHCl_3$/EtOH gave analytically pure crystals for surface experiments. ^{1}H NMR (600 MHz, CD_2Cl_2, 22 °C) δ = 7.99 (d, *J* = 1.8 Hz, 1H), 7.84 (d, *J* = 1.7 Hz, 1H), 7.65 – 7.58 (m, 3H), 7.57 – 7.52 (m, 2H), 7.53 – 7.37 (m, 11H), 7.36 – 7.32 (m, 2H), 7.13 – 7.07 (m, 2H). ^{13}C NMR (151 MHz, CD_2Cl_2, 22 °C) δ = 144.2, 143.6, 143.3, 142.1, 139.5, 139.3, 139.00, 138.9, 138.0, 134.3, 133.9, 133.6, 131.6, 131.3, 131.2, 130.9, 130.8, 130.3, 130.0, 129.9, 129.8, 129.7, 129.6, 129.6, 129.2, 128.2, 128.0, 91.7, 91.7. HRMS (EI^+) *m/z*: $[C_{36}H_{22}I_2]^+$ calcd for $[C_{36}H_{22}I_2]^+$ 707.9811; found 707.9809.

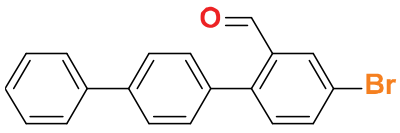

102

4-bromo-[1,1':4',1''-terphenyl]-2-carbaldehyde (**102**) A 50 mL two-neck round bottom equipped with a reflux condenser was charged under N_2 with 5-bromo-2-iodobenzaldehyde (1.00 g, 3.22 mmol), 4-biphenylboronic acid (669 mg, 3.38 mmol), K_2CO_3 (480 mg, 3.47 mmol) and

$PdCl_2(PPh_3)_2$ in degassed DME (11 mL) and degassed H_2O (1.3 mL). The reaction mixture was stirred at 80 °C for 18 h. The reaction mixture was diluted with CH_2Cl_2 and washed with H_2O and saturated aqueous NaCl, dried over $MgSO_4$, and concentrated on a rotary evaporator. Column chromatography (SiO_2; 10% CH_2Cl_2/hexane) yielded **102** (823 mg, 2.45 mmol, 76%) as a colorless solid. ^{1}H NMR (300 MHz, $CDCl_3$, 22 °C) δ = 9.99 (s, 1H), 8.17 (d, *J* = 2.1 Hz, 1H), 7.78 (dd, *J* = 8.2, 2.2 Hz, 1H), 7.75 – 7.68 (m, 2H), 7.68 – 7.62 (m, 2H), 7.52 – 7.36 (m, 6H). ^{13}C NMR (151 MHz, $CDCl_3$, 22 °C) δ = 190.8, 144.1, 141.4, 140.0, 136.4, 135.4, 135.0, 132.4, 130.6, 130.4, 129.0, 127.8, 127.3, 127.1, 122.3. HRMS (EI^+) *m/z*: $[C_{19}H_{13}BrO]^+$ calcd for $[C_{19}H_{13}BrO]^+$ 336.0150; found 336.0154.

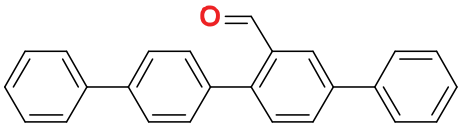

103

[1,1':4',1'':4'',1'''-quaterphenyl]-2''-carbaldehyde (**103**) A 50 mL two-neck round bottom equipped with a reflux condenser was charged under N_2 with **102** (470 mg, 1.39 mmol), phenylboronic acid (187 mg, 1.53 mmol) and $Pd(PPh_3)_4$ in degassed DME (10 mL) and degassed aqueous Na_2CO_3 (2 M, 10 mL). The reaction mixture was stirred at 80 °C for 18 h. The reaction mixture was cooled to 24 °C, filtered, washed with H_2O and the precipitate was collected. Column chromatography (SiO_2; 0 – 50% CH_2Cl_2/hexane) yielded **103** as a colorless solid (438 mg, 1.31 mmol, 94%). ^{1}H NMR (400 MHz, $CDCl_3$, 22 °C) δ = 10.11 (s, 1H), 8.27 (d, *J* = 2.0 Hz, 1H), 7.94 (dd, *J* = 8.0, 2.1 Hz, 1H), 7.78 – 7.67 (m, 6H), 7.62 (d, *J* = 8.0 Hz, 1H), 7.56 – 7.47 (m, 6H), 7.44 – 7.37 (m, 2H). ^{13}C NMR (101 MHz, $CDCl_3$, 22 °C) δ = 192.5, 144.5, 141.3, 140.9, 140.4, 139.6, 136.5, 134.2, 132.2, 131.5, 130.7, 129.1, 129.1, 128.1, 127.84, 127.4, 127.3, 127.2, 126.2. HRMS (EI^+) *m/z*: $[C_{25}H_{18}O]^+$ calcd for $[C_{25}H_{18}O]^+$ 334.1358; found 334.1357.

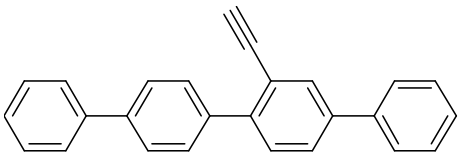

104

2''-ethynyl-1,1':4',1'':4'',1'''-quaterphenyl (**104**) A 10 mL Schlenk flask was charged under N_2 with LDA (2M in THF/n-heptane/ethyl benzene, 0.36 mL) in anhydrous THF (1 mL). The reaction mixture was cooled to −78 °C and Me_3SiCHN_2 (2M in diethyl ether, 0.36 mL) was added dropwise. The reaction mixture as stirred at −78 °C for 30 min. **103** (200 mg, 0.598 mmol) in anhydrous THF (3 mL) was added dropwise at −78 °C and the reaction was stirred at 24 °C for 5 h. The reaction

mixture was quenched with AcOH and H_2O until bubbling stopped, extracted with CH_2Cl_2, washed with H_2O and saturated aqueous NaCl solution, dried over Na_2SO_4, and concentrated on a rotary evaporator. Column chromatography (SiO_2; 5% CH_2Cl_2/hexane) yielded **104** (157 mg, 0.474 mmol, 79%) as a colorless solid. ^{1}H NMR (600 MHz, CD_2Cl_2, 22 °C) δ = 7.90 (d, *J* = 2.0 Hz, 1H), 7.77 – 7.65 (m, 9H), 7.53 (d, *J* = 8.0 Hz, 1H), 7.48 (td, *J* = 7.7, 3.1 Hz, 4H), 7.39 (dt, *J* = 9.8, 7.4 Hz, 2H), 3.19 (s, 1H). ^{13}C NMR (151 MHz, $CDCl_3$, 22 °C) δ = 142.8, 140.9, 140.5, 140.2, 139.8, 138.9, 132.8, 130.2, 129.8, 129.0, 128.9, 127.9, 127.9, 127.5, 127.3, 127.1, 126.9, 120.9, 83.3, 80.5. HRMS (EI$^+$) *m/z*: $[C_{26}H_{18}]^+$ calcd for $[C_{26}H_{18}]^+$ 330.1409; found 330.1415

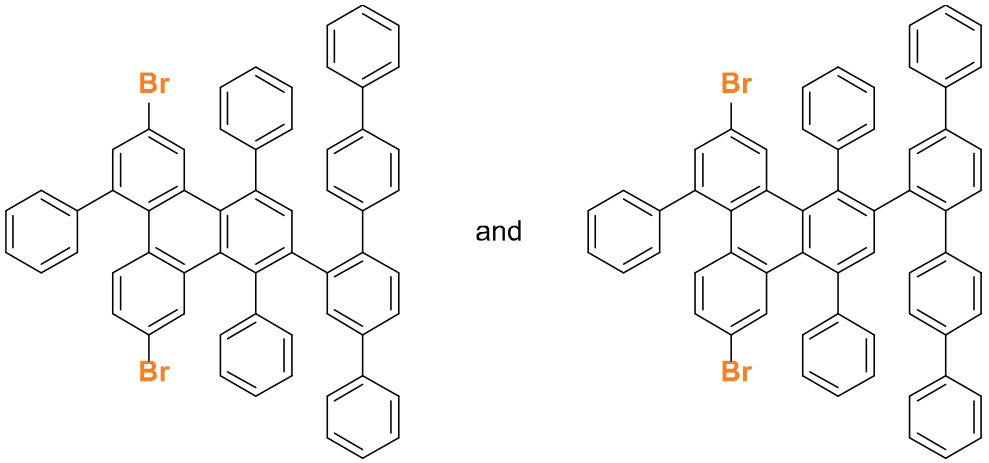

82 mixture of two isomers

2-([1,1':4',1'':4'',1'''-quaterphenyl]-2''-yl)-6,11-dibromo-1,4,9-triphenyltriphenylene (**82**) A 5 mL sealable tube was charged under N_2 with **80** (61 mg, 0.098 mmol) and **104** (47 mg, 0.142 mmol) in degassed *o*-xylene (1 mL). The reaction mixture was stirred 145 °C for 4 hours. The reaction mixture was concentrated on a rotary evaporator. Column chromatography (SiO_2; 20% CH_2Cl_2/hexane) yielded **82** (15 mg, 0.016 mmol, 17%) as a colorless solid and mixture of two isomers. Vapor diffusion recrystallization from MeOH/*o*-xylene yielded isomer **82A**. Recrystallization from layered MeOH/*o*-xylene yielded isomer **82B**. ^{1}H NMR (400 MHz, CD_2Cl_2, 22 °C, mixture of 2 isomers) δ = 7.87 – 7.81 (m, 3H), 7.78 (d, *J* = 2.0 Hz, 1H), 7.72 – 7.64 (m, 6H), 7.64 – 7.56 (m, 2H), 7.55 – 7.41 (m, 14H), 7.41 – 7.29 (m, 10H), 7.28 – 7.17 (m, 9H), 7.18 – 7.04 (m, 5H), 6.96 – 6.77 (m, 6H), 6.20 (s, 1H). ^{13}C NMR (151 MHz, CD_2Cl_2, 22 °C) δ = 143.9, 143.5, 143.3, 143.3, 142.1, 142.0, 141.6, 141.5, 141.2, 141.2, 141.1, 140.8, 140.7, 140.4, 140.4, 140.3, 140.3, 140.0, 140.0, 139.8, 139.6, 139.5, 138.7, 138.1, 137.5, 137.0, 134.8, 134.8, 134.7, 134.5, 134.1, 133.9, 133.6, 133.4, 132.6, 132.5, 132.3, 132.1, 131.8, 131.7, 131.5, 131.4, 131.1, 131.1, 130.8, 130.7, 130.4, 130.3, 130.0, 129.9, 129.8, 129.4, 129.2, 129.2, 129.2, 129.0, 128.8, 128.7, 128.3, 128.3, 128.1, 128.0, 128.0, 127.8, 127.7, 127.7, 127.5, 127.5, 127.3, 127.2, 126.9, 126.9, 126.7, 126.7, 120.0, 120.0, 119.9, 119.8. HRMS (ESI-TOF) *m/z*: $[C_{60}H_{38}Br_2]^+$ calcd for $[C_{60}H_{39}Br_2]^+$ 917.1424; found 917.1422.

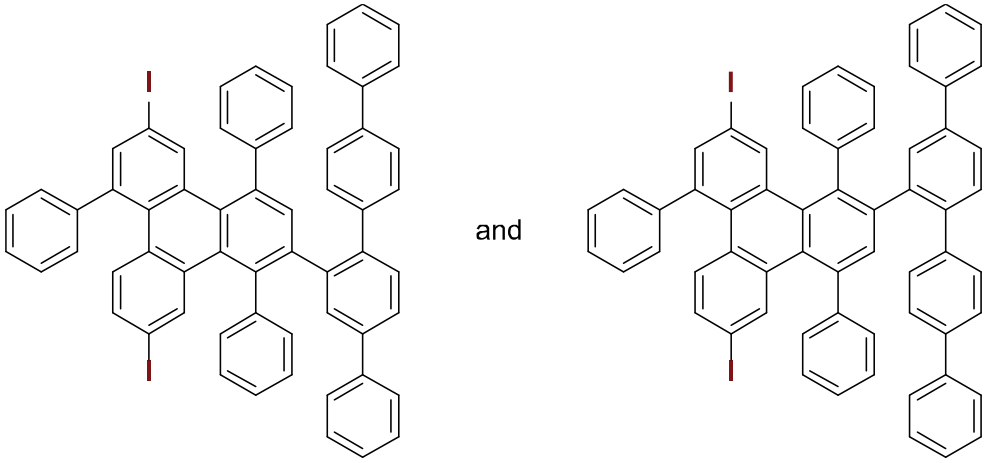

105 mixture of two isomers

2-([1,1':4',1'':4'',1'''-quaterphenyl]-2''-yl)-6,11-diiodo-1,4,9-triphenyltriphenylene (**105**) A 5 mL sealable tube was charged under N_2 with **97** (67 mg, 0.095 mmol) and **104** (47 mg, 0.142 mmol) in degassed *o*-xylene (1 mL). The reaction mixture was stirred 145 °C for 4 hours. The reaction mixture was concentrated on a rotary evaporator. Column chromatography (SiO_2; 0−10% CH_2Cl_2/hexane) yielded **105** (39 mg, 0.038 mmol, 40%) as a mixture of two isomers. Vapor diffusion recrystallization from MeOH/*o*-xylene yielded isomers **105 A:B** as a 2:1 ratio. Recrystallization from layered MeOH/*o*-xylene yielded isomer **105 A:B** as a 1:3 ratio. ^{1}H NMR (600 MHz, CD_2Cl_2, 22 °C, 1:3 mixture of isomers) δ = 7.90 (d, *J* = 1.7 Hz, 1H), 7.82 (s, 1H), 7.77 (d, *J* = 2.0 Hz, 1H), 7.74 (d, *J* = 1.8 Hz, 1H), 7.66 (ddd, *J* = 8.0, 4.1, 1.7 Hz, 3H), 7.60 (d, *J* = 9.8 Hz, 2H), 7.53 – 7.42 (m, 11H), 7.38 – 7.31 (m, 7H), 7.27 – 7.20 (m, 6H), 7.14 (s, 1H), 7.11 (dd, *J* = 5.4, 3.6 Hz, 4H), 7.09 – 7.03 (m, 6H), 7.00 – 6.97 (m, 1H), 6.95 – 6.90 (m, 1H), 6.89 – 6.85 (m, 2H), 6.82 (d, *J* = 8.2 Hz, 1H), 6.22 – 6.15 (m, 2H). ^{13}C NMR (151 MHz, CD_2Cl_2, 22 °C, mixture of 2 isomers) δ = 144.0, 143.4, 143.2, 142.0, 141.9, 141.6, 141.5, 141.3, 141.2, 140.8, 140.5, 140.4, 140.4, 140.3, 140.1, 140.0, 139.9, 139.6, 139.5, 139.2, 139.1, 138.7, 138.6, 138.3, 138.1, 138.0, 137.5, 137.0, 134.8, 134.8, 134.6, 134.4, 134.1, 133.8, 133.5, 133.2, 132.5, 132.3, 132.0, 131.6, 131.4, 131.2, 130.8, 130.4, 130.3, 130.0, 130.0, 129.9, 129.8, 129.8, 129.6, 129.4, 129.3, 129.2, 129.2, 128.3, 128.1, 128.0, 127.9, 127.7, 127.7, 127.5, 127.4, 127.4, 127.3, 126.9, 126.9, 126.8, 126.7, 91.9, 91.7, 91.6, 91.6. HRMS (ESI-TOF) *m*/*z*: $[C_{60}H_{38}I_2]^+$ calcd for $[C_{60}H_{38}I_2]^+$ 1012.1058; found 1012.1066.

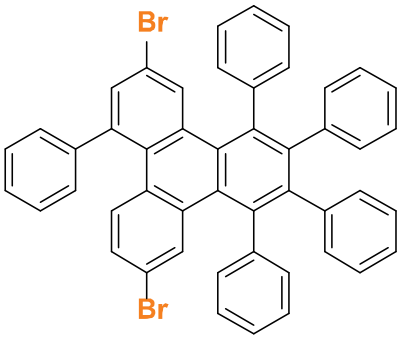

83

6,11-dibromo-1,2,3,4,8-pentaphenyltriphenylene (**83**)A 5 mL sealable tube was charged under N_2 with **80** (60 mg, 0.097 mmol) and 1,2-diphenylethyne (17 mg, 0.097 mmol) in diphenyl ether (21 mg. The reaction mixture was degassed by 2 freeze-pump-thaw cycles. The reaction mixture was stirred 240 °C for 24 hours. The reaction mixture was cooled to 24 °C. Column chromatography (SiO_2; 0–10% CH_2Cl_2/hexane) yielded **83** (19 mg, 0.024. 25% over 2 steps). ^{1}H NMR (400 MHz, CD_2Cl_2, 22 °C) δ = 7.66 (d, *J* = 2.1 Hz, 1H), 7.57 (d, *J* = 2.1 Hz, 1H), 7.47 – 7.31 (m, 6H), 7.29 – 7.02 (m, 13H), 6.99 – 6.89 (m, 5H), 6.87 (dd, *J* = 8.9, 2.0 Hz, 1H), 6.79 – 6.73 (m, 3H). ^{13}C NMR (151 MHz, CD_2Cl_2, 22 °C) δ = 143.5, 142.6, 142.2, 142.1, 142.1, 142.0, 140.6, 140.6, 137.8, 137.4, 137.1, 134.7, 134.6, 133.4, 132.8, 132.5, 132.4, 132.1, 132.0, 131.8, 131.6, 131.4, 131.3, 130.0, 129.8, 129.6, 129.3, 129.0, 128.9, 128.7, 128.0, 127.7, 127.4, 127.3, 127.3, 126.3, 126.1, 126.1, 120.3, 120.1. HRMS (EI$^+$) *m/z*: $[C_{48}H_{30}Br_2]^+$ calcd for $[C_{48}H_{30}Br_2]^+$ 764.0714; found 764.0713.

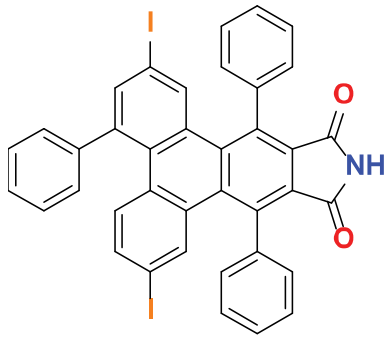

109

2,7-diiodo-4,9,13-triphenyl-10H-phenanthro[9,10-f]isoindole-10,12(11H)-dione (**109**) A 5 mL sealable reaction tube was charged under N_2 with **97** (67 mg, 0.095 mmol) and malemide (10 mg, 0.11 mmol) in nitromethane (1 mL). The reaction mixture was stirred at 210 °C for 24 hours. The reaction mixture was cooled to 24 °C and concentrated to dryness and the resulting solid was sonicated in MeOH and filtered. Column chromatography (SiO_2; 20% acetone/hexane) yielded **109** (15 mg, 0.019 mmol. 20% over 2 steps) as an orange/tan solid. Recrystallization from CH_2Cl_2/MeOH gave analytically pure crystals for surface experiments. ^{1}H NMR (600 MHz,

Acetone, 22 °C) δ = 8.02 (d, *J* = 1.8 Hz, 1H), 7.90 (d, *J* = 1.8 Hz, 1H), 7.70 (d, *J* = 1.8 Hz, 1H), 7.66 (ddt, *J* = 6.7, 5.3, 3.4 Hz, 2H), 7.59 – 7.55 (m, 5H), 7.55 – 7.51 (m, 3H), 7.47 – 7.36 (m, 6H), 7.21 (dd, *J* = 8.7, 1.8 Hz, 1H), 7.14 (d, *J* = 8.7 Hz, 1H). ^{13}C NMR (151 MHz, Acetone, 22 °C) δ = 167.6, 143.1, 142.5, 140.6, 139.2, 138.6, 138.1, 138.1, 137.4, 137.0, 136.3, 135.1, 134.1, 134.0, 132.1, 131.8, 131.6, 130.9, 130.4, 130.1, 130.0, 129.6, 129.5, 129.4, 128.6, 92.3, 92.1. HRMS (ESI-TOF) *m*/*z*: $[C_{38}H_{21}I_2NO_2]^+$ calcd for $[C_{38}H_{20}I_2NO_2]^+$ 775.9589; found 775.9594.

Bibliography

(1) Novoselov, K. S.; Geim, A. K.; Morozov, S. V; Jiang, D.; Zhang, Y.; Dubonos, S. V; Grigorieva, I. V; Firsov, A. A. *Science* **2004**, *306* (5696), 666–669.

(2) Ghosh, S.; Calizo, I.; Teweldebrhan, D.; Pokatilov, E. P.; Nika, D. L.; Balandin, A. A.; Bao, W.; Miao, F.; Lau, C. N. *Appl. Phys. Lett.* **2008**, *92* (15), 151911.

(3) Balandin, A. A.; Ghosh, S.; Bao, W.; Calizo, I.; Teweldebrhan, D.; Miao, F.; Lau, C. N. *Nano Lett.* **2008**, *8* (3), 902–907.

(4) Lee, C.; Wei, X.; Kysar, J. W.; Hone, J. *Science* **2008**, *321* (5887), 385–388.

(5) *Nat. Mater.* **2007**, *6*, 183–191.

(6) Morozov, S.; Novoselov, K.; Katsnelson, M.; Schedin, F.; Elias, D.; Jaszczak, J.; Geim, A. *Phys. Rev. Lett.* **2008**, *100* (1), 016602.

(7) Wang, X.-L.; Dou, S. X.; Zhang, C. *NPG Asia Mater.* **2010**, *2* (1), 31–38.

(8) Cai, J.; Pignedoli, C. A.; Talirz, L.; Ruffieux, P.; Söde, H.; Liang, L.; Meunier, V.; Berger, R.; Li, R.; Feng, X.; Müllen, K.; Fasel, R. *Nat. Nanotechnol.* **2014**, *9* (11), 896–900.

(9) Vo, T. H.; Shekhirev, M.; Kunkel, D. A.; Morton, M. D.; Berglund, E.; Kong, L.; Wilson, P. M.; Dowben, P. A.; Enders, A.; Sinitskii, A. *Nat. Commun.* **2014**, *5* (1), 3189.

(10) Abbas, A. N.; Liu, G.; Narita, A.; Orosco, M.; Feng, X.; Müllen, K.; Zhou, C. *J. Am. Chem. Soc.* **2014**, *136* (21), 7555–7558.

(11) Li, X.; Wang, X.; Zhang, L.; Lee, S.; Dai, H. *Science* **2008**, *319* (5867), 1229–1232.

(12) Stampfer, C.; Güttinger, J.; Hellmüller, S.; Molitor, F.; Ensslin, K.; Ihn, T. *Phys. Rev. Lett.* **2009**, *102* (5).

(13) Liu, J.; Li, B.-W.; Tan, Y.; Giannakopoulos, A.; Sanchez-Sanchez, C.; Beljonne, D.; Ruffieux, P.; Fasel, R.; Feng, X.; Müllen, K. *J. Am. Chem. Soc.* **2015**, *137* (18), 6097–6103.

(14) Mehdi Pour, M.; Lashkov, A.; Radocea, A.; Liu, X.; Sun, T.; Lipatov, A.; Korlacki, R. A.; Shekhirev, M.; Aluru, N. R.; Lyding, J. W.; Sysoev, V.; Sinitskii, A. *Nat. Commun.* **2017**, *8* (1), 820.

(15) Yang, L.; Park, C. H.; Son, Y. W.; Cohen, M. L.; Louie, S. G. *Phys. Rev. Lett.* **2007**, *99* (18).

(16) Son, Y.-W.; Cohen, M. L.; Louie, S. G. *Phys. Rev. Lett.* **2006**, *97* (21), 216803.

(17) Wang, W.-X.; Zhou, M.; Li, X.; Li, S.-Y.; Wu, X.; Duan, W.; He, L. *Phys. Rev. B* **2016**, *93* (24), 241403.

(18) Abbas, A. N.; Liu, G.; Liu, B.; Zhang, L.; Liu, H.; Ohlberg, D.; Wu, W.; Zhou, C. *ACS Nano* **2014**, *8* (2), 1538–1546.

(19) Han, M.; Özyilmaz, B.; Zhang, Y.; Kim, P. *Phys. Rev. Lett.* **2007**, *98* (20), 206805.

(20) Zhang, X.; Yazyev, O. V; Feng, J.; Xie, L.; Tao, C.; Chen, Y.-C.; Jiao, L.; Pedramrazi, Z.; Zettl, A.; Louie, S. G.; Dai, H.; Crommie, M. F. **2012**.

(21) Tapasztó, L.; Dobrik, G.; Lambin, P.; Biró, L. P. *Nat. Nanotechnol.* **2008**, *3* (7), 397–401.

(22) Bai, J.; Duan, X.; Huang, Y. *Nano Lett.* **2009**, *9* (5), 2083–2087.

(23) Kosynkin, D. V.; Higginbotham, A. L.; Sinitskii, A.; Lomeda, J. R.; Dimiev, A.; Price, B. K.; Tour, J. M. *Nature* **2009**, *458* (7240), 872–876.

(24) Cano-Márquez, A. G.; Rodríguez-Macías, F. J.; Campos-Delgado, J.; Espinosa-González, C. G.; Tristán-López, F.; Ramírez-González, D.; Cullen, D. A.; Smith, D. J.; Terrones, M.; Vega-Cantú, Y. I. *Nano Lett.* **2009**, *9* (4), 1527–1533.

(25) Elías, A. L.; Botello-Méndez, A. R.; Meneses-Rodríguez, D.; Jehová González, V.; Ramírez-González, D.; Ci, L.; Muñoz-Sandoval, E.; Ajayan, P. M.; Terrones, H.; Terrones, M. *Nano Lett.* **2010**, *10* (2), 366–372.

(26) Jiao, L.; Zhang, L.; Wang, X.; Diankov, G.; Dai, H. *Nature* **2009**, *458* (7240), 877–880.

(27) Kim, W. S.; Moon, S. Y.; Bang, S. Y.; Choi, B. G.; Ham, H.; Sekino, T.; Shim, K. B. *Appl. Phys. Lett.* **2009**, *95* (8), 083103.

(28) Jiao, L.; Wang, X.; Diankov, G.; Wang, H.; Dai, H. *Nat. Nanotechnol.* **2010**, *5* (5), 321–325.

(29) Wu, Z.-S.; Ren, W.; Gao, L.; Liu, B.; Zhao, J.; Cheng, H.-M. *Nano Res* **2010**, *3*, 16–22.

(30) Yoon, W.; Lee, Y.; Jang, H.; Jang, M.; Kim, J. S.; Lee, H. S.; Im, S.; Boo, D. W.; Park, J.; Ju, S. Y. *Carbon N. Y.* **2015**, *81* (1), 629–638.

(31) Cai, J.; Ruffieux, P.; Jaafar, R.; Bieri, M.; Braun, T.; Blankenburg, S.; Muoth, M.; Seitsonen, A. P.; Saleh, M.; Feng, X.; Müllen, K.; Fasel, R. *Nature* **2010**, *466* (7305), 470–473.

(32) Chen, Y.-C.; de Oteyza, D. G.; Pedramrazi, Z.; Chen, C.; Fischer, F. R.; Crommie, M. F. *ACS Nano* **2013**, *7* (7), 6123–6128.

(33) Talirz, L.; Söde, H.; Dumslaff, T.; Wang, S.; Sanchez-Valencia, J. R.; Liu, J.; Shinde, P.; Pignedoli, C. A.; Liang, L.; Meunier, V.; Plumb, N. C.; Shi, M.; Feng, X.; Narita, A.; Müllen, K.; Fasel, R.; Ruffieux, P. *ACS Nano* **2017**, *11* (2), 1380–1388.

(34) Ruffieux, P.; Wang, S.; Yang, B.; Sanchez-Sanchez, C.; Liu, J.; Dienel, T.; Talirz, L.; Shinde, P.; Pignedoli, C. A.; Passerone, D.; Dumslaff, T.; Feng, X.; Müllen, K.; Fasel, R. *Nature* **2016**, *531* (7595), 489–492.

(35) Durr, R. A.; Haberer, D.; Lee, Y. L.; Blackwell, R.; Kalayjian, A. M.; Marangoni, T.; Ihm, J.; Louie, S. G.; Fischer, F. R. *J. Am. Chem. Soc.* **2018**, *140* (2), 807–813.

(36) Nguyen, G. D.; Toma, F. M.; Cao, T.; Pedramrazi, Z.; Chen, C.; Rizzo, D. J.; Joshi, T.; Bronner, C.; Chen, Y.-C.; Favaro, M.; Louie, S. G.; Fischer, F. R.; Crommie, M. F. *J. Phys. Chem. C* **2016**, *120* (5), 2684–2687.

(37) Marangoni, T.; Haberer, D.; Rizzo, D. J.; Cloke, R. R.; Fischer, F. R. *Chem. - A Eur. J.* **2016**, *22* (37), 13037–13040.

(38) Cloke, R. R.; Marangoni, T.; Nguyen, G. D.; Joshi, T.; Rizzo, D. J.; Bronner, C.; Cao, T.; Louie, S. G.; Crommie, M. F.; Fischer, F. R. *J. Am. Chem. Soc.* **2015**, *137* (28), 8872–8875.

(39) Chen, Y.-C.; Cao, T.; Chen, C.; Pedramrazi, Z.; Haberer, D.; de Oteyza, D. G.; Fischer, F. R.; Louie, S. G.; Crommie, M. F. *Nat. Nanotechnol.* **2015**, *10* (2), 156–160.

(40) Costa, P. S.; Teeter, J. D.; Enders, A.; Sinitskii, A. *Carbon N. Y.* **2018**, *134*, 310–315.

(41) Nguyen, G. D.; Tsai, H. Z.; Omrani, A. A.; Marangoni, T.; Wu, M.; Rizzo, D. J.; Rodgers, G. F.; Cloke, R. R.; Durr, R. A.; Sakai, Y.; Liou, F.; Aikawa, A. S.; Chelikowsky, J. R.; Louie, S. G.; Fischer, F. R.; Crommie, M. F. *Nat. Nanotechnol.* **2017**, *12* (11), 1077–1082.

(42) Rizzo, D. J.; Kalayjian, A. M.; Rodriguez, H.; Louie, S. G.; Crommie, M. F.; Marangoni, T.; Bronner, C.; Fischer, F. R.; Durr, R. A.; Zhao, W.; Lee, Y.-L. *ACS Nano* **2018**, *12* (3), 2193–2200.

(43) Narita, A.; Feng, X.; Hernandez, Y.; Jensen, S. a; Bonn, M.; Yang, H.; Verzhbitskiy, I. a; Casiraghi, C.; Hansen, M. R.; Koch, A. H. R.; Fytas, G.; Ivasenko, O.; Li, B.; Mali, K. S.; Balandina, T.; Mahesh, S.; De Feyter, S.; Müllen, K. *Nat. Chem.* **2014**, *6*, 126–132.

(44) Rogers, C.; Perkins, W. S.; Veber, G.; Williams, T. E.; Cloke, R. R.; Fischer, F. R. *J. Am. Chem. Soc* **2017**, *139*, 14.

(45) Perkins, W.; Fischer, F. R. *Chem. - A Eur. J.* **2017**, *23* (70), 17687–17691.

(46) Narita, A.; Verzhbitskiy, I. A.; Frederickx, W.; Mali, K. S.; Jensen, S. A.; Hansen, M. R.; Bonn, M.; De Feyter, S.; Casiraghi, C.; Feng, X.; Müllen, K. *ACS Nano* **2014**, *8* (11), 11622–11630.

(47) Hu, Y.; Xie, P.; De Corato, M.; Ruini, A.; Zhao, S.; Meggendorfer, F.; Straasø, L. A.; Rondin, L.; Simon, P.; Li, J.; Finley, J. J.; Hansen, M. R.; Lauret, J. S.; Molinari, E.; Feng, X.; Barth, J. V.; Palma, C. A.; Prezzi, D.; Müllen, K.; Narita, A. *J. Am. Chem. Soc.* **2018**, *140* (25), 7803–7809.

(48) Yang, X.; Dou, X.; Rouhanipour, A.; Zhi, L.; Räder, H. J.; Müllen, K. *J. Am. Chem. Soc.* **2008**, *130* (13), 4216–4217.

(49) Li, G.; Yoon, K.-Y.; Zhong, X.; Zhu, X.; Dong, G. *Chem. - A Eur. J.* **2016**, *22* (27), 9116–9120.

(50) El Gemayel, M.; Narita, A.; Dössel, L. F.; Sundaram, R. S.; Kiersnowski, A.; Pisula, W.; Hansen, M. R.; Ferrari, A. C.; Orgiu, E.; Feng, X.; Müllen, K.; Samorì, P. *Nanoscale* **2014**, *6* (12), 6301–6314.

(51) Vo, T. H.; Shekhirev, M.; Lipatov, A.; Korlacki, R. A.; Sinitskii, A. *Faraday Discuss.* **2014**, *173*, 105–113.

(52) Vo, T. H.; Perera, U. G. E.; Shekhirev, M.; Mehdi Pour, M.; Kunkel, D. A.; Lu, H.; Gruverman, A.; Sutter, E.; Cotlet, M.; Nykypanchuk, D.; Zahl, P.; Enders, A.; Sinitskii, A.; Sutter, P. *Nano Lett.* **2015**, *15* (9), 5770–5777.

(53) Vo, T. H.; Shekhirev, M.; Kunkel, D. A.; Orange, F.; Guinel, M. J.-F.; Enders, A.; Sinitskii, A. *Chem. Commun.* **2014**, *50* (32), 4172–4174.

(54) Tan, Y.-Z.; Yang, B.; Parvez, K.; Narita, A.; Osella, S.; Beljonne, D.; Feng, X.; Müllen, K. *Nat. Commun.* **2013**, *4* (1), 2646.

(55) Keerthi, A.; Radha, B.; Rizzo, D.; Lu, H.; Cabanes, V. D.; Cheng-, I.; Hou, Y.; Beljonne, D.; Jérô Me Cornil, J.; Casiraghi, C.; Baumgarten, M.; Mü, K.; Narita, A. **2017**.

(56) Cloke, R. R.; Marangoni, T.; Nguyen, G. D.; Joshi, T.; Rizzo, D. J.; Bronner, C.; Cao, T.; Louie, S. G.; Crommie, M. F.; Fischer, F. R. *J. Am. Chem. Soc.* **2015**.

(57) Casiraghi, C.; Prezzi, D. **2017**.

(58) Verzhbitskiy, I. A.; Corato, M. De; Ruini, A.; Molinari, E.; Narita, A.; Hu, Y.; Schwab, M. G.; Bruna, M.; Yoon, D.; Milana, S.; Feng, X.; Müllen, K.; Ferrari, A. C.; Casiraghi, C.; Prezzi, D. *Nano Lett.* **2016**, *16* (6), 3442–3447.

(59) Malard, L. M.; Pimenta, M. A.; Dresselhaus, G.; Dresselhaus, M. S. *Phys. Rep.* **2009**, *473* (5-6), 51–87.

(60) Zschieschang, U.; Klauk, H.; Müeller, I. B.; Strudwick, A. J.; Hintermann, T.; Schwab, M. G.; Narita, A.; Feng, X.; Müellen, K.; Weitz, R. T. *Adv. Electron. Mater.* **2015**, *1* (3), 1400010.

(61) Bennett, P. B.; Pedramrazi, Z.; Madani, A.; Chen, Y.-C.; de Oteyza, D. G.; Chen, C.; Fischer, F. R.; Crommie, M. F.; Bokor, J. *Appl. Phys. Lett.* **2013**, *103* (25), 253114.

(62) Llinas, J. P.; Fairbrother, A.; Borin Barin, G.; Shi, W.; Lee, K.; Wu, S.; Yong Choi, B.; Braganza, R.; Lear, J.; Kau, N.; Choi, W.; Chen, C.; Pedramrazi, Z.; Dumslaff, T.; Narita, A.; Feng, X.; Müllen, K.; Fischer, F.; Zettl, A.; Ruffieux, P.; Yablonovitch, E.; Crommie, M.; Fasel, R.; Bokor, J. *Nat. Commun.* **2017**, *8* (1), 633.

(63) Wan, L. F.; Cho, E. S.; Marangoni, T.; Shea, P.; Kang, S.; Rogers, C.; Zaia, E.; Cloke, R. R.; Wood, B. C.; Fischer, F. R.; Urban, J. J.; Prendergast, D. *Chem. Mater.* **2019**, *31* (8), 2960–2970.

(64) Huang, Y.; Mai, Y.; Beser, U.; Teyssandier, J.; Velpula, G.; van Gorp, H.; Straasø, L. A.; Hansen, M. R.; Rizzo, D.; Casiraghi, C.; Yang, R.; Zhang, G.; Wu, D.; Zhang, F.; Yan, D.; De Feyter, S.; Müllen, K.; Feng, X. *J. Am. Chem. Soc.* **2016**, *138* (32), 10136–10139.

(65) Shekhirev, M.; Vo, T. H.; Kunkel, D. A.; Lipatov, A.; Enders, A.; Sinitskii, A. *RSC Adv.* **2017**, *7* (86), 54491–54499.

(66) Li, W.; Moon, S.; Wojcik, M.; Xu, K. *Nano Lett.* **2016**, *16* (8), 5027–5031.

(67) Blake, P.; Hill, E. W.; Castro Neto, A. H.; Novoselov, K. S.; Jiang, D.; Yang, R.; Booth, T. J.; Geim, A. K. *Appl. Phys. Lett.* **2007**, *91* (6), 063124.

(68) Hell, S. W. *Science* **2007**, *316* (5828), 1153–1158.

(69) Huang, B.; Babcock, H.; Zhuang, X. *Cell* **2010**, *143* (7), 1047–1058.

(70) Hauser, M.; Wojcik, M.; Kim, D.; Mahmoudi, M.; Li, W.; Xu, K. Correlative Super-Resolution Microscopy: New Dimensions and New Opportunities. *Chemical Reviews*, 2017, *117*, 7428–7456.

(71) Patterson, G.; Davidson, M.; Manley, S.; Lippincott-Schwartz, J. *Annu. Rev. Phys. Chem.* **2010**, *61* (1), 345–367.

(72) Berro, A. J.; Berglund, A. J.; Carmichael, P. T.; Kim, J. S.; Liddle, J. A. *ACS Nano* **2012**, *6* (11), 9496–9502.

(73) Stöhr, R. J.; Kolesov, R.; Xia, K.; Reuter, R.; Meijer, J.; Logvenov, G.; Wrachtrup, J. *ACS Nano* **2012**, *6* (10), 9175–9181.

(74) Boott, C. E.; Laine, R. F.; Mahou, P.; Finnegan, J. R.; Leitao, E. M.; Webb, S. E. D.; Kaminski, C. F.; Manners, I. *Chem. - A Eur. J.* **2015**, *21* (51), 18539–18542.

(75) Kisley, L.; Brunetti, R.; Tauzin, L. J.; Shuang, B.; Yi, X.; Kirkeminde, A. W.; Higgins, D. A.; Weiss, S.; Landes, C. F. *ACS Nano* **2015**, *9* (9), 9158–9166.

(76) Onogi, S.; Shigemitsu, H.; Yoshii, T.; Tanida, T.; Ikeda, M.; Kubota, R.; Hamachi, I. *Nat. Chem.* **2016**, *8* (8), 743–752.

(77) Lieber, E.; Rao, C. N. R.; Chao, T. S.; Hoffman, C. W. W. *Anal. Chem.* **1957**, *29* (6), 916–918.

(78) Liu, Y.; Wang, X.; Wan, W.; Li, L.; Dong, Y.; Zhao, Z.; Qiu, J. *Nanoscale* **2016**, *8* (4), 2159–2167.

(79) Dertinger, T.; Pallaoro, A.; Braun, G.; Ly, S.; Laurence, T. A.; Weiss, S. *Q. Rev. Biophys.* **2013**, *46* (2), 210–221.

(80) Gustafsson, N.; Culley, S.; Ashdown, G.; Owen, D. M.; Pereira, P. M.; Henriques, R. *Nat. Commun.* **2016**, *7* (1), 12471.

(81) Culley, S.; Tosheva, K. L.; Matos Pereira, P.; Henriques, R. *Int. J. Biochem. Cell Biol.* **2018**, *101*, 74–79.

(82) Bahr, J. L.; Tour, J. M. *Chem. Mater.* **2001**, *13* (11), 3823–3824.

(83) *Heterogenized Homogeneous Catalysts for Fine Chemicals Production*; Barbaro, P., Liguori, F., Eds.; Catalysis by Metal Complexes; Springer Netherlands: Dordrecht, 2010; Vol. 33.

(84) Fukuzumi, S.; Lee, Y. M.; Nam, W. Immobilization of Molecular Catalysts for Enhanced Redox Catalysis. *ChemCatChem*, 2018, *10*, 1686–1702.

(85) Ferré, M.; Pleixats, R.; Wong Chi Man, M.; Cattoën, X. *Green Chem.* **2016**, *18* (4), 881–922.

(86) Molnár, Á.; Papp, A. *Coord. Chem. Rev.* **2017**, *349*, 1–65.

(87) Haag, R.; Roller, S. Springer, Berlin, Heidelberg, 2012; pp 1–42.

(88) Oh, S.; Gallagher, J. R.; Miller, J. T.; Surendranath, Y. *J. Am. Chem. Soc.* **2016**, *138* (6), 1820–1823.

(89) Qiao, X.; Li, Q.; Schaugaard, R. N.; Noffke, B. W.; Liu, Y.; Li, D.; Liu, L.; Raghavachari, K.; Li, L. *J. Am. Chem. Soc.* **2017**, jacs.6b12530.

(90) Coates, J. In *Encyclopedia of Analytical Chemistry*; John Wiley & Sons, Ltd: Chichester, UK, 2006.

(91) Schlapbach, L.; Züttel, A. *Nature* **2001**, *414* (6861), 353–358.

(92) Armaroli, N.; Balzani, V. *ChemSusChem* **2011**, *4* (1), 21–36.

(93) Tollefson, J. *Nature* **2010**, *464* (7293), 1262–1264.

(94) GRANT, D. *Solid-State Hydrog. Storage* **2008**, 357–380.

(95) Brewster, T. P.; Miller, A. J. M.; Heinekey, D. M.; Goldberg, K. I. *J. Am. Chem. Soc.* **2013**, *135* (43), 16022–16025.

(96) Zucker, S. P.; Wossidlo, F.; Weber, M.; Lentz, D.; Tzschucke, C. C. *J. Org. Chem* **2017**, *82*, 36.

(97) Söde, H.; Talirz, L.; Gröning, O.; Pignedoli, C. A.; Berger, R.; Feng, X.; Müllen, K.; Fasel, R.; Ruffieux, P. *Phys. Rev. B* **2015**, *91*, 45429.

(98) Wagner, P.; Ewels, C. P.; Adjizian, J. J.; Magaud, L.; Pochet, P.; Roche, S.; Lopez-Bezanilla, A.; Ivanovskaya, V. V; Yaya, A.; Rayson, M.; Briddon, P.; Humbert, B. *J. Phys. Chem. C* **2013**, *117* (50), 26790–26796.

(99) Luo, Y.-R.; Luo, Y.-R. *Comprehensive handbook of chemical bond energies*; CRC Press, 2007.

(100) Ruffieux, P.; Urgel, J. I.; Berger, R.; Feng, X.; Stolz, S.; Muntwiler, M.; Narita, A.; Dumslaff, T.; Müllen, K.; Sánchez-Sánchez, C.; Di Giovannantonio, M.; Dienel, T.; Fasel, R.; Widmer, R.; Deniz, O. *ACS Nano* **2017**, *12* (1), 74–81.

(101) Rizzo, D. J.; Veber, G.; Cao, T.; Bronner, C.; Chen, T.; Zhao, F.; Rodriguez, H.; Louie, S. G.; Crommie, M. F.; Fischer, F. R. *Nature* **2018**, *560* (7717), 204–208.

(102) Merino-Díez, N.; Garcia-Lekue, A.; Carbonell-Sanromà, E.; Li, J.; Corso, M.; Colazzo, L.; Sedona, F.; Sánchez-Portal, D.; Pascual, J. I.; de Oteyza, D. G. *ACS Nano* **2017**, *11* (11), 11661–11668.

(103) Chen, Z.; Wang, H. I.; Bilbao, N.; Teyssandier, J.; Prechtl, T.; Cavani, N.; Tries, A.; Biagi, R.; De Renzi, V.; Feng, X.; Kläui, M.; De Feyter, S.; Bonn, M.; Narita, A.; Müllen, K. *J. Am. Chem. Soc.* **2017**, *139* (28), 9483–9486.

(104) Abdurakhmanova, N.; Amsharov, N.; Stepanow, S.; Jansen, M.; Kern, K.; Amsharov, K. *Carbon N. Y.* **2014**, *77*, 1187–1190.

(105) Aghdassi, N.; Franke, J. H.; Zhong, D.; Müllen, K.; Linden, S.; Zacharias, H.; Feng, X.; Timmer, A.; Fuchs, H.; Chi, L.; Zhang, H. *Phys. Rev. Lett.* **2012**, *108* (21), 216801.

(106) Jacobberger, R. M.; Kiraly, B.; Fortin-Deschenes, M.; Levesque, P. L.; McElhinny, K. M.; Brady, G. J.; Rojas Delgado, R.; Singha Roy, S.; Mannix, A.; Lagally, M. G.; Evans, P. G.; Desjardins, P.; Martel, R.; Hersam, M. C.; Guisinger, N. P.; Arnold, M. S. *Nat. Commun.* **2015**, *6* (1), 8006.

(107) Kiraly, B.; Mannix, A. J.; Jacobberger, R. M.; Fisher, B. L.; Arnold, M. S.; Hersam, M. C.; Guisinger, N. P. *Appl. Phys. Lett.* **2016**, *108* (21), 213101.

(108) Gerowska, M.; Hall, L.; Richardson, J.; Shelbourne, M.; Brown, T. *Tetrahedron* **2012**, *68* (3), 857–864.

(109) Comba, P.; Krämer, R.; Mokhir, A.; Naing, K.; Schatz, E. *Eur. J. Inorg. Chem.* **2006**, *2006* (21), 4442–4448.

(110) Bravo, V.; Gil, S.; Costero, A. M.; Kneeteman, M. N.; Llaosa, U.; Mancini, P. M. E.; Ochando, L. E.; Parra, M. *Tetrahedron* **2012**, *68* (24), 4882–4887.

(111) Andrievskii, A. M.; Gorelik, M. V; Linko, R. V; Grachev, M. K. *ISSN Russ. J. Org. Chem. Orig. Russ. Text ©* **2013**, *49* (10), 1070–4280.

(112) Rapenne, G.; Jimenez-Bueno, G. *Tetrahedron* **2007**, *63*, 7018–7026.

(113) Dempsey, G. T.; Bates, M.; Kowtoniuk, W. E.; Liu, D. R.; Tsien, R. Y.; Zhuang, X. *J. Am. Chem. Soc.* **2009**, *131* (51), 18192–18193.

(114) Durr, R. A. The Rational Design and Synthesis of Graphene Nanoribbons and Graphene Nanoribbon Functional Nanoarchitectures, 2017.